2015

Proxy Development and Application for Reconstructing the Surface Ocean Carbonate System

Brittney J. Marshall
University of South Carolina - Columbia

PROXY DEVELOPMENT AND APPLICATION FOR RECONSTRUCTING THE SURFACE OCEAN CARBONATE SYSTEM

by

Brittney J. Marshall

Bachelor of Science
College of Charleston, 2009

Submitted in Partial Fulfillment of the Requirements

For the Degree of Doctor of Philosophy in

Geological Sciences

College of Arts and Sciences

University of South Carolina

2015

Accepted by:

Robert C. Thunell, Major Professor

Claudia Benitez-Nelson, Committee Member

Howie D. Scher, Committee Member

Howard J. Spero, Committee Member

Lacy Ford, Vice Provost and Dean of Graduate Studies

DEDICATION

I am deeply thankful for the guidance and support of the teachers, faculty members and fellow students that I have interacted with throughout my 12 years of higher education. No professor has inspired me as much as my undergraduate advisor, Dr. Leslie Sautter of the College of Charleston. She showed me that a woman can not only succeed and excel in science, but she can do so without sacrificing part of what defines her as a woman: compassion, enthusiasm, optimism, and a desire to educate and inspire. For this, and for her ever-lasting support, I dedicate my dissertation to Leslie.

In regards to support, no one has shown me so much as my wonderful husband, who understands so little of science, but will listen to me talk about it for hours. He does this because he wants nothing more than for me to succeed in my career and to be proud of what I've accomplished. Thanks for the breakfasts in bed, the words of encouragement and for being proud of me when I can't quite manage to be proud of myself. Most of all, thank you for taking on the challenge of marrying a Ph.D. student in her fourth year and for hanging in there over the last few months of barely contained insanity. For your commitment and all around amazingness, I also dedicate my dissertation to you, (Magic) Matt Kesser.

ACKNOWLEDGEMENTS

A million times thank you to Eric Tappa and Wayne Buckley for their assistance with data collection throughout my Ph.D. Thank you to our undergraduate researchers, Katie Radke, Amanda Williams, Jessica Holm, and Courtney Swink for your help with the tedious task of picking and weighing forams. Thank you to my lab mates Emily Osborne and Natalie Umling for all of the scientific banter and the amazing friendships. Thank you to Michael Henehan for being my science soul mate, for including me on so many of your research endeavors and for being part of mine. Thank you to Sambuddha Misra and Michael Bizimis for your geochemistry advice and for being my favorite know-it-alls. Thank you to my committee members, Claudia Benitez-Nelson, Howie Scher and Howie Spero for all of your advice and encouragement. Thank you to my family for all of the love and support you've given me throughout my life. Most importantly, thank you to Bob Thunell for being an amazing advisor and human being. Joining your lab was the best decision of my academic career and I treasure your mentorship and kindness. #bestbossever. =)

Funding for this research was provided by NSF awards 1039503, 0752037 and 1258991, as well as a 2014 University of South Carolina School of Arts and Sciences Dean's Dissertation Fellowship.

ABSTRACT

Over the last two centuries, human activities have led to an unprecedented rate of carbon input into the atmosphere and oceans resulting in an alarmingly rapid decline in surface ocean pH, a process referred to as ocean acidification (OA). This process is leading to an observed decline in the carbonate ion concentrations ($[CO_3^{2-}]$) in seawater – an ion that a large number of marine organisms (e.g. corals, foraminifera) utilize to secrete their skeletons and shells. The ability to identify past ocean acidification events using the marine sedimentary record can shed light on future impacts of the modern OA dilemma. Planktonic foraminifera have the ability to record the physical and chemical properties of the seawater in which they calcified, therefore the fossil shells of foraminifera serve as archives for past climatic and oceanographic conditions. Here, we present a new proxy surface ocean $[CO_3^{2-}]$ – planktonic foraminferal area density – and establish methods for a known proxy for surface ocean pH – the boron isotopic composition of foraminiferal calcite ($\delta^{11}B$). These proxies are used to reconstruct changes in the surface ocean carbonate system of the eastern equatorial Pacific over the last 35, 000 years using marine sediment core TR163-19 collected from the Cocos Ridge (2°16'N, 90°57'W, 2,348 m). The stable carbon and oxygen isotopic compositions of two morphotypes of planktonic foraminifer *Orbulina universa* collected from the Cariaco Basin, Venezuela are also investigated, with results suggesting that the two morphotypes record different environmental signals in the calcite shells and should not be used together during paleoceanographic reconstructions.

TABLE OF CONTENTS

LIST OF TABLES

LIST OF FIGURES

CHAPTER 1

PLANKTONIC FORAMINIFERAL AREA DENSITY AS A PROXY FOR SURFACE OCEAN CARBONATE ION CONCENTRATION: A CALIBRATION STUDY FROM THE CARIACO BASIN, VENEZUELA[1]

[1]Marshall, B.J., Thunell, R.C., Henehan, M.J., Astor, Y., Wejnert, K.E. (2013), *Paleoceanography* 28, 363–376. Reprinted with permission of publisher.

1.1 ABSTRACT

Biweekly sediment trap samples and concurrent hydrographic measurements collected between March 2005 and October 2008 from the Cariaco Basin, Venezuela are used to assess the relationship between $[CO_3^{2-}]$ and the area densities (ρ_A) of two species of planktonic foraminifera (*Globigerinoides ruber* (pink) and *Globigerinoides sacculifer)*. Calcification temperatures were calculated for each sample using species-appropriate oxygen isotope ($\delta^{18}O$) temperature equations that were then compared to monthly temperature profiles taken at the study site in order to determine calcification depth. Ambient $[CO_3^{2-}]$ was determined for these calcification depths using alkalinity, pH, temperature, salinity, and nutrient concentration measurements taken during monthly hydrographic cruises. ρ_A, which is representative of calcification efficiency, is determined by dividing individual foraminiferal shell weights (± 0.43 μg) by their associated silhouette areas and taking the sample average. The results of this study show a strong correlation between ρ_A and ambient $[CO_3^{2-}]$ for both *G. ruber* and *G. sacculifer* ($R^2 = 0.89$ and 0.86 respectively), confirming that $[CO_3^{2-}]$ has a pronounced effect on the calcification of these species. Though the ρ_A for both species reveal a highly significant ($p < 0.001$) relationship with ambient $[CO_3^{2-}]$, linear regression reveals that the extent to which $[CO_3^{2-}]$ influences foraminiferal calcification is species-specific. Hierarchical regression analyses indicate that other environmental parameters (temperature and $[PO_4^{3-}]$) do not confound the use of *G. ruber* and *G. sacculifer* ρ_A as a predictor for $[CO_3^{2-}]$. This study suggests that *G. ruber* and *G. sacculifer* ρ_A can be used as reliable proxies for past surface ocean $[CO_3^{2-}]$.

1.2 INTRODUCTION

Changes in the carbon dioxide (pCO_{2aq}) concentration of the oceans alter surface ocean pH and in turn seawater carbonate ion concentrations [CO_3^{2-}]. Over the last two centuries, anthropogenic input of carbon into the atmosphere and oceans has resulted in an unprecedented rapid decline in surface ocean pH, a process referred to as ocean acidification [OA; *Caldiera and Wickett*, 2003, *Honisch et al.*, 2012; *Zeebe et al.*, 2012]. Though the uptake of ~30% of the anthropogenic CO_2 by the ocean has mitigated modern pCO_{2atm} rise [*Sabine et al.*, 2004], the resulting decline in calcite and aragonite saturation states has had an adverse effect on several key marine organisms and ecosystems [*Riebesell et al.*, 2000; *Caldiera and Wicket*, 2003; *Orr et al.*, 2005; *Hoegh-Guldberg et al.*, 2007, *Moy et al.*, 2009]. With some exceptions [*Iglesias-Rodriquez et al.*, 2008; *Ries et al.*, 2009], marine calcifiers - including several species of planktonic foraminifera - have exhibited reduced rates of calcification when grown in low pH and low [CO_3^{2-}] waters [Table 1.1; *Spero et al.*, 1997; *Bijma et al.*, 1999, 2002; *Wolf-Gladrow et al.*, 1999; *Riebesell et al.*, 2000; *Russell et al.*, 2004; *Lombard et al.*, 2010; *Manno et al.,* 2012]. In addition to having an adverse effect on the calcification efficiency of these organisms, a reduction in calcification rates of marine plankton will likely have a significant impact on the marine carbon cycle, as calcification is a process that increases aqueous CO_2 [*Wolf-Gladrow et al.*, 1999; *Zeebe and Wolf-Gladrow*, 2001]. Thus, on short time scales a decrease in calcification will result in an increase in the ocean's ability

to take up atmospheric CO_2 [*Feely et al.*, 2004], but would ultimately reduce the total flux of calcite and organic carbon to the deep ocean over longer time scales, which serves as a significant long-term carbon sink [*Armstrong et al.*, 2002; *Klass and Archer*, 2002; *Ridgwell and Zeebe*, 2005; *Zeebe*, 2012].

Since planktonic foraminifera are responsible for up to 80% of the total calcium carbonate ($CaCO_3$) accumulated in surface sediments [*Schiebel*, 2002], it is important to understand the extent to which their calcification will be affected by decreasing [CO_3^{2-}] associated with OA. The quantification of the relationship between [CO_3^{2-}] and planktonic foraminiferal calcification provides a useful proxy for determining past changes in ocean carbonate chemistry, as well as estimates of past pCO_{2atm}. It has been shown that a positive linear relationship exists between planktonic foraminiferal size-normalized shell weight (SNW) and ambient [CO_3^{2-}] [*Spero et al.*, 1997; *Bijma et al.*, 1999, *Barker and Elderfield*, 2002]. Rates of calcification increase in conjunction with increasing seawater [CO_3^{2-}], resulting in a thickening of the shell wall and an increase in mean shell weight [*Spero et al.*, 1997; *Bijma et al.*, 1999; *Russell et al.*, 2004].

Culture studies have shown a decline in calcification efficiency with decreasing [CO_3^{2-}] for a wide variety of foraminiferal species commonly used in paleoclimatic and paleoceanographic reconstructions (Table 1.1). Most studies of sediment core and water column material (plankton tow and sediment trap) report a stronger influence of [CO_3^{2-}] on foraminiferal calcification than what has been reported in culture studies (Table 1.1). It has been suggested that the shallower slopes reported in culture studies could have been a result of the foraminifera not having completed their entire life cycle in culture conditions [*Bijma et al.*, 2002].

Additional differences amongst studies investigating the influence of $[CO_3^{2-}]$ on foraminiferal calcification arise from the variety of methodologies used to estimate changes in calcification. While some studies estimate or measure calcification rate or shell thickness, most studies use SNW to estimate a change in shell thickness or density in response to changes in $[CO_3^{2-}]$ (Table 1.1). In order to isolate the contribution of shell thickness to weight measurements, the influence of size on the overall weight of the foraminiferal test must be taken into account. Prior studies have examined the relationship between $[CO_3^{2-}]$ and shell weight using two general methods for size normalization: sieve-based weight [SBW; *Broecker and Clark*, 2001a, *Naik et al.*, 2010, *de Villiers*, 2004] and measurement-based weight [MBW; *Barker and Elderfield*, 2002, *Beer et al.*, 2010a, *Aldridge et al.*, 2012]. The SBW is the simpler of the two methods, in which the mean bulk weights are determined from traditionally used narrow size fractions. The use of MBW, which is a more effective method for reducing the influence of size on weight measurements [*Beer at al.*, 2010b], normalizes mean bulk weights taken from narrow size fractions using equation (1) below, where *parameter* refers to either silhouette area or diameter:

$$\mathrm{MBW}_{\mathrm{parameter}} = \frac{\text{mean SBW}_{\mathrm{sample}} \times \text{mean parameter}_{\text{size fraction}}}{\text{mean parameter}_{\mathrm{sample}}} \qquad (1)$$

Most SNW studies, regardless of the normalization method used, reveal a positive linear relationship between foraminiferal shell weights and $[CO_3^{2-}]$, although there are significant inter and intra-species differences (Table 1.1). However, a number of studies have found contradictory results, reporting either a negative [*G. ruber* (white); *Beer et al.*, 2010a] or no relationship [*Neogloboquadrina pachyderma*; *de Villiers*, 2004,

Gonzelez-Mora et al., 2008] between shell weight and [CO_3^{2-}]. In these cases, it was suggested that other environmental parameters, or more generally optimal growth conditions [*de Villiers*, 2004], govern calcification efficiency for these species.

A temperature effect on foraminiferal calcification has been reported in a number of studies [*Bé et al.*, 1973, *Hecht*, 1976, *Hemleben et al.*, 1987, *Schmidt et al.*, 2004, *Lombard et al.,* 2009]. These studies indicate that the size of foraminiferal tests varies with temperature, giving an additional reason for size normalization when using shell weight as a proxy for [CO_3^{2-}]. Likewise, several studies have reported a potential relationship between SNW and temperature [*Barker and Elderfield*, 2002, *Beer et al.*, 2010a, *Aldridge et al.*, 2011]. However, this observed relationship between SNW and temperature can also be explained by a [CO_3^{2-}] effect as the two parameters co-vary in surface waters. *Barker and Elderfield* [2002] evaluated the influence of temperature on *Globigerina bulloides* SNW by comparing shell weights across the most recent glacial-interglacial transition. They found that average shell weights were higher during the last glacial period when SST was low and [CO_3^{2-}] was high, concluding that [CO_3^{2-}], not temperature, was the dominant factor influencing calcification rates. A recent culture study using *N. pachyderma* (sinistral) specimens showed that the calcification rates of both juvenile and adult specimens decreased by 30% and 21%, respectively when grown in low [CO_3^{2-}] waters, but were unaffected by an increase in ambient temperature while keeping [CO_3^{2-}] constant [*Manno et al.*, 2012].

Other authors have suggested that nutrient concentrations ([PO_4^{3-}] and [NO_3^-]) may affect foraminiferal calcification efficiency – either by enhancing calcification [*Bijma et al.*, 1992; *Barker and Elderfield*, 2002] or by hindering it [*Aldridge et al.*,

2012]. For example, based on a North Atlantic plankton tow study, *Aldridge et al.* [2012] found that the MBW of *G. bulloides* had a strong negative correlation with $[PO_4^{3-}]$. However, *Aldridge et al.* [2012] do not consider the strong collinearity that exists between $[PO_4^{3-}]$ and $[CO_3^{2-}]$ ($R^2 = -0.85$). Simply put, when $[PO_4^{3-}]$ is increasing in surface waters, $[CO_3^{2-}]$ is decreasing, making it difficult to determine which environmental parameter best explains the observed variability in *G. bulloides* MBW.

The objective of the current study is to better quantify the relationship between foraminiferal calcification and $[CO_3^{2-}]$ by utilizing a more precise method of eliminating the contribution of shell size to shell weight through area density (ρ_A; $\mu g/\mu m^2$) calculations. The method for deriving ρ_A presented in this study uses the weight and silhouette area of individual shells of *G. ruber* (355-650 μm) and *G. sacculifer* (425-850 μm), allowing for the use of a broad size fraction while investigating the relationship between calcification efficiency and ambient $[CO_3^{2-}]$. The Cariaco Basin, Venezuela is an ideal study area to investigate the relationship between seawater $[CO_3^{2-}]$ and planktonic foraminiferal ρ_A as this region is characterized by the seasonal upwelling of low pH, low temperature, and low $[CO_3^{2-}]$ waters. In this study, we use linear regression modeling to investigate the relationships amongst foraminiferal ρ_A, ambient $[CO_3^{2-}]$, temperature and $[PO_4^{3-}]$ at the depth of calcification.

1.3 The Cariaco Basin

1.3.1 Regional Setting

The Cariaco Basin is located on the continental shelf of northern Venezuela and is

divided into two sub-basins by a 900 m saddle (Figure 1.1). Climatological conditions in the basin are controlled by the seasonal migration of the Intertropical Convergence Zone (ITCZ) and the associated latitudinal position of the easterly Trade Winds. The ITCZ is in its most southerly position during the boreal winter and early spring (November – May). During this time the easterlies are positioned over the basin and generate Ekman-induced upwelling, which results in minimum sea surface temperatures (~22°C), maximum salinity (>36.8), elevated nutrient concentrations and high primary production [*Thunell et al.*, 2000; *Muller-Karger et al.*, 2001; 2010; *Goñi et al.*, 2003]. During the summer and early fall (August – October) the ITCZ migrates to its most northerly position; trade winds decrease over the basin and upwelling ceases, allowing sea surface temperatures to reach their maximum (~28-29°C), while nutrient concentrations and primary production are mutually diminished. The northerly position of the ITCZ over the Cariaco Basin at this time also increases precipitation, resulting in lower salinities in the surface waters (< 36.6).

The CARIACO oceanographic time series began in November 1995 with the goal of providing a link between surface processes and the sediment record [*Muller-Karger et al.*, 2000, 2001; *Thunell et al.*, 2000; *Goñi et al.*, 2003]. A bottom tethered mooring (10°30′ N and 65°31′ W) with automated sediment traps at five depths (150, 230, 410, 800, and 1200 m) continuously measures the flux of settling particles and provides bi-weekly samples that can be examined and compared to monthly hydrographic data. The samples used in this study are from the upper three sediment traps. The planktonic foraminifera collected from these samples display excellent preservation, with specimens frequently having intact spines. Since its inception, the program has collected a wide-

range of hydrographic data at discrete depths throughout the water column (0 - 1300 m) on a monthly basis. All hydrographic data for the Cariaco Time Series is archived at http://www.imars.usf.edu/CAR.

1.3.2 The Carbonate System in the Cariaco Basin

The ocean carbonate system can be quantitatively defined by the following six parameters: total dissolved inorganic carbon (DIC), total alkalinity (A_T), pH, [CO_3^{2-}], total CO_2 in seawater ([CO_2] = [$CO_{2(aq)}$] + H_2CO_3), and bicarbonate ([HCO_3^-]). One can use the combination of any two of these parameters, in combination with temperature, salinity, pressure, and nutrient concentrations, to calculate the entire carbonate system [see *Zeebe and Wolf-Gladrow*, 2001 and *Zeebe*, 2012 for a review of the carbonate system]. For our study, pH and total alkalinity are the only two parameters directly measured during the monthly hydrographic cruises. The carbonate system in the Cariaco Basin is influenced by a number of water column biogeochemical processes including primary production and respiration, $CaCO_3$ precipitation and dissolution, and the remineralization and consumption of organic matter [*Astor et al.*, 2005]. Additionally, physical factors such as seasonal upwelling, changes in evaporation and precipitation ratios, advection of Caribbean waters into the basin, air-sea gas exchange, and riverine input also impact the carbonate system in the basin. These processes collectively yield surface water (1 m depth) pH values that range from 8.03 to 8.11 during the study period (March 2005 – September 2008) [http://www.imars.usf.edu/CAR]. The oxidation of organic matter in the basin, coupled with increased CO_2 solubility associated with decreasing water temperatures, causes a rapid decline in pH values with increasing depth.

These processes, in combination with a lower average alkalinity at intermediate depths (2407 μmol/kg at 100 m vs. 2418 μmol/kg at the surface), yield an average pH value of 7.91 at 100 m depth throughout the course of the study period.

1.4 Materials and Methods

1.4.1 Foraminiferal Collection

Bi-weekly sediment trap samples were collected between May 2005 and September 2008 in cups containing a buffered formalin solution, ensuring good preservation of the foraminiferal tests. Shells of planktonic foraminiferal species *G. ruber* and *G. sacculifer* were separated from the sediment trap samples using the settling method described by *Bé et al.* [1959]. The shells were washed, wet sieved (> 125 μm) and examined under a stereo binocular microscope. After washing, microscopic observation of the foraminiferal tests revealed clean surfaces, free of surficial organic matter (OM). All *G. ruber* (pink) and G. *sacculifer* (sac-less) individuals were wet picked and allowed to dry (> 1 week) prior to weighing in an environmentally-controlled weighing room. Following a 45-minute oxidative treatment (30% H_2O_2 with 0.1M NH_4OH) on a select number of samples (n =4), it was determined that differences between the pre and post-treatment shell weights within the analytical error associated with the weight measurements (±0.43 μg, repeat weighing of individual *Orbulina universa*; n = 60). This indicates that the settling and washing techniques were efficient in removing surficial OM and that oxidative cleaning is unnecessary for the samples used

in this study. The microscopic imaging program Macnification 2.0 (Orbicule – Mac OS X Leopard) was used to sort *G. ruber* (355-650 μm) and *G. sacculifer* (425-850 μm) into their corresponding size fractions based on Feret's diameter (the longest distance between two points on the test).

1.4.2 Area Density Analysis

Individual foraminiferal shells from each sample population were weighed using a Metler Tolledo microbalance and photographed with an inverted light microscope for size analysis. Macnification 2.0 uses an RGB-filter to determine individual foraminiferal 2-D (silhouette) areas. Calibration for the silhouette area and Feret's diameter measurements was performed using a microscale image taken at the same magnification as the foraminiferal images (50x). Foraminiferal shells are positioned to capture the maximum silhouette area of each individual, corresponding to the umbilical or spiral sides for both *G. ruber* and *G. sacculifer*. The difference in average areas for the spiral and umbilical orientations were determined to be negligible based on analyses performed on sample populations of *G. ruber* (n = 15, area difference between orientations = 0.15 %) and *G. sacculifer* (n = 12, area difference between orientations = 0.40 %). ρ_A ($\mu g/\mu m^2$) is determined by dividing individual weights by their corresponding silhouette area and taking the sample average (n > 10, mean = 18).

1.4.3 Temperature Calculations and Calcification Depths

Randomly selected individuals (n = 4 to 8) from each sample population were

analyzed for oxygen isotope composition to determine calcification temperature. Oxygen isotope analyses were performed on a GV IsoPrime stable isotope ratio mass spectrometer (long-term standard reproducibility = ±0.07‰) and are reported relative to Vienna Pee Dee Belemnite (V-PDB). Calcification temperatures for each sample were determined using the following species-appropriate $\delta^{18}O$- temperature equations:

G. ruber (*Bemis et al.*, 1998): $T\ (^{\circ}C) = 14.90 - 4.80\ (\delta_c - \delta_w)$ (2)

G. sacculifer (*Mulitza et al.*, 2003): $T\ (^{\circ}C) = 14.91 - 4.35\ (\delta_c - \delta_w)$ (3)

Where δ_c is the $\delta^{18}O$ of the foraminiferal calcite and δ_w is the $\delta^{18}O$ of the calcifying waters. Time-equivalent $\delta^{18}O_w$- estimates were established using the $\delta^{18}O_w$-salinity equations from *McConnell et al.* [2009] for the Cariaco Basin for both upwelling (equation 4) and non-upwelling conditions (equation 5).

$\delta^{18}O_w = 0.80\ (\pm 0.08) \times (\text{salinity}) - 28.53\ (\pm 3.0)$ (4)

$\delta^{18}O_w = 0.27\ (\pm 0.04) \times (\text{salinity}) - 8.77\ (\pm 1.3)$ (5)

The $\delta^{18}O_w$ values are scaled from SMOW to PDB by subtracting 0.27‰ [*Bemis et al.*, 1998]. The $\delta^{18}O$-derived calcification temperatures were then compared to the measured water column temperatures to determine calcification depths and the associated

instrumental temperature, salinity, nutrient, pH and alkalinity needed for calculating $[CO_3^{2-}]$. It should be noted that a $[CO_3^{2-}]$- δ_c relationship has been observed in culture studies (Spero et al., 1997). To our knowledge, no calibration of this relationship exists for either *G. ruber* or *G. sacculifer* making it difficult to model this effect on the samples used in this study. Using the $\Delta\delta^{18}O$-$[CO_3^{2-}]$ model presented in King and Howard (2005), where $\Delta\delta^{18}O$ is the difference between the measured δ_c from the foraminiferal samples and the predicted δ_c based on the instrumental temperatures., we find that there is no correlation between $[CO_3^{2-}]$ and $\Delta\delta^{18}O$ for the sediment trap samples used in this study, suggesting that $[CO_3^{2-}]$ is not a controlling factor for this offset.

1.4.4 Carbonate Parameter Calculations

Monthly records of aqueous $[CO_3^{2-}]$ were generated for the study site using CO2SYS.xls [*Pelletier et al.* 2007, version 16] and the constants of *Lueker et al.* [2000] and *Dickson et al.* [1990]. $[CO_3^{2-}]$ values were calculated for the upper 130 meters at discrete depth intervals (1, 7, 15, 25, 35, 55, 75, 100, 130 m) using A_T, pH, temperature, salinity, and nutrient concentration measurements taken during monthly hydrographic cruises, and accounting for the depth (i.e. pressure) of collection. The measurement error for $[CO_3^{2-}]$, calculated from the errors associated with each carbonate parameter used for its calculation, is less than ± 1.3 μmol/kg for all the samples used in this study. A comprehensive description of the methodologies used to collect monthly hydrographic data in the Cariaco Basin can be found at http://www.imars.usf.edu/CAR.

Assuming an average three-week life span for both *G. ruber* and *G. sacculifer* [*Bijma et al.*, 1990] and a 1-day settling period to reach the trap depths of 150 and 410 m

[sinking speed = 300 m/day; *Takahashi and Bé*, 1984], the foraminifera collected in the biweekly sediment traps calcified in waters 8 to 22 days prior to the time the trap opened for collection. Thus, in all possible cases, we used hydrographic data that fell close to or within this range of day difference to pair with the average foraminiferal ρ_A.

1.4.5 Regression Analyses

Simple, multiple and hierarchical regression analyses [IBM SPSS; *Miles and Shevlin*, 2001] were used to quantify the relationships between the response variable (foraminiuferal ρ_A) and the predictor variables ($[CO_3^{2-}]$, temperature and $[PO_4^{3-}]$). Simple linear regression analysis (SLR) was used to determine the bivariate relationship between individual response and predictor variables. Various types of multiple linear regression analyses (MLR) were performed to examine the relationships between ρ_A and the predictor variables, as well as to examine the covariance amongst the predictor variables themselves. Both SLR and MLR can yield unreliable statistical outcomes for cases of multiple co-varying predictor variables – a condition called collinearity or multicollinearity. Collinearity can be an issue in upwelling systems such as the Cariaco Basin as it is difficult to de-couple co-varying environmental variables and determine the actual amount each variable contributes to changes in the response variable (e.g. ρ_A). To examine the collinearity amongst the three predictor variables, two types of MLR were performed. The first used each predictor variable in turn as the dependent variable and the other two predictor variables as the dependent variables (Table 1.2). The coefficient of determination (R^2) resulting from these multivariate regression analyses is indicative of the amount of variance shared by the dependent variable (one of the predictor

variables) with the independent variables (the other two predictor variables), essentially quantifying the redundancy one predictor variable shares with the other predictor variables. Two other collinearity diagnostics, tolerance ($1-R^2$) and variance inflation factor (VIF; $(1-R^2)^{-1}$), were determined using MLR with ρ_A as the dependent variable and $[CO_3^{2-}]$, temperature and $[PO_4^{3-}]$ as the independent variables (Table 1.3). Collinearity in two or more predictor variables will inflate the variance and standard errors associated with a regression analysis, thus a strong R^2 is the result of redundant predictor variables as opposed to a set of good independent predictor variables. In general, tolerance values below 0.50 and VIF values above 2 are indicative of an issue with collinearity amongst the independent variables [*Miles and Shevlin*, 2001].

One way the current study addresses the issue of collinearity by leaving the values for one predictor variable (X_1) unchanged, but removing its covariance with the other two predictor variables (X_2, X_3) by regressing them on X_1 and generating their residuals. For example, the residuals of temperature and $[PO_4^{3-}]$ (T_{Cres}, $[CO_3^{2-}]$ and $[PO_4^{3-}]_{res}$, $[CO_3^{2-}]$) were quantified using equations 11 and 12 for *G. ruber* and 17 and 18 for *G. sacculifer* from Table 1.4 in order to determine the predicted values for calcification temperature and phosphate concentrations based on their relationship with $[CO_3^{2-}]$. The residuals were then calculated by subtracting the predicted values from the measured values. The residuals represent the variability in temperature and phosphate that is unrelated to their covariance with $[CO_3^{2-}]$. By using the residuals as opposed to the original calcification temperature and phosphate concentrations, we are able to estimate what additional influence these parameters have on *G. ruber* and *G. sacculifer* ρ_A once $[CO_3^{2-}]$ has been considered. Hierarchical multiple regression analysis (HMR) was used to determine the

relative predictive capabilities of each variable for *G. ruber* and *G. sacculifer* ρ_A by assessing the change in R^2 (ΔR^2) and the significance of this change ($p\ \Delta R^2$) as each predictor variable is added sequentially to the regression model. In addition to the R^2, ΔR^2, and $p\ \Delta R^2$, the beta or standardized coefficient (β) is also reported as this is indicative of the percentage of a standard deviations (SD) that the response variable (ρ_A) would change for a 1 SD change in the predictor variable (Tables 1.5 and 1.6). Each model assumes that X_1 is the dominant predictor variable and assesses the relative contributions of X_2 and X_3 while holding all previously added variable(s) constant (Tables 1.5). When using HMR, each predictor variable is added to the regression equation in an order specified by the researcher based on prior observations or an established theory. For the first model, we use the results of previous studies (*Barker and Elderfield*, 2002; *Naik et al.*, 2010; *Manno et al.*, 2012) to establish the order of the variables, using $[CO_3^{2-}]$ as X_1 and T_{Cres}, $[CO_3^{2-}]$ and $[PO_4^{3-}]_{res}$, $[CO_3^{2-}]$ as X_2 and X_3, respectively.. Models 2-4 placed the residuals of $[CO_3^{2-}]$ either second or third during HMR to determine if it still contributed significantly to predicting ρ_A once the other variables had been considered.

1.5 Results and Discussion

1.5.1 Size-Fraction Relevance and Utilization

A potential limiting factor in traditional SNW studies is the requirement that samples be restricted to narrow size fractions in an attempt to eliminate the contribution of size to the measured weights. However, the use of narrow size fractions may limit the

number of foraminiferal shells per sample and a small sample size increases the error associated with size-normalized weight or ρ_A estimations as defined by the following error estimation equation [*Beer et al.*, 2010a; *Aldridge et al.*, 2012]:

$$\text{SNW or } \rho_A \text{ error} = \text{SNW or } \rho_A \times (n)^{-1} \quad (6)$$

A large number of individuals per sample greatly decrease the chances of having biased weight or ρ_A estimations. In this study, shell weight and silhouette area estimates were made for individual foraminifera as opposed to groupings of individuals, allowing for the application of ρ_A analysis over a wider size-fraction (425-850 μm for *G. sacculifer* and 355-650 μm for *G. ruber*). SLR comparing ρ_A to the mean silhouette area for each sample reveals no statistically significant relationship for either species (Figure 1.2; R^2 = 0.02, p = ns for *G. ruber*; R^2= 0.00, p = ns for *G. sacculifer*). We therefore conclude that the area density method used in this study is very effective at removing the influence of *G. ruber* and *G. sacculifer* shell size on ρ_A. These results support the use of broader shell size fractions in ρ_A studies. A concern with using broader size fractions for ρ_A and SNW analysis is that the morphology and calcification of foraminifera can change throughout ontogeny [*Bé et al.*, 1980; *Hemleben et al.*, 1989]. For example, during gametogenesis and following the formation of a sac-like final chamber, *G. sacculifer* secretes a calcite crust over its entire shell, increasing the thickness of the shell by an average of 9 μm [*Bé et al.*, 1980]. In this study, only sac-less *G. sacculifer* individuals were used for ρ_A analysis in the effort to eliminate the complication of gametogenic calcite formation in this species. *Globigerinoides ruber* does not precipitate gametogenic calcite [*Caron et al.*, 1990], but it is possible that the influence of $[CO_3^{2-}]$ on calcification could vary throughout ontogeny for both *G. ruber* and *G. sacculifer*. Both field and culture studies

have shown that ontogeny, and by extension size fraction utilization, does not have a significant influence on *G. ruber* (white) and *O. universa* SNW-[CO_3^{2-}] calibrations [*Beer et al.*, 2010a; *Bijma et al.*, 2002]. To test whether the use of broader size fractions has an impact on the calibration equations derived for ρ_A and [CO_3^{2-}], we examined the relationship between these two variables for three different size fractions of both *G. ruber* (355-500; 500-650; 355-650 μm) and *G. sacculifer* (425-650; 650-850; 425-850 μm; Figure 1.3). We found that the percent change in ρ_A that occurred with a change in [CO_3^{2-}] from 200 to 300 μmol/kg (%Δ[CO_3^{2-}]$_{200-300}$) ranged from 44 to 50% for the three *G. ruber* size fractions (Table 1.4; equations 8-10) and from 20 to 29% for the various *G. sacculifer* size fractions (Table 1.4; equations 14-16). The correlation coefficients are lower and the ρ_A error higher for the narrower size fractions due to the smaller number of individuals per sample in these size fractions ($n > 2$; Figure 1.3). We speculate that the small difference in ρ_A change between the different size fractions is likely due to the difference in the number of individuals per sample, resulting in significant errors associated with the average ρ_A calculations for the narrower size fractions. Based on these observations, we conclude that the small range in %Δ[CO_3^{2-}]$_{200-300}$ for ρ_A exhibited by the different size fractions illustrates that ontogeny does not significantly affect the relationship between ρ_A and [CO_3^{2-}]. The broader size fractions (355-650 μm for *G. ruber*, 425-850 μm for *G. sacculifer*) used in this study yield the largest number of individuals per sample and smallest errors and are therefore optimal for generating the calibration equations. Thus, only the data for the broader size fractions will be considered from here on.

1.5.2 Calcification Depth and Temperature Estimates

Calcification temperatures derived from the $\delta^{18}O$ analyses for each sample were paired with the closest time-equivalent measured water column temperatures. The instrumental temperatures rather than the $\delta^{18}O$-derived temperatures are used for the carbonate calculations and statistical analyses in order to maintain consistency with the rest of the hydrographic data used in this study. Average temperatures were comparable to previously published optimum temperatures for both *G. ruber* [26 °C for this study vs. 27 °C from *Mulitza et al.*, 1998] and *G. sacculifer* [23 °C for this study vs. 22 °C from *Mulitza et al.*, 1998]. The instrumental temperatures values for the upper 130 m for the 3-year study period, along with the estimated calcification depths for *G. ruber* (black circles) and *G. sacculifer* (blue diamonds) from each sediment trap sample are shown in Figure 1.4a. The mean calcification depth for *G. ruber* is 16 (± 19) m, which is consistent with this species living in the surface mixed layer in the Cariaco Basin [*Miro*, 1971;*Tedesco et al.*, 2007] and falls within the previously observed depth range of 0-50 m [*Hemleben et al.*, 1989; *Farmer et al.*, 2007].

The estimated calcification depths for *G. sacculifer* range from 15-100 m, with the mean being ~ 50 (± 28) m. These results are in line with previous depth estimates for the species from the Cariaco Basin [*Wejnert*, 2011]. For both species, calcification depth changes seasonally in response to shifts between upwelling and non-upwelling regimes in the basin (Figure 1.4a). Changes in calcification depth are likely a response to changes in ambient water density at depth due to transitions between upwelling and non-upwelling regimes and to a certain extent species-specific preferences to live at a depth

characterized by an optimal temperature, salinity, light, and/or chlorophyll and nutrient regimes [*Hemleben et al.*, 1989; *Sautter and Thunell*, 1991a; *Tedesco et al.*, 2007].

1.5.3 Carbonate System Calculations

The $[CO_3^{2-}]$ record for the upper 120 m over the course of the study period is shown in Figure 1.4b, along with the calcification depths determined for each sample population for both species. The $[CO_3^{2-}]$ at the calcification depths for *G. ruber* ranged between 215 and 270 µmol/kg (mean = 240 µmol/kg) throughout the study period, coinciding with calcite saturation states (Ω_{calc}) ranging from 5.0 to 6.5 (mean = 5.7). $[CO_3^{2-}]$ and Ω_{calc} for *G. sacculifer* were on average lower than those for *G. ruber* (165 – 240 µmol/kg, mean $[CO_3^{2-}]$ = 200 µmol/kg, mean Ω_{calc} = 4.7), in agreement with *G. sacculifer's* deeper depth habitat.

1.5.4 Carbonate, Temperature and Phosphate Controls on Foraminiferal ρ_A

SLR revealed that the ρ_A for both species has a highly significant ($p < 0.001$) relationship with ambient $[CO_3^{2-}]$ (Table 1.4; Figure 1.3a). SLR performed using temperature as the predictor variable for ρ_A also revealed a significant positive-linear relationship (Figure 1.5a,b). In comparison, SLR using $[PO_4^{3-}]$ as the predictor variable revealed a less significant negative-linear relationship with G. ruber ρ_A ($p < 0.05$), with no significant relationship between *G. sacculifer* ρ_A and $[PO_4^{3-}]$ (Figure 5c,d). Additionally, SLR using $[CO_3^{2-}]$ as the predictor variable and calcification temperature

and [PO_4^{3-}] concentrations individually as the response variables yielded significant bivariate correlation amongst these variables, with the exception of *G. sacculifer* [PO_4^{3-}] and [CO_3^{2-}] (Table 1.4, Figure 1.5). Table 1.4 shows the results of the MLR using each predictor variable interchangeably as the dependent variable, with the other predictor variables serving as the independent variables. For both species, [CO_3^{2-}] and temperature are highly redundant with the other environmental parameters (R^2 = 0.86 and 0.82 and R^2 = 0.98 and 0.98 for *G. ruber* and *G. sacculifer,* respectively). MLR using [PO_4^{3-}] as the dependent variable and temperature and [CO_3^{2-}] as the independent variables reveal that [PO_4^{3-}] is moderately redundant with temperature and [CO_3^{2-}] for both G. ruber and G. sacculifer (R^2 = 0.44 and 0.26, respectively). By substituting in a variable we know does not share a statistically significant relationship with the predictor variables (i.e. mean area, R^2 = 0.00, 0.01, 0.04 and R^2 = 0.01, 0.01, and 0.05 for *G. ruber* and *G. sacculifer* [CO_3^{2-}], temperature and [PO_4^{3-}], respectively), we can quantify the specific redundancy each predictor variable shares with another (Table 1.4). This test revealed that *G. ruber* temperature and [PO_4^{3-}] are 81 and 42% redundant with [CO_3^{2-}] and that *G. sacculifer* temperature and [PO_4^{3-}] are 98 and 30% redundant with [CO_3^{2-}].

The tolerance and VIF statistics were less than 0.2 and greater than 5, respectively, for both [CO_3^{2-}] and temperature for both species, revealing a strong case for collinearity for these variables (Table 1.3). Substituting in the residuals of temperature (T_{Cres}, [CO_3^{2-}]) and [PO_4^{3-}] ([PO_4^{3-}]res, [CO_3^{2-}]) revealed no collinearity with [CO_3^{2-}]. For both species, the tolerance and VIF diagnostics for [PO_4^{3-}] did not indicate a strong case for collinearity with the other predictor variables. However, due its redundancy with the other predictor variables (Table 1.4), [PO_4^{3-}] is treated for possible

collinearity with [CO_3^{2-}] or temperature in the subsequent HMR analyses. These results suggest that [CO_3^{2-}] and temperature, particularly with the *G. sacculifer* data, are nearly indistinguishable from one another in regression analyses.

Based on the results of these statistical analyses, we hypothesize that the relationships exhibited between one predictor variable and ρ_A could be due to its strong collinearity with another predictor variable that serves as the dominant predictor for ρ_A. This hypothesis is graphically represented in Figure 1.5. Figures 1.5a and b show the relationships between temperature and ρ_A and temperature and [CO_3^{2-}] for *G. ruber* (left) and *G. sacculifer* (right), while Figure 1.5c and 1.5d illustrates the same relationships for [PO_4^{3-}]. The slopes of the best-fit lines illustrated in each graph cannot be directly compared as they are on different scales. However, the correlation coefficients (R) for both species are similar in all cases, suggesting that the relationship between ρ_A and temperature or [PO_4^{3-}] could be due to that variables collinearity with [CO_3^{2-}].

Four HMR models were run in order to determine the relative contributions of each predictor variable to ρ_A. The means, standard deviations, and number of data points (n) for each variable used in the HMR models are included in Table 1.6. The R^2, the R^2 change (ΔR^2), the significance of the ΔR^2 (p ΔR^2), and the standardized coefficient (β) for each model are listed in Table 1.3. The first model uses results from prior studies examining the dominant control variable on foraminiferal calcification [*Barker and Elderfield*, 2002; *Naik et al.*, 2010; *Manno et al.*, 2012] to determine the ordering of predictor variables for HMR, with [CO_3^{2-}], and the residuals of calcification temperature and [PO_4^{3-}] based on their relationship with [CO_3^{2-}] (T_{Cres}, [CO_3^{2-}] and $[PO_4^{3-}]_{res}$, [CO_3^{2-}]) serve as X_1, X_2, and X_3, respectively. The R^2 values from model 1 indicate that [CO_3^{2-}]

accounts for 89 and 86% of the variability seen in ρ_A for *G. ruber* and *G. sacculifer,* respectively. For both *G. ruber* and *G. sacculifer*, ΔR^2 for the additions of T_{Cres}, $[CO_3^{2-}]$ and $[PO_4^{3-}]_{res}$, $[CO_3^{2-}]$ were insignificant, with each accounting for ~ 0-2% of the variability in ρ_A once $[CO_3^{2-}]$ was controlled for in the model. Significantly larger β – values for $[CO_3^{2-}]$ relative to those for T_{Cres}, $[CO_3^{2-}]$ and $[PO_4^{3-}]_{res}$, $[CO_3^{2-}]$ are indicate of a strong dominance of $[CO_3^{2-}]$ for predicting variability in ρ_A.

The other three models were performed on both species to test if $[CO_3^{2-}]$ still played a significant role in predicting ρ_A when placed second or third in the ordering of predictor variables. For the *G. ruber* data, the addition of $[CO_3^{2-}]$ as X_2 and X_3 in models 2 and 4 following the addition of temperature generated a significant contribution to the R^2 of the model, while the addition of temperature as X_2 and X_3 following the addition of $[CO_3^{2-}]$ in models 1 and 3 did not contribute significantly to the R^2 of the model. However, the ordering of temperature and $[CO_3^{2-}]$ in models 1-4 for *G. sacculifer* did not make a significant difference in the model output. This is likely a result of the strong – nearly perfect – collinearity that exists between *G. sacculifer* $[CO_3^{2-}]$ and temperature (Tables 1.2 and 1.3), thus making them indistinguishable during HMR. The predictor variables for *G. ruber* are slightly less collinear, and thus provide us with better estimates of the relative contributions of $[CO_3^{2-}]$ and temperature to the variability in ρ_A. Taken together with the knowledge that *G. ruber* temperature and $[CO_3^{2-}]$ are 81% redundant, these results indicate that $[CO_3^{2-}]$ is the dominant factor controlling ρ_A and that model 1 most accurately reflects the relative contributions of each predictor variable. Based on this model we cannot say with any confidence that either calcification temperature or $[PO_4^{3-}]$ have an impact on the variability in *G. ruber* or *G. sacculifer* ρ_A, or by extension

calcification efficiency. We conclude that $[CO_3^{2-}]$ alone acts as an excellent predictor for both *G. ruber* and *G. sacculifer* ρ_A and the SLR equations reported in Table 1.4 (equations 7, 8, 13, 14), serve as reliable calibration equations.

The ρ_A of *G. ruber* (pink; 355-650 μm) ranged from 1.04 to 1.31 × 10^{-4} μg/μm^2 over the 3-year study period with an average of 1.18 × 10^{-4} μg/ μm^2, yielding a strong positive linear relationship with $[CO_3^{2-}]$ ($R^2 = 0.89$, $p < 0.001$, 3a). *Globigerinoides sacculifer* (425-850 μm) ρ_A ranged from 1.45 to 1.81 × 10^{-4} μg/ μm^2 with an average of 1.62 × 10^{-4} μg/ μm^2 and also correlated strongly with ambient $[CO_3^{2-}]$ ($R^2 = 0.86$, $p <$ 0.001, Figure 1.3a). The relationships between foraminiferal ρ_A and $[CO_3^{2-}]$ reported in Table 1.4 are in line with the results of prior studies reporting an adverse effect of reduced $[CO_3^{2-}]$ associated with ocean acidification on the calcification of planktonic foraminfera [*Spero et al.*, 1997; *Bijma et al.*, 1999, *Barker and Elderfield*, 2002; *Russell et al.*, 2004; *Mekik and Raterink*, 2008; *Moy et al.* 2009; *Lombard et al.*, 2010; *Manno et al.*, 2012].

The slopes and y-intercepts for *G. ruber* reported for this study (Table 1.4) reveal a more sensitive relationship with $[CO_3^{2-}]$ than those for *G. sacculifer*, with a 200 to 300 μm/kg change in $[CO_3^{2-}]$ ($\%\Delta[CO_3^{2-}]_{200\text{-}300}$) resulting in a change in ρ_A of 44% for *G. ruber* and 27% for *G. sacculifer* (Table 1.1). It has been well documented that different species of planktonic foraminifera undergo varying degrees of isotopic fractionation and elemental incorporation during the calcification process due to various vital effects associated with calcification [*Erez*, 1978; *Spero*, 1992; *Wolf-Gladrow et al.*, 1999; *Zeebe et al.*, 2008; *Henehan et al.*, 2013]. Though the ρ_A for *G. ruber* and *G. sacculifer* reflects changes in ambient seawater $[CO_3^{2-}]$, the $[CO_3^{2-}]$ at the site of calcification could vary

amongst species due to differences in both foraminiferal and symbiont vital effects [calcification, photosynthesis, respiration; *Jorgensen et al.*, 1985*; Rink et al.*, 1998; *Wolf-Gladrow et al.*, 1999; *Bentov et al.*, 2009]. Thus, when using ρ_A or any other measure of shell weight as a proxy for past surface-ocean $[CO_3^{2-}]$, it is necessary to use species-specific equations like those provided in this study.

An additional consideration for the use of foraminiferal ρ_A as a proxy for $[CO_3^{2-}]$ is the extent to which foraminifera are preserved in marine sediment samples [*Barker et al.*, 2004; *Gibbs et al.*, 2010]. The dissolution of planktonic foraminiferal calcite due to a low $[CO_3^{2-}]$ at depth would result in lower foraminiferal ρ_A and complicate the use of ρ_A as a proxy for surface-ocean $[CO_3^{2-}]$. Conversely, the addition of secondary calcite would increase the shell thickness and hence the ρ_A of foraminifera. Thus, foraminiferal specimens should be collected from well above the lysocline for the study region and thoroughly examined for signs of dissolution and/or the precipitation of secondary calcite prior to being used for ρ_A- $[CO_3^{2-}]$ reconstructions.

1.5.5 Comparison to Previous Studies

Foraminiferal ρ_A cannot be directly compared to previous studies that investigated the relationship between foraminiferal calcification efficiency using SNW, shell thickness measurements or calculations, or calcification rates as the units are not the same (Table 1.1). Additionally, this study differs from most other field studies in that we use $[CO_3^{2-}]$ at the predicted depth of calcification rather than surface water $[CO_3^{2-}]$ to generate of our calibration equations. We can compare the various shell weight proxies more directly by

examining the change in each proxy resulting from a 200 to 300 μm/kg change in [CO_3^{2-}]. These changes in calcification were determined using regression equations reported in the respective studies or regression equations derived from digitized figures (Table 1.1). For studies that did not include [CO_3^{2-}] values, the %Δ reported in Table 1.1 represent either a reported %Δ in the study [*Spero et al*., 1997], or a change in SBW observed over the course of a geologic period characterized by significant changes in surface water [CO_3^{2-}] [*Moy et al.*, 2009; *de Moel et al.*, 2009; *Naik et al.*, 2010]. $\%\Delta[CO_3^{2-}]_{200\text{-}300}$ varies widely depending on the species studied and the proxies used. The average $\%\Delta[CO_3^{2-}]_{200\text{-}300}$ reported for *G. sacculifer* is 32% (Table 1.1), which is close to the $\%\Delta[CO_3^{2-}]_{200\text{-}300}$ reported for this species in this study (27%), though this percentage was derived from both culture and core studies that vary widely in the range in [CO_3^{2-}] and methods for determining calcification. The $\%\Delta[CO_3^{2-}]_{200\text{-}300}$ for G. *sacculifer* reported in this study is most similar to the percent change in *G. sacculifer* SBW reported in a core study spanning 25,000 yrs BP to 1,000 yrs BP [*Naik et al.*, 2010].

The results from *Beer et al.*, [2010a] are highly inconsistent with the results for *G. ruber* (pink) presented here, with *Beer et al.*, [2010a] reporting a negative correlation between *G. ruber* (white) MBW and [CO_3^{2-}] collected from the Arabian Sea. Recent studies have distinguished between five different genetic types for the white variety of *G. ruber* [*Aurahs et al.*, 2011], characterized broadly by two distinct morphotypes: sensu stricto (s.s.) and sensu lato [s.l.; *Wang*, 2000]. These morphotypes have different depth habitats and temperature preferences and thus paleoceanographic and paleoclimatic studies should distinguish between them [*Hecht and Savin*, 1972; *Wang*, 2000; *Kuroyanagi et al.,* 2008; *Numberger et al.*, 2009; *Aurahs et al.*, 2011]. This difference in

calcification habitat, as well as the evident difference in shell geometry (s.l. is more heavily calcified than s.s.; Durrant, J. and M. Henehan, unpublished data), would likely result in a significant differences in the MBW for the two *G. ruber* (white) morphotypes. The differences between the results from *Beer et al.*, [2010a] and the results from other SNW studies also using *G. ruber* (white) collected from the Arabian Sea [*de Moel et al.*, 2009; *Naik et al.*, 2010] may be due to *Beer et al.*, [2010a] not distinguishing between the two morphotypes which we know to be present in this region [*de Moel et al.*, 2009; *Aurahs et al.*, 2011], and whose relative abundances may have changed as sampling traversed upwelling and non-upwelling waters. The use of *G. ruber* (pink) in the current study and *G. ruber* (white) of an undetermined morphotype by *Beer et al.*, [2010a] make comparisons difficult between the two studies. Our results are closest to those reported in *de Moel et al.*, [2009], who used the SBW of *G. ruber* (white; both morphotypes in equal distributions amongst samples), but had a much narrower range in $[CO_3^{2-}]$ compared to the current study. As this is the first study reporting on the effect of $[CO_3^{2-}]$ on the calcification in the pink variety of *G. ruber*, we can only state that the $\%\Delta[CO_3^{2-}]_{200\text{-}300}$ reported here (44%) falls within the range of most percent changes reported in studies using other species (5 to 155%, with the majority between 5 and 50%). Thus, our results for the magnitude of change in ρ_A per unit change in $[CO_3^{2-}]$ for both *G. ruber* and *G. sacculifer* are comparable to those changes previously reported in foraminiferal calcification- $[CO_3^{2-}]$ studies.

1.6 CONCLUSIONS

The results of this study suggest that surface $[CO_3^{2-}]$ is responsible for 89 and 86% of the variability in ρ_A for both *G. ruber* (pink) and *G. sacculifer*, respectively, and by extension calcification efficiency, with no significant evidence that temperature or $[PO_4^{3-}]$ contribute to ρ_A in these species. Thus, the ρ_A of *G. ruber* and *G. sacculifer* should serve as a reliable proxy for past $[CO_3^{2-}]$ using the species-specific equations reported in Table 1.4. It is recommended that only well-preserved foraminiferal shells with an absence of secondary calcite be used in down-core ρ_A reconstructions of past $[CO_3^{2-}]$. The ρ_A technique described in this study should be particularly useful for down-core studies where foraminiferal shell numbers are limited and the use of a broad size range is required.

Table 1.1 Compilation of known studies assessing the relationship between planktonic foraminiferal calcification and $[CO_3^{2-}]$.

Species/Study	Sample Type	Size Fraction (μm)	Size-Normalizing Method	Range in $[CO_3^{2-}]$ (μM/kg)	Correlation with $[CO_3^{2-}]$	% Δ $[CO_3^{2-}]_{200-300}$
			Orbulina universa			
Spero et al. [1997]	culture	-	-	75-774 (699)	positive	37[d]
Bijma et al. [1999]	culture	500-600 (100)	SBW	40-150 (110)[b]	positive, R^2=0.55	24.3
	culture	500-600 (100)	SBW	180-640 (460)[b]	positive, R^2=0.67	12.8
Russell et al. [2004]	culture	427-653 (226)	shell thickness	76-468 (392)[b]	positive, R^2=0.97	15.1
	culture	427-667 (240)	SBW	77-480 (404)[b]	positive, R^2=0.65	18.3
Lombard et al. [2010][a]	culture	427-667 (240)	calcification rate	77-480 (404)[b]	positive, R^2=0.04	7.7-14.7
			Globigerina bulloides			
Barker and Elderfield [2002]	core top	300-355 (55)	MBW	206-257 (51)[c]	positive, R^2=0.67	155.5
	core top	300-355 (55)	SBW	199-264 (65)[c]	positive, R^2=0.31	63.9
Gonzalez-Mora et al. [2008]	core	250-300 (50)	SBW	150-250 (100)[c]	positive	-
Moy et al. [2009]	sediment trap/core top	300-355 (55)	SBW	153-189 (36)[c]	positive	35[e]
	sediment trap/core top	355-425 (70)	SBW	153-189 (36)[c]	positive	30[e]
Beer et al. [2010a]	plankton net	200-250 (50)	MBW	166-276 (110)[c]	positive, R^2=0.38	16.6
Aldridge et al. [2012]	plankton net	150-200 (50)	MBW	148-181 (40)[c]	positive, R^2=0.35	62.6
	plankton net	200-250 (50)	MBW	148-181 (40)[c]	positive, R^2=0.56	47.5
			Pulleniatina obliquiloculata			
Naik and Naidu [2007]	core top	350-420 (70)	MBW	-	positive	-
Mekik and Raterink [2008]	core top	420-520 (100)	MBW	145-225 (80)[b]	positive, R^2=0.67	200.0
			Neogloboquadrina dutertrei			
Naik and Naidu [2007]	core top	350-420 (70)	MBW	-	positive	-
Mekik and Raterink [2008]	core top	355-415 (60)	MBW	120-225 (105)[b]	positive, R^2=0.64	76.8
			Globorotalia truncatulinoides			
Barker and Elderfield [2002]	core	300-355(55)	SBW	216-264 (48)[c]	positive, R^2=0.44	38.2
			Neogloboquadrina pachyderma			
Barker and Elderfield [2002]	core	250-300 (50)	MBW	199-264 (65)	positive, R^2=0.65	53.3
Gonzalez-Mora et al. [2008]	core	250-300 (50)	SBW	-	no response	-
Manno et al. [2012]	culture	100-200 (100)	calcification rate	60-120 (60)[c]	positive	21-30
			Globorotalia inflata			
Barker and Elderfield [2002]	core	300-355(55)	SBW	200-268 (68)[c]	positive, R^2=0.77	70.7
			Globogerinoides ruber			
Gonzalez-Mora et al. [2008]	core	250-300 (50)	SBW	-	positive	-
de Moel et al. [2009]	core	250-300 (50)	SBW	(6.5; 18)	positive	25.0[f]
	core	300-355 (55)	SBW	(6.5; 18)	positive	25.0[f]
	core	250-500 (250)	shell thickness	(6.5; 18)	positive	35.0[f]
Beer et al. [2010a]	plankton net	200-250 (50)	MBW	251-284 (33)[c]	negative, R^2= 0.78	-88.6
	plankton net	250-315 (65)	MBW	261-285 (24)[c]	negative, R^2=0.64	-74.2
	plankton net	315-355 (40)	MBW	262-284 (22)[c]	negative, R^2=0.50	-71.5
This study (pink)	sediment trap	355-650 (295)	ρ_A	215 - 270 (55)[b]	positive, R^2=0.89	44.1
	sediment trap	355-500 (145)	ρ_A	215 - 270 (55)[b]	positive, R^2=0.73	49.6
	sediment trap	500-650 (150)	ρ_A	215 - 270 (55)[b]	positive, R^2=0.82	43.8
			Globogerinoides sacculifer			
Bijma et al. [2002]	culture	493-575 (82)	SBW	100 - 620 (520)[b]	positive, R^2=0.39	7.7
	culture	582-663 (81)	SBW	100 - 620 (520)[b]	positive, R^2=0.22	4.6
	culture	762-845 (83)	SBW	100 - 620 (520)[b]	positive, R^2=0.28	5.4
Naik and Naidu [2007]	core top	350-420 (70)	MBW	240 - 250 (10)[b]	positive	157.7
Lombard et al. [2010][a]	culture	372-446 (74)	calcification rate	72 - 566 (494)[b]	positive, R^2=0.03-0.07	6.3-8.1
Naik et al. [2010]	core	503-699 (196)	SBW	61-106 (36)[c]	positive	32.3[g]
This study (no sac)	sediment trap	425-800 (350)	ρ_A	165 - 240 (70)[b]	positive, R^2=0.86	27.1
	sediment trap	425-650 (225)	ρ_A	165 - 240 (70)[b]	positive, R^2=0.79	29.1
	sediment trap	650-850 (200)	ρ_A	165 - 240 (70)[b]	positive, R^2=0.55	19.5

Table 1.2 MLR assessing the collinearity amongst predictor variables [CO_3^{2-}], temperature (T_C), [PO_4^{3-}], and mean area.

	$Y = a + b_1(X_1) + b_2(X_2)$				
Species	**Y**	**X_1**	**X_2**	**R^2**	***p***
G. ruber	[CO_3^{2-}] (µmol/kg)	T_C (°C)	[PO_4^{3-}] (µmol/kg)	0.86	< 0.001
	T_C (°C)	[CO_3^{2-}] (µmol/kg)	[PO_4^{3-}] (µmol/kg)	0.82	< 0.001
	[PO_4^{3-}] (µmol/kg)	[CO_3^{2-}] (µmol/kg)	T_C (°C)	0.44	< 0.05
	[CO_3^{2-}] (µmol/kg)	T_C (°C)	mean area (µm^2)	0.81	< 0.001
	[CO_3^{2-}] (µmol/kg)	[PO_4^{3-}] (µmol/kg)	mean area (µm^2)	0.27	ns
	T_C (°C)	[CO_3^{2-}] (µmol/kg)	mean area (µm^2)	0.81	< 0.001
	T_C (°C)	[PO_4^{3-}] (µmol/kg)	mean area (µm^2)	0.24	ns
	[PO_4^{3-}] (µmol/kg)	[CO_3^{2-}] (µmol/kg)	mean area (µm^2)	0.42	ns
	[PO_4^{3-}] (µmol/kg)	T_C (°C)	mean area (µm^2)	0.21	ns
G. sacculifer	[CO_3^{2-}] (µmol/kg)	T_C (°C)	[PO_4^{3-}] (µmol/kg)	0.98	< 0.001
	T_C (°C)	[CO_3^{2-}] (µmol/kg)	[PO_4^{3-}] (µmol/kg)	0.98	< 0.001
	[PO_4^{3-}] (µmol/kg)	[CO_3^{2-}] (µmol/kg)	T_C (°C)	0.26	ns
	[CO_3^{2-}] (µmol/kg)	T_C (°C)	mean area (µm^2)	0.98	< 0.001
	[CO_3^{2-}] (µmol/kg)	[PO_4^{3-}] (µmol/kg)	mean area (µm^2)	0.39	ns
	T_C (°C)	[CO_3^{2-}] (µmol/kg)	mean area (µm^2)	0.98	< 0.001
	T_C (°C)	[PO_4^{3-}] (µmol/kg)	mean area (µm^2)	0.17	ns
	[PO_4^{3-}] (µmol/kg)	[CO_3^{2-}] (µmol/kg)	mean area (µm^2)	0.30	ns
	[PO_4^{3-}] (µmol/kg)	T_C (°C)	mean area (µm^2)	0.27	ns

Table 1.3 Collinearity diagnostics Tolerance and VIF resulting from MLR with predictor variables [CO_3^{2-}], temperature and [PO_4^{3-}] and response variable ρ_A.

	$Y = a + b_1(X_1) + b_2(X_2) + b_3(X_3)$				Tolerance[a]			VIF[b]		
Species	Y	X_1	X_2	X_3	T_1	T_2	T_3	VIF_1	VIF_2	VIF_3
G. ruber	ρ_A (10^{-4} µg/ µm2)	[CO_3^{2-}] (µmol/kg)	T_C (°C)	[PO_4^{3-}] (µmol/kg)	0.1	0.2	0.56	7.32	5.62	1.79
	ρ_A (10^{-4} µg/ µm2)	[CO_3^{2-}] (µmol/kg)	T_{Cres}, [CO_3^{2-}] (°C)	$[PO_4^{3-}]_{res}$, [CO_3^{2-}] (µmol/kg)	1.00	0.9	0.87	1.00	1.15	1.15
G. sacculifer	ρ_A (10^{-4} µg/ µm2)	[CO_3^{2-}] (µmol/kg)	T_C (°C)	[PO_4^{3-}] (µmol/kg)	0	0	0.74	47.07	45.4	1.4
	ρ_A (10^{-4} µg/ µm2)	[CO_3^{2-}] (µmol/kg)	T_{Cres}, [CO_3^{2-}] (°C)	$[PO_4^{3-}]_{res}$, [CO_3^{2-}] (µmol/kg)	1.00	1	0.96	1.00	1.04	1

[a]Tolerances less than 0.2 and [b]VIF greater than 5 indicate collinearity amongst the predictor variables.

Table 1.4 SLR equations and associated correlation statistics.

Species	Equation Number	Y = a + b(X) Y	X	a	b	n	R	R^2	*p*	Std. error of estimate
G. ruber (pink)	7	$[CO_3^{2-}]$ (µmol/kg)	ρ_A (355-650µm; 10^{-4} µg/ µm2)	2.390 (±52.66)	201.663 (±44.50)	14	0.94	0.89	< 0.001	±6.34
	8	ρ_A (355-650µm; 10^{-4} µg/ µm2)	$[CO_3^{2-}]$ (µmol/kg)	0.119 (±0.24)	0.00442 (±0.001)	14	0.94	0.89	< 0.001	±0.03
	9	ρ_A (355-500µm; 10^{-4} µg/ µm2)	$[CO_3^{2-}]$ (µmol/kg)	0.00801 (±0.47)	0.00488 (±0.002)	13	0.86	0.73	< 0.001	±0.06
	10	ρ_A (500-650µm; 10^{-4} µg/ µm2)	$[CO_3^{2-}]$ (µmol/kg)	0.126 (±0.33)	0.00441 (±0.001)	13	0.91	0.82	< 0.001	±0.04
	11	T_C (°C)	$[CO_3^{2-}]$ (µmol/kg)	7.516 (±5.72)	0.075 (±0.02)	14	0.89	0.80	< 0.001	±0.72
	12	$[PO_4^{3-}]$ (µmol/kg)	$[CO_3^{2-}]$ (µmol/kg)	0.392 (±0.29)	−0.001 (±0.002)	4	0.60	−0.36	< 0.05	±0.04
G. sacculifer	13	$[CO_3^{2-}]$ (µmol/kg)	ρ_A (425-850µm; 10^{-4} µg/ µm2)	−118.224 (±84.74)	195.687 (±52.10)	13	0.93	0.86	< 0.001	±9.63
	14	ρ_A (425-850µm; 10^{-4} µg/ µm2)	$[CO_3^{2-}]$ (µmol/kg)	0.745 (±0.24)	0.00440 (±0.001)	13	0.93	0.86	< 0.001	±0.045
	15	ρ_A (425-650µm; 10^{-4} µg/ µm2)	$[CO_3^{2-}]$ (µmol/kg)	0.669 (±0.36)	0.00465 (±0.002)	12	0.65	0.77	< 0.001	±0.07
	16	ρ_A (650-850µm; 10^{-4} µg/ µm2)	$[CO_3^{2-}]$ (µmol/kg)	1.022 (±0.53)	0.00328 (±0.003)	12	0.88	0.43	< 0.001	±0.09
	17	T_C (°C)	$[CO_3^{2-}]$ (µmol/kg)	10.577 (±1.31)	0.064 (±0.006)	13	0.99	0.98	< 0.001	±0.25
	18	$[PO_4^{3-}]$ (µmol/kg)	$[CO_3^{2-}]$ (µmol/kg)	0.863 (±0.52)	−0.003 (±0.004)	13	0.48	−0.23	< 0.1	±0.15

Table 1.5 Heirarchical Regression Model and statistical output for the predictors of ρ_A.

	$Y = a + b_1(X_1) + b_2(X_2) + b_3(X_3)$						p	Beta		
Species - model	Y	X_1	X_2	X_3	R^2	ΔR^2	ΔR^2	β_1	β_2	β_3
G. ruber - 1	ρ_A (10^{-4} µg/ µm2)	$[CO_3^{2-}]$ (µmol/kg)	–	–	0.89	0.89	< 0.001	0.94	–	–
	ρ_A (10^{-4} µg/ µm2)	$[CO_3^{2-}]$ (µmol/kg)	T_{Cres}, $[CO_3^{2-}]$ (°C)	–	0.91	0.02	ns	0.94	0.13	–
	ρ_A (10^{-4} µg/ µm2)	$[CO_3^{2-}]$ (µmol/kg)	T_{Cres}, $[CO_3^{2-}]$ (°C)	$[PO_4^{3-}]_{res}$, $[CO_3^{2-}]$ (µmol/kg)	0.92	0.01	ns	0.94	0.17	−0.01
2	ρ_A (10^{-4} µg/ µm2)	T_C (°C)	–	–	0.81	0.81	< 0.001	0.90	–	–
	ρ_A (10^{-4} µg/ µm2)	T_C (°C)	$[CO_3^{2-}]_{res}$, T_C (µmol/kg)	–	0.90	0.10	< 0.01	0.90	0.31	–
	ρ_A (10^{-4} µg/ µm2)	T_C (°C)	$[CO_3^{2-}]_{res}$, T_C (µmol/kg)	$[PO_4^{3-}]_{res}$, T_C (µmol/kg)	0.91	0.01	ns	0.90	0.25	−0.10
3	ρ_A (10^{-4} µg/ µm2)	$[PO_4^{3-}]$ (µmol/kg)	–	–	0.36	0.36	< 0.05	−0.60	–	–
	ρ_A (10^{-4} µg/ µm2)	$[PO_4^{3-}]$ (µmol/kg)	$[CO_3^{2-}]_{res}$, $[PO_4^{3-}]$ (µmol/kg)	–	0.89	0.54	< 0.001	−0.60	0.73	–
	ρ_A (10^{-4} µg/ µm2)	$[PO_4^{3-}]$ (µmol/kg)	$[CO_3^{2-}]_{res}$, $[PO_4^{3-}]$ (µmol/kg)	T_{Cres}, $[PO_4^{3-}]$ (°C)	0.92	0.02	ns	−0.60	0.43	0.34
4	ρ_A (10^{-4} µg/ µm2)	$[PO_4^{3-}]$ (µmol/kg)	–	–	0.36	0.36	< 0.05	−0.60	–	–
	ρ_A (10^{-4} µg/ µm2)	$[PO_4^{3-}]$ (µmol/kg)	T_{Cres}, $[PO_4^{3-}]$ (°C)	–	0.88	0.52	< 0.001	−0.60	0.72	–
	ρ_A (10^{-4} µg/ µm2)	$[PO_4^{3-}]$ (µmol/kg)	T_{Cres}, $[PO_4^{3-}]$ (°C)	$[CO_3^{2-}]_{res}$, $[PO_4^{3-}]$ (µmol/kg)	0.92	0.04	< 0.05	−0.60	0.34	0.43
G. sacculifer - 1	ρ_A (10^{-4} µg/ µm2)	$[CO_3^{2-}]$ (µmol/kg)	–	–	0.86	0.86	< 0.001	0.93	–	–
	ρ_A (10^{-4} µg/ µm2)	$[CO_3^{2-}]$ (µmol/kg)	T_{Cres}, $[CO_3^{2-}]$ (°C)	–	0.87	0.00	ns	0.93	0.09	–
	ρ_A (10^{-4} µg/ µm2)	$[CO_3^{2-}]$ (µmol/kg)	T_{Cres}, $[CO_3^{2-}]$ (°C)	$[PO_4^{3-}]_{res}$, $[CO_3^{2-}]$ (µmol/kg)	0.87	0.00	ns	0.93	0.08	0.04
2	ρ_A (10^{-4} µg/ µm2)	T_C (°C)	–	–	0.86	0.86	< 0.001	0.93	–	–
	ρ_A (10^{-4} µg/ µm2)	T_C (°C)	$[CO_3^{2-}]_{res}$, T_C (µmol/kg)	–	0.87	0.00	ns	0.93	0.06	–
	ρ_A (10^{-4} µg/ µm2)	T_C (°C)	$[CO_3^{2-}]_{res}$, T_C (µmol/kg)	$[PO_4^{3-}]_{res}$, T_C (µmol/kg)	0.87	0.00	ns	0.93	0.07	0.04
3	ρ_A (10^{-4} µg/ µm2)	$[PO_4^{3-}]$ (µmol/kg)	–	–	0.16	0.16	ns	−0.40	–	–
	ρ_A (10^{-4} µg/ µm2)	$[PO_4^{3-}]$ (µmol/kg)	$[CO_3^{2-}]_{res}$, $[PO_4^{3-}]$ (µmol/kg)	–	0.86	0.70	< 0.001	−0.40	0.84	–
	ρ_A (10^{-4} µg/ µm2)	$[PO_4^{3-}]$ (µmol/kg)	$[CO_3^{2-}]_{res}$, $[PO_4^{3-}]$ (µmol/kg)	T_{Cres}, $[PO_4^{3-}]$ (°C)	0.87	0.01	ns	−0.40	0.40	0.47
4	ρ_A (10^{-4} µg/ µm2)	$[PO_4^{3-}]$ (µmol/kg)	–	–	0.16	0.16	ns	−0.40	–	–
	ρ_A (10^{-4} µg/ µm2)	$[PO_4^{3-}]$ (µmol/kg)	T_{Cres}, $[PO_4^{3-}]$ (°C)	–	0.86	0.71	< 0.001	−0.40	0.84	–
	ρ_A (10^{-4} µg/ µm2)	$[PO_4^{3-}]$ (µmol/kg)	T_{Cres}, $[PO_4^{3-}]$ (°C)	$[CO_3^{2-}]_{res}$, $[PO_4^{3-}]$ (µmol/kg)	0.87	0.00	ns	−0.40	0.47	0.38

Table 1.6 HMR descriptive statistics.

Species	Variable	Mean	Std. Deviation	n
G. ruber	ρ_A (10^{-4} µg/ µm2)	1.18	0.086	14
	$[CO_3^{2-}]$ (µmol/kg)	240.49	18.41	14
	T_C (°C)	25.51	1.54	14
	$[PO_4^{3-}]$ (µmol/kg)	0.05	0.04	14
	Tc_{res}, $[CO_3^{2-}]$ (°C)	0.00	0.69	14
	$[PO_4^{3-}]_{res,}$ $[CO_3^{2-}]$ (µmol/kg)	0.00	0.04	14
	$[CO_3^{2-}]_{res}$, T_C (µmol/kg)	0.00	8.20	14
	$[PO_4^{3-}]_{res,}$ T_C (µmol/kg)	0.00	0.04	14
	$[CO_3^{2-}]_{res}$, $[PO_4^{3-}]$ (µmol/kg)	0.00	1.43	14
	Tc_{res}, $[PO_4^{3-}]$ (°C)	0.00	14.7	14
G. sacculifer	ρ_A (10^{-4} µg/ µm2)	1.62	0.12	13
	$[CO_3^{2-}]$ (µmol/kg)	199.23	24.78	13
	T_C (°C)	23.39	1.61	13
	$[PO_4^{3-}]$ (µmol/kg)	0.25	0.16	13
	Tc_{res}, $[CO_3^{2-}]$ (°C)	0.00	0.24	13
	$[PO_4^{3-}]_{res,}$ $[CO_3^{2-}]$ (µmol/kg)	0.00	0.14	13
	$[CO_3^{2-}]_{res}$, T_C (µmol/kg)	0.00	3.75	13
	$[PO_4^{3-}]_{res,}$ T_C (µmol/kg)	0.00	0.14	13
	$[CO_3^{2-}]_{res}$, $[PO_4^{3-}]$ (µmol/kg)	0.00	21.75	13
	Tc_{res}, $[PO_4^{3-}]$ (°C)	0.00	1.44	13

Table 1.7 Sediment trap samples and coupled hydrographic data collected from the Cariaco Basin

G. ruber	Trap open	Hydro	Day	n	n	n	Mean weight	Mean area	Mean ρ_A		$\delta^{18}O$ temp	Temperature	Calcification	Calcification		$[PO_4^{3-}]$	$[Si(OH)_4]$	Alkalinity		$[CO_3^{2-}]$	$[CO_3^{2-}]$ range	
Sample ID	date	date	difference	(355-650µm)	(355-500µm)	(500-650µm)	(µg) (±σ)	($1x10^5$ µm^2) (±σ)	($1x10^{-4}$ µg/µm^2) (±σ)	$\delta^{18}O$ (‰)	(°C)	(°C)	Depth (mbsl)	Depth Range (mbsl)	Salinity	(µmol/kg)	(µmol/kg)	(µmol/kg)	pH	(µmol/kg)	(µmol/kg)	Ω_{calc}
CAR19_9	09/07/05	08/10/05	-28	23	14	9	19.58 (±5.97)	1.65 (±0.43)	1.20 (±0.16)	-1.51	26.41	26.28	1	1-4	36.92	0.03	0.00	2407	8.062	245.89	245-246	5.83
CAR19_12	10/19/05	10/05/05	-14	11	5	6	20.61 (±3.60)	1.59 (±0.30)	1.31 (±0.13)	-1.73	27.26	27.25	35[a]	32-35	36.74	0.04	0.60	2401	8.083	260.88	260-265	6.18
CAR20_9	03/07/06	02/07/06	-28	29	10	19	19.43 (±2.91)	1.77 (±0.21)	1.11 (±0.11)	-1.18	23.92	23.68	1	1-4	36.88	0.02	0.29	2454	8.069	235.89	235-236	5.58
CAR20_11	04/04/06	03/16/06	-19	26	17	9	17.28 (±4.45)	1.54 (±0.32)	1.14 (±0.16)	-1.46	26.28	24.50	1	1-2	36.88	0.04	0.25	2454	8.035	227.79	–	5.39
CAR22_1	11/08/06	11/02/06	-6	25	10	15	23.67 (±7.23)	1.83 (±0.49)	1.29 (±0.09)	-2.25	29.33	28.72	1	–	36.26	0.04	0.97	2379	8.096	272.12	–	6.52
CAR22_4	12/20/06	12/05/06	-15	15	9	6	18.43 (±5.26)	1.61 (±0.38)	1.14 (±0.11)	-1.63	24.78	25.00	35	35-45	36.69	0.06	0.60	2394	8.063	236.15	222-236	5.58
CAR22_9	02/28/07	02/06/07	-22	11	4	7	16.66 (±4.65)	1.58 (±0.36)	1.10 (±0.14)	-1.29	24.05	23.26	1	–	36.76	0.08	1.87	2421	8.041	218.65	–	5.17
CAR22_12	04/11/07	03/06/07	-36	13	6	7	18.04 (±3.19)	1.59 (±0.34)	1.15 (±0.10)	-1.15	23.64	24.60	1	1-5	36.75	0.04	1.20	2494	8.029	229.24	220-229	5.43
CAR23_2	05/30/07	05/08/07	-22	51	16	35	21.30 (±4.16)	1.76 (±0.38)	1.22 (±0.13)	-1.39	25.99	26.18	1	1-5	36.88	0.03	0.93	2417	8.043	238.28	225-238	5.65
CAR23_7	08/08/07	07/03/07	-36	22	16	6	17.59 (±4.11)	1.43 (±0.28)	1.23 (±0.16)	-1.67	27.07	26.48	1	1-3	36.88	0.04	0.00	2420	8.060	248.13	–	5.88
CAR23_11	10/03/07	09/04/07	-29	10	9	1	18.47 (±3.35)	1.38 (±0.25)	1.30 (±0.12)	-1.85	27.66	26.49	25	17-26	36.38	0.02	3.40	2383	8.121	268.50	266-268	6.39
CAR24_4	01/08/08	12/11/07	-28	11	5	6	18.52 (±5.80)	1.54 (±0.52)	1.08 (±0.09)	-1.24	23.85	24.64	55	55-63	36.77	0.18	2.21	2394	8.023	218.31	207-218	5.13
CAR25_1	05/28/08	05/06/08	-22	13	5	8	19.93 (±5.86)	1.91 (±0.41)	1.04 (±0.15)	-1.17	24.33	23.76	25	22-25	36.98	0.09	1.76	2422	8.020	214.55	214-219	5.05
CAR25_11	09/24/08	09/10/08	-14	22	2	20	25.40 (±3.19)	2.06 (±0.23)	1.24 (±0.13)	-1.70	26.36	26.60	35	27-38	36.45	0.00	1.35	2400	8.077	252.54	242-252	5.99
G. sacculifer	Trap open	Hydro	Day	n	n	n	Mean weight	Mean area	ρ_A		$\delta^{18}O$ temp	Temperature	Calcification	Calcification		$[PO_4^{3-}]$	$[Si(OH)_4]$	Alkalinity		$[CO_3^{2-}]$	$[CO_3^{2-}]$	
Sample ID	date	date	difference	(425-850µm)	(425-650µm)	(650-850µm)	(µg) (±σ)	($1x10^5$ µm^2) (±σ)	($1x10^{-4}$ µg/µm^2)	$\delta^{18}O$ (‰)	(°C)	(°C)	Depth (mbsl)	Depth Range (mbsl)	Salinity	(µmol/kg)	(µmol/kg)	(µmol/kg)	pH	(µmol/kg)	(µmol/kg)	Ω_{calc}
CAR18_11	03/31/05	03/08/05	-23	17	13	4	33.43 (±15.45)	2.11 (±0.74)	1.53 (±0.32)	-0.74	22.43	22.39	55	50-60	36.89	0.36	2.57	2427	7.943	179.36	177-188	4.20
CAR19_11	10/05/05	10/05/05	0	23	14	9	41.69 (±12.69)	2.42 (±0.62)	1.71 (±0.17)	-1.06	23.43	24.05	75	75-90	36.86	0.19	1.13	2421	8.008	212.01	196-221	4.96
CAR20_9	03/07/06	02/07/06	-28	29	17	12	35.17 (±12.19)	2.38 (±0.57)	1.45 (±0.28)	-0.68	21.13	21.05	55	45-60	36.77	0.43	4.26	2436	7.921	165.39	163-172	3.86
CAR20_11	04/04/06	03/16/06	-19	14	6	8	43.24 (±12.63)	2.96 (±0.87)	1.46 (±0.13)	-0.59	21.68	21.36	55	38-55	36.80	0.34	2.05	2425	7.938	171.51	171-185	4.02
CAR21_8	08/23/06	08/03/06	-20	10	5	5	35.65 (±11.29)	2.35 (±0.59)	1.51 (±0.25)	-0.63	21.68	21.84	35	20-44	36.83	0.20	1.84	2413	7.934	171.77	158-179	4.04
CAR22_1	11/08/06	11/02/06	-6	12	–	12	50.30 (±7.90)	3.03 (±0.38)	1.66 (±0.16)	-1.50	24.94	25.10	75	70-84	36.61	0.19	1.23	2404	8.023	221.80	211-224	5.21
CAR22_13	04/25/07	04/10/07	-15	10	7	3	36.04 (±10.34)	2.40 (±0.51)	1.48 (±0.16)	-0.98	22.31	21.68	25	20-25	36.75	0.23	1.37	2404	7.958	177.84	177-191	4.19
CAR23_2	05/30/07	05/08/07	-22	11	9	2	36.70 (±12.49)	1.99 (±0.57)	1.81 (±0.26)	-1.07	23.76	25.36	15	15-22	36.88	0.10	0.89	2406	8.049	234.28	219-234	5.54
CAR23_7	08/08/07	07/03/07	-36	21	15	6	36.43 (±14.41)	2.15 (±0.69)	1.67 (±0.29)	-1.31	24.46	23.71	15	12-16	36.86	0.06	0.00	2415	7.984	199.70	199-217	4.71
CAR23_11	10/03/07	09/04/07	-29	15	12	3	40.50 (±11.04)	2.39 (±0.64)	1.71 (±0.17)	-1.12	23.53	24.12	75	75-92	36.65	0.33	2.52	2392	8.004	207.45	184-207	4.87
CAR25_2	06/04/08	05/06/08	-29	10	6	4	37.70 (±10.10)	2.26 (±0.37)	1.67 (±0.33)	-0.93	23.31	23.20	35	28-34	36.96	0.21	2.55	2426	7.986	198.92	196-208	4.68
CAR25_8	08/13/08	08/05/08	-8	11	4	7	47.51 (±19.08)	2.71 (±0.98)	1.73 (±0.11)	-1.49	25.00	25.97	15	15-19	36.73	0.01	1.36	2421	8.054	241.42	231-241	5.72
CAR25_11	09/24/08	09/10/08	-14	11	5	6	46.35 (±10.58)	2.75 (±0.60)	1.69 (±0.21)	-1.09	22.85	24.23	100	94-114	36.83	0.59	2.53	2409	8.001	209.20	181-209	4.88

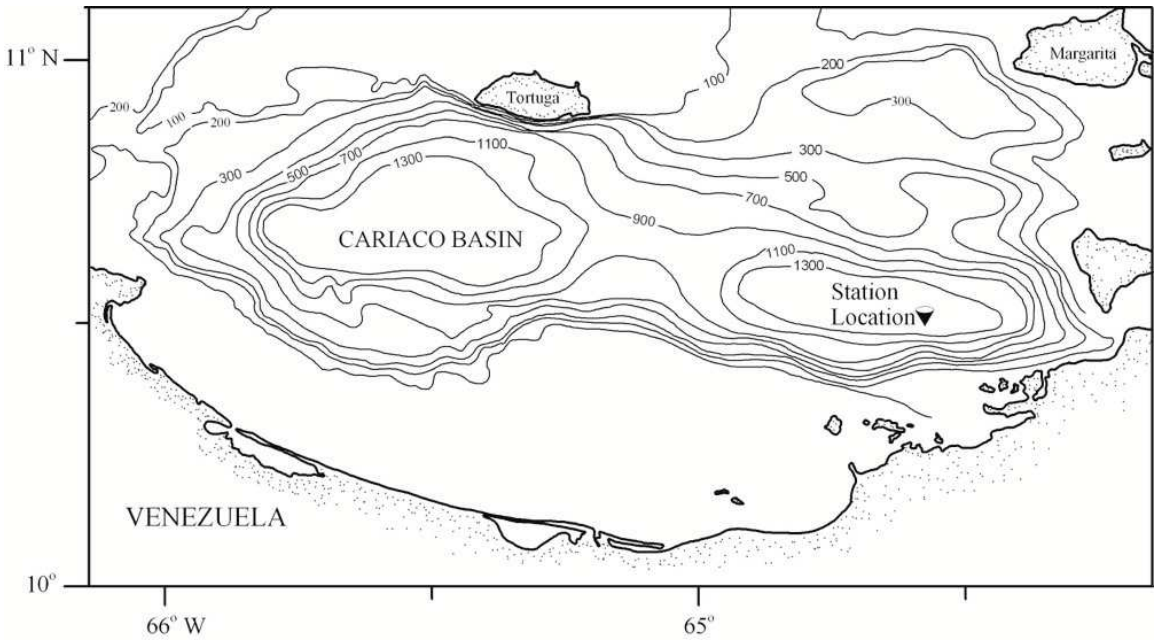

Figure 1.1 Bathymetric map of the Cariaco Basin showing the location of the sediment trap mooring (10°30′ N and 65°31′ W).

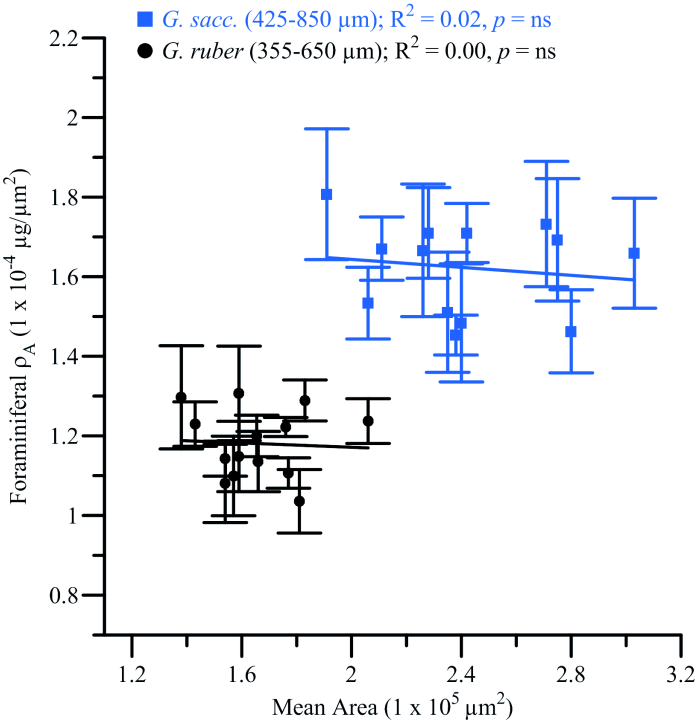

Figure 1.2 ρ_A and mean area relationship.

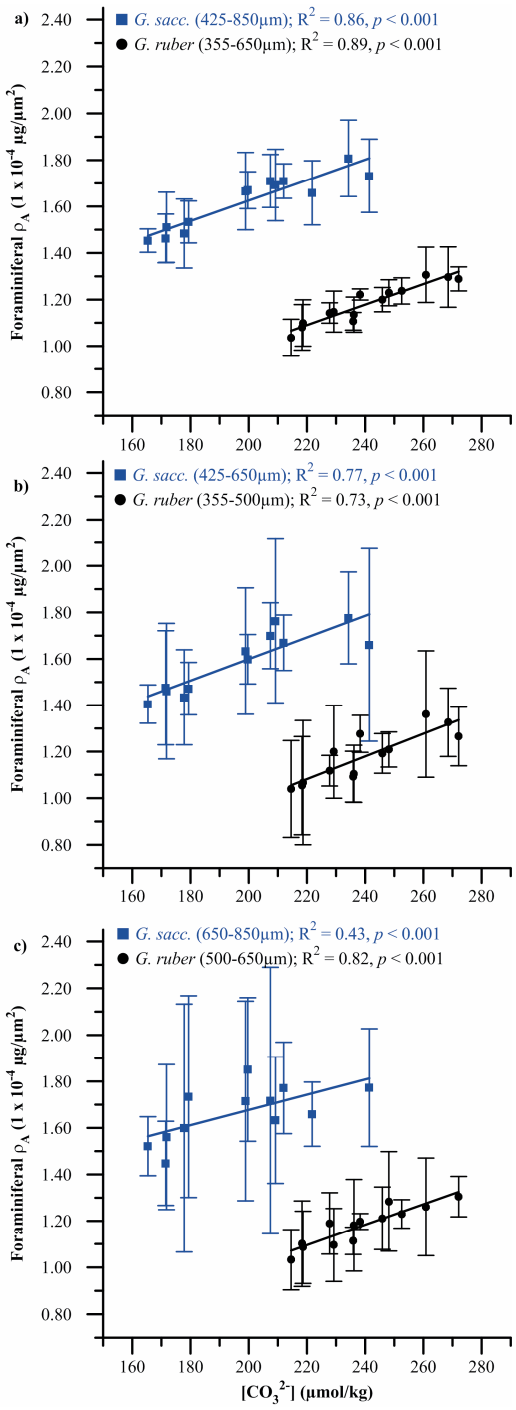

Figure 1.3 $[CO_3^{2-}]$ - ρ_A relationships for both *G. ruber* and *G. sacculifer* for size fractions (a) 355-650 and 425-850 µm (b) 355-500 and 425-650 µm and (c) 500-650 and 650-850 µm. Error bars represent the ρ_A multiplied by the reciprocal of the number of individuals in each sample populations. Samples with $n > 2$ were included for (b) and (c) in order to compare to the broader size fraction samples presented in (a; $n \geq 10$).

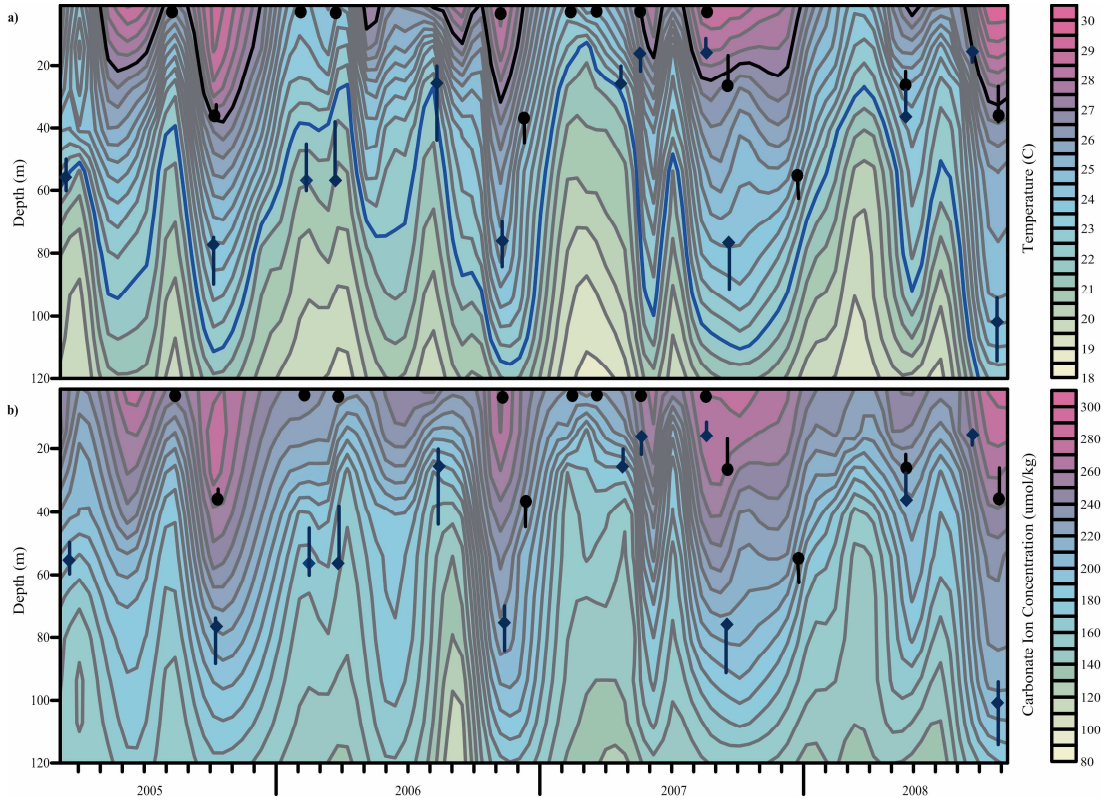

Figure 1.4 Contour plots of a) temperature and b) $[CO_3^{2-}]$ from March, 2005 through October, 2008 in the Cariaco Basin for the upper 160 m of the water column. Calcification depths, estimated from $\delta^{18}O$-derived calcification temperatures, are shown for *G. ruber* (black circles) and *G. sacculifer* (blue diamonds). Also shown are the estimated depth ranges for each sample estimated from the instrumental and $\delta^{18}O$-derived calcification temperatures (see auxiliary material for more details). Optimal growth temperatures for both *G. ruber* (black line) and *G. sacculifer* (blue line) are also plotted [*Mulitza et al.*, 1998] to compare to the estimated calcification depths for both species.

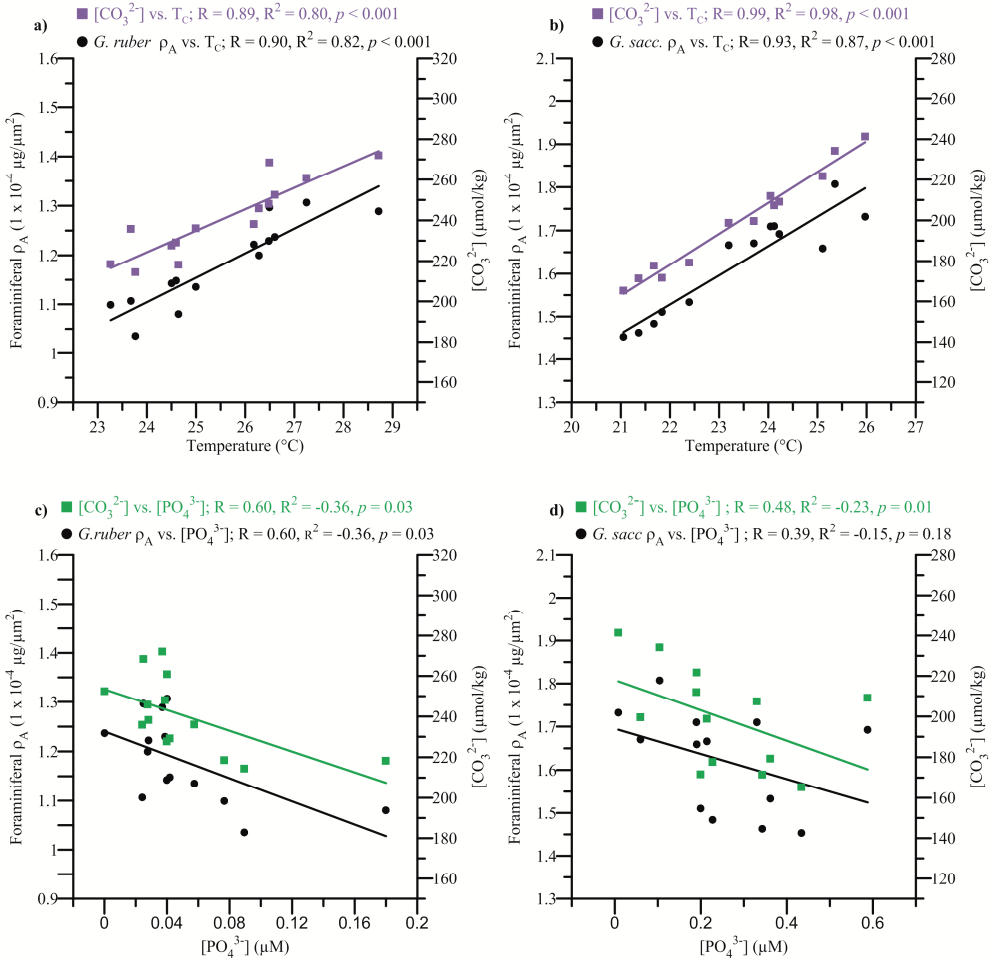

Figure 1.5 Temperature - ρ_A and temperature - $[CO_3^{2-}]$ relationships for *G. ruber* (a) and *G. sacculifer* (b). Also shown are $[PO_4^{3-}]$ - ρ_A and $[PO_4^{3-}]$ - $[CO_3^{2-}]$ relationships for *G. ruber* (c) and *G. sacculifer* (d).

CHAPTER 2

MORPHOMETRIC AND STABLE ISOTOPIC DIFFERENTIATION IN *ORBULINA UNIVERSA* MORPHOTYPES FROM THE CARIACO BASIN, VENEZUELA.

2.1 ABSTRACT

Morphometric characteristics of *Orbulina universa* (d' Orbigny) were used to differentiate morphotypes present in sediment trap samples collected from the Cariaco Basin, Venezuela. In particular, wall thickness and weight-area relationships were used to separate shells into thin (M_{thin}) and thick (M_{thick}) morphotypes. M_{thick} (mean thickness = 28 μm) comprises 75% of the total *O. universa* in these samples and has morphometric characteristics similar to that of the previously described Type I Caribbean genotype, whereas M_{thin} (mean thickness = 13 μm) is comparable to the Type III Mediterranean genotype. The flux of M_{thick} increases during periods of upwelling, whereas M_{thin} fluxes shows no systematic relationship with changing hydrographic regimes in the basin. The $\delta^{18}O$ and $\delta^{13}C$ of M_{thick} are on average 0.34 ‰ higher and 0.38 ‰ lower, respectively, than those of M_{thin}, suggesting that they calcify their final spherical chamber at different depths in the water column and/or differ in their vital effects. Additionally, the absolute offset in the stable isotopic compositions of the two morphotypes varies as a function of surface ocean stratification. During periods of upwelling, the $\delta^{18}O$ and $\delta^{13}C$ offsets between M_{thin} and M_{thick} are on average 0.15 and 0.25

‰, respectively. The $\delta^{18}O$ and $\delta^{13}C$ offsets between the two morphotypes increase to 0.55 and 0.41‰ during non-upwelling periods. We attribute the higher $\delta^{18}O$ offsets during non-upwelling periods to a difference in final chamber calcification depth and the combined effects of temperature ($\delta^{18}O$), $\delta^{13}C$ DIC ($\delta^{13}C$), irradiance ($\delta^{13}C$) and [CO_3^{2-}] ($\delta^{18}O$ and $\delta^{13}C$). These data provide field evidence that thin and thick morphotypes of *O. universa* experience different environmental conditions during the formation of their final chamber and, therefore, should not be used together in geochemical analyses for reconstructing past surface ocean conditions.

2.2 Introduction

2.2.1 Overview

The fossil shells of planktonic foraminifera serve as important sedimentary archives for studying past climatic and oceanographic conditions. However, proxy signals preserved in foraminiferal shells have been shown to vary significantly between species (Erez, 1978; Hemleben et al., 1989, Spero, 1998; Spero et al., 2003), with species identifications being strongly reliant on morphological concepts (Saito et al., 1981; Tendal 1990). As a result of these interspecies differences, which are generally attributed to vital effects or ecological factors such as depth habitat and/or seasonal preferences, species-specific proxy calibrations are necessary in order to produce the most reliable estimates of past ocean conditions (Hemleben et al., 1989; Spero et al., 1997; Bijma et al., 1998; Bemis et al., 2002). Despite attempts to differentiate between morphologically defined species, the paleoceanographic community has long recognized the existence of morphotypes within

species of planktonic foraminifera, often finding a large range in morphologies within a single population (Kennett, 1976; Be et al., 1983; Deuser et al, 1981; 1987; 1989). A handful of studies report significant stable isotopic and trace metal differences amongst the various morphotypes of some species of planktonic foraminifera (Healy-Williams, 1985; Deuser et al., 1981; 1987; Bijma et al., 1998; Wang et al., 2000; Steinke et al., 2005; Richey et al., 2012). However, the significance of morphological variation was not apparent until the first genetic studies of foraminifera. These studies revealed that many morphologically defined species are complexes of cryptic genetic variants (Darling et al., 1996; 1997; 1999; de Vargas et al., 1997; 1999, 2001; Huber et al., 1997; Kucera and Darling, 2002; Darling and Wade, 2008). For example, fifty-four cryptic species have been identified among nine modern planktonic foraminiferal morphospecies commonly used for paleoceanographic reconstructions (Kucera and Darling, 2002; Darling and Wade, 2008; Morard et al., 2013). Several studies suggest that cryptic species can differ in their ecological preferences (Huber et al., 1997; Darling et al., 1999; de Vargas et al., 1999, 2003; Stewart et al., 2001; Kuroyanagi and Kawahata, 2004; Morard et al., 2009; Aurahs et al., 2011; Morard et al., 2013) and emphasize the importance of distinguishing between genotypes for paleoceanographic reconstructions (Kucera and Darling, 2002). Based on these findings, it is likely that a morphotype/genotype "lumping" approach for geochemical, morphometric and distribution analyses introduces a significant amount of noise into paleoclimate records. Thus, the ability to discriminate between these different genetic types within sediment samples may greatly enhance the usefulness of various planktonic foraminiferal proxies (Darling and Wade, 2008).

In some cases, taxonomic "lumping" may be easily revised within the framework of the morphospecies concept. For example, some genetically distinct variants of *Globigerinodes ruber* (Type IIa and Type Pink) can be differentiated easily based on differences in chamber morphometrics and pigmentation (Aurah et al., 2011). Some cryptic species, however, are not distinguished from one another based on easily identifiable morphological differences (Knowlton, 1993). *Orbulina universa* (d' Orbigny), a species commonly used in climate proxy development (Spero and Williams, 1988; Sanyal et al., 1996; Spero et al., 1997; Bemis et al., 1998; Lea et al, 1999; Ren et al., 2012), has three known genetic variants – Caribbean (Type I), Sargasso (Type II) and Mediterranean (Type III; Darling et al., 1996; 1997; de Vargas et al., 1997,1999; Morard et al., 2009). Several studies have mapped the geographic distribution of *O. universa* genotypes in the North and South Atlantic, Caribbean Sea, Western Pacific Ocean, Southern California Bight and Indian Ocean (Darling et al., 1997a,b, 1997; de Vargas et al., 1997,1999; Morard et al., 2009, 2013), and have linked their relative abundances to changes in sea surface chlorophyll concentrations (de Vargas et al., 1999). For example, plankton tow samples collected off Puerto Rico and Bermuda revealed the presence of both the Caribbean and Sargasso genotypes (de Vargas et al., 1997), which are defined as the oligotrophic and extreme oligotrophic genetic varieties of *O. universa* (de Vargas et al., 1999). *Orbulina universa* collected from upwelling region in the Atlantic and off the coast of California (Catalina Island) have been identified as the Mediteranean cryptic species, which is considered the eutrophic variant of *O. universa* (de Vargas et al., 1999). Morard et al. (2009) further documented the presence of all three cryptic species at a

Caribbean sampling site (C-Marz 5; 14°01'N, 54°91'W), only 1,200 km NW of the Cariaco Basin sediment trap mooring.

These three cryptic species of *O. universa* are morphologically very similar, but subtle differences in the pore space distribution and shell wall thickness have been used to distinguish them under a scanning electron microscope (SEM; Morard et al., 2009). However, this is a time consuming process and the identification of the cryptic species in this way does not always permit subsequent geochemical analysis of the shells due to sample processing for SEM analysis. The current study presents a framework for the identification of morphotypes and potentially cryptic species of *O. universa*. Our results suggest that there are currently two morphotypes of *O. universa* (M_{thin} and M_{thick}) present in the Cariaco Basin that can be separated on the basis of shell morphology. We also present carbon and oxygen isotope data in an attempt to better constrain the ecological preferences and final spherical chamber calcification depths of the two morphotypes.

2.2.2 Orbulna universa: Life Cycle, Habitat Preferences and Morphometric Variability

Early studies of the habitat preferences and morphological characteristics of *O. universa* treated its morphotypes as ecophenotypic variants, all belonging to the same genetic species but exhibiting phenotypic variation under different environmental conditions (Hecht et al., 1976; Bé et al., 1973; Colombo and Cita, 1980). These studies defined *O. universa* as a subtropical to tropical species with a preference for dwelling within the photic zone between the surface-mixed layer and shallow thermocline. The temperature ranges reported for *O. universa* differ regionally, but generally fall between 9

and 30 °C (Bradshaw, 1959; Tolderlund and Bé, 1971; Bouvier-Soumagnac and Duplessy, 1985; Sautter and Thunell, 1991a; Darling and Wade, 2008).

During the early portion of its ~1 month life cycle (Hemleben and Bijma, 1994), *O. universa* has a multi-chambered trochospiral form, ornamented with calcite spines that serve as a home for a cloud of photosynthetic dinoflagellate symbionts. During the last 2-9 days of its life cycle, *O. universa* precipitates a large, spherical final chamber that comprises 90-95% of its total calcite and thickens continuously until gametogenesis (Spero et al., 1988; 2015). During gametogenesis, *O. universa* retracts its spines and adds a thin veneer of calcite that contributes ~ 4-20% to the final shell calcite prior to the release of its gametes (Hamilton et al., 2008). Small and large pores on the final chamber serve as pathways for gas exchange and food and symbiont transport into and out of the cell protoplasm, respectively (Bé et al., 1980; Spero, 1987; 1988). Pore distribution is established at the time of the final chamber formation (Spero, 1988), and is believed to be distinctly different amongst the genetic varieties of *O. universa* (Morard et al., 2009).

Size variations in the final spherical chamber of *O. universa* have been linked to changes in calcification temperature (Schmidt et al., 2004; Lombard et al., 2009), whereas thickness variations have been associated with changes in the carbonate ion concentration ($[CO_3^{2-}]$) and variations in water column irradiance (related to symbiont photosynthesis; Lea et al., 1995; Lombard et al., 2010; Spero et al., 2015). Porosity variations in *O. universa* specimens have been attributed to changes in oxygen concentrations, such that porosity increases as oxygen concentrations decrease (Colombo and Cita, 1980). However, since *O. universa* lives most of its life cycle within the photic zone, which is oversaturated with respect to oxygen, changes in oxygen concentration is

an unlikely contributor to porosity variations. Additionally, the discovery of porosity and thickness variations amongst cryptic species of *O. universa* complicates these earlier ecophenotypic concepts (Morard et al., 2009).

Deuser et al. (1981) and Deuser (1987) were the first to suggest a difference in calcification depths for morphotypic variants of *O. universa* based on sediment trap material collected from the Sargasso Sea (32°54'N, 64°15'W). These studies report the presence of thin (5-10 μm) and thick (up to 30 μm) morphotypes of *O. universa* and find that the thick walled variety secretes shells that have up to 0.5 ‰ higher $\delta^{18}O$ values than the thin-walled variety (Deuser et al., 1981b). The thin morphotype comprised 65-80% of the collected *O. universa* at this location and was present year-round, though in higher abundances during periods of increased stratification. The thick-walled variety was far less abundant (20-35%), and is only present in this region of the North Atlantic during the spring when the mixed layer is deep. Based on oxygen isotopic compositions of pooled sediment trap shells and depth-stratified plankton tow samples, Deuser (1981b) concluded that the thinner of the two morphotypes calcified at depths between 25-50 m, while the thicker morphotype calcified in deeper water. The thickness variations between the two morphotypes were ultimately contributed to the presence or absence of gametogenic calcite, though later studies suggest that the *O. universa* morphotypes from these studies may represent different cryptic species (Hamilton et al., 2008). Deuser et al. (1987) also report that the differences between the oxygen isotopic compositions of the thick and thin varieties of *O. universa* is minimal during periods when the mixed layer is deep and increases rapidly as a more stratified water column is established.

2.2.3 The Cariaco Basin Ocean Time Series

The Cariaco Basin is located on the continental shelf of northern Venezuela (Figure 1). Because of the shallow sills (~130 m) surrounding the basin, the deep waters are not well ventilated. This restricted nature of the basin, combined with seasonally high productivity, results in anoxic waters below ~250 m. The Cariaco Ocean Time Series was established in November 1995 and provides a repository of biweekly sediment trap samples collected at discrete depths throughout the water column ((10°30′ N and 65°31′ W; 150, 230, 410, 800 and 1200 m). Monthly hydrographic data are also available for comparison with sediment trap data. These samples have been used to assess and further calibrate a variety of paleoceanographic proxies (Goni et al., 2004; Wejnert et al., 2013; Marshall et al., 2013; Turich et al., 2013).

The physical and chemical characteristics of Cariaco Basin surface waters vary seasonally in response to the migration of the Intertropical Convergence Zone (ITCZ). When the ITCZ is in its most northerly position (August-October), temperatures and pH are high and salinity and nutrient concentrations are low in the surface waters (Figure 2). As the ITCZ shifts further south during boreal winter and early spring, the basin is exposed to strong easterly trade winds that result in Ekman-induced upwelling (Astor et al., 2013). This results in lower temperatures and pH and higher salinities and nutrient concentrations in the surface waters. The dynamic nature of the basin allows us to observe a wide range of hydrographic conditions and assess their impact on the planktonic foraminifera that calcify within the basin.

2.3 METHODS

2.3.1 SEDIMENT TRAP AND WATER PROPERTY COLLECTIONS

Biweekly sediment trap samples collected between August 2005 and July 2008 from the trap moored at 410 m depth were used in this study. The foraminifera were separated from a quarter split of each sample cup using the settling method presented in Bé (1959). The samples were then wet sieved (>125 μm) and washed prior to being examined under a stereo binocular microscope. All *O. universa* specimens within the quarter split were wet picked and counted. The number of specimens in each sample ranged from 13 to 56, with an average of 33. The fluxes of each morphotype were calculated using the following equation:

$$\text{Flux (n/m/day)} = 4n/(0.5\ \text{m})/\text{days} \qquad (1)$$

where n is the number of a given morphotype in a quarter split of each sample population, 0.5 m is the cross-sectional area of the sediment trap and days is the duration of the collection period (7-14 days; Tedesco et al., 2003).

Monthly temperature, salinity, oxygen, pH, chlorophyll and nutrient concentrations measured at the sediment trap mooring location were compared to the

morphotype fluxes, oxygen isotope-derived calcification temperatures, and morphometric characteristics of the *O. universa* specimens. Irradiance measurements for the upper 75 m of the water column are also available for select samples throughout the study period (Lorenzoni et al., 2011). Temperature and salinity measurements were used to establish mean calcification depths of the final sphere for each morphotype (this procedure is described in section 2.5). A comprehensive listing of the monthly hydrographic data for the entire Cariaco Basin time series can be found at http://www.imars.usf.edu/CAR. Because the vast majority (90-95%) of *O. universa* sphere calcite is produced during the last 2-9 days of its life cycle (Spero et al., 2015) and considering a 1 to 2-day settling period to reach the trap depth of 410 m (sinking speed = 300 m/day; Takahashi and Bé, 1984), the foraminifera collected in the biweekly sediment traps could have calcified from 8 days prior to 11 days after the time the trap opened for collection. To account for this, we paired the sediment trap samples with hydrographic data that fell closest to or within this time range when possible. The dates for the beginning of each sediment trap collection period, the paired date of hydrographic data collection, and the values for the surface ocean hydrographic measurements (upper 100 m average) are reported in Table 1.

We use the coastal upwelling index (M; m^3/s), estimated based on the cross-shore Ekman transport per 100 m of coastline, to identify periods of upwelling and non-upwelling throughout the study period (Astor et al., 2013):

$$M = \tau_x/f \qquad (2)$$

where *M* is the meridonal Ekman transport, τ_x is the zonal wind stress derived from nearby meteorological stations and *f* is the Coriolis parameter. The monthly upwelling index anomaly is then calculated by dividing M by the average M for the entire time series (Jan. 1996 – Nov. 2011), with a negative anomaly representing periods of enhanced upwelling. Here, we define an upwelling period as an upwelling index anomaly ≤ 0.

2.3.2 Foraminiferal Morphometric Calculations

Individual foraminifera (n = 13-56 per sample) were weighed on a high-precision Mettler Toledo microbalance (±0.43 ug) and photographed using an inverted microscope equipped with a Canon Rebel XSI. The photographs were then uploaded into the microscopic imaging program Macnification 2.0 for diameter and silhouette area analysis. Calibrations for the silhouette area and diameter measurements were performed using a microscale image taken at the same magnification as the foraminiferal images (50x). The area densities (ρ_A) of individual *O. universa* were calculated using the methods presented in Marshall et al. (2013), where

$$\rho_A\,(\mu g/\mu m^2) = \text{weight/silhouette area} \qquad (3)$$

The mean area densities (ρ_A) for each sediment trap sample were calculated by averaging the ρ_A of all *O. universa* specimens in a given sample. A total of 494 *O. universa*

specimens were measured for weight, silhouette area, diameter, and area density in this study.

2.3.3 *Orbulina universa* Morphotype Distinction

The area densities of individuals were used to create groupings of *O. universa* morphotypes for each of the 15 sediment trap samples. Examples of this method applied to two of the samples (20-8 and 23-4) are shown in Figure 3a and 3b. The area densities for all samples are shown in Figure 3c. As the groupings were created, the weights and areas of each group exhibited distinct positive linear relationships (Figure 3d-e), providing a secondary means of distinguishing *O. universa* morphotypes. The morphotype-specific weight-area relationships for all samples are shown in Figure 3f. All but one sample exhibited two distinct morphotype groupings, a thin morphotype (M_{thin}) and a relatively thick morphotype (M_{thick}). For the sample containing a single morphotype (21-3), we compare the mean weight, area and area density to the ranges exhibited by each morphotype and are able to easily classify this group as M_{thick} (Figures 3c and 3f).

2.3.4 SEM Analysis

Orbulina universa individuals from two of the samples (20-7 and 22-7; n = 42) used in the morphometric analysis were also examined on a Tescan Vega 3 SBU variable pressure scanning electron microscope (SEM). The *O. universa* shells were gently

broken, adhered to carbon tape and gold sputter-coated to prevent charging of the specimen during imaging. Porosity measurements were made on these specimens by gathering images normal to the inner shell wall in order to minimize optical distortion of the pores (Be et al., 1973; Spero et al., 1988). The outer edges of each individual were used to measure shell thickness. Images were uploaded into the microscopic imaging program Macnification 2.0 to characterize porosity and thickness variations between the two morphotypes. Porosities were calculated within the maximum region of the inner shell determined to be at a normal angle to the center of the shell. Small and large pores were manually marked and their areas summed. Small, large and total pore areas were divided by the total area of the surveyed region and multiplied by 100 to calculate porosity.

SEM-measured thicknesses were averaged from 5 measurements taken at random along the shell edge. We use the relationships between the area densities and measured thicknesses of samples 20-7 and 22-7 to derive morphotype-specific equations for estimating the thicknesses of Mthin and Mthick (Tables 2, Figure 4a and b). These equations were used to calculate thickness for all specimens examined in this study. The porosities and calculated thicknesses were used to characterize the morphotypes and compare them to the previously published porosity and thickness measurements for the three known cryptic species of *O. universa (Morard et al, 2009).* We also use the SEM images to assess whether or not the specimens had undergone gametogenic

calcification, defined by the presence or absence of a gametogenic calcite layer on spine bases (Table 2).

2.3.5 Estimated Calcification Depth and Temperature

Following the morphometric analyses, groupings of one to eight *O. universa* shells from each morphotype (diameter > 500 μm) were analyzed for oxygen and carbon isotopes using a GV IsoPrime stable isotope ratio mass spectrometer (long-term standard reproducibility is ± 0.06 ‰ for $\delta^{13}C$ and 0.07 ‰ for $\delta^{18}O$). The isotopic values are reported relative to Vienna Pee Dee Belemnite (V-PDB). Calcification temperatures were estimated from the oxygen isotopic compositions of *O. universa* using the following species-specific equation developed by Bemis et al. (1998):

$$T\ (^{\circ}C) = 16.5 - 4.80\ (\delta_c - (\delta_w - 0.27)) \quad (4)$$

where δ_c is the $\delta^{18}O$ of the foraminiferal calcite and δ_w is the $\delta^{18}O$ of the calcifying waters which are scaled from SMOW to PDB by subtracting 0.27 ‰. Here, we use the low light (LL) equation because the optimal light level for *O. universa* (P_{max} = 386 μEinst m^{-2} s^{-1}; Spero et al., 1999) generally occurs within the upper 20 m of the water column in the Cariaco Basin and declines rapidly thereafter (Lorenzoni et al., 2011). δ_w was estimated using the $\delta^{18}O$ - salinity relationship for Cariaco Basin (McConnell et al., 2009):

$$\delta_w = 0.34\ (\pm 0.09) \times (\text{salinity}) - 11.5\ (\pm 3.4) \quad (5)$$

The calculated calcification temperatures were then compared to measured temperatures in order to determine the average calcification depth of the final chamber. Additional

measured and calculated hydrographic parameters (i.e., salinity, pH, alkalinity, [CO_3^{2-}], water density, oxygen, nutrient, irradiance and chlorophyll concentrations) at the estimated calcification depth were then used to define the environment of the two *O. universa* morphotypes during the final 2-9 days of calcification. Carbonate ion concentration ([CO_3^{2-}]) was calculated using alkalinity, pH, salinity, temperature and nutrient concentrations and CO2SYS.xls (Pelletier et al. 2007, version 16). The isotopic measurements were restricted to the greater than 500 µm size fraction, with a range of 540 to 665 µm in an effort to isolate any effect of size on $\delta^{18}O$ and $\delta^{13}C$ (Bouvier-Soumagnac and Duplessy, 1985; Elderfield et al., 2002; and Friedrich et al., 2012).

2.4 Results

2.4.1 Biometric Characteristics

We find two biometrically distinct *O. universa* morphotypes in the Cariaco sediment trap samples, which are easily differentiated by thin (M_{thin}) and thick (M_{thick}) shell walls. All of the morphometric data is summarized in Table 3. The mean silhouette areas of the M_{thin} and M_{thick} are 2.64 (±0.54) and 2.75 (± 0.63) x 10^5 µm^2, respectively, and are not significantly different (paired comparison T-test; $p = 0.330$, t = -1.01). Measured diameters were also similar for the two morphotypes, ranging between 330 and 688 µm for M_{thin} (mean = 570 µm) and 330-715µm for M_{thick} (mean = 585 µm; $p = 0.284$, t = -1.12). In contrast, the mean weights for the two morphotypes are significantly different from one another, with a mean weight of 32 (±10; range = 4 - 66) µg for M_{thin} and 59 (±13, range = 17-110) µg for M_{thick} ($p = 0.000$, t = -8.94).

Because the two morphotypes exhibit similar mean sizes, the weight differences must be a result of a difference in shell thickness. Indeed, significant differences in the mean area densities (M_{thin} = 1.16 (± 0.22) x 10^4 µg/µm^2, M_{thick} = 2.13 (± 0.28) x 10^4 µg/µm^2) and calculated thicknesses (M_{thin} = 13 (±2; range = 6-22) µm, M_{thick} = 28 (±4; range = 19-41) µm) of the two morphotypes indicate that M_{thick} is characterized by a thicker shell wall (p = 0.000, t = -13.16 for area density; p = 0.000, t = -17.56 for thickness). The SEM measured shell thickness and porosity values for sediment trap samples 20-7 and 22-7 can be found in Table 2. Sample images of both morphotypes, including those of the pores and shell edges, are presented in Figure 5. Examination of shell wall images revealed that pre-gametogenic individuals are present in both morphotype groups, being only slightly more abundant for M_{thin} than M_{thick} (38% vs. 23%, respectfully; Table 2). The SEM measured and calculated thicknesses agree on average within 0.1 µm (Table 2, n = 40), indicating that the ρ_A- thickness equations for the two morphotypes are effective at estimating *O. universa* shell thickness (Table 2). The imaged M_{thin} specimens have an average porosity of 8% (±1; range = 6-10 %, n = 11), while M_{thick} specimens have an average porosity of 15% (±2.5; range = 11-20 %, n = 28) and differ significantly from one another (p = 0.000, t = -8.750). Relative to M_{thin}, M_{thick} is characterized by higher average small (8.4% vs. 5.7%) and large porosities (14.6% vs. 8.4%; Figure 6). The two morphotypes exhibit a similar range in small porosities (M_{thin} = 3.0 - 8.9%; M_{thick} = 4.8 - 12.0%), thus, the majority of the porosity differences between the two morphotypes can be attributed to differences in large porosity (M_{thin} = 0.0 – 4.4%; M_{thick} = 1.8 - 11.3%; Figure 6).

2.4.2 Accuracy of Method

Unlike thickness, which increases continually for *O. universa* after the final spherical chamber has been secreted (Spero et al., 2015), pore distribution remains constant once the final chamber has been fully formed (Spero, 1998). Though the apparent porosity would be greater on the outer surface of thicker shells as pore walls angle outwards toward the surface of the shell (Spero et al., 1998), porosity measurements on the inner shell wall are representative of the pore distribution at the time of final chamber calcification. If we assume that inner shell porosity is the most defining and constant morphometric parameter for distinguishing between genotypes in a given region (Morard et al., 2009), we can use the porosity measurements for samples 20-7 and 22-7 to determine the accuracy of the morphometric method presented in this study for identifying morphotypes of *O. universa*. Morard et al., (2009) report porosities ranging from 12-30% and 6-10% for the Caribbean and Mediterranean cryptic species collected from the C-MarZ sites, respectively. If we divide the porosity measurements for samples 20-7 and 22-7 (Table 2) into these ranges, we find that approximately 85% of M_{thin} and 77% of M_{thick} are associated with a single porosity range. Specifically, the large majority of M_{thin} is associated with the lower porosity range (6-10%), while M_{thick} is largely associated with the higher porosity range (11-20%). We suspect that the main cause for the misidentification of *O. universa* M_{thick} as M_{thin} is the absence of gametogenic calcite in M_{thick}, which would affect both the area density and weight-area relationships of a specimen. Indeed, we find that more than 50% of the misidentified M_{thick} specimens had not undergone gametogenic calcification based on the SEM images of the shell wall (Table 2). The two M_{thin} specimens misidentified as M_{thick} have

anomalously thick test walls as compared to those observed from the other M_{thin} specimens. In summary, the morphometric methods presented in this study identified the correct morphotype for ~ 80% of the *O. universa* specimens, with the majority of misidentifications attributed to the absence of gametogenic calcite in M_{thick} group.

Compared to earlier geometric methods for calculating shell thickness in *O. universa* (see Billups and Spero, 1995 for method description), we find that the ρ_A method presented in this study is more effective at accurately estimating shell thickness, particularly for thicker shells (Figure 4c). This may be due to the necessity to apply a porosity correction to geometrically calculated thickness, which is a morphometric trait that varies amongst the morphotypes and cryptic species (Morard et al., 2009; this study). Though we applied porosity corrections using the average porosities for each morphotype (M_{thin} = 8%, M_{thick} = 15%), we found that the geometrically determined thicknesses increasingly underestimated measured thicknesses as shell thickness increased.

2.4.3 Seasonal Changes in Morphotype Abundances

The abundances and fluxes of M_{thin} and M_{thick} are listed in Table 1. M_{thick} is the more abundant of the two morphotypes, comprising on average 75% of the total *O. universa* specimens in the sediment trap samples. When comparing the fluxes of M_{thin} and M_{thick} to the time-equivalent monthly averaged upwelling index (Astor et al., 2013), we find that the fluxes of M_{thick} are higher during upwelling periods (mean upwelling flux = 17 shells/m/day, mean non-upwelling flux = 9 shells/m/day; Figure 7). In contrast, there is no difference in flux for M_{thin} between upwelling and non-upwelling periods

(mean flux upwelling = 5 shells/m/day, mean flux non-upwelling = 5 shells/m/day). However, we observe the lowest fluxes in M_{thin} during peak upwelling periods (Samples 21-3 (0 shells/m/day) and 23-1 (2 shells/m/day)).

2.4.4 Oxygen and Carbon Isotopes

The bulk (average of both morphotypes) and morphotype-specific oxygen and carbon isotopic data for *O. universa* are listed in Table 4. The sample means presented in Table 4 are weighted based on the number of individuals per sample analysis in order to give more weight to those samples containing more *O. universa* individuals. A paired comparison T-test revealed that for both carbon and oxygen isotopes, the differences between M_{thin} and M_{thick} are highly significant ($t = 4.390$, $p = 0.001$ and $t = -5.294$, $p = 0.000$ for $\delta^{13}C$ and $\delta^{18}O$, respectively). The $\delta^{18}O$ and $\delta^{13}C$ of M_{thick} are on average 0.34 ‰ higher and 0.38 ‰ lower, respectively, than those of M_{thin} (Figures 8 and 9). The offset in $\delta^{18}O$ and $\delta^{13}C$ values of M_{thin} and M_{thick} is higher during non-upwelling periods ($\delta^{18}O$ offset = 0.55 ‰; $\delta^{13}C$ offset = 0.41 ‰) relative to upwelling periods ($\delta^{18}O$ offset = 0.15 ‰; $\delta^{13}C$ offset = 0.25 ‰; Figure 10, see discussion section 4.2 for further explanation).

2.4.5 Final Chamber Calcification Depths and Hydrographic Parameters

The mean $\delta^{18}O$ values from each sample were used to calculate calcification temperatures for the individual morphotypes using equations 4 and 5 (Table 5). M_{thin} and M_{thick} had

average calcification temperatures for the final *O. universa* chamber of 23.3 and 21.6 °C, respectively, which are within the optimal temperature range proposed for *O. universa* (22-28°C; Caron et al., 1987; Lombard et al., 2009). The two morphotypes have distinctly different average depths at which the final spherical chamber calcifies, with M_{thick} calcifying at deeper depths (25-130 m) than M_{thin} (7-100 m; Figure 2). Specifically, M_{thick} is adding its final chamber in waters characterized by lower temperatures (21-23°C), pH (7.85 – 8.01), [O_2] (100 - 175 μmol/kg) and chlorophyll concentrations (0-750 ng/L). Final chamber calcification for M_{thin} occurs at higher temperatures (mean = 22-24 °C), pH (mean = 7.93-8.04), [O_2] (100 - 200 μmol/kg), and chlorophyll concentrations (60 - 830 ng/L) (Table 5). Salinities at the estimated calcification depths for both morphotypes are very similar and closely correspond with the salinity maximum in the basin (36.8).

The calcification depths for both morphotypes varied throughout the 3-year time series, with both calcifying at shallower depths during upwelling periods (Figure 2). Differences in the depths of calcification for the two morphotypes tend to be small during periods of upwelling, and increase during periods of non-upwelling and enhanced stratification. Temperature, salinity and density (σ_T) were relatively constant at the depth of calcification for both species over the study period (Table 5; Figure 2). In contrast, chlorphyll concentrations were more highly variable at the estimated depths of calcification for both morphotypes, but consistently higher for M_{thin} (mean Chl = 400 vs. 300 ng/L for M_{thick}).

2.5 Discussion

2.5.1 Morphotype Identification

The morphometric methods presented here are effective at differentiating between the *O. universa* genotypes, which are not readily distinguishable under a simple stereo binocular microscope. SEM imaging, while an effective way of distinguishing *O. universa* genotypes (Morard et al., 2009), is destructive to the shell and does not allow for subsequent geochemical analysis. Though we acknowledge that changes in temperature, food availability, light intensity and carbonate ion concentration ($[CO_3^{2-}]$) influence the morphometrics of the *O. universa* final chamber (Bé et al., 1973; Nijma et al., 1992; Barker and Elderfield, 2002; Lea et al., 2004; Schmidt et al., 2004; Lombardet al., 2009; Lombard et al., 2010; Marshall et al., 2013), it is possible to assign an individual or group of individuals to a given morphotype by comparing the mean weight, area and ρ_A to the ranges exhibited by the thick and thin morphotypes (Figure 3c and 3f), as was done using sample 21-3. and carbonate ion concentration ($[CO_3^{2-}]$) likely influence the morphometrics of the *O. universa* final chamber (Bé et al., 1973; Lea et al., 1995; Barker and Elderfield, 2002; Schmidt et al., 2004; Lombard et al., 2009; 2010; Marshall et al., 2013), this does not appear to inhibit the identification of thin and thick *O. universa* morphotypes using the methods presented in this study. It is also possible to assign an individual or group of individuals to a given morphotype by comparing the mean weight, area and ρ_A to the ranges exhibited by the thick and thin morphotypes (Figure 3c and 3f), as was done using sample 21-3.

The porosity differences exhibited by the thin and thick morphotypes may be a result of ecophenotypic and/or genetic controls (Figure 6). In foraminifera, small pores are used for gas transport, while large pores are used for food and symbiont transport into and out of the protoplasm (Bé et al., 1980; Spero, 1987; 1988). Small and large pore distribution is set at the time of final chamber calcification (Table 2; Spero et al., 1988). Differences in large porosities between the two morphotypes may be attributed to differences in food supply, prey size and/or symbiont density, while differences in smaller porosity may be attributed to changes in gas concentrations (e.g. oxygen) in their respective final chamber calcification environments. However, higher large and small porosities in M_{thick} relative to M_{thin} are inconsistent with some of these ecophenotypic concepts. For example, oxygen concentrations are super saturated and are on average within 23 μmol/kg at the calcification depths of the two morphotypes, suggesting that small porosities shoud be comparable between the two morphotypes (Table 5). Though we might expect higher symbiont density for the shallower-dwelling morphotype due to higher light levels, chlorophyll concentrations are higher at M_{thin} estimated calcification depths, suggesting a greater food supply for the less porous morphotype (Table 5).

Porosity differences could also be attributed to genetic differences between the two morphotypes (Morard et al., 2009). Although genetic testing could not be performed on the *O. universa* morphotypes in this study due to the preservation of sediment trap samples in formalin, we use the phenotypic characteristics of the three identified cryptic species of *O. universa* (de Vargas et al., 1999; Morard et al., 2009; 2013) to determine the genetic variety of the two morphotypes recognized in our study. Morard et al. (2009) report the presence of all three cryptic species of *O. universa* at the C-MarZ sampling

sites in the Carribean Sea, although only two Sargasso specimens were reported for these locations. Due to the high productivity in the Cariaco Basin (Muller-Karger et al., 2001) and the fact that the Sargasso cryptic species is only found in great abundances in the oligotrophic regions of the world's oceans (de Vargas et al., 1999), we think it is highly unlikely that this cryptic species is present in the Cariaco Basin. The biometrics of M_{thin} are characteristic of the Mediterranean cryptic species described at the nearby C-MarZ sampling site (mean thickness = 6 (±2.5) μm, range = 2-10 μm; mean porosity = 8 (±0.01) %, range = 6-10 %), while M_{thick} is defined by biometrics comparable to those of the Caribbean crypic species (mean thickness = 21 (±6.8) μm, range = 5-27 μm; mean porosity = 19 (±4) %; range = 12-25%). Additionally, the temperature (21-27°C; Figure 2) and chlorophyll concentrations (350 vs. 250 ng/L) in the Cariaco Basin surface waters over the study period are optimal for the presence of both species (de Vargas et al., 1999; Morard et al., 2009; 2013). Based on morphometrics and the hydrographic conditions of the Cariaco surface waters, we conclude that M_{thin} and M_{thick} are the Mediterranean and Caribbean cryptic species, respectively.

2.5.2 Oxygen and Carbon Isotopic Variability

We find that a relationship exists between the offset in $\delta^{18}O$ and $\delta^{13}C$ values of M_{thin} and M_{thick} and the relative stratification of the upper water column, inferred from the monthly upwelling index anomaly (Figure 10; Astor et al., 2013). With the exception of one sample ($\delta^{13}C$ only; 23-1; Table 4), the offset between the $\delta^{18}O$ and $\delta^{13}C$ of M_{thin} and M_{thick} covary perfectly with the monthly upwelling index anomaly. Interestingly, Deuser

(1987) reports similar findings stating that the differences between the $\delta^{18}O$ of the thin and thick morphotypes of *O. universa* from the Sargasso Sea decreased when the surface mixed layer reached depths of 75-100 m. The cause for the isotopic differences exhibited between M_{thin} and M_{thick}, as well as the relationship between the isotopic differences and surface ocean stratification, can be best explained by a difference in the average final chamber calcification depth of the *O. universa* morphotypes. As previously reported in Billups and Spero (1995), we find no significant relationship between the stable isotopic compositions and *O. universa* shell diameter (Figure 11) and thickness (Figure 12) for thin and thick morphotype groups when considered separately, implying that there is no size or diameter influence on stable isotopic compositions of individual morphotypes. Additionally, the differences in the isotopic compositions of the two morphotypes cannot be explained by seasonal differences in occurrence, as both forms are present throughout the year. The $\delta^{18}O$ composition of *O. universa* is primarily a function of temperature in the Cariaco Basin as salinity, and thus $\delta^{18}O_w$, is relatively constant (Table 5). Changes in irradiance (Spero et al., 1992) and pH/$[CO_3^{2-}]$ (Spero et al., 1997; Bemis et al., 1998; Wolf-Gladrow et al., 1999) may also influence the $\delta^{18}O$ compositions of the two morphotypes. However, the combined effect of $[CO_3^{2-}]$ and irradiance is minimal on the $\delta^{18}O$ of *O. universa*, with a maximum decrease in $\delta^{18}O$ of 0.30 to 0.33 ‰ under high light (386 µEinst m^{-2} s^{-1}) relative to low light scenarios (0 µEinst m^{-2} s^{-1}; Spero and Williams, 1988; Spero, 1992) and a decrease in $\delta^{18}O$ of 0.14 ‰ for a $[CO_3^{2-}]$ increase of 60 µmol/kg (maximum offset for the two morphotypes, Table 5).

In order to better understand how the combination of these effects influence the $\delta^{18}O$ compositions of our two morphotypes, we developed a conceptual model using the

above mentioned parameter depth profiles and average final chamber calcification depths for the two morphotypes for an upwelling (sample 21-8; 13a-d) and non-upwelling (sample 22-1; 13e-h) period (25 and 35 m for M_{thin} and 55 and 100 m for M_{thick} for upwelling and non-upwelling periods, respectively; see Table 6 for parameter values and calculations and Figure 13 for depth profiles). In the model, we use equations 4 and 5 to determine the expected $\delta^{18}O_{calcite}$ at the average depths of final chamber calcification for each morphotype during upwelling and non-upwelling periods (Table 5). In doing so, we were able show that modeled $\delta^{18}O_{calcite}$ offsets between the two morphotypes are minimal during periods of upwelling ($\delta^{18}O_{calcite}$ M_{thin}-M_{thick} = -0.05‰) and maximal during periods of non-upwelling ($\delta^{18}O_{calcite}$ M_{thin}-M_{thick} = -0.55‰). This is mostly attributed to changes in in situ temperature at the respective calcification depths of the two morphotypes. The effect of irradiance on the $\delta^{18}O$ of foraminifera is negligible for the measured irradiance values of 1 - 54 μE m^{-2} s^{-1} (Spero et al., 1992). However, increases in $[CO_3^{2-}]$ can result in a decrease in $\delta^{18}O$ as illustrated in Spero et al. (1997):

$$\delta^{18}O = 1.56 - 0.002\ [CO_3^{2-}] \qquad (6)$$

Thus, the $[CO_3^{2-}]$ effect contributes an additional $\delta^{18}O_{calcite}$ M_{thin}-M_{thick} offset of -0.02 and -0.07 ‰ based on the calculated in-situ $[CO_3^{2-}]$ of the two morphotypes for upwelling and non-upwelling periods, respectively. The total $\delta^{18}O_{calcite}$ M_{thin}-M_{thick} offset for upwelling (-0.07 ‰) and non-upwelling periods (-0.62 ‰) are comparable to the average offsets observed throughout the study period (-0.15 ‰ for upwelling and -0.54

for non-upwelling periods). Thus, the offsets in $\delta^{18}O$ between the two morphotypes can be explained by a difference in final chamber calcification depth and the associated differences in in-situ temperature and $[CO_3^{2-}]$.

The same principals can be applied to explain the $\delta^{13}C$ differences exhibited by M_{thin} and M_{thick} by using upwelling/non-upwelling $\delta^{13}C$ DIC profiles that are derived using the $\delta^{13}C$ DIC- $[PO_4^{3-}]$ relationship from Ortiz et al. (2000):

$$\delta^{13}C \text{ DIC} = -0.96 [PO_4^{3-}] + 1.7 \quad (7)$$

We caution that this equation was derived for the California Current system and may not be ideal for the Cariaco Basin, but it is applicable for the purpose of this conceptual model. The $\delta^{13}C$ DIC of the surface waters is high due to the preferential utilization of ^{12}C during photosynthesis and decreases with depth due to the remineralization of organic matter and release of ^{12}C (Figure 13). Considering only changes in $\delta^{13}C$ DIC with depth, we estimate a predicted $\delta^{13}C_{calcite}$ M_{thin}-M_{thick} offset of 0.13 and 0.17 ‰ for upwelling and non-upwelling periods, respectively. We also consider the combined effects of light intensity and $[CO_3^{2-}]$ on the predicted $\delta^{13}C$ and $\delta^{18}O$ offsets for the two morphotypes. Foraminiferal $\delta^{13}C$ is more highly sensitive to changes in light intensity and $[CO_3^{2-}]$ than is $\delta^{18}O$, with increases in $\delta^{13}C$ as great as 1.1 to 1.8 ‰ for HL relative to LL conditions and a decrease in $\delta^{13}C$ of 0.42 ‰ for a 60 µmol/kg increase in $[CO_3^{2-}]$ (Spero and Williams, 1988; 1989; Lea et al., 1995; Spero et al., 1997). The irradiance effect is attributed to the preferential uptake of ^{12}C by the

symbionts during photosynthesis, producing a ^{13}C-enriched microenvironment for foraminiferal calcification (Spero et al., 1999). For the upwelling scenario (13a-d), the irradiance values at 25 and 35 m are 54 and 21 μE m^{-2} $s^{-}1$, respectively. For the non-upwelling scenario, the irradiance values at 55 and 100 m are 20 and 1.25 μE m^{-2} $s^{-}1$, respectively. This would contribute an additional $\delta^{13}C$ offset of 0.22 and 0.52 ‰ between M_{thin} and M_{thick} for upwelling and non-upwelling periods, respectively, based on the culture calibrations of Spero and Williams (1988):

$$\delta^{13}C = 1.50 \times I^{0.106} \quad (8)$$

The carbonate ion effect would result in an additional -0.05 and -0.22 ‰ offset in $\delta^{13}C$ values for M_{thin} relative M_{thick} for upwelling and non-upwelling periods, respectively, based on the culture calibration of Spero et al., 1997:

$$\delta^{13}C = 3.56 - 0.006 [CO_3^{2-}] \quad (9)$$

As they have an opposing influence on $\delta^{13}C$ calcite, the $[CO_3^{2-}]$ effect mutes the strong influence of the irradiance effect on $\delta^{13}C$ calcite. Thus, the model predicts a $\delta^{13}C_{calcite}$ M_{thin}-M_{thick} offset of 0.30 and 0.47 ‰ for upwelling non-upwelling periods, respectively, due to the combined influence of $\delta^{13}C$ DIC, irradiance and $[CO_3^{2-}]$. These predicted offsets are comparable to the average observed offsets throughout the study

period of 0.25 and 0.41 ‰ for upwelling non-upwelling periods, respectively. Thus, elevated $\delta^{13}C$ in the shallower-dwelling M_{thin} relative to the deeper-dwelling M_{thick}, particularly during non-upwelling periods, may be due in large part to elevated symbiont photosynthesis during periods when M_{thin} is calcifying in higher light levels than M_{thick}, with additional contributions due to differences in in-situ $\delta^{13}C$ DIC and $[CO_3^{2-}]$.

Another possible explanation for the stable isotopic differences between the two *O. universa* morphotypes is a difference in vital effects, assuming that the two morphotypes represent the Caribbean and Mediterranean cryptic species of *O. universa.* Vital effects is a term used to collectively describe differences in the geochemical compositions between species due to life processes (Spero et al. 1991; Zeebe et al., 2008). Just as there is a need to establish species-specific equations for various climate proxies (Wefer and Berger, 1991; Spero 1998), it is likely that species-specific calibrations based on revised genetic taxonomies will be required as cryptic species continue to be identified. A preliminary study was conducted using cultured *O. universa* specimens collected from Catalina Island, California and Puerto Rico (H. Spero, pers. communication). This study collected juvenile *O. universa* from the upper 3-5 m of the water column in both locations and cultured the foraminifera at temperatures ranging from 9-29°C. Only a single cryptic species of *O. universa* has been identified in the California Current System (Mediterranean (Type III; Kucera and Darling, 2002) and the Caribbean cryptic species (Type I) has been identified in Puerto Rico (de Vargas et al., 1999). The results reveal that no systematic offset in the $\delta^{18}O$-temperature relationship exists between the *O. universa* specimens collected off Puerto Rico and Catalina Island. Though no genetic testing was performed to verify the genotypes of the cultured *O.*

universa, this study suggests that there is no difference in the vital effects of the cultured *O. universa* from the two different regions. Thus, the most likely explanation for the isotopic difference exhibited by the two morphotypes in the present study is that they differ in the average depths at which they calcify their final spherical chambers, as discussed earlier in this section.

2.5.3 Implications for Existing O. universa Calibration Equations

As previously mentioned, the estimated final chamber calcification depths for the two morphotypes identified in this study are characterized by an ~ 2°C temperature offset. These differences represent ~ half of the sea surface temperature change from the Last Glacial Maximum to the Holocene in the Caribbean (Schmidt et al., 2004; Foster et al., 2008). Because the isotopic offsets between the two morphotypes vary with the degree of surface ocean stratification, these differences may be muted in regions defined by a deep surface mixed layer. Conversely, larger isotopic offsets may exist between depth-stratified *O. universa* morphotypes/cryptic species in regions defined by a more highly stratified surface ocean. The results of this study provide evidence that morphotypes of *O. universa*, though similar in their basic phenotypic expression, differ in their geochemical makeup and preferred calcification environments. Thus, it is important to distinguish between them in the effort to eliminate scatter in paleoclimatic reconstructions.

2.6 CONCLUSION

Using morphometric measurements, we identify two distinct morphotypes of *O. universa* collected from sediment trap samples in the Cariaco Basin, Venezuela. We are unable to definitively assign each morphotype to a previously defined genotype (de Vargas et al., 1999) due to the use of formalin solution to preserve the sediment trap samples. However, using porosity and thickness measurements, as well as previously established ecological preferences (de Vargas et al., 1999; Morard et al., 2009), we conclude that the two morphotypes identified in this study represent the Caribbean and Mediterranean cryptic species of *O. universa*. The thin morphotype is defined by 0.34 ‰ higher and 0.38 ‰ lower average $\delta^{13}C$ and $\delta^{18}O$ values, respectively, than the thick morphotype, suggesting that they calcify their final chambers at different depths within the water column. The average estimated final chamber calcification depth offset of ~ 20 m results in an average calcification temperature offset of ~ 2°C. The absolute offsets between *O. universa* morphotype $\delta^{13}C$ and $\delta^{18}O$ values increase/decrease during periods of non-upwelling/upwelling in the Cariaco Basin due to changes in the depth gradients of temperature, $\delta^{13}C$ DIC, irradiance and $[CO_3^{2-}]$. The relationship between the magnitude of morphotype $\delta^{13}C$ and $\delta^{18}O$ offset and surface ocean stratification suggests that the isotopic offsets between morphotypes may vary regionally depending on the depth of the mixed layer. These data provide evidence that *O. universa* morphotypes differ in their calcification environment and that the lumping of these morphotypes for geochemical

analysis should be avoided as it may cause a significant amount of scatter in paleoreconstructions. We recommend further research involving the genetic and subsequent geochemical analysis of *O. universa* collected from depth-stratified plankton tow samples to further explore the presence and geochemical differences amongst *O. universa* cryptic species in the world's oceans.

Table 2.1 Morphotype fluxes and surface hydrographic parameters (0-100 m average). Grey shaded samples correspond with upwelling periods.

Sample ID	Trap Date	Hyrdo Date	Date Difference	M_{thin} (n)	M_{thick} (n)	Total (n)	Flux M_{thin} (n/m/day)	Flux M_{thick} (n/m/day)	Combined Flux (n/m/day)	Temp (°C)	Salinity	$[PO_4^{3-}]$ (µmol/kg)	Chl (ng/L)	O_2 (µmol/kg)	pH
19_5	7/13/05	7/12/05	-1	5	13	18	3	7	10	24.13	36.89	0.18	210	169	8.01
19_8	8/24/05	8/10/05	-14	8	35	43	5	20	25	22.84	36.89	0.25	176	160	7.99
19_11	10/5/05	10/5/05	0	9	17	26	5	10	15	26.92	36.70	0.10	206	183	8.06
20_7*	2/7/06	2/7/06	0	12	38	50	7	22	29	22.14	36.81	0.26	1401	173	7.98
20_8	2/21/06	2/7/06	-14	13	43	56	7	25	32	22.14	36.81	0.26	1401	173	7.98
21_3	6/14/06	6/6/06	-8	0	21	21	0	12	12	23.65	36.88	0.09	163	167	8.00
21_8	8/23/06	8/3/06	-20	14	33	47	8	19	27	22.61	36.77	0.25	291	149	7.96
21_13	11/1/06	10/10/06	-22	5	13	18	3	7	10	24.24	36.68	0.19	366	175	8.01
22_1	11/8/06	11/2/06	-6	10	3	13	6	2	7	26.73	36.44	0.11	126	182	8.06
22_7*	1/31/07	2/6/07	6	13	23	36	7	13	21	21.48	36.71	0.38	1761	156	7.95
22_9	2/28/07	3/6/07	6	11	22	35	6	13	19	21.40	36.69	0.38	509	150	7.94
23_1	5/16/07	5/8/07	-8	4	34	38	2	19	22	23.00	36.81	0.28	192	155	7.95
23_4	6/27/07	7/3/07	6	5	28	33	3	16	19	23.01	36.80	0.29	312	152	7.96
23_11	10/3/07	10/9/07	6	18	20	38	10	11	22	25.99	36.63	0.10	215	179	8.05
24_4	1/8/08	1/10/08	2	8	11	19	5	6	11	25.44	36.78	0.12	312	189	8.04
MEAN			**-4**	**9**	**24**	**33**	**5**	**13**	**19**	**23.71**	**36.75**	**0.22**	**509**	**168**	**8.00**

Table 2.2 Thickness, porosity, diameter and area density values for samples Car20-7 and 22-7.

Sample	Sample #	Morphotype	Gam/Pre-Gam	Measured Thickness (µm)	ρ_A-Calculated Thickness (µm)	Geometric-Calculated Thickness (µm)	Small Porosity (%)	Large Porosity (%)	Total Porosity (%)	Diameter (µm)	ρ_A (1 x 10^4 µg/µm^2)
20_7	1	thin	P	7.8	11.65	12.32	8.9	0.0	8.9	424.36	1.13
20_7	4	thin	G	17.1	17.5	17.1	4.0	3.5	7.5	497.16	1.69
20_7	6*	thin	G	23.0	21.0	20.5	5.8	2.3	8.1	491.83	2.02
20_7	8*	thin	G	20.0	21.7	21.3	6.2	3.6	9.8	624.49	2.09
20_7	14	thin	P				7.4	1.4	8.8	575.62	1.07
20_7	23	thin	P	9.4	14.0	13.9	5.1	3.3	8.5	599.85	1.35
20_7	37	thin	P	14.2	15.0	14.7	4.9	2.8	7.7	650.02	1.45
20_7	45	thin	P				7.2	3.3	8.8	577.55	1.41
22_7	15	thin	G	12.4	11.5	11.4	6.5	3.9	10.1	547.24	1.11
22_7	20	thin	G	16.8	14.1	14.3				551.22	1.37
22_7	24	thin	G	16.4	13.3	13.5	3.8	2.6	6.4	539.27	1.29
22_7	25	thin	G	14.8	12.9	13.1				606.95	1.25
22_7	43	thin	G	12.2	11.5	11.6	3.0	4.4	7.5	551.69	1.12
20_7	9	thick	G	36.3	34.7	30.0	6.1	8.4	14.5	629.91	2.57
20_7	10	thick	G	30.6	33.5	27.0	7.9	7.8	15.7	619.04	2.48
20_7	16	thick	P	18.2	23.2	19.7	9.5	2.1	11.5	622.77	1.73
20_7	17	thick	G	26.3	27.4	22.2	6.2	5.3	11.5	636.07	2.04
20_7	18*	thick	G	16.7	18.2	15.2	11.8	1.9	13.7	573.97	1.38
20_7	20	thick	P	23.0	26.6	31.6	10.6	3.1	13.7	565.95	1.98
20_7	27	thick	G	30.6	34.6	26.5	7.2	8.7	15.9	693.76	2.56
20_7	28*	thick	P	18.6	16.9	14.0	11.1	1.9	13.0	607.98	1.29
20_7	29*	thick	P	15.6	13.6	11.1	4.8	11.1	15.8	667.32	1.06
20_7	33*	thick	G	13.6	10.1	8.3	6.2	7.2	13.4	610.12	0.79
22_7	7	thick	G	24.6	24.6	21.0				629.36	1.84
22_7	9	thick	G	34.3	26.6	22.2	9.7	5.5	15.3	600.7	1.98
22_7	10	thick	G	35.6	29.9	24.9	8.1	10.5	18.7	639.62	2.22
22_7	11	thick	G	25.1	21.8	17.5	8.3	5.1	13.4	697.17	1.64
22_7	13	thick	G	32.1	29.3	23.7	9.8	10.3	20.0	638.97	2.18
22_7	19	thick	G	24.7	27.9	23.9	5.2	7.2	12.4	513.88	2.08
22_7	23	thick	G	32.4	32.8	26.8	7.7	11.3	19.1	597.08	2.43
22_7	26	thick	G	24.9	24.4	20.5	8.7	6.7	15.4	605.36	1.82
22_7	27*	thick	P	10.3	13.0	10.4	8.7	2.9	11.6	544.19	1.00
22_7	28	thick	G	33.1	31.7	28.0				536.81	2.35
22_7	29	thick	G	17.2	20.2	17.6	6.5	6.7	13.2	603.04	1.52
22_7	30	thick	G	35.9	31.1	25.3	8.9	10.8	19.6	641.07	2.31
22_7	31*	thick	G	18.4	18.3	15.3	5.7	7.7	13.4	623.12	1.39
22_7	32	thick	G	36.1	34.7	28.4	7.8	5.5	13.4	582.5	2.57
22_7	35	thick	P	19.9	21.2	17.1	12.0	1.8	13.8	588.87	1.59
22_7	36	thick	G	22.2	21.1	17.2				571.99	1.59
22_7	37*	thick	P	8.5	9.7	7.5	10.1	2.3	12.5	587.6	0.76
22_7	38	thick	G	24.5	23.9	20.2	9.8	5.0	14.9	585.4	1.79
22_7	39	thick	G	22.2	23.6	20.0	10.6	7.1	17.6	623.67	1.76
22_7	41	thick	G	22.5	22.0	19.7	7.6	5.0	12.6	607.91	2.16
22_7	42	thick	G	17.4	24.4	12.2	9.0	3.8	12.9	650.22	1.65
MEAN M_{thin}				**14.9**	**14.9**	**14.9**	**5.7**	**2.8**	**8.4**	**556.7**	**1.41**
1σ M_{thin}				**4.4**	**3.6**	**3.4**	**1.8**	**1.3**	**1.1**	**60.7**	**0.33**
MEAN M_{thick}				**24.2**	**24.2**	**20.2**	**8.4**	**6.2**	**14.6**	**609.5**	**1.82**
1σ M_{thick}				**7.9**	**7.1**	**6.4**	**2.0**	**3.0**	**2.5**	**41.0**	**0.51**

* indicates specimens that were misidentified using the morphotmetric methods presented in this study.

Table 2.3 Morphometrics for *O. universa* Morphotypes.

Area							
Sample ID	Trap Date	All Morphotypes Area (1 x 10^{-5} µm^2)	1σ	M_{thin} Area (1 x 10^{-5} µm^2)	1σ	M_{thick} Area (1 x 10^{-5} µm^2)	1σ
19_5	7/13/05	2.61	5.60	2.99	4.08	2.46	5.52
19_8	8/24/05	2.39	6.70	2.62	5.14	2.34	6.96
19_11	10/5/05	2.50	5.13	2.79	4.76	2.33	4.90
20_7	2/7/06	2.87	5.42	2.71	5.09	2.92	5.49
20_8	2/21/06	2.82	5.79	2.34	5.45	2.94	5.19
21_3	6/14/06	2.81	6.78	0.00	0.00	2.81	6.78
21_8	8/23/06	2.70	5.77	2.57	6.23	2.82	4.89
21_13	11/1/06	2.49	5.80	2.04	6.86	2.66	4.52
22_1	11/8/06	2.76	4.03	2.79	4.35	2.66	3.24
22_7	1/31/07	2.70	6.16	2.42	6.73	2.84	24.22
22_9	2/28/07	2.53	6.53	2.31	6.82	2.64	6.21
23_1	5/16/07	3.29	3.72	3.31	6.15	3.29	3.48
23_4	6/27/07	2.77	4.46	2.58	6.34	2.80	4.14
23_11	10/3/07	2.63	4.62	2.71	4.55	2.56	4.69
24_4	1/8/08	2.99	4.17	2.81	3.65	3.12	4.18
MEAN		**2.72**	**5.38**	**2.46**	**5.08**	**2.75**	**6.29**
Diameter							
Sample ID	Trap Date	All Morphotypes Diameter (µm)	1σ	M_{thin} Diameter (µm)	1σ	M_{thick} Diameter (µm)	1σ
19_5	7/13/05	565.00	64.35	608.39	38.27	548.75	65.64
19_8	8/24/05	584.20	83.19	571.84	50.19	531.66	87.88
19_11	10/5/05	577.06	60.76	585.74	52.40	533.20	59.93
20_7	2/7/06	597.52	58.94	581.47	62.54	602.59	57.69
20_8	2/21/06	608.16	64.70	543.76	64.38	605.07	58.34
21_3	6/14/06	615.57	77.69			615.57	77.69
21_8	8/23/06	599.82	64.93	564.51	72.47	593.68	53.99
21_13	11/1/06	576.91	67.38	505.41	88.95	580.14	45.98
22_1	11/8/06	581.78	43.29	564.17	31.51	587.07	46.30
22_7	1/31/07	576.78	73.70	546.38	78.55	592.63	70.36
22_9	2/28/07	588.15	79.05	528.28	90.06	571.96	70.127
23_1	5/16/07	637.90	38.35	641.68	70.06	637.45	34.65
23_4	6/27/07	594.99	47.90	560.21	60.44	594.19	44.99
23_11	10/3/07	583.97	49.92	583.73	46.64	564.85	52.24
24_4	1/8/08	616.48	39.83	600.90	40.13	618.26	35.83
MEAN		**594**	**61**	**570**	**60**	**585**	**57**
Weight							
Sample ID	Trap Date	All Morphotypes Weight (µg)	1σ	M_{thin} Weight (µg)	1σ	M_{thick} Weight (µg)	1σ
19_5	7/13/05	54.07	14.93	50.14	11.28	55.58	16.27
19_8	8/24/05	44.07	16.38	32.33	11.72	44.07	16.38
19_11	10/5/05	45.37	14.19	33.81	8.85	51.49	12.67
20_7	2/7/06	57.01	20.47	32.46	20.47	64.76	16.35
20_8	2/21/06	54.39	21.19	24.18	8.15	61.59	14.69
21_3	6/14/06	62.57	19.28			62.57	19.28
21_8	8/23/06	48.65	18.25	32.05	11.16	58.13	11.57
21_13	11/1/06	45.43	19.54	19.88	11.50	55.25	10.97
22_1	11/8/06	37.30	17.25	29.21	8.72	64.27	4.97
22_7	1/31/07	45.78	19.77	26.98	11.57	57.34	12.26
22_9	2/28/07	42.64	18.28	27.19	13.89	49.73	15.61
23_1	5/16/07	68.75	14.87	49.60	17.28	71.00	13.09
23_4	6/27/07	59.32	19.69	20.58	5.28	65.57	12.58
23_11	10/3/07	42.71	12.37	33.82	7.22	50.71	10.45
24_4	1/8/08	52.96	20.56	32.38	6.36	67.93	12.14
MEAN		**50.73**	**17.80**	**31.76**	**10.96**	**58.66**	**13.28**

Area Density

Sample ID	Trap Date	All Morphotypes ρ_A (1×10^{-4} µg/µm^2)	1σ	M_{thin} ρ_A (1×10^4 µg/µm^2)	1σ	M_{thick} ρ_A (1×10^4 µg/µm^2)	1σ
19_5	7/13/05	2.07	3.98	1.66	1.87	2.22	3.43
19_8	8/24/05	1.84	4.06	1.21	2.55	1.99	2.72
19_11	10/5/05	1.85	5.34	1.20	1.39	2.19	2.64
20_7	2/7/06	1.96	5.39	1.19	2.59	2.19	3.38
20_8	2/21/06	1.81	5.38	0.95	2.09	2.07	2.60
21_3	6/14/06	2.21	3.23	0.00	0.00	2.21	3.23
21_8	8/23/06	1.76	5.14	1.23	1.72	2.07	2.60
21_13	11/1/06	1.76	5.58	0.95	2.82	2.07	1.78
22_1	11/8/06	1.35	6.33	1.03	1.56	2.43	1.93
22_7	1/31/07	1.66	5.45	1.05	3.03	1.98	3.14
22_9	2/28/07	1.62	4.56	1.13	3.25	1.88	2.62
23_1	5/16/07	2.07	3.26	1.46	3.03	2.13	2.45
23_4	6/27/07	2.14	6.26	0.80	1.46	2.35	3.34
23_11	10/3/07	1.65	4.79	1.25	1.50	2.00	3.74
24_4	1/8/08	1.75	5.59	1.15	1.69	2.18	2.29
MEAN		**1.83**	**4.96**	**1.08**	**2.04**	**2.13**	**2.79**

Calculated Thickness

Sample ID	Trap Date	All Morphotypes Thickness (µm)	1σ	M_{thin} Thickness (µm)	1σ	M_{thick} Thickness (µm)	1σ
19_5	7/13/05	26.32	7.19	17.25	2.05	30.86	3.26
19_8	8/24/05	24.08	6.33	13.26	2.51	26.55	3.79
19_11	10/5/05	24.14	8.36	13.06	1.34	29.35	3.68
20_7	2/7/06	25.29	8.17	16.65	4.74	27.41	6.33
20_8	2/21/06	23.73	7.96	10.69	2.06	27.67	3.63
21_3	6/14/06	29.63	4.51			29.63	4.51
21_8	8/23/06	23.42	7.27	13.48	1.70	27.64	3.63
21_13	11/1/06	23.01	8.24	10.69	2.78	27.75	2.48
22_1	11/8/06	16.40	9.44	11.51	1.54	32.68	2.69
22_7	1/31/07	21.72	8.40	9.96	1.63	24.93	6.03
22_9	2/28/07	20.75	6.94	12.54	3.21	25.04	3.65
23_1	5/16/07	27.39	5.24	15.77	2.99	28.56	3.42
23_4	6/27/07	28.51	8.95	9.29	1.44	31.61	4.67
23_11	10/3/07	20.76	7.69	13.68	1.52	26.78	5.22
24_4	1/8/08	22.28	8.77	12.72	1.81	29.24	3.20
MEAN		**23.83**	**7.56**	**12.90**	**1.67**	**28.38**	**4.01**

Table 2.4 Oxygen and carbon isotopic compositions for M_{thin} and M_{thick}. All means are weighted to the number of individuals per sample analysis (n).

Sample Name	Both morphotypes $\delta^{13}C$ (‰)	Both morphotypes $\delta^{18}O$ (‰)	n	M_{thin}	$\delta^{13}C$ (‰)	$\delta^{18}O$ (‰)	n	Mean Thickness (µm)	Mean Diameter (µm)	M_{thick}	$\delta^{13}C$ (‰)	$\delta^{18}O$ (‰)	n	Mean Thickness (µm)	Mean Diameter (µm)
CAR 19-5					1.79	-0.73	4	17.7	578		1.45	-0.36	3	32.8	570
											1.41	-0.71	4	31.5	578
MEAN	**1.56**	**-0.62**	**11**		**1.79**	**-0.73**		**18**	**578**		**1.43**	**-0.56**		**32**	**575**
1σ	**0.21**	**0.21**									**0.03**	**0.24**		**1**	**6**
CAR 19-8					1.35	-0.51	3	14.0	592		0.65	-0.11	1	25.1	608
					1.51	-0.96	5	12.5	554		0.47	-0.12	1	27.8	616
											0.88	-0.02	3	33.3	601
											0.87	-0.37	7	23.7	576
MEAN	**1.08**	**-0.46**	**20**		**1.45**	**-0.79**		**13**	**568**		**0.82**	**-0.24**		**27**	**588**
1σ	**0.40**	**0.35**			**0.12**	**0.32**		**1**	**27**		**0.20**	**0.15**		**4**	**17**
CAR 19-11					1.90	-1.37	1	14.4	586		0.39	0.00	1	28.7	580
					1.60	-0.67	7	13.3	585		1.17	-0.18	4	34.6	542
											0.92	-0.21	5	28.7	544
MEAN	**1.27**	**-0.44**	**18**		**1.64**	**-0.76**		**13**	**585**		**0.97**	**-0.18**		**31**	**547**
1σ	**0.59**	**0.55**			**0.21**	**0.49**		**1**	**1**		**0.39**	**0.11**		**3**	**21**
CAR 20-8					0.91	-0.40	1	12.3	636		0.97	-0.48	1	28.1	642
					1.17	-0.36	8	10.2	554		1.07	-0.03	1	31.4	641
											1.23	-0.33	3	32.9	576
											1.27	-0.73	4	33.4	666
											0.97	-0.19	5	26.7	593
MEAN	**1.13**	**-0.38**	**23**		**1.14**	**-0.37**		**10**	**563**		**1.12**	**-0.38**		**30**	**617**
1σ	**0.14**	**0.22**			**0.18**	**0.03**		**1**	**58**		**0.14**	**0.27**		**3**	**38**
CAR 21-3											1.35	-0.85	1	27.6	644
											0.67	-0.19	1	28.8	556
											1.17	-0.42	1	34.1	556
											1.79	-0.49	3	28.5	583
											1.06	-0.11	3	33.3	591
											1.06	-0.58	5	26.9	636
											1.22	-0.75	6	26.5	606
MEAN	**1.22**	**-0.53**	**20**								**1.22**	**-0.53**		**28**	**605**
1σ	**0.34**	**0.27**									**0.34**	**0.27**		**3**	**35**
CAR 21-8					1.64	-0.93	4	14.7	648		0.97	-0.36	1	32.6	635
					1.33	-0.41	5	13.1	594		1.62	-0.59	3	31.1	582
											0.78	-0.47	6	26.5	643
MEAN	**1.25**	**-0.56**	**19**		**1.47**	**-0.64**		**14**	**618**		**1.05**	**-0.49**		**29**	**624**
1σ	**0.38**	**0.23**			**0.22**	**0.37**		**1**	**38**		**0.44**	**0.11**		**3**	**33**
CAR 21-13					2.07	-0.61	1	14.7	599		1.45	-0.32	4	26.6	569
					1.29	-0.98	1	10.3	546		0.79	-0.32	5	28.8	609
MEAN	**1.19**	**-0.41**	**11**		**1.68**	**-0.80**		**12**	**573**		**1.08**	**-0.32**		**28**	**591**
1σ	**0.53**	**0.31**			**0.55**	**0.26**		**3**	**37**		**0.47**	**0.00**		**2**	**28**
CAR 22-1					1.67	-1.03	7	11.0	575		1.16	-0.41	3	32.7	564
MEAN	**1.51**	**-0.84**	**10**		**1.67**	**-1.03**		**11**	**575**		**1.16**	**-0.41**		**33**	**564**
1σ	**0.36**	**0.44**													
CAR 22-9					0.69	-1.23	1	9.5	569		0.86	0.07	1	24.0	571
					1.93	-0.70	1	13.5	636		1.05	-0.46	1	29.8	570
					1.52	-0.44	5	15.6	583		1.71	-0.33	1	27.1	638
											1.25	0.09	4	24.7	578
											1.14	-0.32	5	26.0	625
MEAN	**1.29**	**-0.32**	**19**		**1.46**	**-0.59**		**14**	**589**		**1.19**	**-0.16**		**26**	**601**
1σ	**0.42**	**0.42**			**0.63**	**0.41**		**3**	**35**		**0.32**	**0.25**		**2**	**33**

Table 2.5 Sample depths and hydrographic data for M_{thin} and M_{thick}. Grey shaded regions indicate upwelling periods. All parameters are those collected at the estimated calcification depths.

M_{thin}

Sample ID	Trap Date	Hyrdo Date	Date Difference	$\delta^{13}C$ (‰)	$\delta^{18}O$ (‰)	$\delta^{18}O$ Temp (°C)	Temperature (°C)	Temp Difference (°C)	Depth (m)	Salinity	$[PO_4^{3-}]$ (µmol/kg)	Chl (ng/L)	O_2 (µmol/kg)	$[CO_3^{2-}]$ (µmol/kg)	pH	Sigma T (g/cm^3)	Irradiance (µE m^{-2} s^{-1})
19_5	7/13/05	7/12/05	-1	1.41	-0.71	23.4	23.1	0.3	45	36.9	0.24	418	152	181	7.99	25.3	
19_8	8/24/05	8/10/05	-14	1.42	-0.71	23.7	24.0	-0.3	15	37.0	0.04	215	181	202	8.02	25.1	
19_11	10/5/05	10/5/05	0	1.64	-0.76	23.4	23.4	0.0	88	36.9	0.28	169	147	195	7.98	25.2	
20_8	2/21/06	2/7/06	-14	1.14	-0.37	22.0	22.0	-0.1	35	36.8	0.35	834	139	169	7.95	25.6	10
21_3	6/14/06	6/6/06	-8														
21_8	8/23/06	8/3/06	-20	1.31	-0.65	23.0	22.5	0.5	15	36.9	0.00	757	178	198	8.01	25.5	218
21_13	11/1/06	10/10/06	-22	1.51	-1.05	24.2	24.1	0.1	75	36.7	0.05	832	192	176	8.04	24.9	
22_1	11/8/06	11/2/06	-6	1.67	-1.03	24.6	24.2	0.4	88	36.7	0.25	93	154	204	8.00	24.9	
22_9	2/28/07	3/6/07	6	1.46	-0.59	22.8	23.0	-0.2	7	36.7	0.03	801	206	225	8.02	25.2	514
23_1	5/16/07	5/8/07	-8	1.95	-0.68	23.5	24.0	-0.5	18	36.9	0.12	250	164	208	8.01	25.1	454
23_4	6/27/07	7/3/07	6	0.80	-0.46	22.2	22.2	0.0	45	36.8	0.41	217	129	161	7.93	25.5	21
23_11	10/3/07	10/9/07	6	1.28	-1.05	23.5	23.1	0.5	100	36.7	0.38	60	103	181	7.96	25.2	
24_4	1/8/08	1/10/08	2	1.50	-0.87	23.5	23.5	0.0	45	36.8	0.30	366	146	190	7.97	25.1	
MEAN			**-6**	**1.43**	**-0.74**	**23.3**	**23.3**	**0.0**	**47.92**	**36.8**	**0.20**	**418**	**158**	**191**	**7.99**	**25.2**	**243.45**
1σ				**0.29**	**0.22**	**0.8**	**0.8**	**0.3**	**32.35**	**0.1**	**0.15**	**304**	**28**	**18**	**0.03**	**0.2**	**235.71**

M_{thick}

Sample ID	Trap Date	Hyrdo Date	Date Difference	$\delta^{13}C$ (‰)	$\delta^{18}O$ (‰)	$\delta^{18}O$ Temp (°C)	Temperature (°C)	Temp Difference (°C)	Depth (m)	Salinity	$[PO_4^{3-}]$ (µmol/kg)	Chl (ng/L)	O_2 (µmol/kg)	$[CO_3^{2-}]$ (µmol/kg)	pH	Sigma T (g/cm^3)	Irradiance (µE m^{-2} s^{-1})
19_5	7/13/05	7/12/05	-1	1.45	-0.36	21.7	21.8	-0.1	88	36.9	0.40	103	135	154	7.94	25.7	
19_8	8/24/05	8/10/05	-14	0.82	-0.24	21.4	21.2	0.2	55	36.8	0.40	124	139	169	7.95	25.9	
19_11	10/5/05	10/5/05	0	0.97	-0.18	20.6	20.8	-0.2	130	36.8	0.45		124	158	7.92	25.9	
20_8	2/21/06	2/7/06	-14	1.12	-0.38	22.0	22.0	0.0	35	36.8	0.35	834	139	169	7.95	25.6	10
21_3	6/14/06	6/6/06	-8	1.19	-0.54	22.7	22.8	-0.1	35	36.9	0.13	221	141	182	7.97	25.4	
21_8	8/23/06	8/3/06	-20	1.05	-0.49	22.3	22.5	-0.2	15	36.9	0.00	757	178	169	8.01	25.5	218
21_13	11/1/06	10/10/06	-22	1.08	-0.32	20.7	20.5	0.3	115	36.7	0.56		124	148	7.89	25.9	
22_1	11/8/06	11/2/06	-6	1.16	-0.41	21.7	21.9	-0.2	115	36.7	0.43		133	170	7.94	25.6	
22_9	2/28/07	3/6/07	6	1.19	-0.16	20.8	20.8	0.0	55	36.7	0.50	104	126	159	7.91	25.8	7
23_1	5/16/07	5/8/07	-8	1.20	-0.56	22.9	22.7	0.2	25	36.9	0.15	250	153	186	7.97	25.5	240
23_4	6/27/07	7/3/07	6	0.83	-0.42	22.0	22.2	-0.2	45	36.8	0.41	217	129	161	7.93	25.5	21
23_11	10/3/07	10/9/07	6	1.08	-0.46	20.7	20.1	0.6	130	36.7	0.75		103	134	7.85	26.0	
24_4	1/8/08	1/10/08	2	1.00	-0.39	21.2	21.4	-0.2	75	36.7	0.50	135	125	153	7.91	25.7	
MEAN			**-6**	**1.09**	**-0.38**	**21.6**	**21.6**	**0.0**	**70.58**	**36.8**	**0.39**	**305**	**135**	**162**	**7.93**	**25.7**	**99.25**
1σ				**0.16**	**0.13**	**0.8**	**0.9**	**0.3**	**40.98**	**0.1**	**0.20**	**284**	**18**	**14**	**0.04**	**0.2**	**118.71**

Table 2.6 Conceptual model for carbon and oxygen isotopic differences in the Carico Basin *Orbulina unviersa* morphotypes.

$\delta^{18}O$ (‰)		Upwelling (21-8)	Non-upwelling (22-1)	N-U difference
	M_{thin} depth (m)	25	55	
	M_{thick} depth (m)	35	100	
	Temperature C			
	M_{thin} Temperature	21.84	25.61	
	M_{thick} Temperature	21.57	23.34	
	Offset ($M_{thin-Mthick}$)	0.27	2.27	
	Salinity			
	M_{thin} salinity	36.83	36.57	
	M_{thick} salinity	36.82	36.79	
	Offset ($M_{thin-Mthick}$)	0.02	-0.22	
	Predicted $\delta^{18}O$ water (‰)[a]			
	M_{thin} predicted $\delta^{18}O_w$ (‰)	1.02	0.94	
	M_{thick} predicted $\delta^{18}O_w$ (‰)	1.02	1.01	
	Offset ($M_{thin-Mthick}$)	0.01	-0.07	
	Predicted $\delta^{18}O$ calcite (‰)[b]			
	M_{thin} predicted $\delta^{18}O$ (‰)	-0.36	-1.23	
	M_{thick} predicted $\delta^{18}O$ (‰)	-0.31	-0.69	
I	Offset ($M_{thin-Mthick}$)	-0.05	-0.55	-0.50
	$[CO_3^{2-}]$ (µmol/kg)			
	M_{thin} $[CO_3^{2-}]$ (µmol/kg)	169	227	
	M_{thick} $[CO_3^{2-}]$ (µmol/kg)	160	190	
	Offset ($M_{thin-Mthick}$)	8	37	
	Predicted $\delta^{18}O$ calcite (‰)[c]			
	M_{thin} predicted $\delta^{18}O$ (‰)	1.22	1.11	
	M_{thick} predicted $\delta^{18}O$ (‰)	1.24	1.18	
II	Offset ($M_{thin-Mthick}$)	-0.02	-0.07	-0.06
	$\delta^{18}O$ (‰) Offset ($M_{thin-Mthick}$ ‰)			
I + II	Modeled offset (M_{thin}-M_{thick} ‰)	-0.07	-0.62	-0.55
	Measured offset (M_{thin}-M_{thick} ‰)	-0.15	-0.54	-0.40

$\delta^{13}C$ (‰)		Upwelling (21-8)	Non-upwelling (22-1)	N-U difference
	M_{thin} depth (m)	25	55	
	M_{thick} depth (m)	35	100	
	$[PO_4^{3-}]$ (µmol/kg)			
	M_{thin} $[PO_4^{3-}]$ (µmol/kg)	0.20	0.13	
	M_{thin} $[PO_4^{3-}]$ (µmol/kg)	0.33	0.31	
	Offset ($M_{thin-Mthick}$)	-0.13	-0.18	
	Predicted $\delta^{13}C$ DIC (‰)[d]			
	M_{thin} predicted $\delta^{13}C$ (‰)	1.51	1.58	
	M_{thick} predicted $\delta^{13}C$ (‰)	1.38	1.40	
	Offset ($M_{thin-Mthick}$ ‰)	0.13	0.17	
	Predicted $\delta^{13}C$ calcite (‰)[e]			
	M_{thin} predicted $\delta^{13}C$ (‰)	1.51	1.58	
	M_{thick} predicted $\delta^{13}C$ (‰)	1.38	1.40	
I	Offset ($M_{thin-Mthick}$ ‰)	0.13	0.17	0.04
	$[CO_3^{2-}]$ (µmol/kg)			
	M_{thin} $[CO_3^{2-}]$ (µmol/kg)	169	227	
	M_{thick} $[CO_3^{2-}]$ (µmol/kg)	160	190	
	Offset ($M_{thin-Mthick}$; µmol/kg)	8	37	
	Predicted $\delta^{13}C$ calcite (‰)[f]			
	M_{thin} predicted $\delta^{13}C$ (‰)	2.55	2.20	
	M_{thick} predicted $\delta^{13}C$ (‰)	2.60	2.42	
II	Offset ($M_{thin-Mthick}$ ‰)	-0.05	-0.22	-0.17
	Irradiance (µE m^{-2} s^{-1})			
	M_{thin} Irradiance (µE m^{-2} s^{-1})	54	20	
	M_{thick} Irradiance (µE m^{-2} s^{-1})	21	1	
	Offset ($M_{thin-Mthick}$)	33	19	
	Predicted $\delta^{13}C$ calcite (‰)[g]			
	M_{thin} predicted $\delta^{13}C$ (‰)	2.29	2.06	
	M_{thick} predicted $\delta^{13}C$ (‰)	2.07	1.54	
III	Offset ($M_{thin-Mthick}$ ‰)	0.22	0.52	0.31
	$\delta^{13}C$ (‰) Offset ($M_{thin-Mthick}$ ‰)			
I + II + III	Modeled offset (M_{thin}-M_{thick} ‰)	0.30	0.47	0.18
	Observed offset (M_{thin}-M_{thick} ‰)	0.25	0.41	0.16

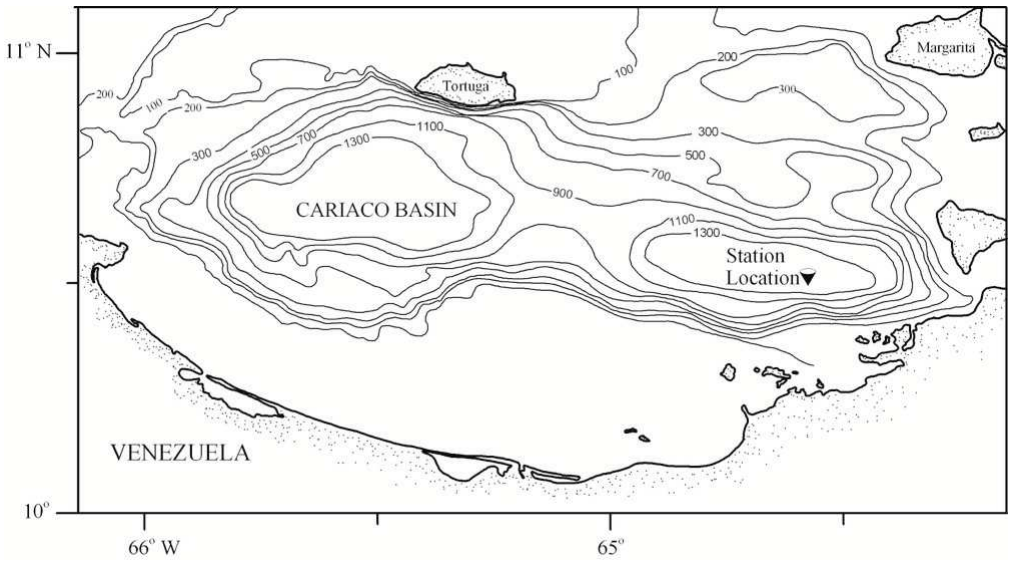

Figure 2.1 Bathymetric map of the Cariaco Basin showing the location of the sediment trap mooring (10°30′ N and 65°31′ W)..

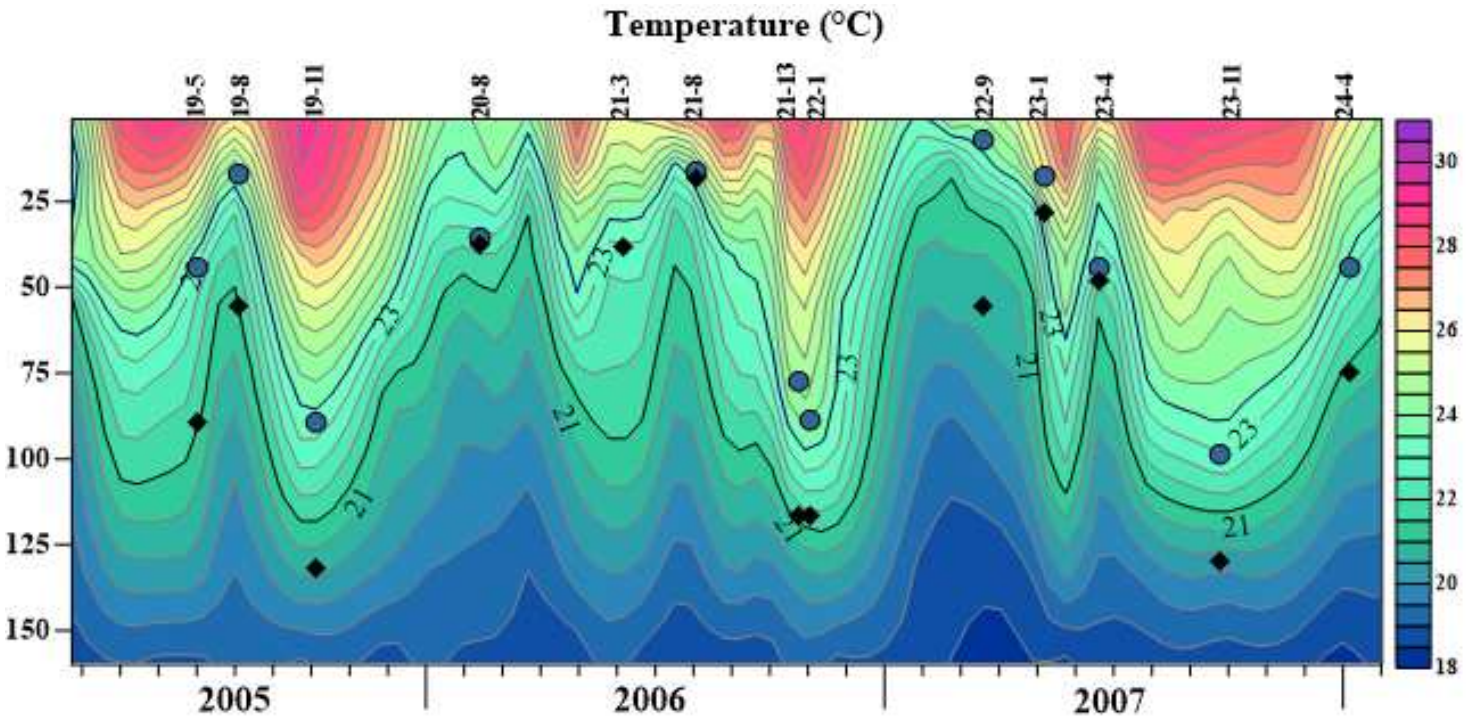

Figure 2.2 Temperature record for the upper 130 m throughout the study period. Estimated calcification depths of *O. universa* M_{thin} (blue circles) and M_{thick} (black diamonds) are plotted for the study period.

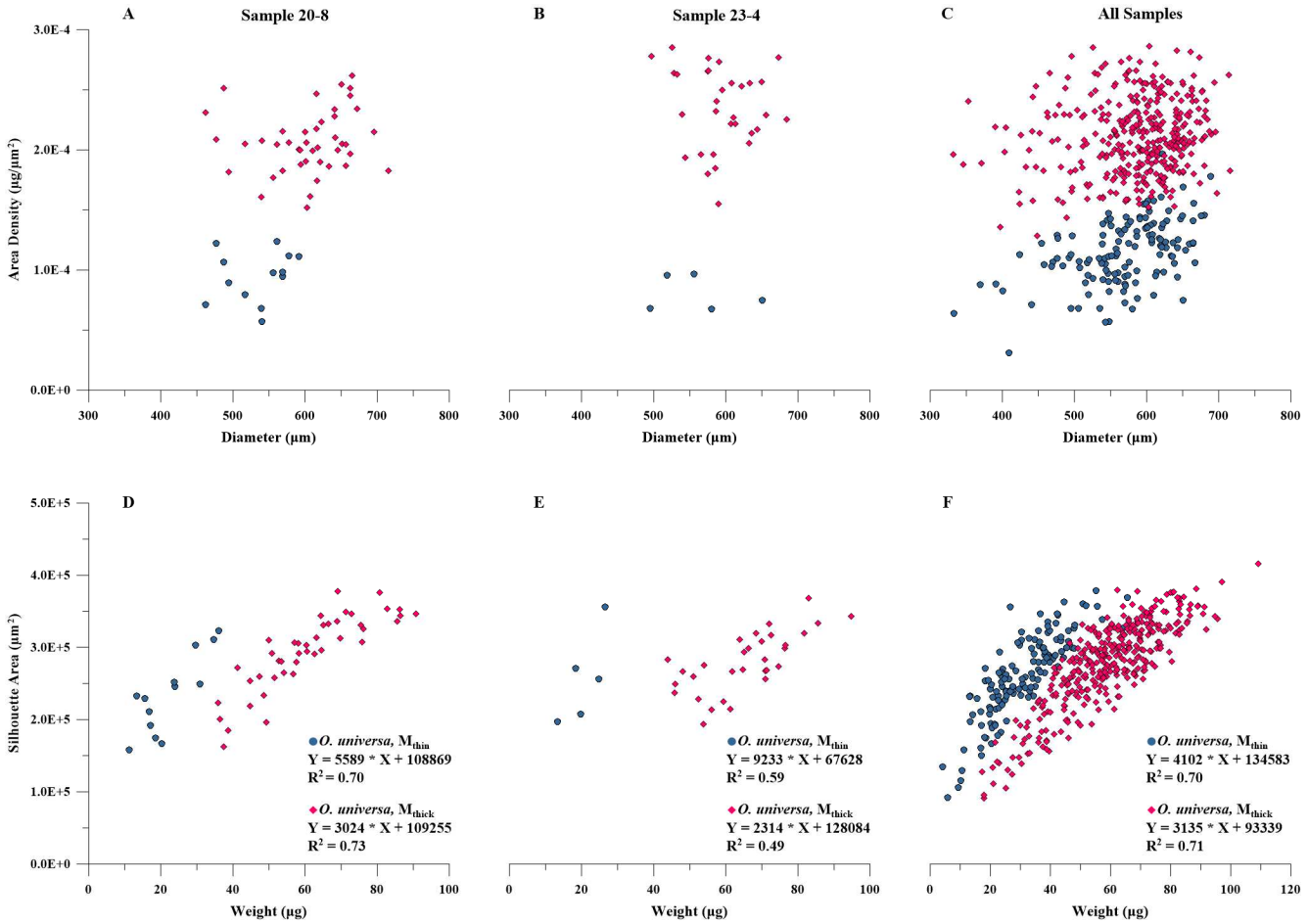

Figure 2.3 The top plots are *O. universa* M_{thin} (blue circles) and M_{thick} (pink diamonds) area density (ρ_A) and silhouette area cross plots for sample 20-8 (a), sample 23-4 (b) and all samples (c). The bottom plots are silhouette area and weight cross plots for sample 20-8 (d), sample 23-4 (e) and all samples (f).

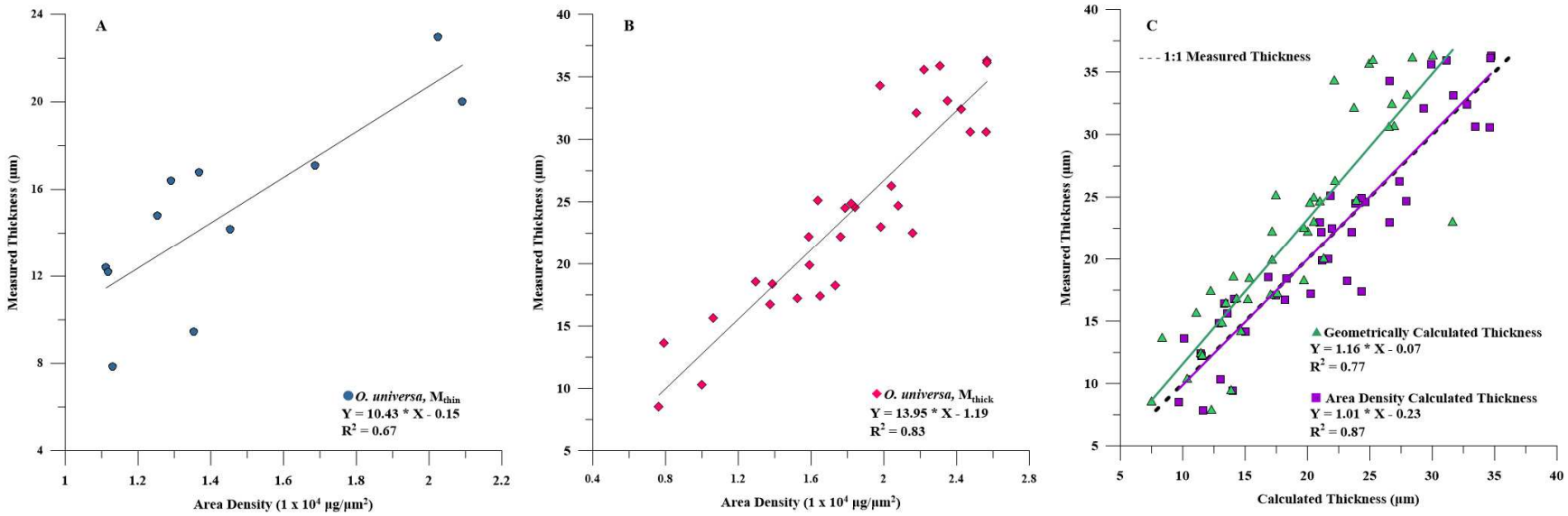

Figure 2.4 Area density (ρ_A) and measured thickness relationships for M_{thin} (a; blue circles) and M_{thick} (b; pink diamonds) from samples 20-7 and 22-7. (c) Comparison between geometric (green triangles) and ρ_A (purple squares) thickness calculations.

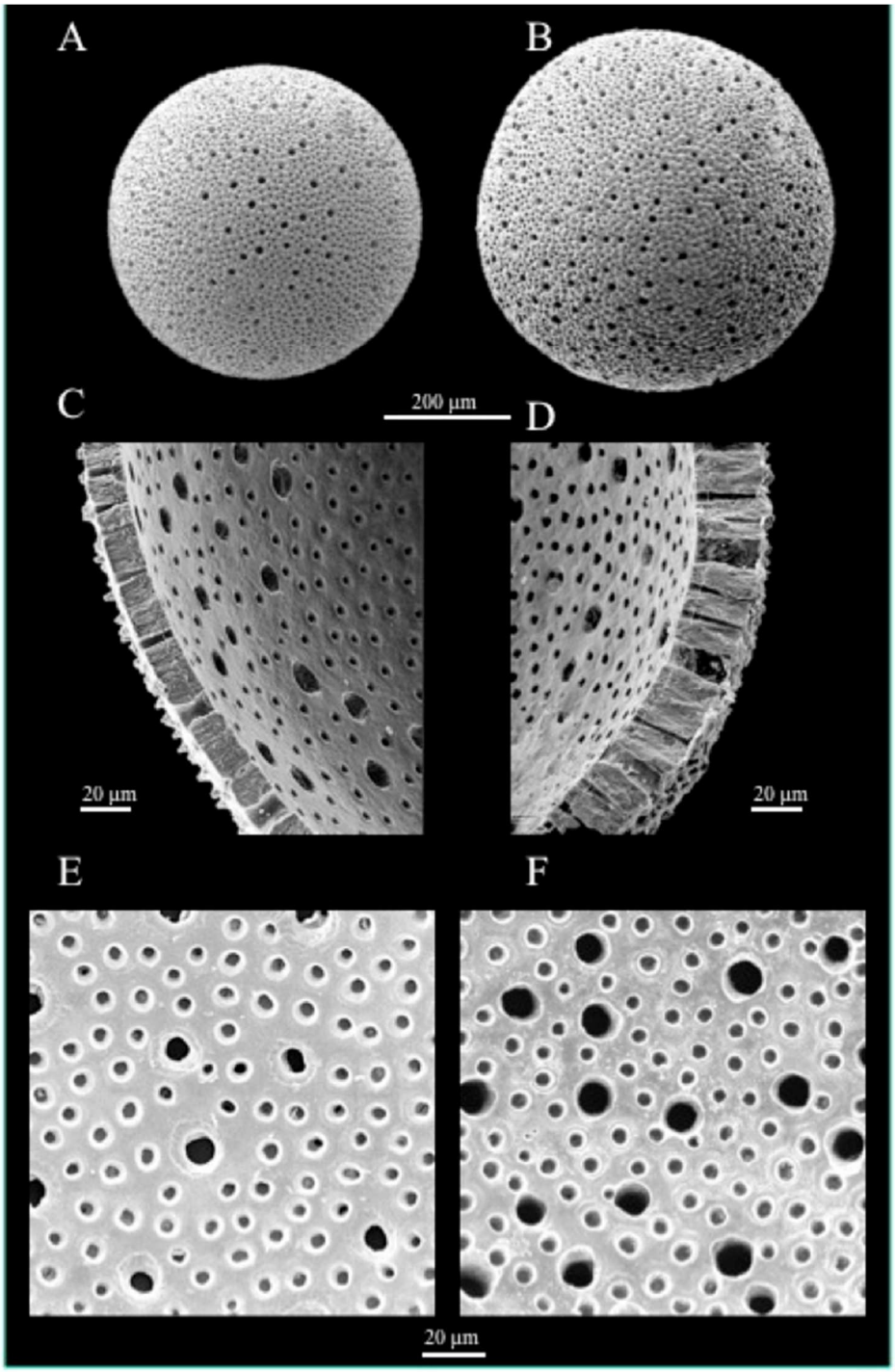

Figure 2.5 SEM images of M_{thin} (a) and M_{thick} (b) whole specimen. M_{thin} (c) and M_{thick} (d) shell edge. M_{thin} (e) and M_{thick} (f) inner surface.

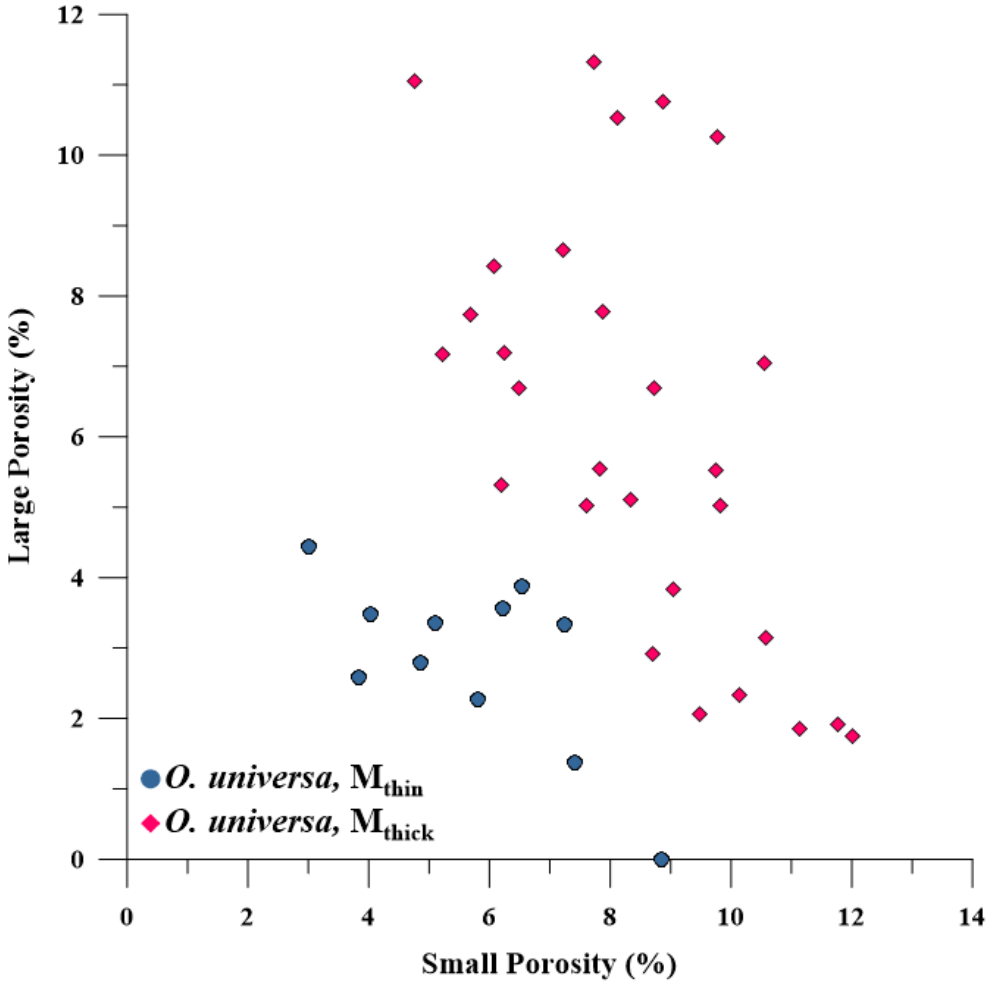

Figure 2.6 Small and large porosity distributions for M_{thin} (blue circles) and M_{thick} (pink diamonds).

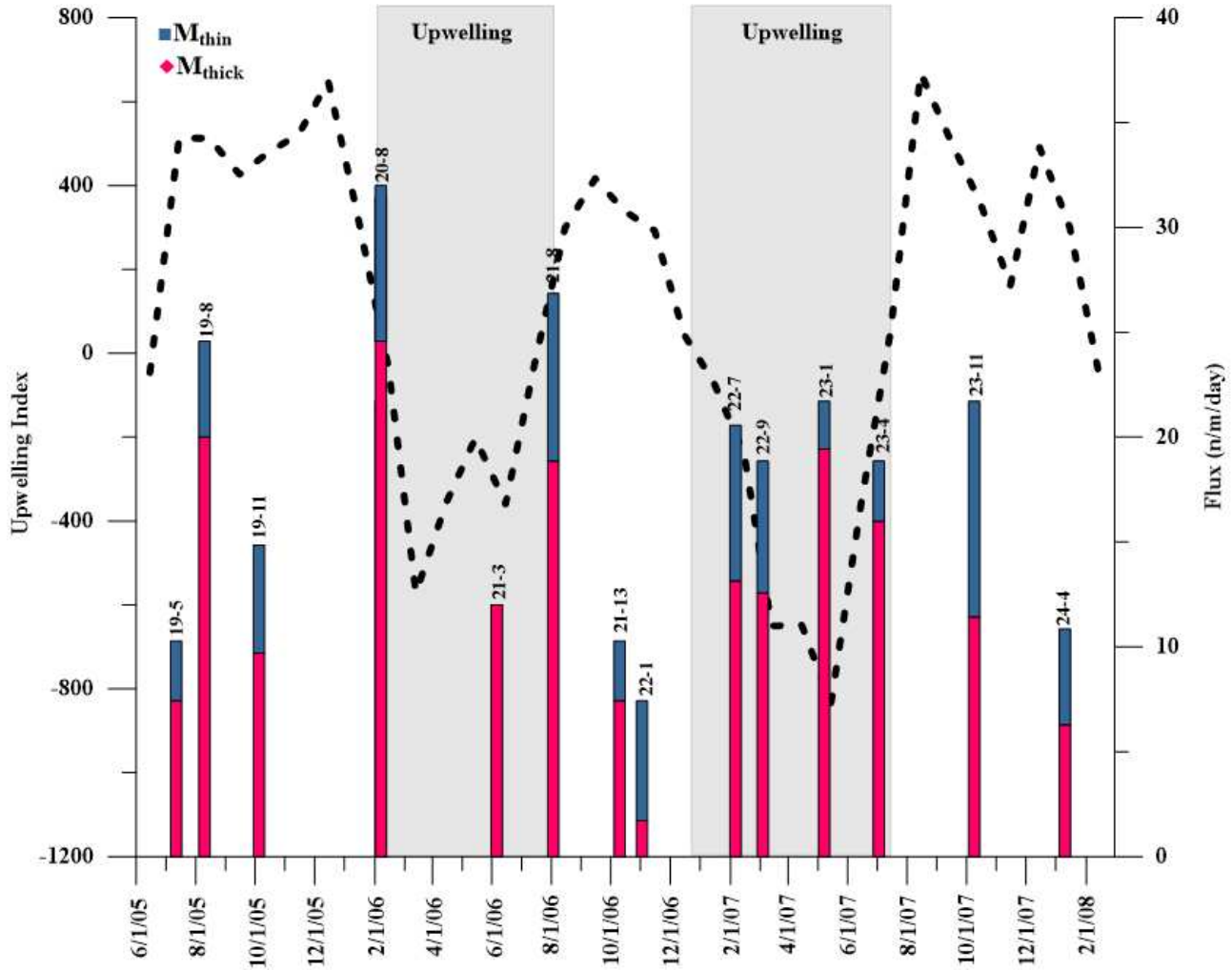

Figure 2.7 M_{thin} (blue) and M_{thick} (pink) fluxes and monthly averaged upwelling index record spanning the sample collection period.

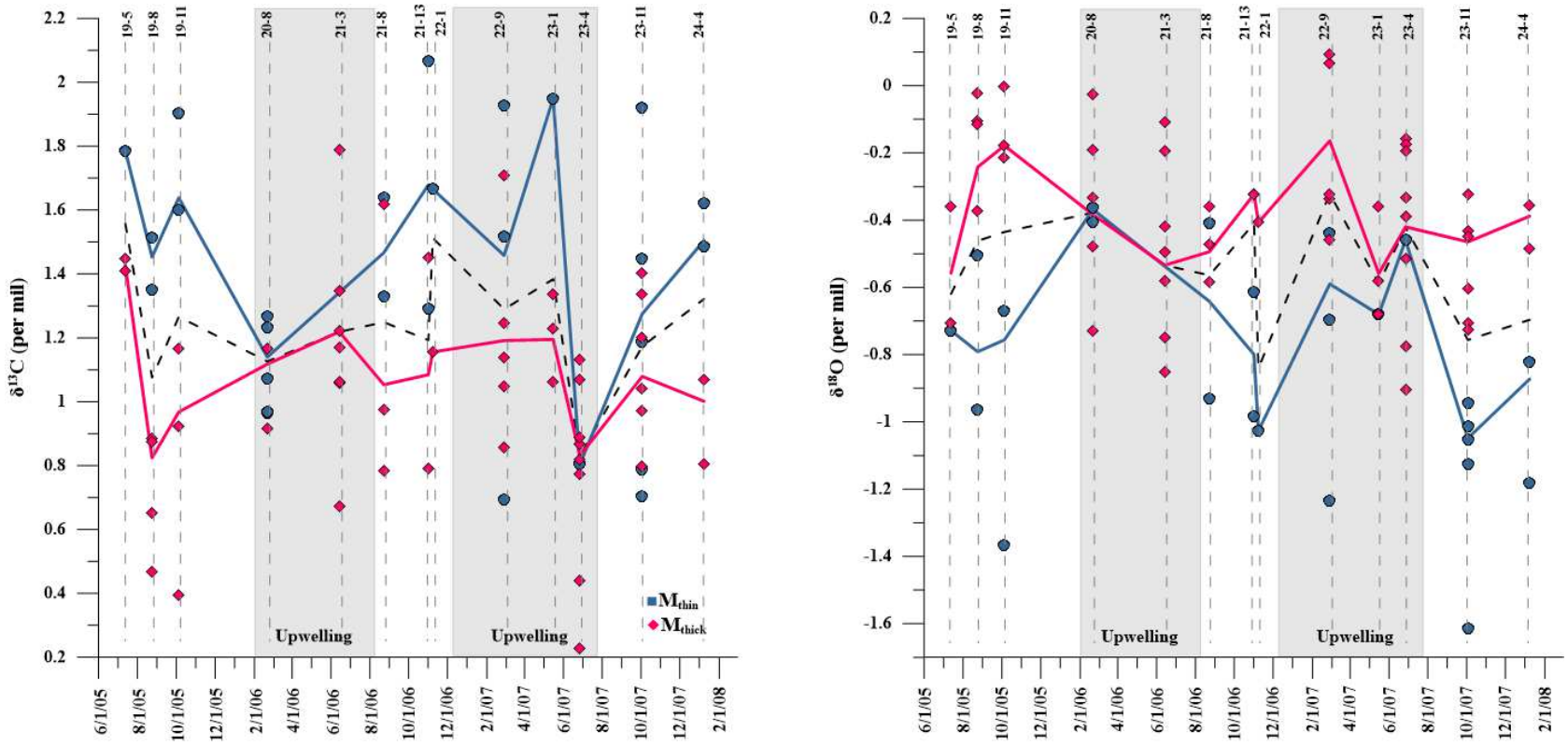

Figure 2.8 Carbon (a) and oxygen (b) isotopic compositions for *O. universa* M_{thin} (blue circles) and M_{thick} (pink diamonds) throughout the study period (n =13). The solid blue and pink lines represent the weighted means of M_{thin} and M_{thick}, respectively, based on the number of individuals used per sample analysis (Table 4). The dashed black line represent the weighted mean of all measured specimens and best represent the values that would be generated when lumping the two morphotypes during stable isotopic analysis.

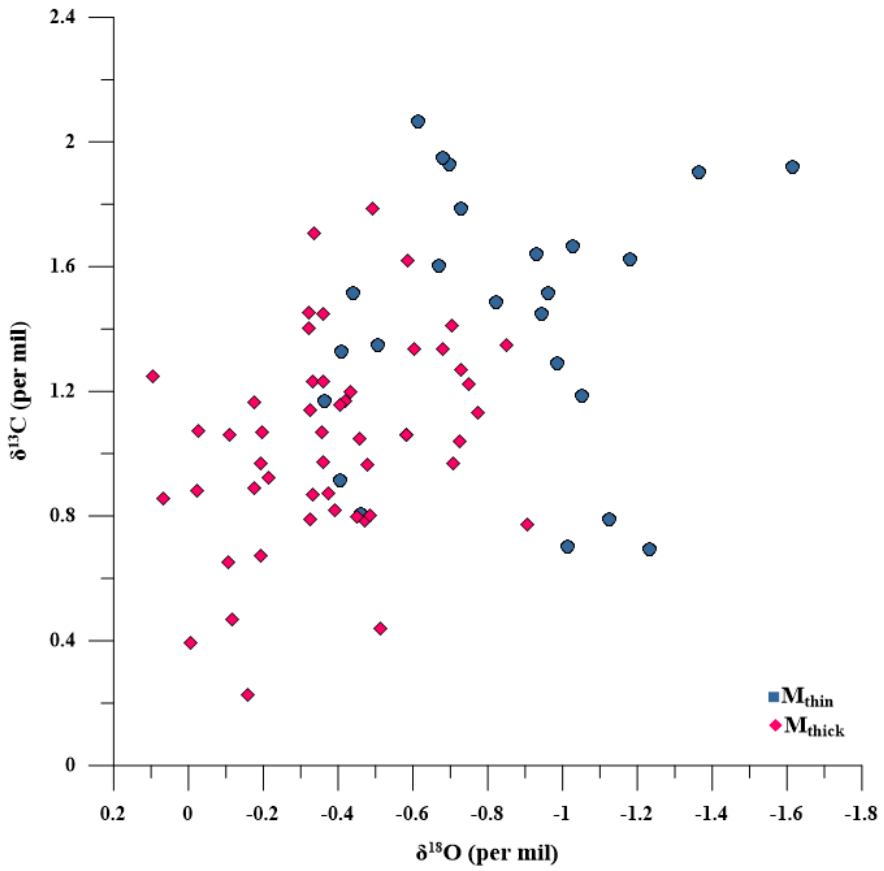

Figure 2.9 M_{thin} and M_{thick} stable isotopic compositions displayed in $\delta^{18}O$ and $\delta^{13}C$ space.

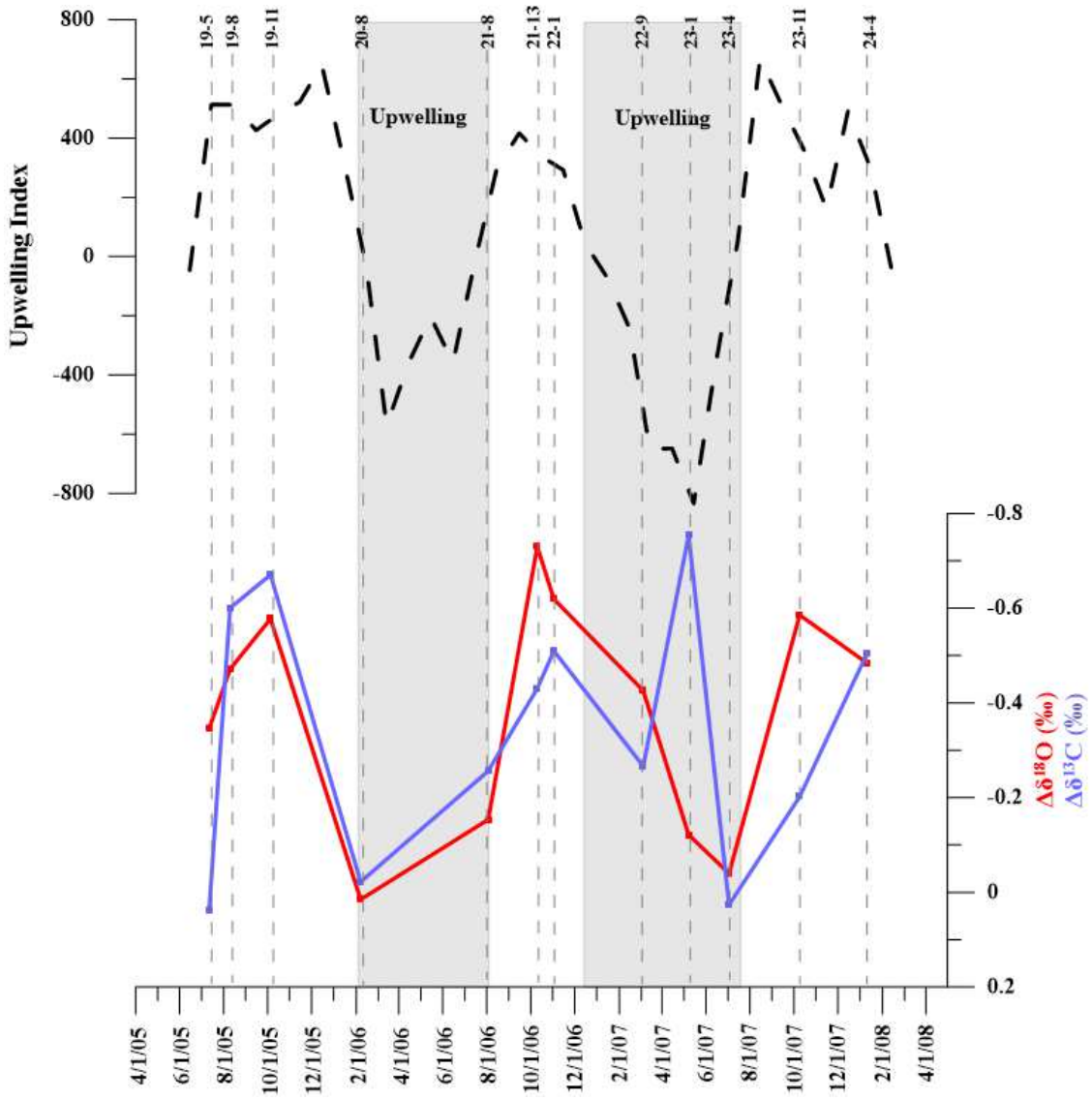

Figure 2.10 The offset between M_{thin} and M_{thick} oxygen ($\Delta\ \delta^{18}O = M_{thin} - M_{thick}$; blue line) and carbon isotopic compositions ($\Delta\ \delta^{13}C = M_{thin} - M_{thick}$; pink line) and the averaged monthly upwelling index (black dashed line).

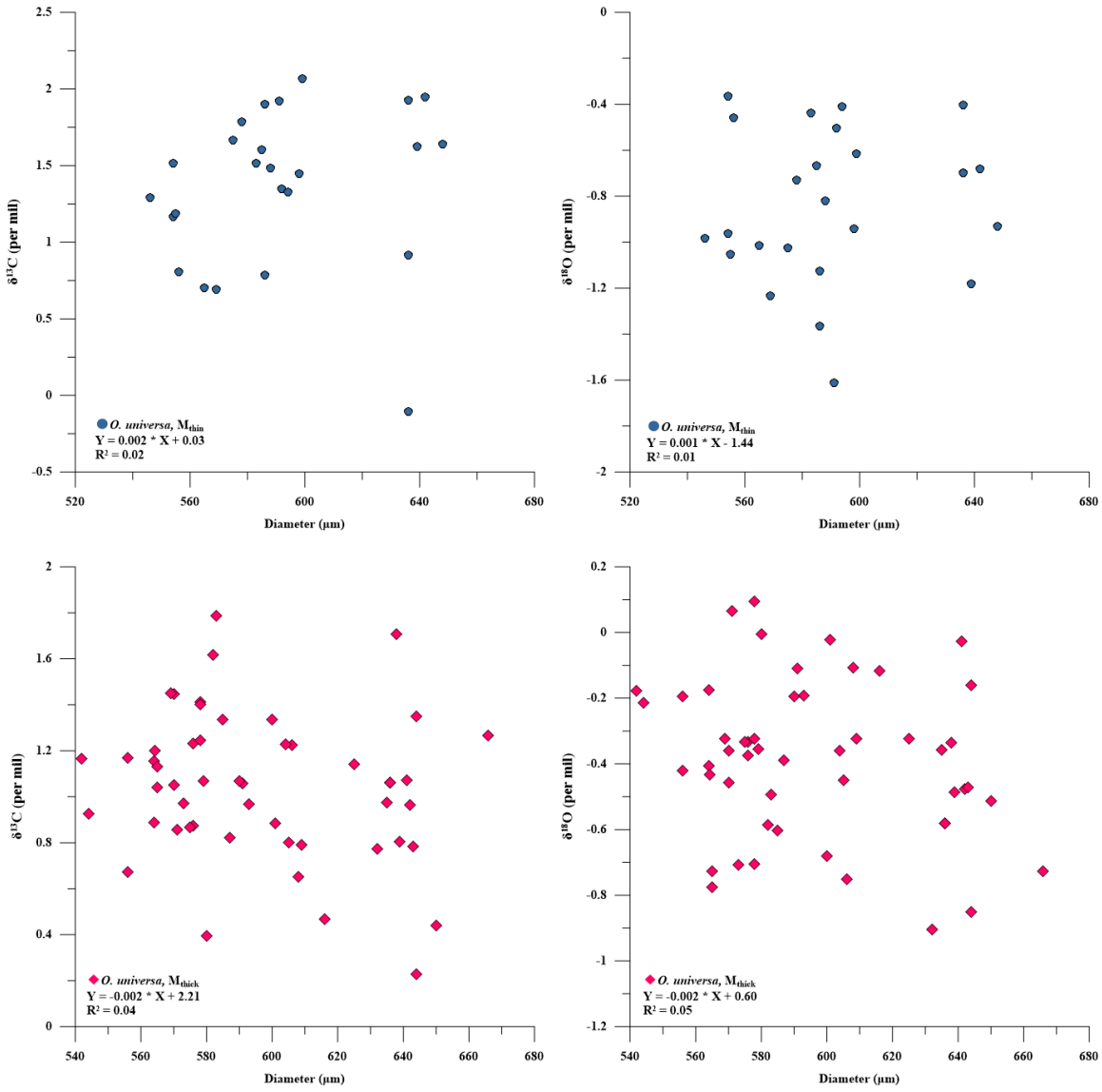

Figure 2.11 Diameter and carbon (a & c) and oxygen (b & d) isotopic relationship with M_{thin} (blue circles) and M_{thick} (pink diamonds).

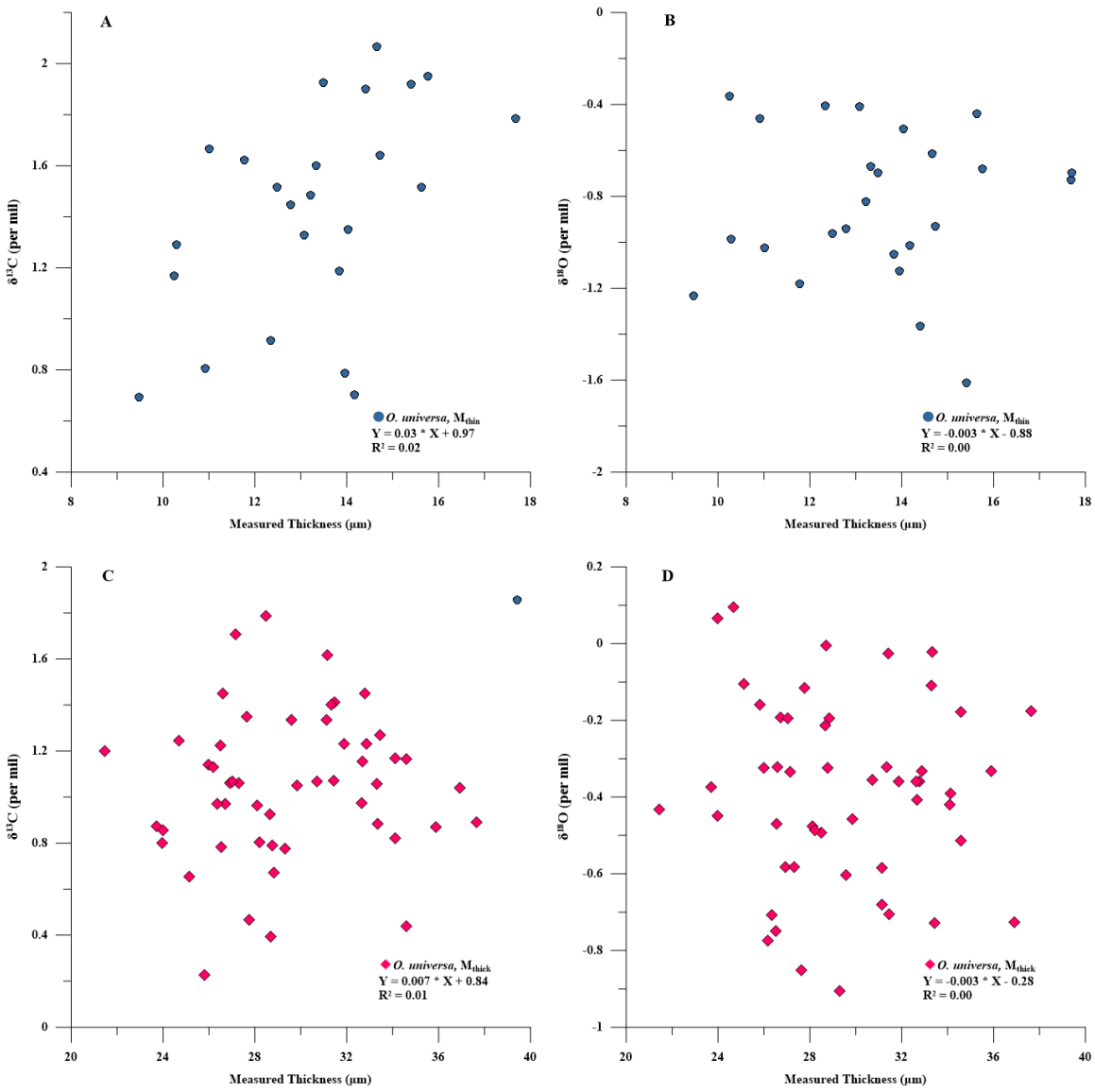

Figure 2.12 Thickness and carbon (a & c) and oxygen (b & d) isotopic relationship with M_{thin} (blue circles) and M_{thick} (pink diamonds).

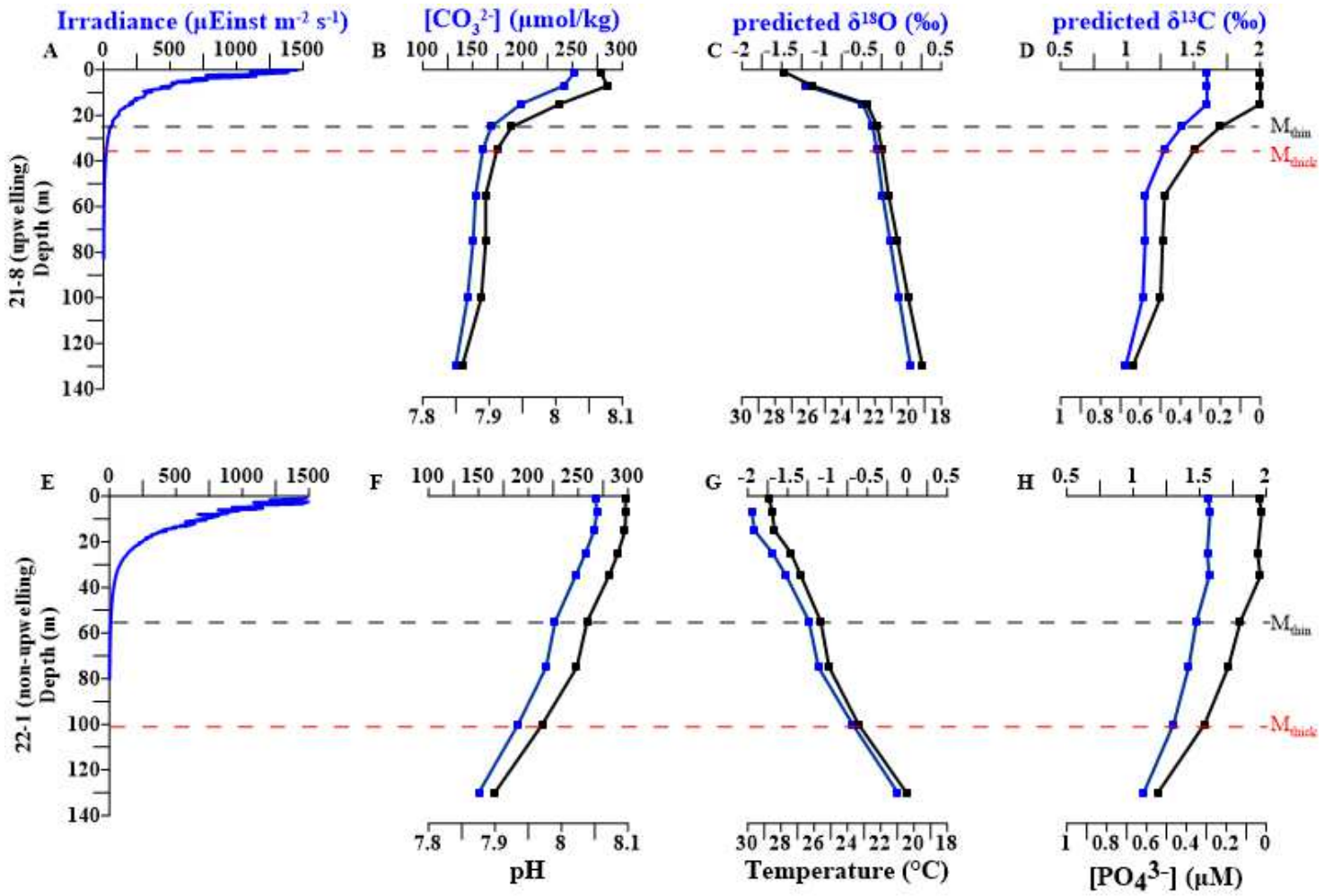

Figure 2.13 Irradiance, $[CO_3^{2-}]$, pH, temperature, predicted $\delta^{18}O$, $[PO_4^{3-}]$, and predicted $\delta^{13}C$ depth profiles for upwelling sample 21-8 (a-d) and non-upwelling sample 22-1 (e-h). Black and red dashed lines mark the average calcification depths of M_{thin} and M_{thick}, respectively.

CHAPTER 3

MICRO-SUBLIMATION AND MC-ICPMS METHOD FOR THE MEASUREMENT OF BORON ISOTOPES IN MARINE CARBONATES

3.1 ABSTRACT

In this study we present a new method developed for the boron isotopic measurement of marine carbonates. Our approach utilizes a micro-sublimation technique for isolating boron from the carbonate matrix, with recoveries ranging from 99.7 - 99.9 % and reduced sample processing time as compared to traditional ion exchange chromatography methods. Boric acid and carbonate standards are analyzed for their boron isotopic ratios using a MC-ICPMS and introduced using a reducing 0.3M HF matrix in order to minimize washout times and better control for mass fractionation. The 2σ value for measured three boric acid standards (2σ = 0.28 - 0.36 ‰; NIST SRM 951, JABA and JABB) and three carbonate standards (2σ = 0.34 - 0.39 ‰; JCT, JCP, and CARO) are within the range of uncertainties reported for other laboratories that use a variety of methods for measuring the boron isotopic composition of marine carbonates. The $\delta^{11}B$ of both the boric acid and carbonate standards measured in this study are within error of their published values. Thus, the micro-sublimation and MC-ICPMS methods presented in this study can measure the boron isotopic compositions of carbonate samples with boron concentrations of 20 ppb or greater, both accurately and precisely.

3.2 INTRODUCTION

3.2.1 THE BORON ISOTOPE PH PROXY

The paleoceanography/paleoclimatology community has put considerable effort into the development of proxies for reconstructing past atmospheric carbon dioxide concentrations (pCO_2) beyond the 800,000-year records provided by ice cores (Petit et al., 2008). The rapid equilibration between atmospheric pCO_2 (atm) and surface ocean pCO_2 (aq) (10 years; Revelle and Suess, 1957) is such that one system provides us with quantitative information about the other. Coupling estimates for surface ocean pH with those for other carbonate system parameters, such as alkalinity, allows us to calculate surface ocean pCO_2 and, therefore, atmospheric pCO_2 (Zeebe and Wolf-Gladrow, 2001). Thus, a reliable proxy for pH that can be applied to the marine sedimentary record would provide us with the ability to identify past ocean acidification events.

Over the past decade, the boron isotopic composition of marine carbonates has become a commonly used proxy for past changes in ocean pH. Both laboratory culture and field studies have shown that the boron isotopic composition ($\delta^{11}B$) of foraminiferal calcite is strongly pH-dependent and can therefore serve as a paleo-pH proxy (Hemming and Hanson, 1992; Vengosh et al., 1991; Hemming and Hönisch, 2007; Foster et al., 2008; Henehan et al., 2013). The boron isotope-pH proxy has been used to reconstruct changes in surface and bottom water pH, as well as calculate atmospheric pCO_2 concentrations that fluctuate in accordance with those recorded in ice cores (Spivack et al., 1993; Sanyal et al., 1995; Pearson and Palmer, 2000; Honisch and Hemming, 2005; Foster et al., 2008; Rae et al., 2011; Henehan et al., 2013). The $\delta^{11}B$-pH proxy is based

on the observation that the relative abundances and isotopic compositions of the two aqueous species of boron – boric acid ($B(OH)_3$) and the borate ion ($B(OH)_4^-$) – are strongly pH dependent (see Zeebe and Wolf-Gladrow, 2001 and Hemming and Hönisch, 2007 for review; Figure 1a and b). The boron isotopic composition of a sample is the ratio of the two stable nuclides of boron - ^{10}B (19.82%) and ^{11}B (80.18%) - and is reported in delta notation relative to certified boric acid reference standard NIST SRM 951:

$$\delta^{11}B\ (‰) = \left[\left(\frac{^{11}B/^{10}B_{sample}}{^{11}B/^{10}B_{NIST951}}\right) - 1\right] \text{ x } 1000 \qquad (1)$$

where $^{11}B/^{10}B_{NIST951} = 4.04363$ (Catanzaro et al., 1970). There is an isotopic offset between the two aqueous boron species due to coordination-controlled vibration differences (~27‰; Klochko et al., 2006), resulting in the following exchange reaction:

$$^{11}B(OH)_3 + ^{10}(BOH)_4^- <-> ^{10}B(OH)_3 + ^{11}B(OH)_4^- \qquad (2)$$

This exchange reaction has an equilibrium constant <1, which means that boric acid is isotopically enriched in ^{11}B relative to borate ion. Hemming and Hanson (1992) found that a variety of biogenic carbonate samples analyzed for their boron isotopic compositions exhibit a narrow range in $\delta^{11}B$ that corresponds with the $\delta^{11}B$ of borate ion

at typical seawater pH. The results of this study suggest that only the tetrahedrally coordinated borate species is incorporated into biogenic carbonate during calcification (Figure 1b). Later studies provided clear evidence that the $\delta^{11}B$ of cultured foraminifera increase with increasing pH (Sanyal et al., 1996; 2001; Henehan et al., 2013; Figure 2), but the relationship between seawater pH and foraminiferal $\delta^{11}B$ differ from that predicted for borate ion by fairly constant, species-specific offsets. Thus, in order to calculate pH from measured $\delta^{11}B$, one needs to know the boron isotopic composition of seawater (39.65 ± 0.41 ‰; Foster et al., 2013), the stoichiometric equilibrium constant ($pK^{\cdot}_B$ = 8.6 at 25°C and 35 ppt; Dickson, 1990), the isotopic fractionation factor between $B(OH)_4^-$ and $B(OH)_3$ (α_B = 1.0272; Klochko et al., 2006), as well as the species-specific offset (α; Hemming and Hönisch, 2007; Henehan et al., 2013). Using these parameters, the pH of seawater can be derived using the following equation:

$$pH = pK^{\cdot}_B - \log\left(\frac{(\delta^{11}B_{SW} - \delta^{11}B_{CaCO_3} - \alpha)}{\delta^{11}B_{SW} - \alpha_B * (\delta^{11}B_{CaCO_3} - \alpha) - 1000 * (\alpha_B - 1)}\right) \quad (3)$$

At present, there are fewer than a dozen laboratories that are measuring the boron isotopic composition of marine carbonates for use in paleo-reconstructions, due in large part to the analytical rigors of making these measurements. For example, the change in $\delta^{11}B$ of modern marine carbonates per unit change in pH is very small (Figure 1) thus achieving low 2σ values during analysis is imperative for attaining reliable estimates (Foster et al., 2013). Table 1 reports the $\delta^{11}B$ and associated 2σ values for a selection of boric acid and carbonate standards measured at a number of these laboratories. These

$\delta^{11}B$ and associated 2σ values were achieved using a variety of different boron isolation and mass spectrometry methods. The standards listed exhibit 2σ values for boric acid standards (2σ range = 0.12 -1.35 ‰) that are comparable to those reported for carbonate standards (2σ range = 0.08 - 0.93‰). However, significantly lower 2σ values for boric acid standard (2σ = 0.29 - 0.61 ‰) relative to carbonate standards (2σ = 0.65 - 2.86 ‰) are reported in a recent inter-laboratory comparison study (Foster et al., 2013). Prior to this study, reporting uncertainties in boron isotopic measurements were generally based on repeat measurements of a single boric acid standard that requires no pre-treatment. Foster et al. (2013) observed that the 2σ values reported during the inter-laboratory calibration of multiple unknown standards were higher than those reported for the same laboratories in earlier studies. This suggests that the higher 2σ values of measured carbonate standards relative to those reported for boric acid standards are likely attributed to boron concentration (sample size) or B/Ca (boron concentration relative to carbonate matrix).

3.2.2 Analytical Challenges

The boron isotopic compositions of marine carbonates have been measured using positive thermal ionization mass spectrometry (P-TIMS; Spivack and Edmond, 1986), negative thermal ionization mass spectrometry (N-TIMS; Hemming and Hanson, 1994; Aggarwal et al., 2009), multi-collector inductively coupled plasma mass spectrometry (MC-ICP-MS; Foster et al., 2008; Henehan et al., 2013), total evaporation thermal ionization mass spectrometry (TE-TIMS; Liu et al., 2013) or most recently by the high

resolution inductively coupled plasma mass spectrometry (HR-ICP-MS; Misra et al., 2014). The measurement of the boron isotopic composition of marine carbonates is complicated by a number of issues associated with sample processing and analysis, all of which can be corrected for using a variety of methods. The current paper describes some new techniques we have developed for making boron isotope measurements using MC-ICPMS.

Biogenic carbonates have relatively low boron concentrations ranging from 10-70 μg/g (Hemming and Hanson, 1992), thus analysis with MC-ICPMS generally require anywhere from 1-5 mg $CaCO_3$ for accurate measurements (Foster et al., 2008). Due to the small amount of boron contained in biogenic carbonates, minute quantities of boron contamination during sample processing and analysis can significantly alter the isotopic composition of a sample. Thus, blank reduction techniques are rigorously applied to attain the desired signal to noise ratio of < 2% (Foster et al., 2008). These methods include the utilization of over-pressured flow hoods equipped with boron-free HEPA filters and the use of only Teflon materials for boron sample processing. Reagents are generally Optima grade, Teflon-distilled, or further treated with boron-specific ion exchange resin or mannitol to reduce boron contamination.

Boron is a low mass element, making it particularly susceptible to mass fraction during analyses on the mass spectrometer. This can be corrected for by using rapid Standard-Sample Bracketing (SSB; Foster et al., 2008). However, reducing the time between sample analyses is hindered by a strong memory effect caused by the volatile nature of boron in its boric acid form, thus requiring long washout times between samples. Laboratories analyzing boron isotopes have overcome this effect by using

either a reducing gas (ammonia; Foster et al., 2008) or a reducing mineral acid (HF; Misra et al., 2014) to capture residual boron, allowing for 2-3 minute washout times.

Boron must also be separated from its sample matrix in order to eliminate matrix dependent instrumental mass bias effects when being analyzed by MC-ICPMS (Foster et al., 2008). Traditional methods for boron extraction from a carbonate sample matrix involve the use of ion exchange chromatography (Spivack and Edmond, 1987; Foster et al., 2008). For example, Foster et al. (2008) load dissolved samples into 25 ml micro-columns containing boron-selective Amberlite IRA 743 resin in a buffered nitric acid solution (pH =5) and then elute using 0.5M HNO_3 following the removal of the matrix with multiple MilliQ water washes. The removal of boron from the resin requires > 20 micro-column rinses and 465 minutes/24 samples for full method application (Van Hoecke et al., 2014). The ion exchange chromatography method exposes the samples to a high level of environmental and reagent boron contamination and is expensive both in terms of time and required consumables.

Gaillardet et al. (2001) introduces an alternative method for extracting boron from an organic-rich matrix using micro-sublimation. This method was later refined for Ca-rich solutions (Wang et al., 2010) and has since been used for isolating boron from carbonate matrices prior to subsequent analysis by ICP-MS (Liu et al., 2013; Misra et al., 2014). Boric acid is volatized at relatively low temperatures (60°C) and can therefore be separated from its carbonate matrix without fractionation if sublimated in a closed environment (Gaillardet et al., 2001). The methods presented in Gaillardet et al. (2001) and Wang et al. (2010) use a 5 ml conical Teflon beaker as the sublimation chamber and the carbonate sample, once dissolved in a small volume of acid (40-50 µl), is pipetted

onto the cap of the beaker. The beaker is then placed, cap-down, on a hotplate set to a stable temperature (70-98°C). Once sublimation has completed (12-18 hrs), the sublimated boric acid droplet is used for isotopic analysis. Gaillardet et al. (2001) reports that even incomplete recoveries of a sublimated 250 ng B boric acid standard (NIST SRM 951) exhibited accurate $\delta^{11}B$ values with no significant isotopic fractionation ($\delta^{11}B$ = 0.03‰, 2σ =0.09‰). However, biogenic carbonate samples seldom contain 250 ng of B, and thus complete recovery (> 99%) is necessary to reduce possible Rayleigh fractionation due to incomplete boron recovery or loss during the high temperature sublimation process (Misra et al., 2014; Van Hoecke et al., 2014). The micro-sublimation method requires only 190 minutes/24 samples for sample preparation and the volume of consumables required for this method are less costly than those required for ion exchange chromatography (Van Hoecke et al., 2014).

In this paper, we outline new methods developed for the boron isotopic measurement of marine carbonates using the micro-sublimation technique to isolate boron from the sample matrix and a Neptune MC-ICPMS for subsequent isotopic analyses.

3.3 Methods

3.3.1 Blank Reduction Procedures

One of the greatest analytical challenges for measuring the boron isotopic composition of marine carbonate samples, which generally contain only 10-15 ppm boron (Hemming and Honisch, 2007), is to reduce the blank accumulation in measured samples

and reagents. In this study, all sample processing for boron isotopic measurements is performed in a laboratory equipped with a sealed, over-pressured flow hood and boron free HEPA filters. Only Teflon labware is utilized within the boron chamber and flow hood. All Teflon labware is first cleaned in aqua regia and rinsed periodically with 10% HCl. The flow hood is also cleaned on regular occasions with acetone to help maintain low blank accumulation. All concentrated reagents used in the boron isotope method (18. 2 MΩ Super-Q ultrapure water, 1 Optima® HCl, 29M trace metal grade HF) are either percolated through a Teflon separatory funnel containing Amberlite IRA 743 resin or teflon-distilled, yielding negligible blanks on the Element ICP-MS (mean [B] = 0.18 ng, n = 4). All diluted reagents are stored in Teflon containers prior to use in the micro-sublimation method.

Teflon vial cleaning is conducted using a modified method from Foster et al. (2008). Labels are first removed using acetone and vials are rinsed three times in Super-Q water (SQ). Following a 2-hour initial reflux in 7M HCl at 120°C (trace metal grade), vials are submerged in a 500 ml Teflon container containing 7M HCl (trace metal grade) for 24-48 hrs (120°C). Vials are the removed, rinsed three times in SQ, and then placed in a second wash containing 7M Optima HCl and Amberlite IRA 743 filtered Super-Q water (ASQ) for 24 - 48 hrs (120°C). Following the second wash, vials are rinsed three times using ASQ, capped and stored in clean Teflon containers until use. A 1-hr final reflux in 10 Optima HCl and ASQ is conducted immediately prior to use for micro-sublimation.

3.3.2 Sample Preparation

Approximately 150-300 individual foraminifera are picked from each sample in order to yield 2-5 mg of $CaCO_3$ for boron isotopic analysis. The foraminifera are lightly crushed between two clean glass slides and placed with a paintbrush into acid-cleaned 1.5 ml micro-centrifuge vials. 50 µl of ASQ is added to each vial prior to a 30 second sonication, after which the supernatant containing clay particles is removed. This step is repeated until the crushed foraminifera are pure white. The samples then undergo an oxidative treatment using 3% H_2O_2 and 0.1N NH_4OH. Prior to dissolution in 75 µl of 2-3M Optima HCl, samples are treated with 0.0005M Optima HCl to remove any adsorbed contaminants. Samples undergo an average 25% mass loss during cleaning. Because carbonate standards JCP and JCT have already been chemically pre-treated, only the final contaminant removal step is applied to these standards prior to dissolution (Okai et al., 2002; Takashi et al., 2004).

3.3.3 Micro-Sublimation Method

The extraction method for removing boron from the carbonate matrix was modified from Wang et al., (2010) and Misra et al. (2014). This micro-sublimation method differs significantly from the traditional ion exchange column chemistry method for boron extraction used in most previous studies (Foster et al., 2008; Rae et al., 2011; Henehan et al., 2013) and relies on the volatile nature of boric acid. For this method, 2 to 5 mg of cleaned carbonate is dissolved in 75 µl of 2M HCl. All boron in the dissolved sample is in the form of boric acid (pH < 2; Wang et al., 2010). Prior to depositing the

dissolved samples in the vial caps, the sutures of the pre-cleaned 5 ml conical Teflon vials are wrapped in Teflon tape in order to reduce mass loss during sublimation. The entire dissolved carbonate sample is deposited in the center of the cap, sealed tightly and weighed (± 0.1 mg, repeat weighing 1 mg calibration weight, n = 20) to monitor mass loss during the sublimation process. The vials are then placed cap-down on an ANALAB hotplate equipped with a Teflon coated heating block set to 98°C and left to sublimate over an 18-20 hour period (Figure 3). After sublimation, the sublimated boric acid droplet is deposited in the conical portion of the Teflon vial, with a small, gelatinous residue remaining in the center of the cap. The hotplate is then turned off and left to cool for at least one hour, until the vials reach room temperature. After the vials have cooled, the droplet is stable and the vial is re-weighed to monitor mass loss. At this point, the residue can be recovered for measurement of [B] on a HR-ICPMS to calculate % boron recovery. The sublimated sample is then pipetted into an acid-washed vial and diluted with 0.3M HF up to a minimum of 250 µl for analysis on the MC-ICPMS.

3.3.4 STANDARDS

The standards used for boron isotopic analysis and their published values are listed in Table 1. The boron isotopic ratios of sample materials are reported relative to NIST SRM 951 ($^{11}B/^{10}B = 4.04367$; Catanzaro et al., 1970), a boric acid reference standard developed by the National Institute of Technology. During a sample run, NIST SRM 951 is measured relative to itself to determine machine precision and accuracy and is also used as the bracketing standard for samples. In this study, JABA and JABB boric

acid standards were also used for preliminary Neptune MC-ICPMS methods development, but not during subsequent sample analysis.

We created an in-house carbonate standard using the planktonic foraminifera *Orbulina universa* from a sediment trap sample (CAR33z #3) collected from the Cariaco Basin, Venezuela. Approximately 9 g of cleaned *Orbulina universa* (B/Ca ~ 51 µmol/mol; E. Osborne, unpublished B/Ca data for *G. menardii* collected from the Cariaco Basin) was dissolved in 2M HCl to create a homogenized 333 ppb stock solution. The concentration of the stock solution was determined in order to create a 50 ppb solution once the 75 µl sublimation droplet is diluted to the required volume of 500 µl for duplicate analyses on the MC-ICPMS (250 µl required per analysis).

Additional carbonate standards, JCP (*Porites* coral; Takashi et al., 2004) and JCT (giant clam; Okai et al., 2002; Takashi et al., 2004), were used to assess the accuracy of the micro-sublimation and MC-ICP-MS methods. All standards are prepared in solutions of 2M HCl and 0.3M HF and amberlite-SuperQ.

3.3.5 MC-ICPMS METHODOLOGY

All samples were analyzed using a Thermo Finnigan Neptune MC-ICPMS housed at the Center for Mass Spectrometry, University of South Carolina. Instrument hardware, typical operating conditions and data acquisition parameters are listed in Table 2. Following Foster et al. (2008), a sample gas test is performed after tuning for each analytical session in order to determine the flow rate associated with the most stable ^{11}B to ^{10}B ratio and lowest level of instrument mass fractionation. This test manipulates the

sample gas rate by small increments (0.02 L/m), while recording the $^{11}B/^{10}B$ and the intensity of ^{11}B. Optimal stability in $^{11}B/^{10}B$ is generally associated with higher gas flows (0.885 L/min) and slightly lower sensitivity (Figure 4). Rather than using a reducing gas to reduce washout times (Foster et al., 2008), we employ the reducing mineral acid method presented in Misra et al. (2014). Specifically, 0.3M HF is used for our wash and standard solutions and is added to all samples during dilutions. Using this method, we require a washout time of only 2.5 minutes to achieve the desired blank to signal ratio of 1-2% (typical ^{11}B = 0.5%, typical ^{10}B = 2.2%). The higher blank to signal ratio for the lighter isotope is attributed to the isobaric interference resulting from $^{40}Ar^{4+}$ on boron at low resolution.

Samples are run manually at low resolution using an online baseline correction and sample-standard bracketing (SSB). A single SSB, including blank correction and 2.5 min washout times, can be completed in 28 minutes, allowing for 17 sample analyses in a single 8-hr analytical session. Each analysis consists of the simultaneous collection of masses 10 and 11 in their corresponding Faraday cups (L3 and H3 for ^{10}B and ^{11}B, respectively) for 3.5 minutes. Instrument mass bias was corrected for by using the average B ratio of bracketing NIST 951 standards when calculating the $\delta^{11}B$ for each sample (Eq. 3.1).

3.4 Results and Discussion

3.4.1 Efficiency of Micro-Sublimation Method

The micro-sublimation method requires 3 hours of sample preparation, 18-20 hours of unattended micro-sublimation and 1 hour of sample post-processing for 10

samples. Thus, the micro-sublimation method reported here requires only half of the time for sample processing as compared to the ion-exchange chromatography method used in most other laboratories (Van Hoecke et al., 2014). For all runs, the mass loss resulting from the micro-sublimation was no more than 5% of the starting volume (mean mass loss = 3.9 ± 0.1 mg (µl), n = 69), though some of this apparent mass loss may be attributed to the lower rigidity of the vials after sublimation. Preliminary tests using the carbonate standard JCP revealed that increasing the time of sublimation from 6 to 18 hours resulted in a decline in the boron isotopic composition and 2 sigma value of the standard (Figure 5). This is in agreement with previous studies stating that the initial sublimated droplet is enriched in ^{11}B (Wang et al., 2010). The boron isotopic composition of the measured JCP ($\delta^{11}B \sim 24.38$ ‰) is close to that of previously published values (mean $\delta^{11}B \sim 24.32$ ‰) after 18 hours of sublimation. Thus, micro-sublimation of samples for 18-20 hours is recommended in order to achieve accurate results.

The [B] of the sublimated droplet and gelatinous residue were measure after an 18-hour sublimation of 10 JCT samples using an ELEMENT HR-ICP-MS (Table 3). Boron concentrations of the sublimated droplets ranged between 110 and 127 ng B for samples weighing between 2.7 and 3.1 mg $CaCO_3$. Boron concentrations in the residues ranged from 0.09 – 0.49 ng B, with recoveries between 99.7 and 99.9%, comparable to those reported in Wang et al., (2010). Procedural blanks run using the same methods yielded a typical blank contribution of 0.15% (0.07-0.28 ng, n = 4) that is comparable to the procedural blanks reported in Wang et al. (2010; 0.04-0.07 ng) and Foster et al.

(2008; 0.07 – 0.1 ng). These blank contributions are considered insignificant compared to average amount of boron per sample (Table 3).

Subtracting the instrument uncertainty (2σ for NIST SRM 951, Table 1) from the 2σ values for micro-sublimated carbonate standards (2σ for JCT, JCP and CARO, Table 1) provides us with a measure of accuracy for the micro-sublimation method ($2\sigma_{ms}$ = -0.02 - 0.03 ‰).

3.4.2 Standard Reproducibility

Tests run using the boric acid standard JABA revealed that for samples with B concentrations ranging from 20 – 100 ppb, sample-standard concentration matching to within 20% produced the most accurate and precise $\delta^{11}B$ values (Figures 6). The tests revealed that concentration matching between higher concentration samples and standards (100 ppb B) is less important in achieving accurate $\delta^{11}B$ values than concentration matching for lower concentration samples and standards (20 ppb; Figure 6). Even with high concentration samples, however, the 2σ values increased as the difference in concentrations between sample and standard increased. Thus, sample solutions generally ranged between 30-80 ppb B and were concentration matched to within 20% (10% for lower samples ≤ 20 ppb) of the NIST SRM 951 boric acid bracketing standard.

Replicate analyses of boric acid standards provide us with an estimate for instrument uncertainty, with an overall 2σ of 0.36‰ for NIST SRM 951 boric acid standard ($\delta^{11}B$ = -0.009; n = 78), 0.32 ‰ for JABA ($\delta^{11}B$ = 10.84; n = 80) and 0.28 ‰

for JABB ($\delta^{11}B$ = -24.48; n = 51). The 2σ values reported for the carbonate standards measured in this study represent a combination of instrument and sample processing uncertainty, with 2σ values of 0.39‰ for JCT ($\delta^{11}B$ = -0.002; n = 22), 0.34‰ for JCP ($\delta^{11}B$ = 24.38; n = 10) and 0.39 for CARO ($\delta^{11}B$ = 16.68; n = 4). Our range in 2σ values for the boron isotopic analysis of marine carbonates using the micro-sublimation technique (2σ = 0.34 – 0.93 ‰) is within the lower range of those reported for other laboratories (2σ = 0.27 - 2.86 ‰; Foster et al., 2013).

3.5 Conclusions

The results of this study illustrate the efficiency of the micro-sublimation method at isolating boron from a carbonate matrix for isotopic analysis on the Neptune MC-ICPMS. The use of a 0.3M HF matrix in substitution of a reducing add gas is effective at decreasing washout times between boron isotope sample analyses to 2.5 minutes, allowing for rapid sample-standard bracketing. The range in 2σ values reported in this study for both boric acid standards (2σ = 0.28 – 0.36 ‰) and carbonate standards (2σ = 0.34 – 0.39 ‰) are comparable to and on the lower end of those reported from other laboratories. Thus, the boron isotopic composition of marine carbonates with [B] greater than 20 ppb can be measured both accurately and precisely using the micro-sublimation and MC-ICPMS methods presented in this study.

Table 3.1 Summary of $\delta^{11}B$ and 2σ values reported from other laboratories for the standards used in this study.

Institution, Method Citation	$\delta^{11}B$ (‰) Measured	2σ	n	Reference	Boron Separation Method	Mass Spec Method
JABA, boric acid						
BIG[1]; Foster et al., 2006	10.79	0.12	6	Aggarwal et al., 2009	Ion-exchange chromotagraphy	MC-ICPMS, Ammonia gas
BIG[1]; Foster et al., 2006	11.12	0.88	3	Aggarwal et al., 2009	Ion-exchange chromotagraphy	TE-TIMS
LDEO[2]; Hemming and Hanson, 1994	10.05	0.80	3	Aggarwal et al., 2009	NA	NTIMS
Wang et al., 2010	10.52	0.36	27	Wang et al., 2010	Microsublimation	MC-ICPMS, Ammonia sol.
Henehan et al., 2013 pers comm	10.91	0.36	10	Foster et al., 2008	Ion-exchange chromotagraphy	MC-ICPMS, Ammonia gas
CEMS	10.84	0.32	80	This Study	Microsublimation	MC-ICPMS, HF wash
JABB, boric acid						
BIG[1]; Foster et al., 2006	-24.30	0.22	6	Aggarwal et al., 2009	Ion-exchange chromotagraphy	MC-ICPMS, Ammonia gas
BIG[1]; Foster et al., 2006	-24.13	0.36	3	Aggarwal et al., 2010	Ion-exchange chromotagraphy	MC-ICPMS, Ammonia gas
LDEO[2]; Hemming and Hanson, 1994	-22.49	0.20	2	Aggarwal et al., 2009	NA	NTIMS
CEMS	-24.48	0.28	51	This Study	Microsublimation	MC-ICPMS, HF wash
NIST SRM 951; boric acid ; Cantanzaro et al., 1970						
Gaillardet et al., 2001	0.02	0.20	9	Gaillardet et al., 2001	Microsublimation	Thomas THN 206 MS
Wang et al., 2010	0.02	0.33	40	Wang et al., 2010	Microsublimation	MC-ICPMS, Ammonia sol.
Jniversity of Cambridge; Misra et al., 201	0.03	0.27	3	Misra et al., 2014	Microsublimation	HR-ICP-MS, HF wash
Liu et al., 2013	NR	1.35	25	Liu et al., 2013	Microsublimation	TE-TIMS
CEMS[3]	-0.01	0.36	78	This Study	Microsublimation	MC-ICPMS, HF wash
CARO; O. universa						
NOCS[4]; Foster et al., 2008	17.19	NR	NR	Michael Henehan, pers comm.	Ion-exchange chromotagraphy	MC-ICPMS, Ammonia gas
CEMS	16.68	0.38	4	This Study	Microsublimation	MC-ICPMS, HF wash
JCT; Giant Clam; Takahashi et al., 2004						
NOCS[4]; Foster et al., 2008	16.14	0.27	9	Michael Henehan, pers comm.	Ion-exchange chromotagraphy	MC-ICPMS, Ammonia gas
CEMS	16.17	0.39	21	This Study	Microsublimation	MC-ICPMS, HF wash
JCP; Porites Coral; Okai et al., 2002						
NOCS[4]; Foster et al., 2008	24.31	0.27	85	Michael Henehan, pers comm.	Ion-exchange chromotagraphy	MC-ICPMS, Ammonia gas
Douville et al., 2010	24.50	0.20	17	Douville et al., 2010	Ion-exchange chromotagraphy	MC-ICPMS, Ammonia gas
Wang et al., 2010	24.22	0.28	NR	Wang et al., 2010	Microsublimation	MC-ICPMS, Ammonia sol.
Ishikawa and Nagaishi, 2011	24.25	0.08	11	Ishikawa and Nagaishi, 2011	NA	P-TIMS
CEMS	24.38	0.34	10	This Study	Microsublimation	MC-ICPMS, HF wash

Table 3.2 Typical operating conditions for the Neptune MC-ICPMS.

Parameter	Isotope Mode
Mass Spectrometer Type	Neptune
Plasm RF Power	1200 W
Nebulizer	Savilex ™ - 50 µl
Spray Chamber	Teflon Scott type (single pass)
Injector	ESI™ Platinum (1.8 mm I.D.)
Sample Cone	Plt - JET
Skimmer Cone	Plt - X
Extraction Voltage	−2000 V
Sample Matrix	0.3 M HF
Uptake Time	60 s
Analysis Time	210 s
Washout Time	150 s
Mass Resolution	Low
Typical Sensitivty B	20-30 V/ppm
Cup Configurations	^{10}B (L3) and ^{11}B (H3)
Blocks	20
Outlier Test	2σ

Table 3.3 Results of total boron recovery test using carbonate standard JCT.

Sample ID	Sample Weight (mg)	$\delta^{11}B$ (‰) Run 1	$\delta^{11}B$ (‰) Run 2	[B] (ng)	[B] residue (ng)	Recovery (%)
JCT_1	2.9	16.0		118.66	0.20	99.8
JCT_2	2.8	16.5	15.99	114.57	0.12	99.9
JCT_3	2.9	15.8	16.22	118.66	0.49	99.6
JCT_4	2.9	16.0		118.66	0.32	99.7
JCT_5	3.1	16.1		126.84	0.26	99.8
JCT_6	2.7	16.6	16.17	110.48	0.18	99.8
JCT_7	2.8	16.4		114.57	0.16	99.9
JCT_8	2.9	16.1		118.66	0.17	99.9
JCT_9	3.1	16.4		126.84	0.09	99.9
JCT_10	2.8	16.2		114.57	0.65	99.4
MEAN	**9.55**	**16.2**		**118.25**	**0.26**	**99.8**
2σ		**0.5**				

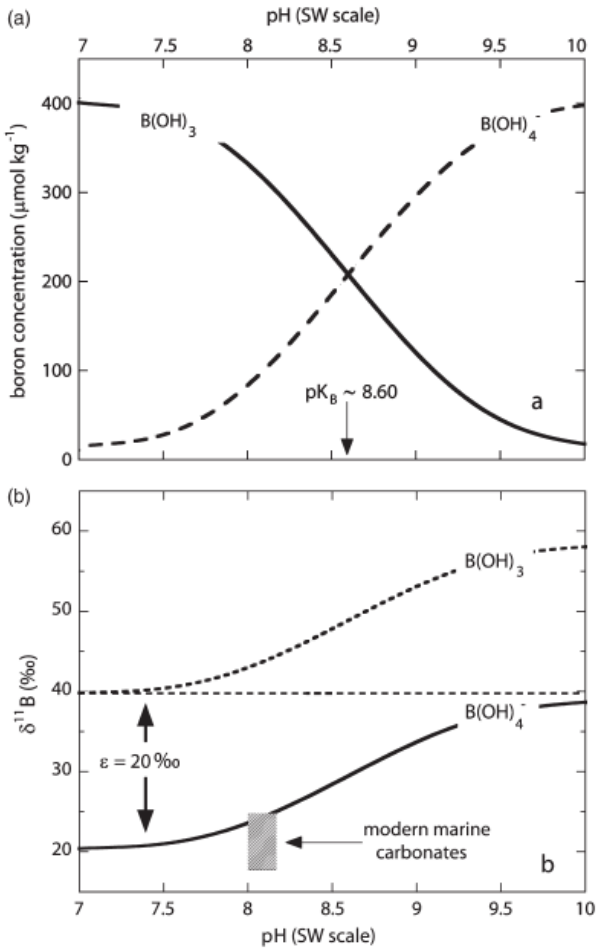

Figure 3.1 (a) concentration and (b) isotopic composition of borate and boric acid in seawater as a function of pH. Also shown is the range in boron isotopic values for modern marine carbonates (from Hemming and Honisch, 2007).

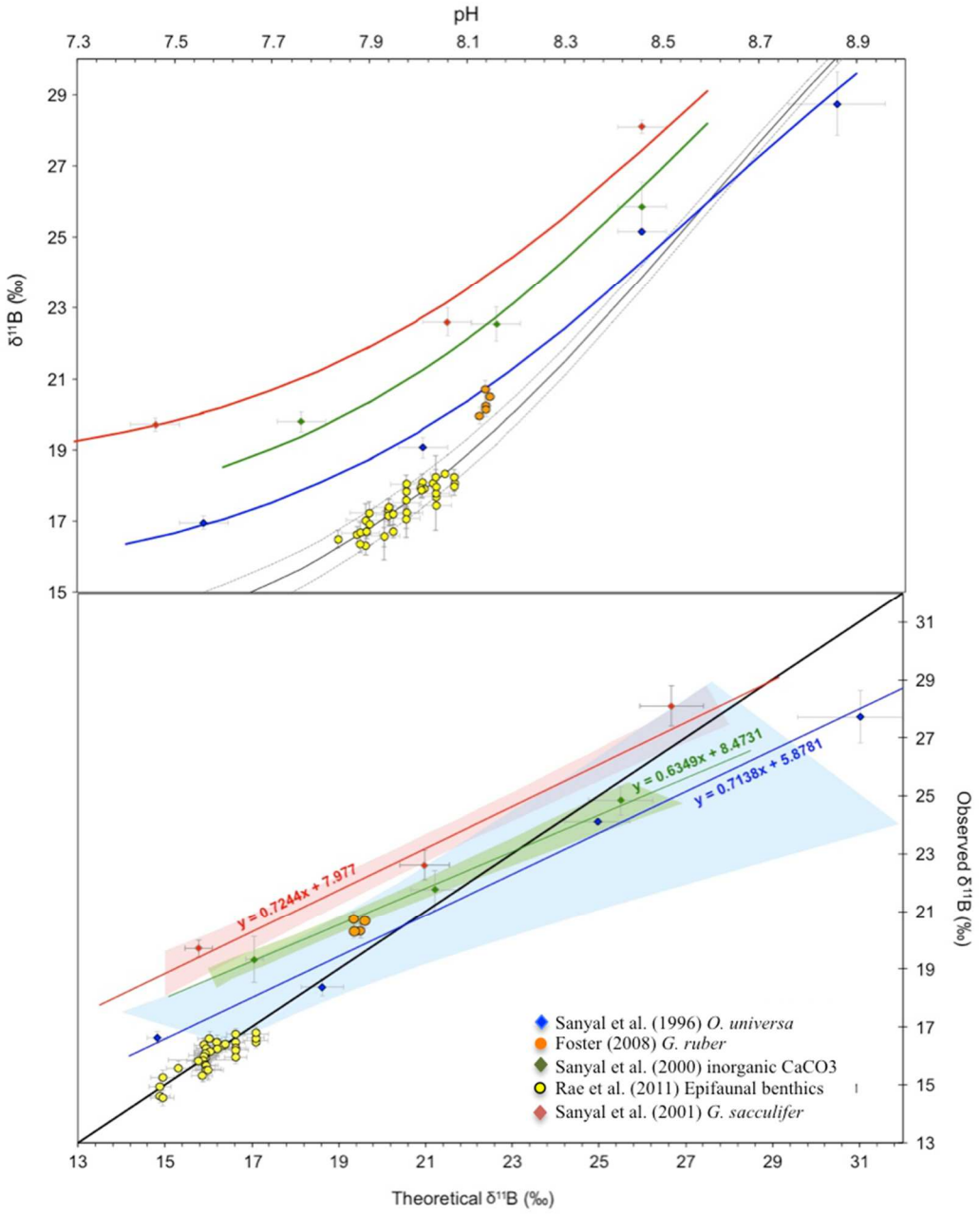

Figure 3.2 Published cultured and inorganic precipitate calibrations for multiple species of foraminifera. All have been normalized to a temperature of 26°C and salinity of 37.2 psu. The black line is the aqueous value of $\delta^{11}B$ borate for these same environmental conditions; note the offset between the foraminiferal $\delta^{11}B$ -pH calibrations and that relationship predicted for aqueous borate (from Henehan et al., 2013).

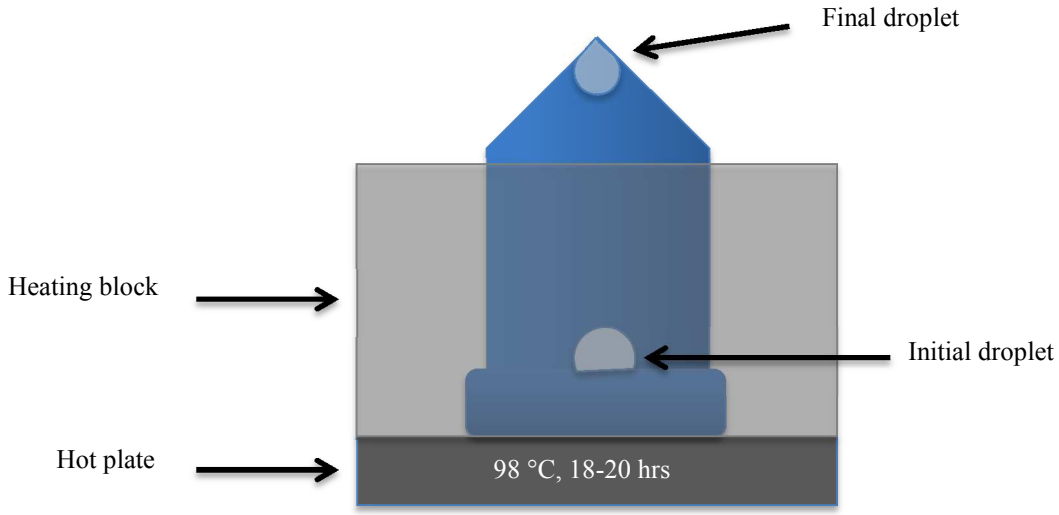

Figure 3.3 Schematic of B purification using the micro-sublimation method.

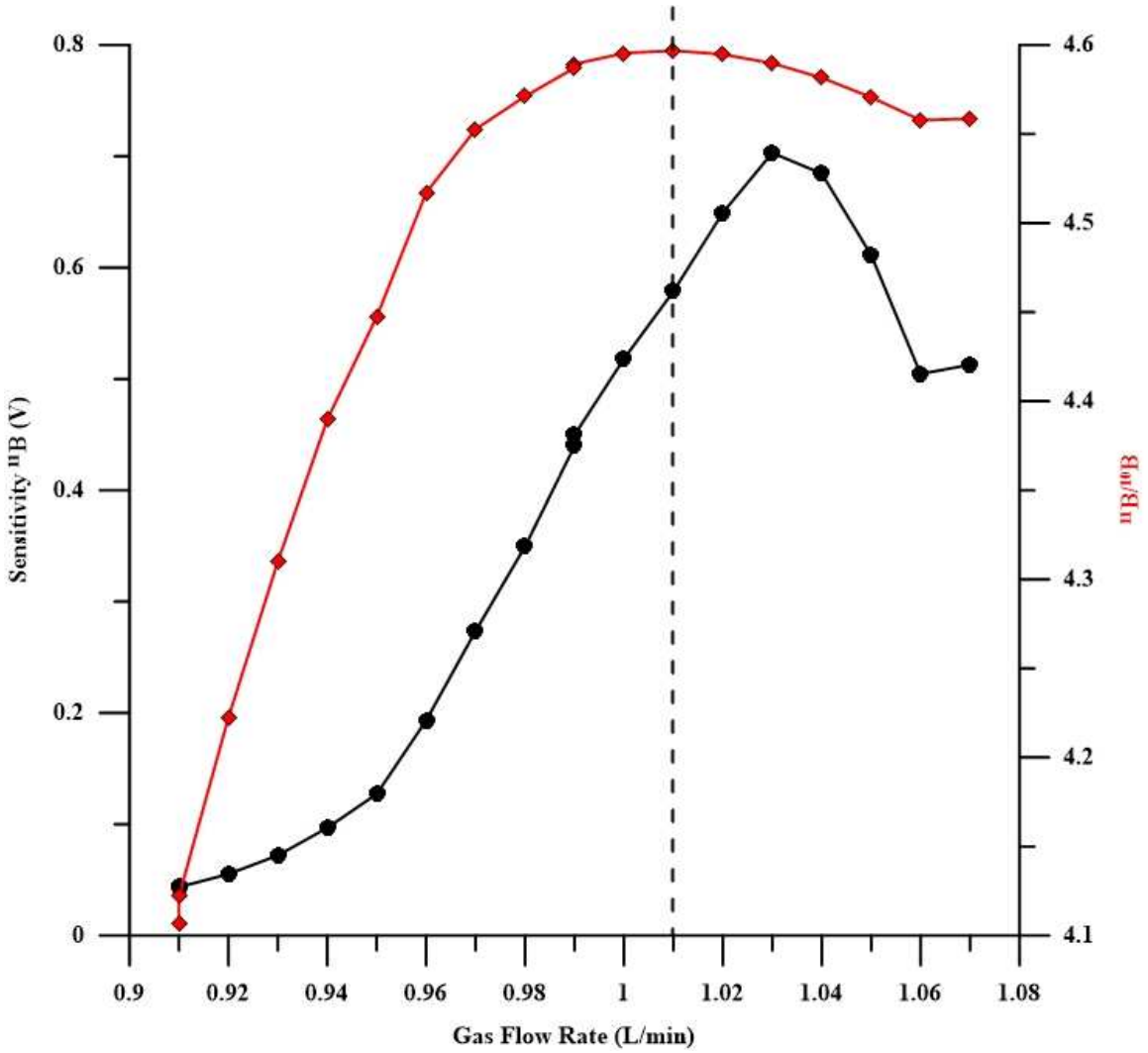

Figure 3.4 An example of the sample gas flow rate test performed before each analytical session. The gas flow rate that correlates with the most stable 11B/10B ratio is chosen in order to reduce mass bias (dashed line).

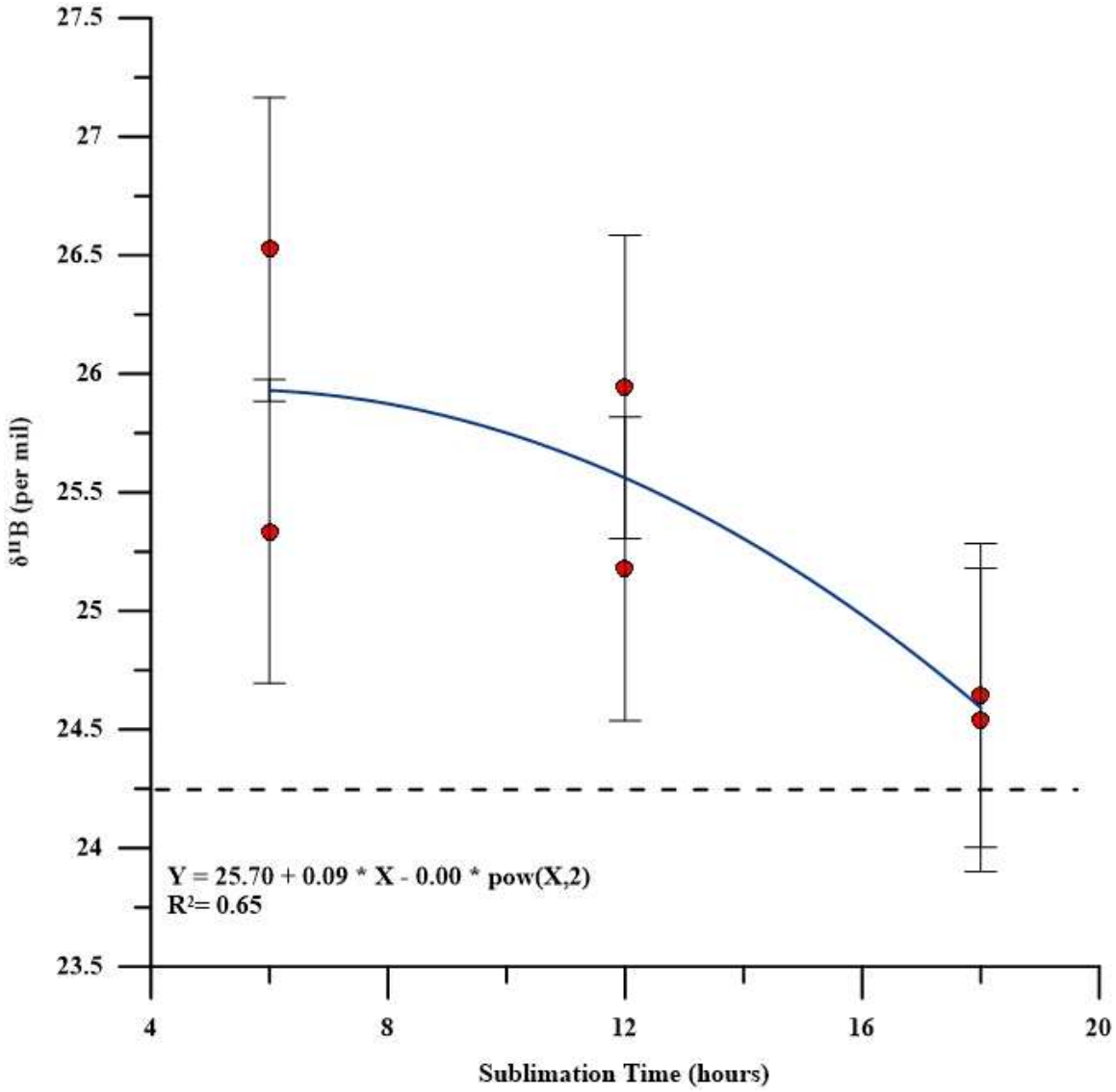

Figure 3.5 The decrease in both $\delta^{11}B$ and 2σ of carbonate standard JCP with increasing sublimation time. The dashed line represents the long-term mean $\delta^{11}B$ measured at CEMS ($\delta^{11}B$ = 24.25 per mil).

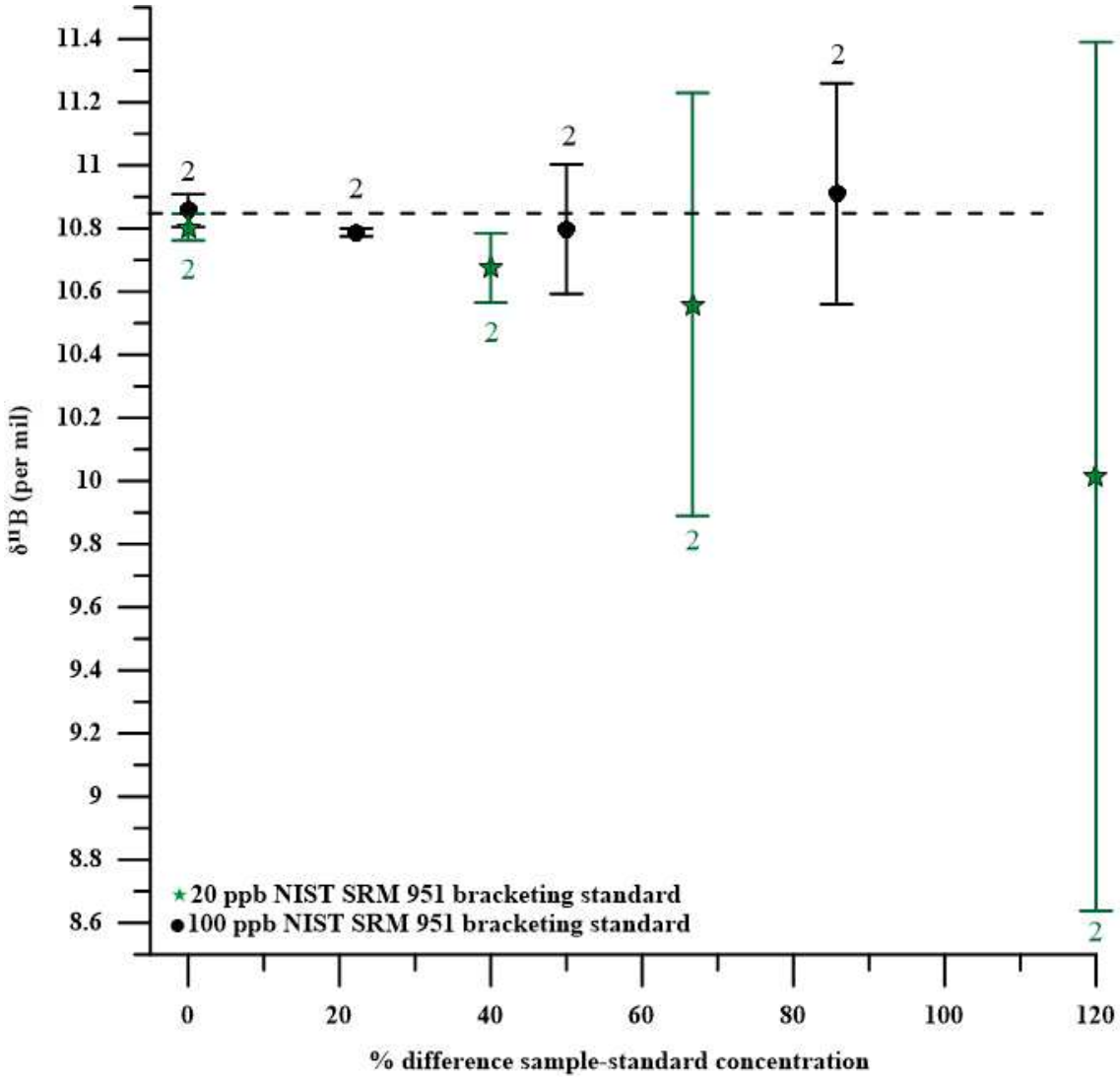

Figure 3.6 Reproducibility (2σ) of JABA boric acid standard as a function of sample-standard boron concentration matching. Green are samples paired with 20 ppb NIST SRM 951 bracketing standard and black circles are samples paired with 100 ppb NIST SRM 951 bracketing standard

CHAPTER 4

CHANGES IN THE EASTERN EQUATORIAL PACIFIC CARBONATE SYSTEM OVER THE LAST GLACIAL CYCLE

4.1. ABSTRACT

We use coupled carbonate system parameters (*G. sacculifer* area density- derived $[CO_3^{2-}]$, alkalinity and $\delta^{11}B$ derived pH) to calculate upper thermocline $pCO2_{aq}$ for the eastern equatorial Pacific ((2°16'N, 90°57'W) over the last 35,000 years. The thermocline-atmospheric pCO_2 difference ($\Delta\, pCO_2$) in this region is higher during the glacial period (167 µatm) relative to the deglacial period and Holocene (28 µatm), indicating a high CO_2 store at thermocline depths during the last glacial. Additionally, the average offset between the raw radiocarbon ages of surface dweller *G. ruber* and thermocline dwelling *N. dutertrei* ($\Delta^{14}C_{duter\text{-}ruber}$) of ~ 1250 ^{14}C years provides further evidence for the storage of ^{14}C-depleted CO_2-rich waters at thermocline depths during the glacial period. $\Delta\, pCO_2$ declines by ~ 200 µatm and $\Delta^{14}C_{duter\text{-}ruber}$ decline by ~ 1000 ^{14}C years during the early deglaciation and by ~ 150 µatm and 1000 ^{14}C years again during the Younger Dryas (YD). A concurrent decline in surface-ocean $[CO_3^{2-}]$ of 50 and 25 µmol/kg, respectfully, during the early deglaciation and YD, and a concurrent increase in atmospheric CO_2 concentrations indicate that EEP thermocline CO_2 was transferred to the atmosphere at these times. We are able to rule out enhanced upwelling as the cause of

this transfer and support the conclusions of earlier studies that indicate the advection of CO_2-rich Southern Ocean waters into the EEP through ocean tunneling. This study provides the first direct evidence for the transfer of CO_2 from thermocline depths to the atmosphere in the EEP during the deglaciation and provides further evidence that this region plays an important role in atmospheric CO_2 change during glacial terminations

4.2 Introduction

4.2.1 Glacial-Interglacial atmospheric CO_2 Change

At present, the eastern equatorial Pacific (EEP) serves as the ocean's largest source of CO_2 to the atmosphere (0.8 to 1.0 Pg C year-1, Takahashi et al, 2009; Figure 1). As a result, it has been suggested that this region plays an important role in the modulation of atmospheric CO_2 concentrations on glacial-interglacial timescales (Spero et al., 2002; Marchitto et al., 2007; Marinez-Boti et al., 2015). Several studies have suggested that the EEP served as a continuous source of CO_2 to the atmosphere throughout the recent glacial-interglacial (G-I) cycle (Pederson et al., 1991; Sanyal et al., 1997; Sanyal and Bijma, 1999). The mechanisms behind rising atmospheric CO_2 concentrations (pCO_{2atm}) during deglaciations have long been debated (Broecker et al., 1998; Archer et al, 2000; Sigman and Boyle, 2000; Anderson et al., 2009; Anderson and Carr, 2014; Marcott et al., 2014), though most recent studies agree on the necessity of an isolated, deep-water carbon pool during glacial times and the release of this carbon to the atmosphere during deglaciations (Sigman and Boyle, 2000; Anderson et al., 2009; Marcott et al., 2014; Skinner et al, 2014). While the Southern Ocean has been strongly

implicated in the rise of pCO_{2atm} during glacial terminations (Sigman and Boyle. 2000; Skinner et al., 2006; Anderson et al., 2009; 2014; Schmitt et al., 2012; Martinez-Boti et al., 2015), reconstructed surface ocean CO_2 concentrations (pCO_{2aq}) from the EEP provide evidence that this region also contributed to rising atmospheric pCO_{2atm} during deglaciations (Martinez-Boti et al., 2015).

Several studies have demonstrated the existence of bipolar thermal and ventilation seesaws that act on millennial timescales associated with Dansgaard-Oecshger (DO) climate oscillations (Broecker et al., 1998; Schmittner and Galbraith, 2008; Ahn and Brook, 2008; Anderson et al, 2009; Barker et al., 2009; Skinner et al., 2010; 2014; Barker an Diz, 2014). Northern hemisphere cold periods (stadials), as recorded by Greenland ice cores, follow abrupt iceberg discharge events in the North Atlantic (Heinrich events, HE; Ahn and Brook, 2008). The timing of these events is coincident with a collapse of Atlantic meridional overturning circulation (AMOC), reduced northward heat transport associated with a more sluggish North Atlantic Deep Water (NADW) formation, and a simultaneous warming around Antarctica (Schmittner and Galbraith, 2008; Anderson et al., 2009; Anderson and Carr, 2010). This rise in Antarctic temperatures during the last deglaciation is coincident with the release of long-sequestered, ^{12}C-enriched CO_2 to the atmosphere (Schmitt et al., 2012). Skinner et al. (2010) presents records of radiocarbon age differences between benthic foraminifera and the atmosphere (B-Atm) collected from the sub-Antarctic Atlantic (core MD07-3076CQ, 44°4.46'S, 14°12.47'W), revealing not only the presence of a radiocarbon-depleted marine carbon pool in the waters surrounding Antarctica during the last glacial period, but also a rapid decline in B-Atm age during Heinrich Stadial 1 (H1; 14.9 – 17.5 kyr).

The decline in B-Atm age during Heinrich Stadial 1 is contemporaneous with the rapid rise of CO_2 and decline in $\delta^{13}C$ of CO_2 in the atmosphere (Monnin et al., 2001; Schmitt et al., 2012). Changes in density stratification (Schmittner and Galbraith, 2008; Skinner et al., 2010), the strength and latitudinal position of trade winds (Anderson et al., 2009), and sea ice extent (Skinner et al, 2010) around Antarctica have all been proposed as mechanisms for driving the evasion of CO_2 from the deep Southern Ocean to the atmosphere during deglaciation.

A prominent foraminiferal stable carbon isotopic ($\delta^{13}C$) minima event occurring during H1 (15-16 kyr BP) is evident throughout Indo-Pacific, south Atlantic and sub-Antarctic (Skinner et al., 2010), as well as equatorial regions (Spero et al., 2002), suggesting that radiocarbon depleted and ^{12}C-enriched waters were transported into the equatorial upwelling regions at this time. Core TR163-19, located just north of the modern upwelling region in the eastern equatorial Pacific (EEP), contains a carbon isotope minima event spanning 20 - 15.9 ky BP, suggesting an influx of low-$\delta^{13}C$ waters into this region at thermocline depths during this time period (Spero and Lea, 2002). This $\delta^{13}C$ minima event is interpreted as the advection of Southern Ocean-sourced waters after the renewal of Circumpolar Deep Water upwelling during H1. A subsequent rise in $\delta^{13}C$ after 15.9 ky BP is attributed to the re-establishment of North Atlantic thermohaline circulation and the influx of nutrient-poor, high $\delta^{13}C$ waters to the Subantarctic Mode Water (SAMW) and EUC (Spero and Lea, 2002). Significant shifts in the surface ocean carbonate system should be evident if the $\delta^{13}C$-minimum was due to the influx of high CO_2 waters sourced from the Southern Ocean into the EEP at this time. Indeed, studies from equatorial Pacific sites south of the equator have suggested that surface ocean CO_2

($pCO2_{aq}$) and atmospheric CO_2 ($pCO2_{atm}$) were in near equilibrium during the LGM (20 kyr BP), but that surface ocean pCO_{2aq} exceeded $pCO2_{atm}$ throughout the deglaciation (ODP site 1238, 1°87'S, 82°78'W; Martinez-Boti et al., 2015). This study provides clear evidence that the EEP, in addition to the Southern Ocean, was a contributor to CO_2 rise during the deglaciation. However, questions regarding the geographic extent of EEP CO_2 evasion and the mechanisms behind the increased flux of CO_2 from the surface ocean to the atmosphere during the deglaciation remain unanswered. Additionally, direct evidence for the presence of CO_2-rich thermocline waters in the EEP during the deglacial period has not yet been documented.

The current study uses planktonic foraminiferal area density (ρ_A), a proxy for carbonate ion concentration [CO_3^{2-}] (Marshall et al., 2013) and boron isotopic composition, a proxy for pH (Honisch and Hemming, 2007; Foster et al., 2008), to examine changes in the ocean carbonate system over the past 35,000 years in the EEP, just north of the modern upwelling region (core TR163-19; 2°16'N, 90°57'W). These two carbonate system parameters are used to generate a record of upper thermocline pCO_2, which is compared to a pCO_2 record from a core collected just south of the equator in the EEP (Marinez-Boti et al., 2015).

4.2.2 Modern and G-I Hydrographic Setting

Marine sediment core TR163-19 (2°16'N, 90°57'W, 2,348 m) was collected at the northeastern-most extent of the modern upwelling region in the EEP (Figure 1). The surface waters (upper 150m) in this region are characterized by a sharp and shallow

thermocline and halocline (Figure 2; Millero et al., 1998). This is in part due to the influx of the cold and high salinity Equatorial Undercurrent (EUC), sourced from Antarctic Intermediate Waters (AAIW, 70%) and North Pacific waters (30%; Goodman et al., 2005), into the region at 75-100 m water depth (Toggweiler et al., 1991; Spero et al., 2002; 2003; Figure 3). The EUC waters are also characterized by higher nutrient concentrations and lower pH (high CO_2) values as compared to the regional surface waters, resulting in strong geochemical gradients with depth (Figure 2). Around 90°W, the EUC splits off into northern and southern components, forming the northward flowing California Undercurrent (CU) and a southward flowing component that joins with the Peru-Chile Undercurrent (PCUC; Figure 3b). The Subantarctic provides most of the surface nutrients to this region through the upwelling of EUC and the PCUC (Goodman et al., 2005). Due to the shallow depth of EUC waters in the EEP, the degree of surface-ocean mixing in the waters overlying the TR163-19 core site is partially controlled by the strength of EUC advective flow into the region. Additionally, surface wind stress and the relative position of the Intertropical Convergence Zone (ITCZ), which migrates about the equator on both seasonal and longer timescales, influence the degree of surface ocean upwelling in the EEP (Zhang et al., 2005; Kienast et al., 2006; Deplazes et al., 2013). Due to these combined physical forcings, the eastward-shoaling EUC waters initially reach the surface along the western side of the Galapagos Islands (1-2°N, 90-92°W) and are then entrained in the PCUC and upwelled along the Peru coastline (Figure 3; Toggweiler et al., 1991; Kessler et al., 2006; Pennington et al., 2006).

In the EEP, the ITCZ currently migrates between 9°N and 2°N of the equator in the Pacific Ocean, with equatorial upwelling occurring between 90°W and 140°W and

3°N and 3°S (Figure 3a and b; Pennington et al., 2006; Schneider et al., 2014). The EEP is also characterized by Ekman-induced coastal upwelling of EUC waters along the Peru-Chile coastlines, which is formally termed Peruvian Coastal Upwelling (PCU; Toggweiler et al., 1991; Pennington et al., 2006). Both of these upwelling systems bring cold, nutrient-rich equatorial undercurrent (EUC) waters to surface and thermocline depths. To the north of this narrow latitudinal strip of upwelling lies a similarly narrow strip of downwelling between 3°N and 6°N and a strip of upwelling in the northern EEP between 6°N and 15°N (Figure 3). The strength and latitudinal extent of these upwelling and downwelling regions in the EEP change seasonally due to the migration of the ITCZ and associated trade winds (Pennington et al., 2006; Figure 3).

Proxy and modeling studies have linked changes in AMOC strength with changes in equatorial Pacific climate (Stott et al., 2002; Zhang et al., 2005; Benway et al., 2006; Kienast et al., 2006; Deplazes et al., 2013). Modeling studies suggest that a slowdown of AMOC during Heinrich events and the YD results in a southward shift of the Intertropical Convergence Zone (ITCZ; Zhang et al., 2005). These model outputs revealed a decline in upwelling and anomalously warm surface waters south of 5°N and enhanced upwelling and anomalously cool surface waters north of 5°N in the EEP as a result of a slowdown in AMOC and a southward shift in the ITCZ. These model outputs are corroborated by proxy evidence suggesting cooler and dryer conditions in the northern EEP during H1 (Benway et al., 2006; ME0005A-43JC, 7°51'N, 83°36'W). Cariaco Basin sediment reflectance data, a proxy for terriginous input and hence precipitation, also suggest a southward shift in the ITCZ during stadials (YD, H1; Deplazes et al., 2013). Additionally, the Cariaco Basin reflectance record illustrates a

more southward position of the ITCZ during the last glacial period relative to today. These latitudinal migrations of the ITCZ about the equator likely differentiate regions of the EEP during periods of rapid climate change due to shifts in the latitudinal extent and strength of upwelling and downwelling regions.

The oxygen isotopic compositions ($\delta^{18}O$) of planktonic foraminifera indicate the depth at which they calcify within the water column. At core site TR163-19, *Neogloboquadrina dutertrei* has been shown to inhabits the deep thermocline, while the $\delta^{18}O$ of *Globigerinoides ruber* indicate that it lives within surface mixed layer (Figure 2; Spero et al., 2003). A third planktonic formaminifera found in the EEP, *Globigerinoides sacculifer*, inhabits the upper thermocline in the waters overlying core TR163-19 (Spero et al., 2003). However, in the coastal upwelling regions off Peru, where core OPD1238 was collected, *G. sacculifer* dwells within the surface mixed layer (Marinez-Boti et al., 2015). The stable isotopic compositions of all three species provide a picture of the water column structure, with *G. sacculifer* and *N. dutertrei* capturing the chemical composition of EUC-imprinted thermocline waters and *G. ruber* recording those of the surface mixed layer at the TR163-19 collection site. Differences between the stable carbon and oxygen isotopic compositions of these species have been used in previous studies to infer changes in thermocline structure and mixed layer depth in the EEP (Spero et al., 2003). Based on the estimated calcification depths of *G. ruber*, *G, sacculifer* and *N. dutertrei* in the EEP, these three species represent a modern surface to thermocline pCO_2 range of 100 to 600 µatm (Figure 2).

4.3 Materials and Methods

4.3.1 Age Model

The original age model for core TR163-19 was established using planktonic foraminiferal oxygen isotope stratigraphy aligned to the SPECMAP stack (Imbrie et al., 1984) and two radiocarbon ages (Lea et al., 2000; 2002; Spero and Lea, 2002). However, the scarcity of oxygen isotope tie points and radiocarbon dates for the upper 150 cm of the core called for further age constraints on this portion of the core. A new age model for the upper 150 cm of the core TR163-19 was developed based on 10 radiocarbon ages of the planktonic foraminifera *Globigerinoides ruber* (Table 1). An additional 11 radiocarbon ages were also obtained for *Neogloboquadrina dutertrei (*Table 1) in order to compare the raw radiocarbon ages of surface-dwelling (*G. ruber*) and thermocline-dwelling (*N. dutertrei*) planktonic foraminifera. Each sample for radiocarbon analysis contained 3-10 mg of monospecific foraminiferal calcite and was measured for at the Keck Carbon Cycle AMS Facility (UC Irvine). Calendar ages were determined using Calib 7.1 and the Marine04 calibration dataset that includes a time-dependent global ocean reservoir correction of about 400 years (Stuvier et al., 2005). A local reservoir age correction (ΔR) of 125 yrs was applied to the raw radiocarbon values as determined from the average ΔR from nearby Galapagos sites ($n = 6$, $1\sigma = 66$). Both the *N. dutertrei* and *G. ruber* age models have strong linear correlation coefficients ($R^2 = 0.99$ and $R^2 = 0.99$, respectively), and exhibit similar slopes (Figure 4). *Neogloboquadrina dutertrei* and *G. ruber* radiocarbon ages from equivalent core depths are offset by an average of 800 yrs for the 35,000-year record, reflecting older ages at thermocline depths relative to surface waters. Ages for all of the core samples were

determined using linear interpolation of the *G. ruber* age model as it is most representative of the atmospheric reservoir age. This age model yields an average sedimentation rate of ~ 5 cm/1,000 years for the last 35,000 years.

4.3.2 Stable Isotopic Measurements

Oxygen ($\delta^{18}O$) and carbon ($\delta^{13}C$) stable isotope measurements were made on *G. ruber* (350-425 μm), *Globigerinoides sacculifer* (425-500 μm) and *N. dutertrei* (500-710 μm). Fifty or more individuals of each species were picked and homogenized for single (*N. dutertrei*), duplicate (*G. ruber*) and triplicate (*G. sacculifer*) analysis on a GV IsoPrime stable isotope ratio mass spectrometer (long-term standard reproducibility is ± 0.06 per mil for $\delta^{13}C$ and 0.07 per mil for $\delta^{18}O$). The average reproducibility of the *G. sacculifer* samples is similar to the long-term standard reproducibly (± 0.05 per mil for $\delta^{13}C$ and 0.08 per mil for $\delta^{18}O$). The isotopic values are reported relative to Vienna Pee Dee Belemnite (VPDB). The $\delta^{18}O$ and $\delta^{13}C$ values have been corrected based on the recommendations of Spero et al. (2003), with $\delta^{18}O$ values normalized to *G. ruber* and $\delta^{13}C$ normalized to the expected $\delta^{13}C$ DIC values from observed species-specific offsets (Table 2).

The boron isotope composition of *G. sacculifer* was used to estimate the pH of the upper thermocline waters throughout the last 35,000 years. Three to eight mg of *G. sacculifer* (> 425 μm) were picked and cleaned following the methods presented in Chapter 3 of this dissertation, as modified from the methods presented in Foster et al. (2008) and Misra et al. (2014). In short, samples were crushed and cleaned for clay contaminants by rinsing in amberlite-filtered Super Q water, prior to an oxidative step to

remove organics, resulting in an average mass loss of 20%. The samples were then dissolved in 75 µl of 2-3M HCl (made with amberlite-filtered Super Q water) prior to boron removal from the carbonate matrix using a modified micro-sublimation technique (Wang et al., 2010; Misra et al., 2014). The sublimated samples were analyzed using a Thermo Finnigan Neptune MC-ICPMS. Standard reproducibility using this method is ± 0.28‰ for boric acid standard NIST SRM 951 ($\delta^{11}B$ = -0.01‰) and ± 0.37‰ for measured carbonate standards (CARO in-house *O. universa* standard, $\delta^{11}B$ = 16.8 ‰; JCT, $\delta^{11}B$ = 16.17‰; and JCP, $\delta^{11}B$ = 24.38‰; Takashi et al., 2004). Samples were measured using sample-standard bracketing and reported relative to NIST NBS 951 using standard delta notation:

$$\delta^{11}B\ (‰) = \left[\left(\frac{^{11}B/^{10}B_{sample}}{^{11}B/^{10}B_{NIST951}}\right) - 1\right] \text{ x } 1000 \qquad (1)$$

4.3.3 Temperature, Salinity and pH Estimations

Down core salinity was estimated using the *G. ruber* Mg/Ca-estimated sea surface temperature (Lea et al., 2002) and $\delta^{18}O$ to calculate surface ocean $\delta^{18}O$ ($\delta^{18}O_{SW}$) using the Bemis et al. (1998) high-light equation:

$$T\ (^{\circ}C) = 14.9 - 4.80\ (\delta_c - \delta_w) \qquad (2)$$

An ice volume correction was applied based on Gaussian interpolation of the benthic foraminiferal isotope sea level reconstructions from Waelbroeck et al. (2002). Finally, sea surface salinity (SSS) was determined using the $\delta^{18}O_{SW}$-salinity relationship for the eastern equatorial Pacific from Benway and Mix (2004):

$$\delta^{18}O_{SW} = 0.25S - 8.52 \quad (3)$$

We used the *G. ruber* Mg/Ca-derived paleo-temperatures reported in Lea et al. (2000). *Globigerinoides sacculifer* and *N. duterei* paleo-temperatures also were estimated using $\delta^{18}O$ calcite measurements and the local $\delta^{18}O_W$ estimated using the salinity- $\delta^{18}O_W$ relationship from Benway and Mix (2004) and salinity measurements at 50 and 100 m depth (Millero et al., 1998) corrected for ice volume changes (Waelbroeck et al., 2002). We estimate calcification temperature for *G. sacculifer* (equation 4) and *N. dutertrei* (equation 5) using the plankton tow calibration equations from Mulitza et al. (2003):

$$T\ (^{\circ}C) = 14.91 - 4.35\ (\delta_c - \delta_w) \quad (4)$$

$$T\ (^{\circ}C) = 14.62 - 4.70\ (\delta_c - \delta_w) \quad (5)$$

Sample $\delta^{11}B$ values were converted to pH using the Sanyal et al. (2001) *G. sacculifer* culture equation fitted to the core top calibration from Foster et al. (2008; Figure 5a). Following the methods of Foster et al. (2012) and Martinez-Boti et al. (2015), the

intercept of the measured $\delta^{11}B$ ($\delta^{11}B_{meas}$ = 18.71‰) and estimated pre-industrial $\delta^{11}B$ borate ($\delta^{11}B_{borate}$ = 17.6‰), estimated from modern surface ocean conditions at 50 m with an adjusted pH value of + 0.1 units (pH = 7.997, T = 19.97°C, S = 34.27, pK^*_B = 8.58, Millero et al., 1998), was adjusted to pass through the core-top value to account for regional variability (Figure 5a). $\delta^{11}B_{meas}$ was then converted into $\delta^{11}B_{borate}$ using the following equation:

$$\delta^{11}B_{borate}\,(‰) = (\delta^{11}B_{meas} - 4.35)/\,0.83 \qquad (6)$$

pH was then determined using:

$$pH = pK^{\cdot}_B - \log\left(\frac{(\delta^{11}B_{SW} - \delta^{11}B_{CaCO_3} - \alpha)}{\delta^{11}B_{SW} - \alpha_B * (\delta^{11}B_{CaCO_3} - \alpha) - 1000 * (\alpha_B - 1)}\right) \qquad (7)$$

where pK^*_B is the stoichiometric equilibrium constant (Dickson, 1990) which is calculated for each sample based on the *G. sacculifer* $\delta^{18}O$-estimated sea surface temperature and estimated salinity, $\delta^{11}B_{SW}$ is the boron isotopic composition of seawater which is equal to 39.65 ± 0.41 ‰ (Foster et al., 2013), and α_B is the isotopic fractionation factor between $B(OH)_4^-$ and $B(OH)_3$ (1.0272; Klochko et al., 2006).

4.3.4 Area Density-[CO_3^{2-}] Reconstructions

Planktonic foraminiferal area density (ρ_A) has recently been shown to be a reliable proxy for carbonate ion concentration ([CO_3^{2-}]) (Marshall et al., 2013). We use the ρ_A of *G. ruber* (s.s.) and *G. sacculifer* (sac-less) to calculate surface-ocean and upper thermocline [CO_3^{2-}], respectively, for our core location using the calibration equation from Marshall et al. (2013). ρ_A is calculated by dividing individual weight measurements by individual silhouette areas (measured using a microscopic imaging program) and taking the sample average (n=40):

$$\rho_A\,(\mu g/\mu m^2) = \text{weight/silhouette area} \qquad (8)$$

For detailed methods see Marshall et al. (2013). As with the $\delta^{11}B$, we adjust the intercept of these equations to pass through the core top measurements (*G. sacculifer* $\rho_A = 1.05 \times 10^{-4}$ µg/µm2, preindustrial [CO_3^{2-}] at 50 m = 160 µmol/kg; *G. ruber* $\rho_A = 1.23 \times 10^{-4}$ $\mu g/\mu m^2$, preindustrial [CO_3^{2-}] at surface = 212 µmol/kg) in order to account for regional differences (Figure 5b). The down core [CO_3^{2-}] records for *G. sacculifer* and *G. ruber* were calculated using the following equations:

$$G.\ sacculifer\ [CO_3^{2-}] = 195.69 \times (\rho_A \times 10^4) - 77.17 \qquad (9)$$

$$G.\ ruber\ [CO_3^{2-}] = 201.66 \times (\rho_A \times 10^4) - 2.20 \qquad (10)$$

$[CO_3^{2-}]$ uncertainty is ± 9.6 µmol/kg based on the standard error of estimate of the calibration equation (Marshall et al., 2013).

4.3.5 pCO_2 CALCULATIONS

Any two carbonate system parameters (pH, total alkalinity (TA), $[CO_3^{2-}]$, pCO_2 etc.) can be used to calculate the remainder of the carbonate system if temperature and salinity are also known (Zeebe and Wolf-Gladrow, 2001). Here, we use the modern local salinity-alkalinity relationship from Millero et al. (1998) to estimate TA:

$$TA_{SAL} = 64.718*S + 38.371 \quad (11)$$

We then calculate pCO_{2aq} using two combinations of carbonate system parameters: (1) TA and pH and (2) $[CO_3^{2-}]$ and pH. Calculations of the carbonate system parameters were made using the CO2Sys v.2.1-2 program (Pierrot et al., 2006) and the constants of Leuker et al. (2000), Dickson et al. (1990), and Lee et al. (2010). For consistency, we use *G. sacculifer* $[CO_3^{2-}]$ and $\delta^{18}O$-derived temperature to pair with the $\delta^{11}B$-derived pH values. It should be noted that the sea surface salinities used to calculate TA and the other carbonate system parameters may be slightly lower (~0.33; Millero et al., 1998) than those at the predicted calcification depth of *G. sacculifer* as these were estimated using the shallower-dwelling *G. ruber* Mg/Ca temperatures and $\delta^{18}O$ measurements. Though salinity and alkalinity have a relatively small influence on the

calculation of the carbonate system parameters, we account for this difference by creating a 1.4 salinity envelope on the TA calculations (Benway and Mix, 2004). All hydrographic and carbonate parameters, stable isotopic measurements, and morphometric measurements can be found in Table 3.

The difference between aqueous pCO_2 and atmospheric pCO_2 ($\Delta pCO_2 = pCO_{2aq} - pCO_{2atm}$) is generally indicative of the flux of CO_2 between the surface oceans and atmosphere (Palmer and Pearson, 2003). Here, we calculate ΔpCO_2 by subtracting interpolated and compiled pCO_{2atm} collected from Antarctic ice cores (Luthi et al., 2008) from the estimated thermocline pCO_{2aq} values for core TR163-19. As these are upper thermocline rather than surface ocean estimations of pCO_2, increases in ΔpCO_2 may not be indicative of the region acting as a source of CO_2 to the atmosphere as the CO_2 could be isolated at depth. However, decreases in ΔpCO_2 represent a loss of CO_2 from thermocline depths. This loss could be attributed to CO_2 evasion to the surface oceans and/or atmosphere, advective transport to other regions, or a decreased supply of CO_2 to thermocline depths.

4.3.6 Upwelling Proxies

We use two independent proxies to reconstruct upwelling intensity in the waters overlying TR163-19 over the last 35,000 years. The difference in $\delta^{18}O$ between *Globigerinoides ruber* and *N. dutertrei* ($\Delta\delta^{18}O_{duter\text{-}ruber}$) serves as a proxy for the upper ocean density gradient or stratification as it reflects the relative depth of the thermocline (Spero et al., 2003; Benway et al., 2006). We compare the $\Delta\delta^{18}O_{duter\text{-}ruber}$ to a record of

%TOC, measured at 5 cm intervals, in order to have a second indicator of surface-ocean mixing. %TOC can be used as a proxy for surface ocean productivity (Pedersen and Calvert, 1990), which generally increases with increased surface ocean mixing and the subsequent upwelling of nutrient-rich waters from deeper depths. %TOC was determined using a Perkins-Elmer 2400 elemental analyzer, following the procedures outlined in Froelich (1980).

4.4 Results

4.4.1 Carbon and Oxygen Isotope Records

The normalized $\delta^{18}O$ and $\delta^{13}C$ records for *G. ruber*, *G. sacculifer* and *N. dutertrei* are shown in Figure 6. The records reveal the expected depth stratification of the three species (Spero et al., 2003), with the surface mixed-layer dwelling *G. ruber* exhibiting the lowest $\delta^{18}O$ and highest $\delta^{13}C$ values, followed by *G. sacculifer* with a deeper, upper thermocline $\delta^{18}O$ and $\delta^{13}C$ signature and the deep thermocline-dwelling *N. dutertrei* exhibiting the highest $\delta^{18}O$ and lowest $\delta^{13}C$ values. All three $\delta^{18}O$ records are marked by an ~1.5‰ decrease between 20 kyr (LGM) and present, reflecting the global ice volume effect (~1.0 ‰; Waelbroeck et al., 2002) and local changes in surface ocean temperatures.

All three species exhibit a range in $\delta^{13}C$ of ~ 0.8‰ throughout the record, though the timing of $\delta^{13}C$ minima differ between the surface dwelling (LGM) and thermocline dwelling species (BA; Figure 6). The trends exhibited by the carbon isotope records of *G. sacculifer* are more similar to those of the thermocline-dweller *N. dutertrei*, rather than

the surface-dweller *G. ruber*, verifying that this species is reflecting the chemical properties of thermocline depths more so than the surface mixed layer. The well-documented deglacial ^{13}C- minima event (Spero et al., 2002; Martinez-Boti et al., 2015) is clearly evident in the *N dutertrei* record, showing a ~ 0.4 ‰ decrease from 21 – 15.5 kyr (Figures 6 and 7). The *G. sacculifer* and *G. ruber* records also exhibit a deglacial decline in $\delta^{13}C$ beginning at 21 kyr, but the $\delta^{13}C$ minimas occur earlier for these species at 18 and 19 kyr, respectively (Figure 6). All three species records show a gradual decline in $\delta^{13}C$ of 0.5 ‰ from 35 kyr – LGM, indicating an increase in respired carbon throughout the water column likely due to enhanced productivity in the surface oceans or the lateral advection of ^{12}C-rich waters during this period. All three $\delta^{13}C$ records show a 0.5 ‰ increase from 14 to 4 kyr (Figure 7). As suggested by Spero et al. (2002), this increase is likely a result of the re-establishment of NADW formation and the advection of nutrient-deplete waters into this region following H1.

4.4.2 Salinity, Temperature and $[CO_3^{2-}]$ Records

Estimates of $\delta^{18}O_{SW}$ generated using *G. ruber* Mg/Ca (Lea et al., 2000) and $\delta^{18}O$ (this study) are consistent with those previously generated for the EEP for the last glacial-interglacial cycle (Benway et al., 2006), with calculated salinity values ranging between 33.6 and 37.8 (Figure 8). The *G. ruber* Mg/Ca temperatures (23 - 27°C Lea et al., 2000) are on average 5°C higher than the *G. sacculifer* $\delta^{18}O$- derived temperatures (18 - 21°C), and are consistent with a surface habitat for *G. ruber* and an upper thermocline habitat for *G. sacculifer* in this region of the EEP (Figure 2). Estimated calcification temperatures

for *N. dutertei* throughout the last 35,000 years are consistent with a deep thermocline calcification environment (13 - 17°C). A 350,000-year Mg/Ca-derived sea surface temperature record derived from TR163-19 *G. ruber* samples exhibits synchronous changes with Antarctic air temperature records (Petit et al., 1999; Lea et al., 2000). *Globigerinoides ruber* records the lowest surface ocean temperatures during the glacial period, likely reflecting a combination of cooler Southern Hemisphere glacial temperatures and enhanced upwelling of cooler subsurface waters at this time (Lea et al., 2000).

G. sacculifer [CO_3^{2-}] values range between 165 and 230 µmol/kg, with an ~ 40 µmol/kg decline in [CO_3^{2-}] from LGM to present (Table 3; Figure 9). Minimas in upper thermocline [CO_3^{2-}] of ~ 180 µmol/kg occur during the glacial period at 34, 31 and 27 kyr and again during the YD. *G. sacculifer* [CO_3^{2-}] values increase by 20 µmol/kg during H1, followed by a rapid 40 µmol/kg decline during the Boeling-Allerod (BA). Upper thermocline [CO_3^{2-}] values increase by 40 µmol/kg following the Younger Dryas (YD) and exhibit a steady decline throughout the Holocene, with the core top recording the lowest [CO_3^{2-}] of 160 µmol/kg.

G. ruber [CO_3^{2-}] ranges from 210 to 272 µmol/kg, with an ~ 50 µmol/kg decline in [CO_3^{2-}] from LGM to present (Figure 10). These records indicate that surface ocean [CO_3^{2-}], as recorded by *G. ruber* ρ_A, remained high throughout the glacial period (mean [CO_3^{2-}] = 260 µmol/kg). Surface ocean [CO_3^{2-}] exhibited a rapid 40 µmol/kg decline from 20 to 18 kyr and maintained low [CO_3^{2-}] concentrations throughout H1 (Figure 10). A rise in surface-ocean [CO_3^{2-}] occurred during the BA, following by a decline during the YD. As with the upper thermocline record, surface ocean [CO_3^{2-}] exhibits a steady

decline throughout the Holocene, reaching minimal values of 210 μmol/kg at ~ 1,500 kyr.

4.4.3 EEP Records $\delta^{11}B$ and pH

Regionally corrected *Globigerinoides sacculifer* $\delta^{11}B$ values vary between 17 and 21 ‰ over the course of the record and trend well with the *G. sacculifer* ρ_A- derived $[CO_3^{2-}]$ record. During the LGM, the TR163-19 $\delta^{11}B$ record is offset by 3.5 ‰ from the $\delta^{11}B$ values derived for the same species at the more southerly EEP location (Marinez-Boti et al., 2015; Figure 9). These two *G. sacculifer* $\delta^{11}B$ EEP records straddle the equator and are therefore in different temperature and salinity regimes. Once pH is derived from the $\delta^{11}B$ records, taking into account down-core temperature and salinity estimations for each core location, the two records show comparable pH values and trends from 16 kyr through the start of the Holocene. The trends exhibited by the two records differ from the LGM through H1, with the more northerly site showing an increase in $\delta^{11}B$ (pH) and the southerly site showing a clear decrease in $\delta^{11}B$ (pH). After 14.1 kyrs, TR163-19 $\delta^{11}B$ begins to decrease through the Holocene. The pH values for TR163-19 for the last 35,000 years range between 7.9 and 8.3. The LGM and core top exhibit no difference in pH value (8.0), with pH shifts as great as 0.3 between the two periods.

4.4.4 Upper Thermocline pCO_2 Reconstructions

pCO_{2aq} reconstructions were performed using *G. sacculifer* $\delta^{11}B$-derived pH paired separately with *G. sacculifer* $[CO_3^{2-}]$ and salinity-based TA_{SAL} reconstructions.

The two pCO_{2aq} records agree within error of one another (with the exception of 27 kyr BP), though pCO_2 estimates are more variable using $[CO_3^{2-}]$ compared to TA_{SAL} (Figure 9; 1σ = 150 vs. 100 ppm). The records for $[CO_3^{2-}]$ and TA_{SAL} covary nicely for much of the record, though the trends diverge during the deglaciation (LGM-YD). The core top pCO_2 value of 470 ppm is comparable to the present day value at 50 m depth at our core location, consistent with the estimated *G. sacculifer* upper thermocline depth habitat (Figure 2). The two pCO_2 records yield an average pCO_{2aq} of 377 ppm from 35 kyr-LGM and 252 ppm from the LGM-present (Figure 9). The ΔpCO_2 (pCO_{2aq} - pCO_{2atm}) suggests that the thermocline in this region of the northern EEP contained an excess supply of CO_2 for the majority of the glacial period (mean ΔpCO_2 = 167 µatm) and lost much of this supply during the deglaciation (mean ΔpCO_2 = 28 µatm).

4.4.5 Thermocline and Surface Age Offsets

Higher age offsets between the surface mixed layer *G. ruber* and thermocline-dwelling species *N. dutertrei* from 30 to 21 kry (1250 ^{14}C years) as compared to the LGM through the Holocene (450 ^{14}C years) suggests the presence of an old, carbon-rich water mass at thermocline depths during the glacial period (Figure 10). Two periods of rapid declines in $\Delta^{14}C_{duter\text{-}ruber}$ of ~ 1000 ^{14}C years occur between 21 and 18 kyr and 13 and 11 kyr, with long periods of stable age offsets between 29 and 23 kyr and 17 and 13 kyr.

4.4.6 The Upwelling History of the EEP

The $\Delta\delta^{18}O_{duter\text{-}ruber}$ for core TR163-19 is smaller during the last glacial as compared to the deglaciation and Holocene, indicating enhanced surface ocean mixing in this region during the last glacial period and more stratified conditions from the onset of deglaciation and through the Holocene (Figure 11). This is consistent with higher average %TOC during the glacial period (0.53%) relative to the deglaciation (0.35%). Interestingly, $\Delta\delta^{18}O_{duter\text{-}ruber}$ and %TOC decline (surface ocean stratification increases) during Heinrich events (H1~15.5-17 kyr, H2~24 kyr and H3~29-30 kyr) and the YD (12.8-11.7 kyr), when a slowdown of the AMOC would have resulted in a southward shift in the ITCZ and associated northeast trade winds (Figure 11; Zhang et al., 2005; Kienast et al., 2006; 2013; Deplazes et al., 2013). Minima in $\Delta\delta^{18}O_{duter\text{-}ruber}$, interpreted as a breakdown in the density gradient and enhanced surface-ocean mixing, occur intermittently during the glacial period (34 kyr, 31 kyr, 28 kyr, 20 kyr) and the Holocene (9 kyr, 4 kyr, 1.5 kyr), but are absent during the deglaciation.

4.5 Discussion

4.5.1 The Mechanisms Behind Upwelling Changes in the EEP

Upwelling in the EEP was strongest during the glacial period, as indicated by the %TOC and $\Delta\delta^{18}O_{duter\text{-}ruber}$ and reduced during the deglaciation (Figure 11). Changes in upwelling intensity appear to be closely linked with shifts in the latitudinal position of the ITCZ (Deplazes et al., 2013), such that increased upwelling occurs when the ITCZ is in a more northerly position during the glacial period and Holocene and increased

stratification occurs when the ITCZ is in its more southerly position during H1 and the YD. A decline in upwelling in this region of the EEP during stadials is consistent with modeling studies that observed a southward shift in the ITCZ and subsequent decline in upwelling south of 5°N in the EEP in response to a shutdown in AMOC (Zhang and Delworth, 2005).

4.5.2 Glacial Respired Carbon Pool at Thermocline Depths in the EEP

The previously documented EEP ^{13}C- minima event (Spero et al., 2002; Martinez-Boti et al., 2015) is evident in the *N. dutertei* record from TR163-19, indicating the influx of respired, light carbon into this region at thermocline depths during the deglaciation. This event is initiated at the same time (21 kyr), though shorter lived in the upper thermocline dwelling *G. sacculifer* and mixed layer dwelling *G. ruber* records (Figures 6 and 7). We speculate that the shorter duration of the ^{13}C- minima event in the *G. ruber* and *G. sacculifer* records is due to a decrease in upwelling at this time (see section 4.3.3 below), which would increase light levels (irradiance) at depth. Spero and DeNiro (1987) and Spero and Williams (1988) illustrate that the $\delta^{13}C$ of foraminiferal calcite can increase as much as 1.7 ‰ when calcifying in high light vs. low light conditions. This is due to increased symbiont activity and an associated increase in the uptake of ^{12}C under high light scenarios. Thus, an increase in light levels associated with an increase in surface ocean stratification likely resulted in higher irradiance values at *G. ruber* and *G. sacculifer* calcification depths and a subsequent increase in foraminiferal $\delta^{13}C$.

In addition to the well-documented deglacial $\delta^{13}C$- minima event, the 35,000-yr record of $\delta^{13}C$ from TR163-19 reveals the occurrence of an earlier $\delta^{13}C$- minima event, of higher magnitude (0.6 ‰ decline), occurring between 34 and 27 kyr (Figure 7). This indicates that respired carbon-rich waters were present at thermocline depths throughout the last 35,000 years in the EEP. The presence of a glacial carbon-rich pool at thermocline depths in the EEP is further supported by the ^{14}C age offsets ($\Delta^{14}C_{duter\text{-}ruber}$) exhibited between *N dutertrei* and *G. ruber* (Figure 10). The source of this older, respired carbon pool at thermocline depths has been explored in earlier studies (Spero et al., 2002; Feldberg and Mix, 2003; Sarmiento et al., 2004; Dubois et al., 2011; Martinez-Boti et al., 2015). These studies indicate the ocean tunneling mechanism for the advection of CO_2 and nutrient-rich waters from the Southern Ocean at thermocline depths in the EEP via the EUC. In addition to the influx of respired carbon from the Southern Ocean, stronger upwelling in our region during the glacial period may have contributed to the earlier glacial $\delta^{13}C$- minima event, as increased upwelling would have increased productivity in the surface oceans and the amount of light carbon transported to thermocline depths (Figure 11). The decline in upwelling during the deglaciation indicates that the most likely source of light carbon at this time was from the advection of Southern Ocean waters via the ocean tunneling mechanism.

As stated earlier, the stable isotopic compositions and core top calculated calcification temperatures and pCO_2 concentrations for *G. sacculifer* indicate that this species is capturing the chemical composition of the upper thermocline (EUC) waters at the TR163-19 core location (Figure 2). The *G. sacculifer* pCO_{2aq} record indicates the presence of CO_2-rich waters in the upper thermocline throughout most of the glacial

period (Figure 7). Though the Δ pCO_2 record would normally suggest that this region in the EEP served as a source of CO_2 to the atmosphere during the glacial period, the Δ pCO_2 record presented in this study represents differences in CO_2 concentrations between thermocline waters and the atmosphere. Thus, peaks in thermocline Δ pCO_2 does not necessarily imply that this region was a source of CO_2 to the atmosphere, as high CO_2 waters may be restricted to thermocline depths. Rather, a decline in thermocline Δ pCO_2 could indicate a decline in the supply of CO_2 to the thermocline via the EUC influx or subsidence, declining productivity or a loss of CO_2 to the surface-ocean and atmosphere. For example, the concurrent surface-dwelling *G. ruber* [CO_3^{2-}] record shows only mild variation during periods of peak glacial thermocline Δ pCO_2 (Figure 10). This indicates that high glacial CO_2 concentrated waters were restricted to thermocline depths, regardless of increased upwelling intensity at this time.

4.5.3 Time of EEP Thermocline CO_2 Ventilation

The timing of thermocline CO_2 ventilation events in the EEP as recorded by TR163-19 $\Delta^{14}C_{duter\text{-}ruber}$ covary nicely with existing ventilation records from the Southern Ocean (core MD07-3076) and with the periods of rising atmospheric CO_2 concentrations as recorded in Antarctic ice cores (Figure 10; Skinner et al., 2010; Luthi et al., 2008). Though the low resolution of this record limits our interpretation of short-term key ventilations events, sometime between 21 and 18.3 kyr old, respired carbon was released from thermocline depths into the surface ocean and atmosphere. This was followed by little change in $\Delta^{14}C_{duter\text{-}ruber}$ from 18 to 13 kyr and a rapid decrease in age difference

during the YD, coincident with the second period of rapidly rising atmospheric CO_2 concentrations in the atmosphere (Figure 10). During these two key periods of CO_2 ventilation, both upper thermocline $\Delta\, pCO_2$ and surface-ocean (*G. ruber*) $[CO_3^{2-}]$ decline, indicating a transfer of CO_2 from the thermocline to the surface oceans (Figure 10). Thus, the timings of both thermocline ventilation events are coincident with the two periods of rapid CO_2 rise in the atmosphere during H1 and the YD.

The near-perfect anti-correlation between the upper thermocline $\Delta\, pCO_2$ record from the EEP and the Southern Ocean deep Atlantic reservoir ages indicates a tight coupling of CO_2 ventilation changes between the two regions. As pointed out by Martinez-Boti et al. (2015), though the Skinner et al. (2010) Southern Ocean ventilation record strongly indicate the Southern Ocean as a dominant contributor to CO_2 evasion to the atmosphere during the H1, little change in Southern Ocean ventilation is observed during the second rapid rise in atmospheric CO_2 that occurs during the YD. The $\Delta^{14}C_{duter\text{-}ruber}$ and $\Delta\, pCO_2$ records presented here further implicate the EEP as a dominant contributor to the atmospheric rise in CO_2 during the YD.

4.5.4 Mechanisms and Regions of CO_2 Evasion in the EEP

Though upwelling intensity does appears to have some control on the supply of high pCO_2 waters to the upper thermocline (Figure 11), it is not appear to be a dominant control on CO_2 evasion to the atmosphere in this region during the glacial period as surface ocean $[CO_3^{2-}]$ remains relatively constants throughout the glacial period when thermocline ΔpCO_2 was highest (Figure 10). Regardless of increased stratification

during the deglaciation, we observe a loss of CO_2 from thermocline depths in the EEP. The synchronous decline in surface-ocean [CO_3^{2-}] as $\Delta\, pCO_2$ and $\Delta^{14}C_{duter\text{-}ruber}$ decrease indicates the transfer of CO_2 from thermocline depths to the surface ocean from the LGM through 15.5 kyr and during the YD. Further, the occurrence of these thermocline ventilation events at the time of atmospheric CO_2 rise as recorded in Antarctic ice cores indicates the transfer of EEP thermocline CO_2 to the atmosphere (Figure 10). However, the decline in upwelling in this region of the EEP at this time indicates that another mechanism is responsible for the transfer of CO_2 from the thermocline waters to the surface ocean and atmosphere (Figure 11).

As previously discussed (Section 4.2.2), EUC waters are currently upwelled at the Galapagos Islands (1-2°N, 90-92°W) and along the Peru coastline, where core ODP1238 was collected. In contrast with the upper thermocline habitat of *G. sacculifer* collected from the TR163-19 collection site, *G. sacculifer* collected from the Peru coastal upwelling region exhibit $\delta^{13}C$ and $\delta^{18}O$ comparable to those recorded in *G. ruber*, indicating that *G. sacculifer* is calcifying in the surface mixed layer at this location (Martinez-Boti et al., 2015). The decline in thermocline $\Delta\, pCO_2$ as recorded from *G. sacculifer* collected from TR163-19 is coincident with a simultaneous rise in surface ocean $\Delta\, pCO_2$ as recorded from *G. sacculifer* collected from ODP1238 during the early deglaciation (Figure 10). This indicated that EUC transferred CO_2-rich waters from the Southern Ocean eastward into the thermocline waters of the EEP and the upwelling regions off the coast of Peru, contributing to atmospheric CO_2 rise. Near surface currents could have acted to transfer the upwelled, high CO_2 waters westward from the Peru coast back to the surface waters around the Galapagos Islands (Kessler, 2006). This, in

addition to equilibration with rising atmospheric CO_2 concentrations, would explain the decline in surface-ocean [CO_3^{2-}] at the TR163-19 ore site during the deglacial period.

4.6 Conclusions

The results of this study illustrate that the thermocline waters of the EEP were bathed in CO_2 - rich waters during the last glacial period (mean ΔpCO_2 = 167 ppm), and that much of this CO_2 was lost to the surface oceans and atmosphere during the deglaciation and Holocene (mean ΔpCO_2 = 28 ppm). Thermocline pCO_{2aq} in this region began to rise again at the onset of the Holocene to modern values of ~ 450 ppm (mean $\Delta pCO_2 \approx$ 190 ppm). We rule out upwelling as the mechanism behind this transfer as two independent upwelling proxies ($\Delta\delta^{18}O_{duter\text{-}ruber}$ and %TOC) indicate an increase in surface ocean stratification in the EEP during the deglaciation. Rather, we conclude that the ocean tunneling mechanism transferred CO_2 – rich waters from the Southern Ocean into the EEP via the Equatorial Undercurrent during H1 and the YD. These waters were upwelling off the coast of Peru and likely eastward of our core location in the EEP. This study provides the first carbonate system evidence for the transfer of CO_2 from EEP thermocline waters to the atmosphere during the two periods of rapidly rising CO_2 concentrations in the atmosphere.

Table 4.1 Raw and corrected radiocarbon ages for *G. ruber* and *N. dutertrei.* Calendar ages were corrected by a ΔR of 125 yrs.

Core Depth m	Fraction Modern	±	$D^{14}C$ (‰)	±	^{14}C age (BP)	±	Lower calendar age (BP)	Med calendar (BP)	Upper calendar age (BP)
					G. ruber				
0	0.7639	0.0024	-236.1	2.4	2165	30	1554	1608	1655
35	0.2928	0.0007	-707.2	0.7	9865	20	10591	10640	10679
45	0.2417	0.0007	-758.3	0.7	11405	25	12684	12744	12791
65	0.1430	0.0007	-857.0	0.7	15620	45	18267	18343	18433
80	0.1049	0.0006	-895.1	0.6	18115	50	21129	21254	21374
85	0.0909	0.0006	-909.1	0.6	19270	60	22476	22584	22666
95	0.0678	0.0007	-932.2	0.7	21620	90	25318	25441	25570
115	0.0409	0.0008	-959.1	0.8	25670	150	28979	29180	29376
125	0.0346	0.0005	-965.4	0.5	27020	120	30669	30783	30906
130	0.0293	0.0007	-970.7	0.7	28360	210	31317	31576	31773
					N. dutertrei				
0	0.7097	0.0024	-290.3	2.4	2755	30	2282	2317	2350
35	0.2999	0.0010	-700.1	1.0	9675	30	10363	10418	10489
45	0.2205	0.0009	-779.5	0.9	12145	35	13395	13456	13510
65	0.1316	0.0009	-868.4	0.9	16290	60	18909	19003	19077
80	0.0857	0.0009	-914.3	0.9	19740	90	22985	23148	23302
85	0.0811	0.0010	-918.9	1.0	20180	110	23521	23675	23836
95	0.0603	0.0008	-939.7	0.8	22560	110	26079	26234	26367
115	0.0365	0.0007	-963.5	0.7	26590	170	30126	30352	30661
125	0.0275	0.0008	-972.5	0.8	28860	250	31793	32228	32627
130	0.0293	0.0007	-970.7	0.7	28360	210	31317	31576	31773

Table 4.2 Carbon and oxygen stable isotopic values for TR163-19.

Core Depth (cm)	Age (kyr)	$\delta^{18}O$ *G. ruber* (‰)	$\delta^{18}O$ *G. sacculifer* (‰)	$\delta^{18}O$ *G. sacculifer* norm. (‰)[a]	$\delta^{18}O$ *N. dutertrei* (‰)	$\delta^{18}O$ *N. dutertrei* norm. (‰)[a]	$\delta^{13}C$ *G. ruber* (‰)	$\delta^{13}C$ *G. ruber* corr. (‰)[b]	$\delta^{13}C$ *G. sacculifer* (‰)	$\delta^{13}C$ *G. sacculifer* corr. (‰)[b]	$\delta^{13}C$ *N. dutertrei* (‰)	$\delta^{13}C$ *N. dutertrei* corr. (‰)[b]	$\Delta\delta^{18}O_{duter\text{-}ruber}$ (‰)
1	1608	-2.1	-1.2	-1.0	-0.3	0.3	1.8	2.7	1.7	1.8	2.0	1.5	1.8
5	2898	-2.2	-1.2	-1.0	0.1	0.7	1.8	2.8	1.9	2.0	2.0	1.5	2.3
10	4189	-1.9	-1.3	-1.1	-0.1	0.5	1.8	2.7	2.0	2.1	2.1	1.6	1.8
15	5479	-2.0	-1.1	-0.9	0.1	0.7	1.9	2.8	1.8	2.0	1.8	1.3	2.1
20	6769	-2.0	-0.7	-0.5	0.1	0.7	1.8	2.7	1.4	1.6	1.9	1.4	2.1
25	8060	-1.7	-0.6	-0.4	0.2	0.8	1.7	2.6	1.5	1.6	1.8	1.3	1.9
30	9350	-1.5	-0.6	-0.4	0.2	0.8	1.4	2.4	1.4	1.6	1.9	1.4	1.7
35	10640	-1.7	-0.7	-0.5	0.2	0.8	1.4	2.4	1.4	1.5	1.7	1.2	1.9
40	11692	-1.5	-0.3	-0.1	0.8	1.4	1.3	2.2	1.4	1.5	1.7	1.2	2.3
45	12744	-1.1	-0.4	-0.2	0.8	1.5	1.3	2.2	1.5	1.6	1.6	1.1	1.9
50	14144	-1.2	-0.1	0.1	0.9	1.5	1.3	2.2	1.2	1.4	1.6	1.1	2.1
55	15544	-1.0	0.1	0.3	1.0	1.6	1.3	2.3	1.6	1.8	1.6	1.1	2.0
60	16943	-0.9	0.0	0.2	1.2	1.8	1.2	2.1	1.4	1.5	1.8	1.3	2.1
65	18343	-0.5	0.4	0.6	1.4	2.0	1.1	2.1	1.3	1.4	1.7	1.2	1.8
70	19314	-0.5	0.1	0.3	1.5	2.1	1.0	2.0	1.5	1.6	1.7	1.2	1.9
75	20284	-0.3	0.2	0.4	1.4	2.0	1.2	2.1	1.5	1.6	1.8	1.3	1.7
80	21254	-0.6	0.2	0.4	1.2	1.8	1.2	2.2	1.7	1.8	2.0	1.5	1.8
85	22584	-0.8	0.1	0.3	1.2	1.8	1.1	2.0	1.5	1.6	1.9	1.4	1.9
90	24013	-0.7	-0.1	0.1	1.5	2.2	1.3	2.3	1.8	1.9	1.9	1.4	2.2
95	25441	-0.5	-0.1	0.1	1.1	1.7	1.3	2.2	1.6	1.7	1.9	1.4	1.6
100	26376	-0.5	0.1	0.2	1.1	1.7	1.2	2.2	1.7	1.8	1.8	1.3	1.6
105	27311	-0.9	0.0	0.2	0.8	1.4	1.1	2.0	1.7	1.9	1.8	1.3	1.6
110	28245	-0.5	0.0	0.2	0.9	1.5	1.3	2.3	2.0	2.1	1.9	1.4	1.4
115	29180	-0.7	-0.1	0.1	0.9	1.5	1.3	2.2	1.5	1.6	1.8	1.3	1.7
120	29982	-0.9	-0.4	-0.2	0.6	1.2	1.5	2.4	1.6	1.8	2.0	1.5	1.5
125	30783	-0.8	-0.2	0.0	0.3	0.9	1.4	2.3	1.7	1.8	2.1	1.6	1.1
130	31576	-0.8	-0.2	0.0	0.7	1.3	1.6	2.5	1.8	1.9	1.9	1.4	1.5
135	32369	-0.9	-0.5	-0.3	0.9	1.5	1.6	2.5	1.9	2.0	2.1	1.6	1.8
140	33162	-1.1	-0.3	-0.1	0.6	1.2	1.4	2.3	1.7	1.8	2.2	1.7	1.6
145	33955	-1.1	-0.4	-0.2	0.3	0.9	1.4	2.4	1.7	1.8	2.3	1.8	1.4
150	34748	-0.9	-0.3	-0.1	0.6	1.2	1.3	2.3	1.7	1.8	1.9	1.4	1.5

Table 4.3 Down core data for TR163-19.

Core Depth (cm)	Age (kyr)	ρ_A *G. sacculifer* (µg/µm²)	$[CO_3^{2-}]$ *G. sacculifer* (µmol/kg)	ρ_A *G. ruber* (µg/µm²)	$[CO_3^{2-}]$ *G. ruber* (µmol/kg)	%TOC	SST (°C) *G.ruber*	SST(°C) *G. sacculifer*	SST(°C) *N. dutertrei*	Salinity (psu)	TA_{SAL} ((µmol/kg)	$\delta^{11}B$ *G. sacculifer* (‰)	pH	Low pCO_{2aq} *G. sacculifer* $[CO_3^{2-}]$ and pH	Mid pCO_{2aq} *G. sacculifer* $[CO_3^{2-}]$ and pH	High pCO_{2aq} *G. sacculifer* $[CO_3^{2-}]$ and pH	Low pCO_{2aq} *G. sacculifer* TA_{SAL} and pH	Mid pCO_{2aq} *G. sacculifer* TA_{SAL} and pH	High pCO_{2aq} *G. sacculifer* TA_{SAL} and pH	ΔpCO_{2aq} *G. sacculifer* $[CO_3^{2-}]$ and pH	ΔpCO_{2aq} *G. sacculifer* TA_{SAL} and pH
1	1608	1.23E-04	189	1.06E-04	211	0.53	26.0	21.1	16.8	34.6	2278.6	17.3	8.0	371	463	579	414	475	546	183	195
5	2898	1.38E-04	218	1.06E-04	211	0.38	25.5	20.8	15.1	33.8	2224.4	18.8	8.1	254	306	369	283	321	365	42	45
10	4189	1.31E-04	206	1.14E-04	228	0.52	26.4	21.4	16.2	35.8	2352.4										
15	5479	1.48E-04	238	1.15E-04	229	0.52	26.1	20.4	15.1	35.2	2316.3	18.4	8.1	313	377	456	319	362	412	102	96
20	6769	1.35E-04	213	1.16E-04	231	0.38	26.2	18.9	15.0	35.2	2319.7										
25	8060	1.52E-04	245	1.28E-04	255	0.63	26.3	18.5	14.9	36.2	2382.3										
30	9350	1.55E-04	251	1.27E-04	255	0.26	27.1	18.5	14.8	37.9	2488.5	20.1	8.2	180	212	250	231	259	291	-81	-5
35	10640	1.46E-04	234	1.14E-04	227	0.26	25.9	19.3	15.1	35.7	2351.1										
40	11692	1.31E-04	206	1.23E-04	246	0.27	25.4	18.1	13.1	35.3	2321.3										
45	12744	1.33E-04	209	1.22E-04	245	0.37	25.5	19.5	13.7	36.4	2394.5	18.6	8.1	244	295	357	309	349	396	62	115
50	14144	1.45E-04	233	1.26E-04	252	0.36	25.2	18.9	14.4	35.0	2304.3	21.2	8.3	123	144	169	170	192	215	-77	-47
55	15544	1.52E-04	245	1.12E-04	223	0.41	25.0	18.7	14.4	35.2	2314.3	20.0	8.2	194	229	271	221	249	280	24	10
60	16943	1.43E-04	229	1.16E-04	231	0.52	24.5	19.1	13.7	35.1	2308.4	21.1	8.3	125	147	172	176	198	222	-70	-41
65	18343	1.40E-04	224	1.09E-04	217	0.54	24.5	17.9	13.2	36.5	2402.6	20.3	8.2	155	183	217	212	238	268	-40	0
70	19314	1.45E-04	232	1.24E-04	249	0.63	23.1	19.2	12.8	35.1	2312.9	19.9	8.2	185	220	261	226	255	287	21	16
75	20284	1.44E-04	231	1.30E-04	260	0.63	23.3	19.0	13.2	35.9	2364.1	17.5	8.0	443	542	667	400	457	522	377	218
80	21254	1.50E-04	242	1.31E-04	261	0.53	23.8	18.8	14.1	35.2	2316.7	19.0	8.1	275	329	393	279	316	357	150	77
85	22584	1.48E-04	239	1.26E-04	253	0.64	23.0	19.0	14.3	33.8	2224.4	18.7	8.1	311	373	449	287	326	370	237	88
90	24013	1.45E-04	232	1.31E-04	262	0.56	23.7	20.0	12.4	34.8	2291.8	20.2	8.2	162	191	227	209	235	265	-11	-3
95	25441	1.51E-04	244	1.27E-04	254	0.60	23.6	19.9	14.2	35.7	2347.0										
100	26376	1.46E-04	235	1.27E-04	253	0.53	23.7	18.9	14.1	36.1	2371.8										
105	27311	1.36E-04	215	1.28E-04	256	0.52	22.6	19.3	15.6	33.6	2215.9	18.4	8.3	302	365	444	192	201	210	217	-38
110	28245	1.45E-04	232	1.32E-04	264	0.87	23.6	19.0	14.6	36.3	2388.6										
115	29180	1.46E-04	235	1.30E-04	260	0.68	23.0	18.9	14.0	35.1	2312.3	17.9	8.0	410	499	609	363	414	472	314	175
120	29982	1.42E-04	228	1.30E-04	261	0.53	22.8	20.0	15.5	34.3	2255.2										
125	30783	1.32E-04	208	1.35E-04	271	0.44	23.3	19.3	16.8	35.4	2331.5	18.2	8.1	303	369	451	338	384	437	160	146
130	31576	1.58E-04	257	1.33E-04	265	0.41	24.7	19.1	14.9	36.3	2387.4	19.7	8.2	214	252	299	240	271	305	22	32
135	32369	1.47E-04	236	1.27E-04	254	0.36	24.5	20.3	13.9	36.0	2370.2										
140	33162	1.50E-04	242	1.25E-04	250	0.38	23.8	19.6	15.4	34.7	2286.9										
145	33955	1.33E-04	209	1.36E-04	272	0.40	24.3	20.0	16.7	35.1	2308.0	16.7	7.9	558	700	885	487	562	649	528	323
150	34748	1.45E-04	233	1.21E-04	242	0.36	23.8	19.6	15.4	35.5	2334.6										

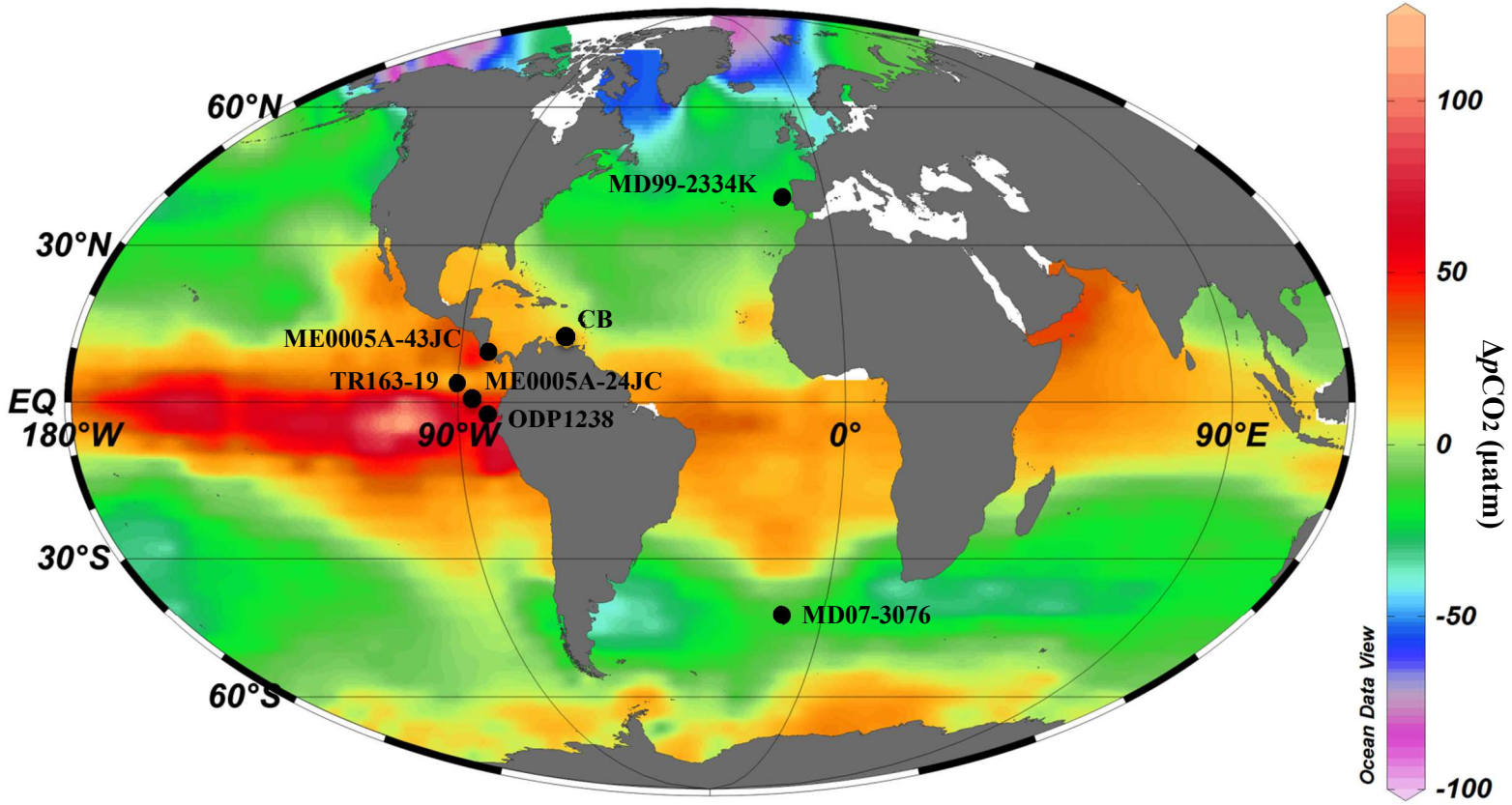

Figure 4.1 Core locations overlain on a mean annual ΔpCO_2 map created using Global Ocean Surface Water Pressure of CO2 database and Ocean Data View (Takahashi et al., 2013).

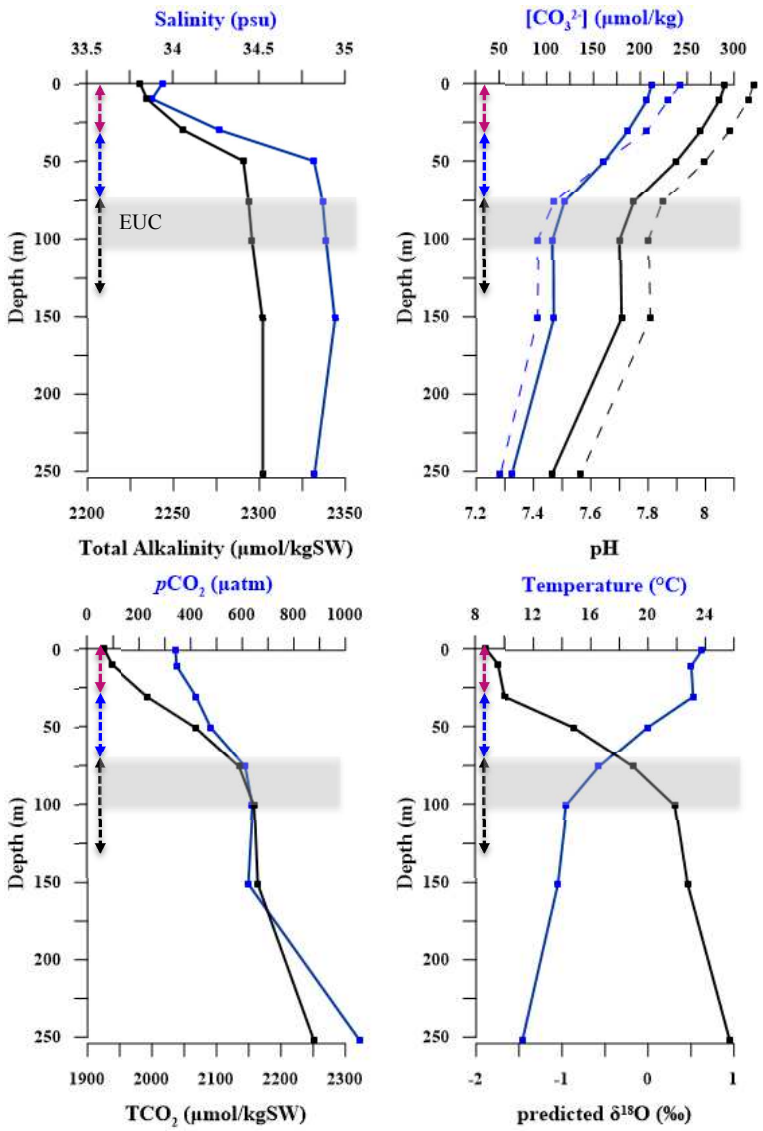

Figure 4.2 Surface ocean properties for the upper 250 m collected from station 8 (1°N, 92°W) during the IRONEX cruises (Millero et al., 1998; collected November, 1993). Dashed pink, blue and black arrows mark the depth habitats of *G. ruber*, *G.sacculifer* and *N. dutertrei*, respectively. A thick, grey band marks the approximate depth of the EUC at TR163-19. Predicted $\delta^{18}O$ was derived using temperature and salinity measurements, the salinity-$\delta^{18}O_w$ equation from Benway and Mix (2006) and the HL equation from Bemis et al. (1998). pCO_2 and $[CO_3^{2-}]$ were derived using TA and pH measurements.

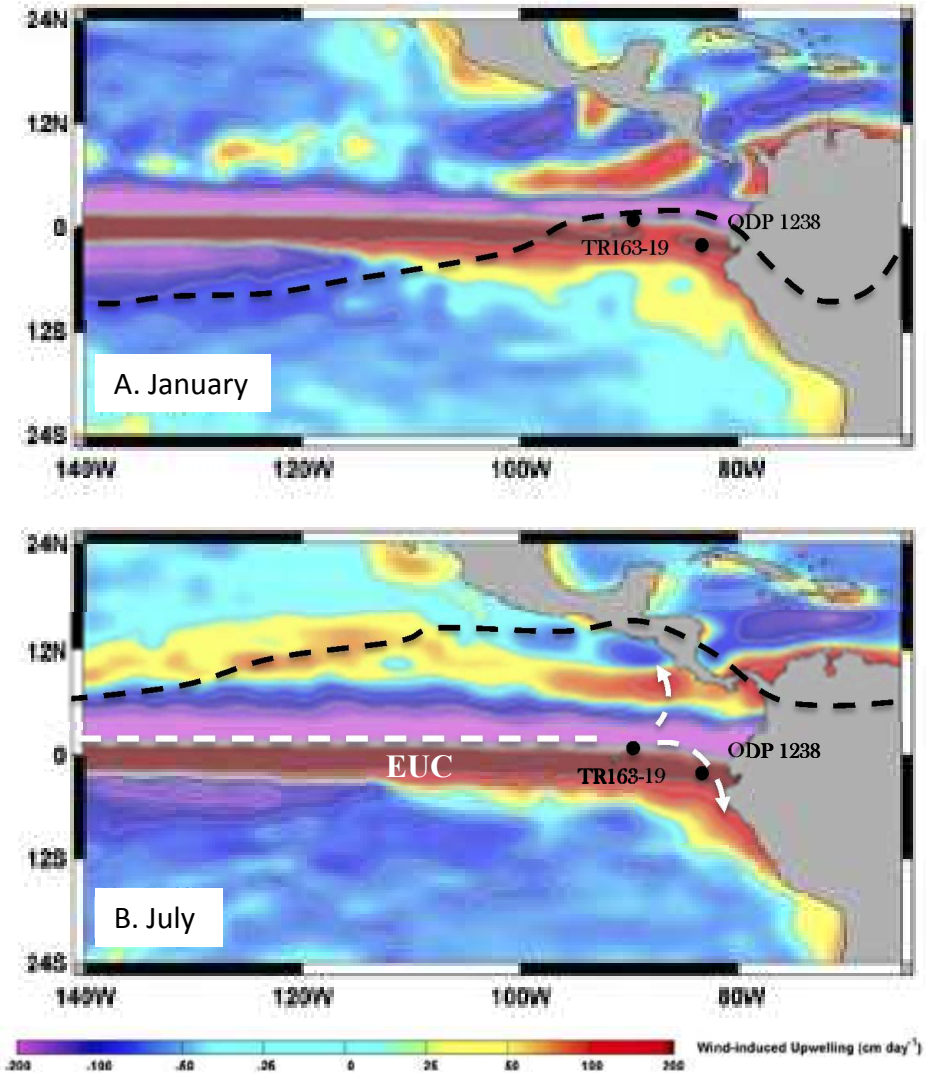

Figure 4.3 Map of the EEP illustrating the seasonal distribution of regions of upwelling and downwelling (Modified from Pennington, 2006). The approximate latitudinal location of the ITCZ in the EEP are shown for January and July (black dashed line). The location and branches of the EUC are shown by the white dashed line. Also shown are the locations of cores TR163-19 and ODP1238.

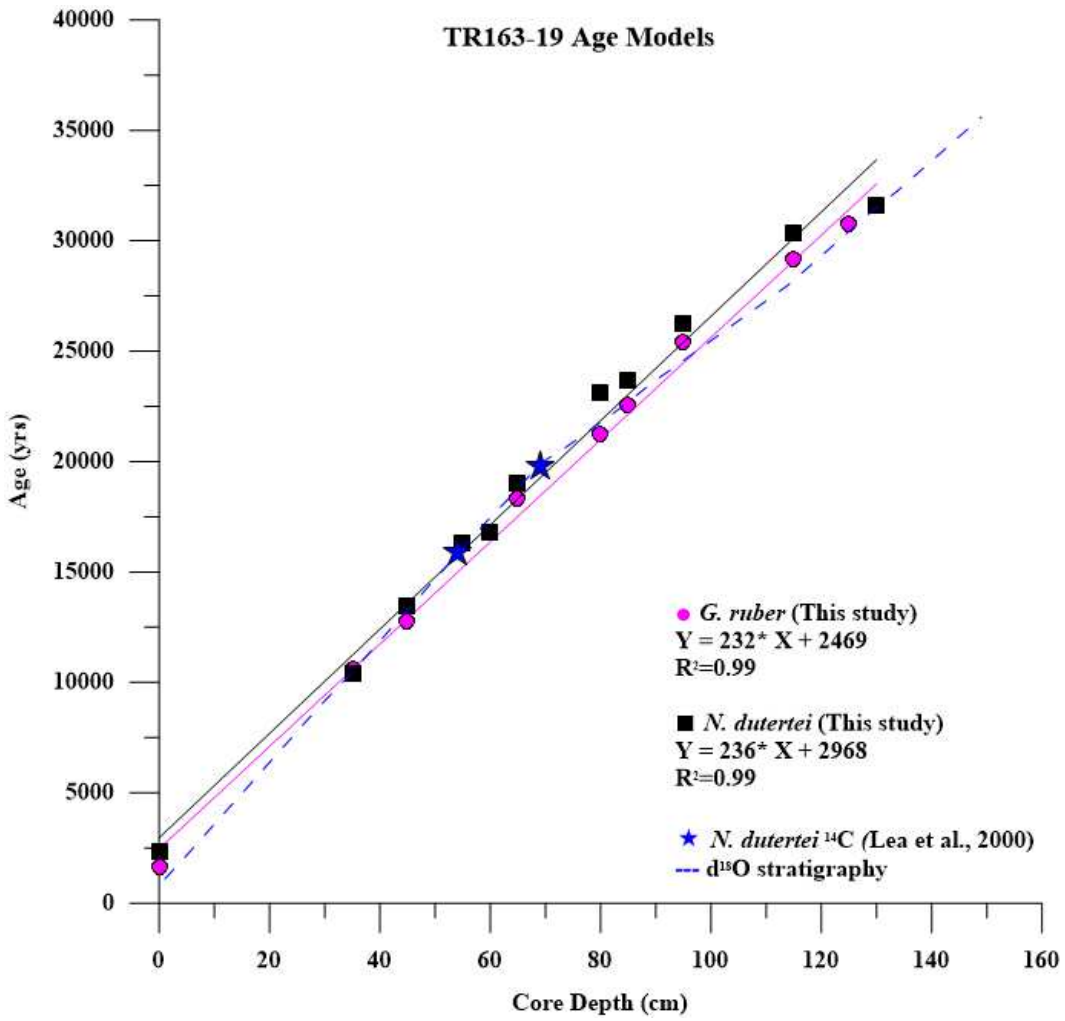

Figure 4.4 Age models for core TR163-19. Black squares and pink circles are the corrected ^{14}C ages for *N. dutertrei* and *G. ruber*, respectively. *N. dutertrei* ^{14}C ages are older than *G. ruber* ages by an average of 800 years. The dashed blue line is the original $\delta^{18}O$ SPECMAP age model for TR163-19 (Lea et al., 2002), with the two *N. dutertrei* ^{14}C ages, which fit well with the *N. dutertrei* ^{14}C age model from this study.

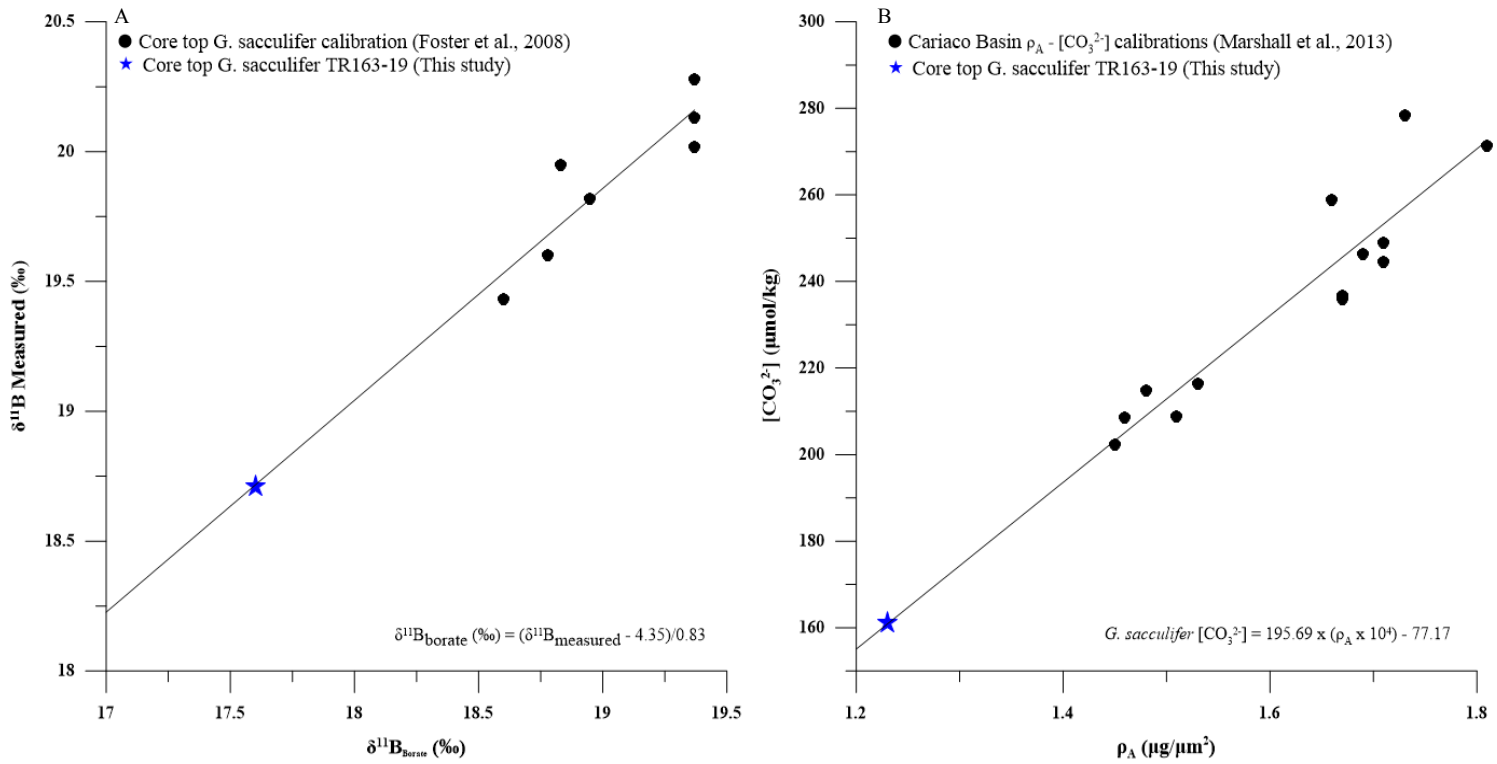

Figure 4.5 $\delta^{11}B_{measured}$-$\delta^{11}B_{Borate}$ (Sanyal et al., 2001) and ρ_A-$[CO_3^{2-}]$ (Marshall et al., 2013) calibrations fit to our core top values.

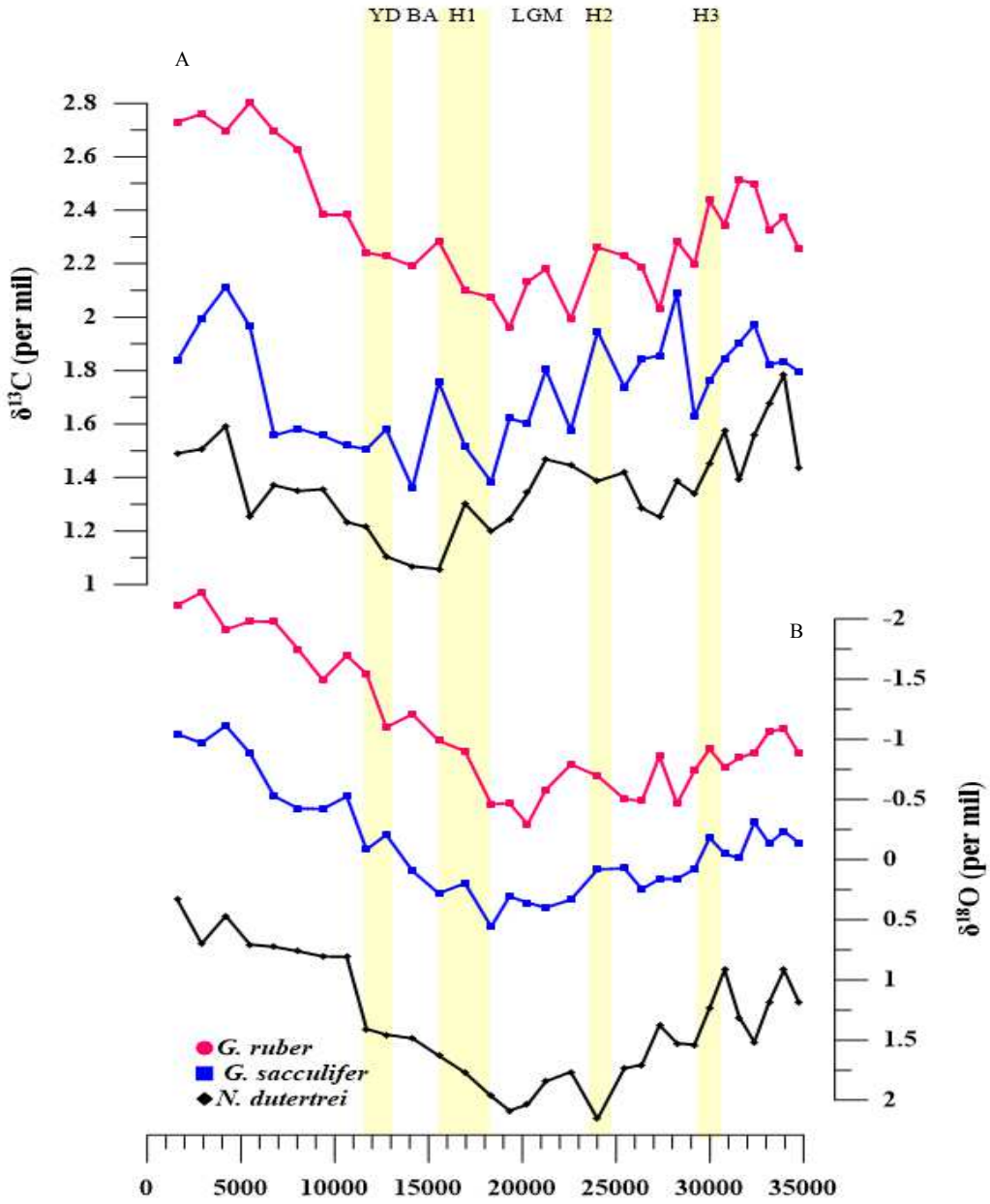

Figure 4.6 (a) DIC -corrected $\delta^{13}C$ records for *G. ruber* (pink), *G. sacculifer* (blue) and *N. dutertrei* (black). (b) *G. ruber* normalized $\delta^{18}O$ records for *G. ruber* (pink), *G. sacculifer* (blue) and *N. dutertrei* (black).

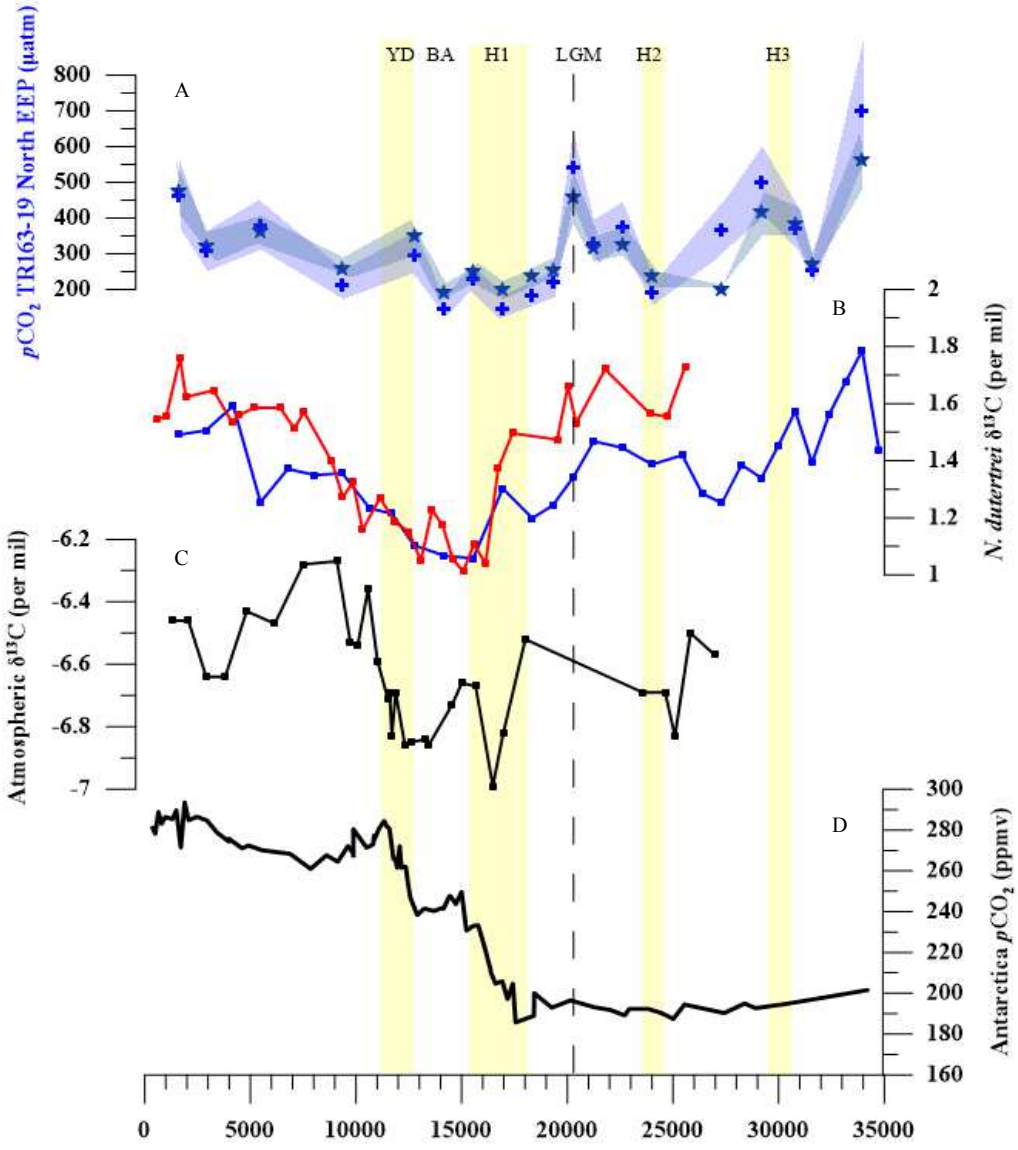

Figure 4.7 (a) Calculated pCO_{2aq} for core TR163-19 using $[CO_3^{2-}]$ and pH (electric blue) and TA_{SAL} and pH (navy blue). (b) DIC -corrected $\delta^{13}C$ records *N. dutertrei* from core TR163-19 (blue) and ODP1238 (red). (c) Record of Antarctic $\delta^{13}C$ of CO_2 from Schmidtt et al. (2012). (d) Record of compiled Antarctic ice core CO_2 concentrations from Luthi et al. (2008).

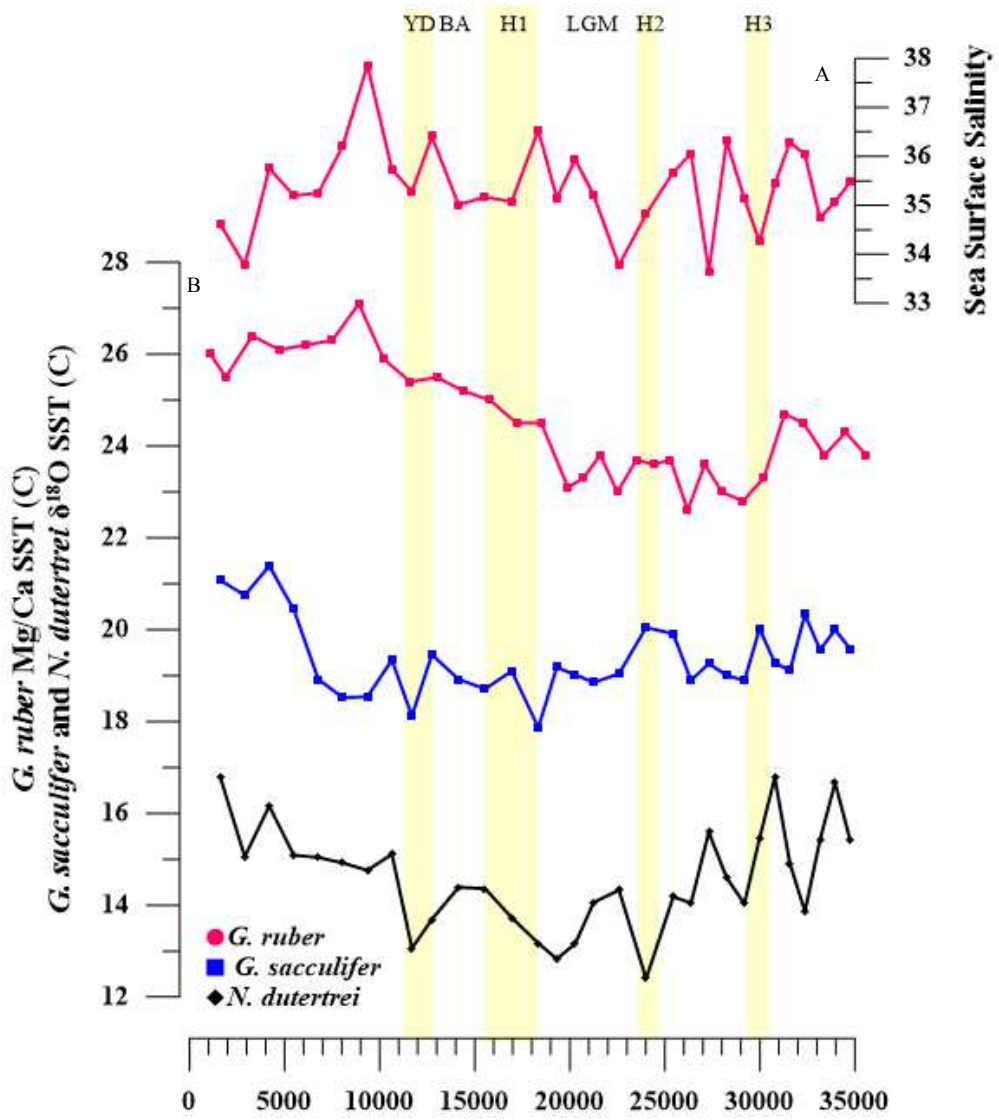

Figure 4.8 (a) TR163-19 salinity record calculated using G. ruber Mg/Ca Temperature (Lea et al., 2002) and $\delta^{18}O$ with the salinity- $\delta^{18}O_w$ relationship from Benway and Mix (2006). (b) Reconstructed paleotemperatures for *G. ruber* (pink, Mg/Ca, Lea et al., 2002), *G. sacculifer* ($\delta^{18}O$; blue), and *N. duterrei* ($\delta^{18}O$; black).

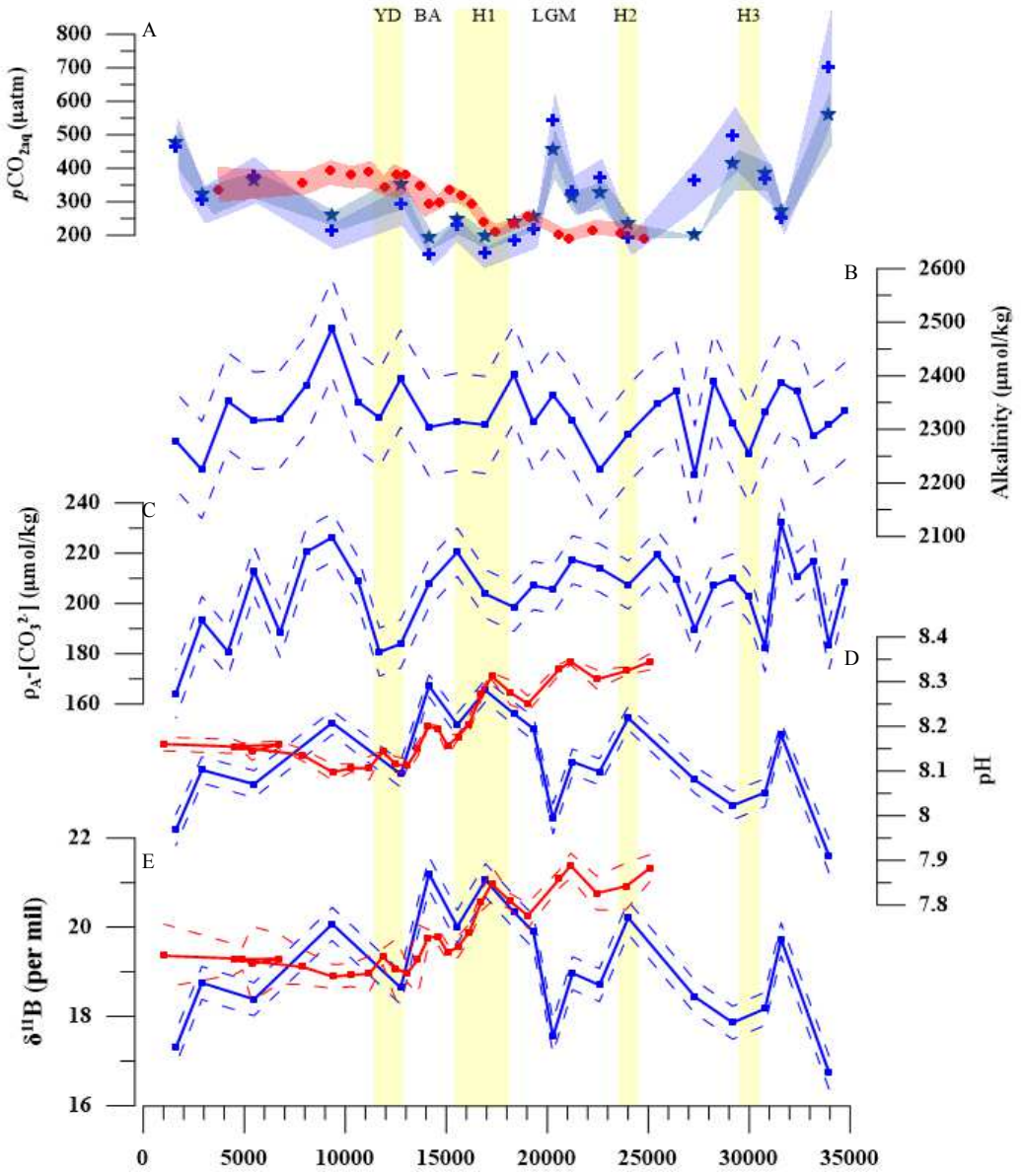

Figure 4.9 (a) Calculated pCO_{2aq} for core TR163-19 using $[CO_3^{2-}]$ and pH (electric blue) and TA_{SAL} and pH (navy blue; this study). Also shown is the pCO_{2aq} record from ODP site 1238 (red; 1°87'S, 82°78'W; Marinez-Boti et al., 2015). (b) Salinity-derived total alkalinity for core TR163-19 (c) TR163-19 *G. sacculifer* ρ_A- derived $[CO_3^{2-}]$. (d) *G. sacculifer* $\delta^{11}B$-derived pH for core TR163-19 (blue; this study)) and ODP site 1238 (red; Marinez-Boti et al., 2015). (e) *G. sacculifer* $\delta^{11}B$ for core TR163-19 (this study) and ODP site 1238 (Marinez-Boti et al., 2015).

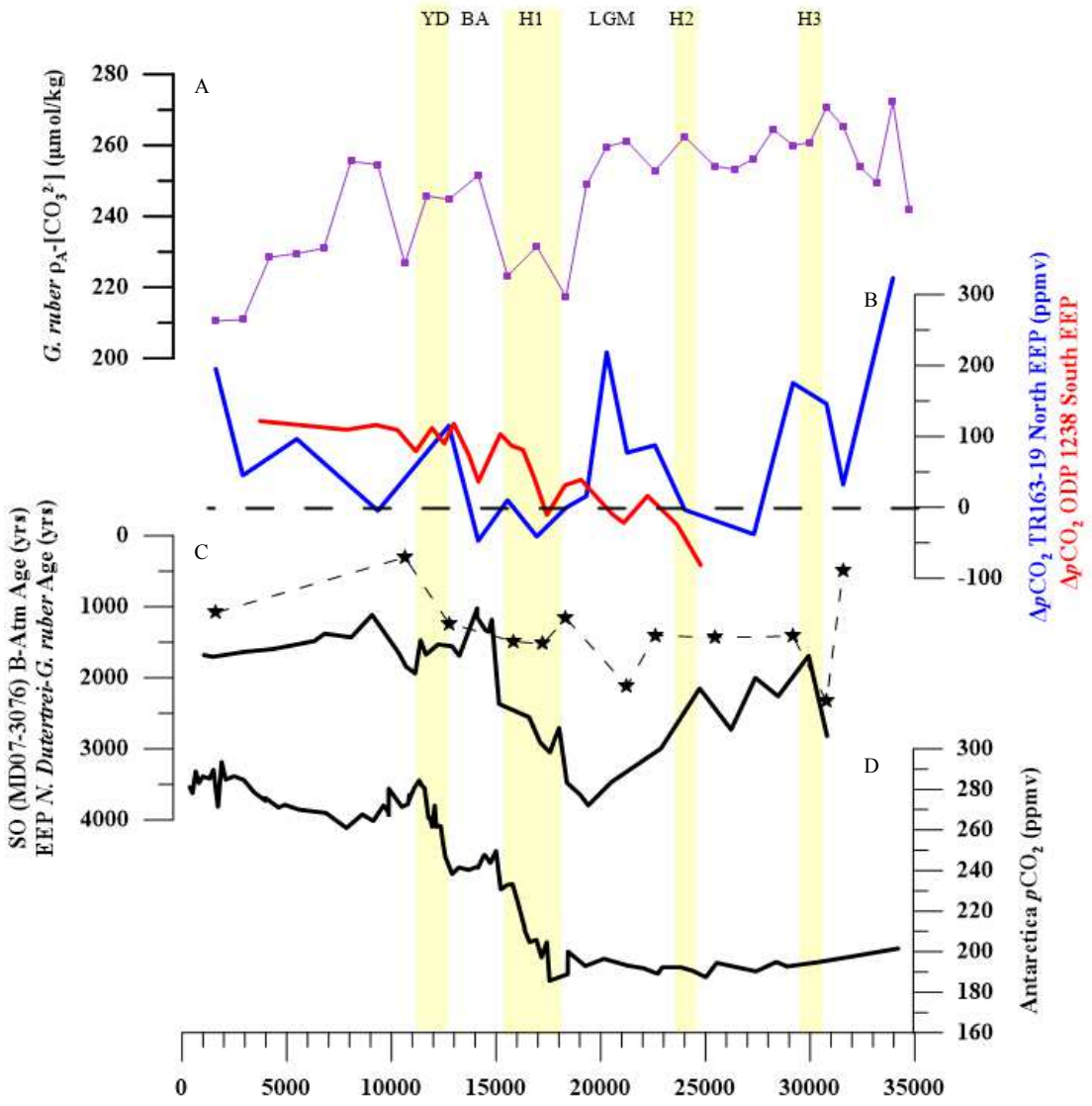

Figure 4.10 (a) TR163-19 *G. ruber* ρ_A- derived $[CO_3^{2-}]$. (b) ΔpCO_2 (pCO_{2aq} - pCO_{2atm}) for core TR163-19 (blue; this study) and ODP site 1238 (red; Marinez-Boti et al., 2015). (c) Deep water reservoir ages (benthic-atmosphere age offset, B-Atm) for S. Ocean core MD07-3076 (black solid line) and raw ^{14}C age offsets between *N dutertrei* and *G. ruber* ($\Delta^{14}C_{duter\text{-}ruber}$) for core TR163-19 (black stars and dashed line) (d) Record of compiled Antarctic ice core CO_2 concentrations from Luthi et al. (2008).

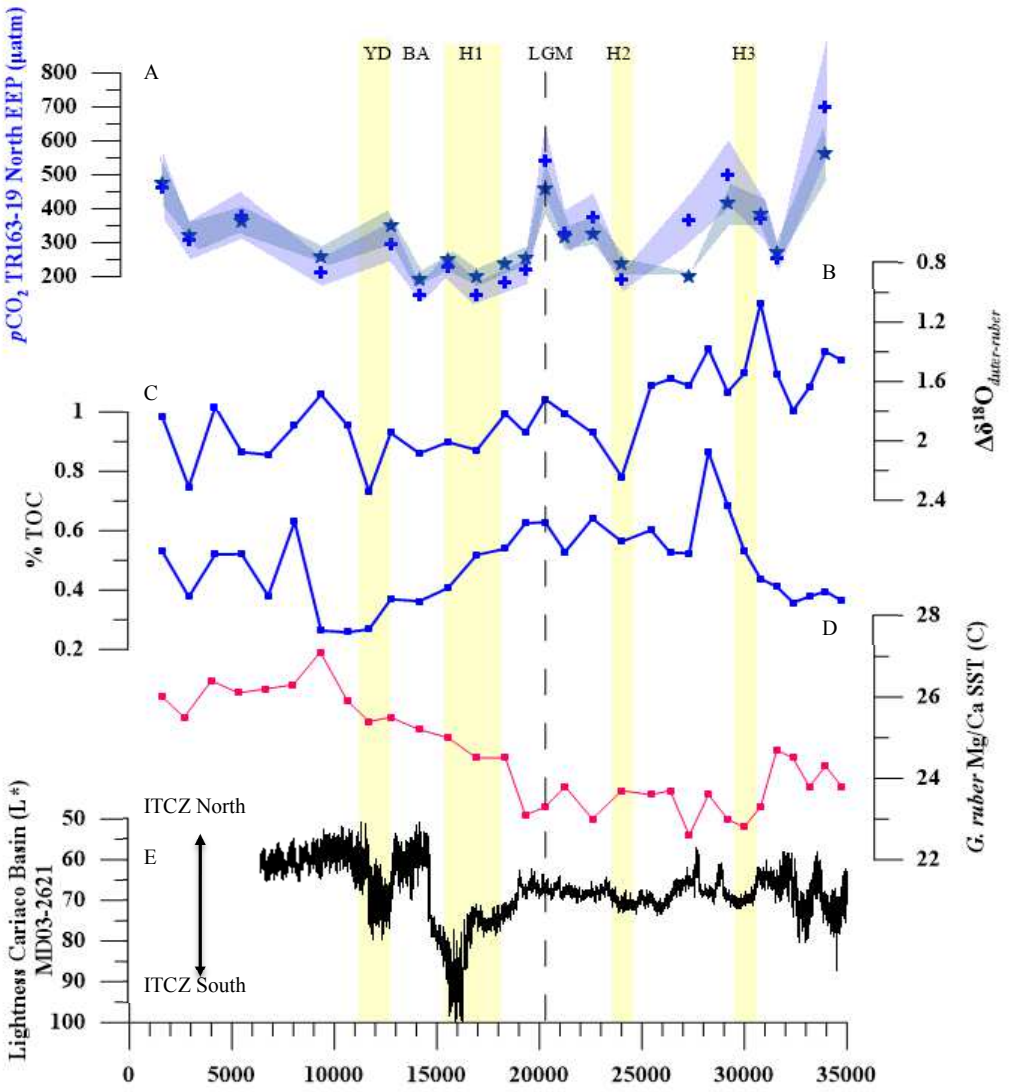

Figure 4.11 (a) Calculated pCO_{2aq} for core TR163-19 using $[CO_3^{2-}]$ and pH (electric blue) and TA_{SAL} and pH (navy blue). (b) $\delta^{18}O$ offset between *Globigerinoides ruber* and *N. dutertrei* ($\Delta\delta^{18}O_{duter-ruber}$), lower values represent periods of enhanced surface-ocean mixing. (C) % TOC, higher values represent increased surface ocean productivity. (D) Reconstructed paleotemperatures for *G. ruber* (pink, Mg/Ca, Lea et al., 2002). (E) Cariaco Basin reflectance data from Deplazes et al. (2013).

REFERENCES

Aldridge, D., C. J. Beer, and D. A. Purdie (2012), Calcification in the planktonic foraminifera *Globigerina bulloides* linked to phosphate concentrations in surface waters of the North Atlantic Ocean, *Biogeosciences*, *9*(5), 1725–1739, doi:10.5194/bg-9-1725-2012.

Aggarwal, J. et al. (2009), How well do non-traditional stable isotope results compare between different laboratories: results from the interlaboratory comparison of boron isotope measurements. J. Anal. At. Spectrom., 24(6), pp.825–831.

Ahn, J. & Brook, E. J. (2007), Atmospheric CO2 and climate from 65 to 30 ka B.P. Geophys Res. Lett. 34, doi:10.1029/2007GL029551.

Anderson, R. F., S. Ali, L. I. Bradtmiller, S. H. H. Nielsen, M. Q. Fleisher, B. E. Anderson, and L. H. Burckle (2009), Wind-driven upwelling in the Southern Ocean and the deglacial rise in atmospheric CO2, *science*, *323*(5920), 1443–1448.

Anderson, R. F., and M.-E. Carr (2010), Uncorking the Southern Ocean's Vintage CO2, *Science*, *328*(5982), 1117–1118, doi:10.1126/science.1190765.

Archer, D., Winguth, A., Lea, D.W., Mahowald, N., 2000. What caused the glacial/interglacial atmospheric pCO2 cycles. Rev. Geophys. 38, 159–189.

Armstrong, R. A., C. Lee, J. I. Hedges, S. Honjo, and S. G. Wakeham (2001), A new, mechanistic model for organic carbon fluxes in the ocean based on the quantitative association of POC with ballast minerals, *Deep Sea Research Part II: Topical Studies in Oceanography*, *49*(1), 219–236, doi:10.1016/S0967-0645(01)00101-1.

Astor, Y. M., M. I. Scranton, F. Muller-Karger, R. Bohrer, and J. García (2005), fCO2 variability at the CARIACO tropical coastal upwelling time series station, *Marine Chemistry*, *97*(3-4), 245–261, doi:10.1016/j.marchem.2005.04.001.

Astor, Y., Lorenzoni, L., Thunell, R., Varela, R., Muller-Karger, F., Troccoli, L., Taylor, G., Scranton, M., Tappa, E., and Rueda, D. (2013), Interannual variability in sea surface temperature and fCO2 changes in the Cariaco Basin, Deep Sea Research II, 93, 33-43.

Aurahs, R., Y. Treis, K. Darling, and M. Kucera (2011), A revised taxonomic and phylogenetic concept for the planktonic foraminifer species Globigerinoides ruber based on molecular and morphometric evidence, *Marine Micropaleontology*, *79*(1-2), 1–14, doi:10.1016/j.marmicro.2010.12.001.

Banderas, R., J. Álvarez-Solas, and M. Montoya (2012), Role of CO₂ and Southern Ocean winds in glacial abrupt climate change, *Climate of the Past*, *8*(3), 1011–1021, doi:10.5194/cp28-1011-2012.

Barker, S., and Elderfield, H. (2002), Foraminiferal Calcification Response to Glacial-Interglacial Changes in Atmospheric CO2, *Science*, *297*(5582), 833–836, doi:10.1126/science.1072815.

Barker, S., P. Diz, M. J. Vautravers, J. Pike, G. Knorr, I. R. Hall, and W. S. Broecker (2009), Interhemispheric Atlantic seesaw response during the last deglaciation, *Nature*, *457*(7233), 1097–1102, doi:10.1038/nature07770.

Barker, S., and P. Diz (2014), Timing of the descent into the last Ice Age determined by the bipolar seesaw, *Paleoceanography*, *29*(6), 489–507, doi:10.1002/2014PA002623.

Barker, S. (2004), Temporal changes in North Atlantic circulation constrained by planktonic foraminiferal shell weights, *Paleoceanography*, *19*(3), doi:10.1029/2004PA001004.

Bé, A. W. H. (1959), A method for rapid sorting of foraminifera from marine plankton samples, *Journal of Paleontology*, *33*(5), 846–848.

Bé, A. W. H., S. M. Harrison, and L. Lott (1973), Orbulina universa d'Orbigny in the Indian Ocean, *Micropaleontology*, *19*(2), 150–192.

Bé, A. W. H. (1980), Gametogenic calcification in a spinose planktonic foraminifer, Globigerinoides-sacculifer (Brady), *Marine Micropaleontology*, *5*(3), 283–310, doi:10.1016/0377-8398(80)90014-6.

Bé, A. W. H., Anderson 0. R., and Caron, D. A. (1983), Sequence of morphological and cytoplasmic changes during gametogenesis in the planktonic foraminifer Globigerinoides sacculifer (Brady). Micropaleontology 29:1-5.

Beer, C. J., R. Schiebel, and P. A. Wilson (2010a), Technical Note: On methodologies for determining the size-normalised weight of planktic foraminifera, *Biogeosciences*, *7*(7), 2193–2198, doi:10.5194/bg-7-2193-201.

Beer, C. J., R. Schiebel, and P. A. Wilson (2010b), Testing planktic foraminiferal shell weight as a surface water [CO32-] proxy using plankton net samples, *Geology*, *38*(2), 103–106. doi: 10.1130/G30150.1.

Bemis, B. E., H. J. Spero, J. Bijma, and D. W. Lea (1998), Reevaluation of the oxygen isotopic composition of planktonic foraminifera: Experimental results and revised paleotemperature equations, *Paleoceanography*, *13*(2), 150–160, doi:10.1029/98PA00070.

Bemis, B. E., H. J. Spero and R. C. Thunell (2002), Using species-specific paleotemperature equations with foraminifera: a case study in the Southern California Bight. *Mar. Micropaleontol*. 46:405-430. (61).

Bentov, S., C. Brownlee, and J. Erez (2009), The role of seawater endocytosis in the biomineralization process in calcareous foraminifera, *Proceedings of the National Academy of Sciences*, *106*(51), 21500–21504.

Benway, H. M., and A. C. Mix (2004), Oxygen isotopes, upper-ocean salinity, and precipitation sources in the eastern tropical Pacific, *Earth and Planetary Science Letters*, *224*(3-4), 493–507, doi:10.1016/j.epsl.2004.05.014.

Billups, K. and H.J. Spero, (1995), Relationship between shell size, thickness and stable isotopes in individual planktonic foraminifera from two equatorial Atlantic cores. *Journal of Foraminiferal Research*, *25*(1), 24–37, doi: 10.2113/gsjfr.25.1.24

Bijma, J., J. Erez, and C. Hemleben (1990), Lunar and semi-lunar reproductive cycles in some spinose planktonic foraminifers, *The Journal of Foraminiferal Research*, *20*(2), 117–127, doi:10.2113/gsjfr.20.2.117.

Bijma, J., C. Hemleben, H. Oberhaensli, and M. Spindler (1992), The effects of increased water fertility on tropical spinose planktonic foraminifers in laboratory cultures, *The Journal of Foraminiferal Research*, *22*(3), 242–256, doi:10.2113/gsjfr.22.3.242.

Bijma, J., Hemleben, C., Huber, B.T., Erlenkeuser, H., Kroon, D. (1998), Experimental determination of the ontogenetic stable isotope variability in two morphotypes of< i> Globigerinella siphonifera</i>(d'Orbigny). Marine Micropaleontology 35, 141–160.

Bijma, J., H. J. Spero, and D. W. Lea (1999). Reassessing foraminiferal stable isotope geochemistery: Impact of the oceanic carbonate system (experimental results), in: Uses of Proxies in Paleoceanography: Examples from the South Atlantic, edited by: G. Fischer and G. Wefer, pp. 489– 512, Springer Verlag, Berlin-Heidelberg, doi: 10.1007/978-3-642-58646-0_20.

Bijma, J., B. Honisch, and R. E. Zeebe (2002), Impact of the ocean carbonate chemistry on living foraminiferal shell weight: Comment on "Carbonate ion concentration in glacial-age deep waters of the Caribbean Sea" by W. S. Broecker and E. Clark, *Geochemistry Geophysics Geosystems*, *3*(11), doi:10.1029/2002GC000388.

Bouvier-Soumagnac, Y., and Duplessy, J.C. (1985). Carbon and oxygen isotopic composition of planktonic foraminifera from laboratory cultures, plankton tows, and recent sediments: Implications for the reconstruction of paleoclimatic conditions and the global carbon cycle: Journal of Foraminiferal Research, v. 15, p. 302-320.

Broecker, W. S. (1998), Paleocean circulation during the Last Deglaciation: A bipolar seesaw?,Paleoceanography, 13(2), 119–121, doi:10.1029/97PA03707.

Broecker, W., and E. Clark (2001a), A dramatic Atlantic dissolution event at the onset of the last glaciation, *Geochemistry, Geophysics, Geosystems*, *2*(11), n/a–n/a, doi:10.1029/2001GC000185.

Bradshaw, J.S. (1959). Ecology of living planktonic foraminifera in the North and equatorial Pacific Ocean. Cushman Found. Foram. Res. Contrib. 10, 25–64.

Caldiera, K., and M. E. Wickett (2003), Anthropogenic carbon and ocean pH, *Nature*, *425*(6956), 365–365. doi:10.1038/425365a.

Caron, D.A., Faber, W.W., Jr., Bé, A.W.H. (1987). Growth of the spinose planktonic foraminifer *Orbulina universa* in laboratory culture and the effect of temperature on life processes. J. mar. Biol. Ass. U.K. 67, 343-358.

Caron, D. A., O. R. Anderson, J. L. Lindsey, W. W. Faber, and E. L. Lim (1990), Effects of gametogenesis on test structure and dissolution of some spinose planktonic-foraminfera and implications for test preservation, *Marine Micropaleontology*, *16*(1-2), 93–116, doi:10.1016/0377-8398(90)90031-G.

Catanzaro, E.J., et al. (1970), Boric assay; isotopic, and assay standard reference materials. US Natl. Bur. Stan. Spec. Publ. 260 (17), 70.

Colombo, M.R., Cita, M.B. (1980), Changes in size and test porosity of Orbulina universa d'Orbigny in the Pleistocene record of Cape Bojador (DSDP Site 397, Eastern North Atlantic). Marine Micropaleontology 5, 13–29.

Darling, K.F., Kroon, D., Wade, C.M., Leigh Brown, A.J. (1996), Molecular phylogeny of the planktonic foraminifera. J. Foram. Res. 26, 324–330.

Darling, K.F., Wade, C.M., Kroon, D., Leigh Brown, A.J. (1997), Planktonic foraminiferal molecular evolution and their polyphyletic origins from benthic taxa. Mar. Micropaleontol. 30, 251–266.

Darling, K. F., Wade, C. M., Kroon, D., Leigh Brown, A. J. & Bijma, J. (1999), The diversity and distribution of modern planktonic foraminiferal small subunit ribosomal RNA genotypes and their potential as tracers of present and past ocean circulations. Paleoceanography 14, 3–12.

Darling, K.F., Wade, C.M. (2008), The genetic diversity of planktic foraminifera and the global distribution of ribosomal RNA genotypes. Marine Micropaleontology 67, 216–238. doi:10.1016/j.marmicro.2008.01.009.

De Moel, H., G. M. Ganssen, F. J. C. Peeters, S. J. A. Jung, D. Kroon, G. J. A. Brummer, and R. E. Zeebe (2009), Planktic foraminiferal shell thinning in the Arabian Sea due to anthropogenic ocean acidification?, *Biogeosciences*, *6*(9), 1917–1925, doi:10.5194/bg-6-1917-2009.

de Vargas, C., Zaninetti, L., Hilbrecht, H. & Pawlovski, J. (1997), Phylogeny and rates of molecular evolution of planktonic foraminifera: SSU rDNA sequences compared to the fossil record. J. Mol. Evol. 45, 285–294.

de Vargas, C., Norris, R., Zaninetti, L., Gibb, S.W., Pawlowski, J. (1999) Molecular evidence of cryptic speciation in planktonic foraminifers and their relation to oceanic provinces. Proceedings of the National Academy of Sciences 96, 2864–2868.

de Vargas, C., Saez, A.G., Medlin, L., Thierstein, H.R. (2003), Super-species in the calcareous plankton. In: Thierstein, H.R., Young, J.R. (Eds.), Coccolithophores, from Molecular Processes to Global Impact. Springer, Berlin, pp. 271–298.

De Villiers, S. (2004), Optimum growth conditions as opposed to calcite saturation as a control on the calcification rate and shell-weight of marine foraminifera, *Marine Biology*, *144*(1), 45–49, doi:10.1007/s00227-003-1183-8.

Deplazes, G. et al. (2013), Links between tropical rainfall and North Atlantic climate during the last glacial period, *Nature Geoscience*, *6*(3), 213–217, doi:10.1038/ngeo1712.

Deuser, W.G., E.H. Ross, C. Hemleben, and M. Spindler (1981), Seasonal changes in species composition, numbers, mass, size, and isotopic composition of planktonic foraminifera settling into the deep Sargasso Sea, Palaeogeogr., Palaeoclimatol. Palaeoecol3., 33, 103-127.

Deuser, W. G. (1987), Seasonal variations in isotopic composition and deep-water fluxes of the tests of perennially abundant planktonic foraminifera of the Sargasso Sea: Results from sediment-trap collections and their paleoceanographic significance, J. Foraminiferal Res., 17(1), 14– 27.

Deuser, W. G., and E. H. Ross (1989), Seasonally abundant planktonic foraminifera of the Sargasso Sea: Succession, deep-water fluxes, isotopic compositions, and paleoceanographic implications, J. Foraminiferal Res., 19(4), 268– 293.

Dickson, A. G. (1990), Thermodynamics of the dissociation of boric-acid in synthetic seawater from 273.15-K to 318.15-K, *Deep-Sea Research Part A-Oceanographic Research Papers*, *37*(5), 755–766, doi:10.1016/0198-0149(90)90004-F.

Douville, E., Paterne, M., Cabioch, G., Louvat, P., Gaillardet, J., Juillet-Leclerc, A., Ayliffe, L. (2010), Abrupt sea surface pH change at the end of the Younger Dryas in the central sub-equatorial Pacific inferred from boron isotope abundance in corals (<i>Porites</i>). Biogeosciences 7, 2445–2459. doi:10.5194/bg-7-2445-2010.

Elderfield, H., Vautravers, M., Cooper, M. (2002), The relationship between shell size and Mg/Ca, Sr/Ca, δ^{18}O, and δ^{13}C of species of planktonic foraminifera: PLANKTONIC FORAMINIFERA. Geochemistry, Geophysics, Geosystems 3, 1–13. doi:10.1029/2001GC000194.

Erez, J. (1978), Vital effect on stable-isotope composition seen in foraminifera and coral skeletons, *Nature*, *273*(5659), 199–202, doi:10.1038/273199a0.

Farmer, E. C., A. Kaplan, P. B. de Menocal, and J. Lynch-Stieglitz (2007), Corroborating ecological depth preferences of planktonic foraminifera in the tropical Atlantic with the stable oxygen isotope ratios of core top specimens, *Paleoceanography*, *22*(3), doi:10.1029/2006PA001361.

Feely, R. A., Sabine, C.L., Lee, K., Berelson, W., J. A. Kleypas, V. J. Fabry, and Millero, F.J. (2004), Impact of Anthropogenic CO2 on the CaCO3 System in the Oceans, *Science*, *305*(5682), 362–366, doi:10.1126/science.1097329.

Feldberg, M.J., Mix, A.C. (2003), Planktonic foraminifera, sea-surface temperatures, and mechanisms of oceanic change in the Peru and south Equatorial Currents,0e150 ka BP. Paleoceanography 18, 1016.

Foster, G.L. (2008), Seawater pH, pCO2 and [CO2−3] variations in the Caribbean Sea over the last 130 kyr: A boron isotope and B/Ca study of planktic foraminifera. Earth and Planetary Science Letters 271, 254–266. doi:10.1016/j.epsl.2008.04.015.

Foster, G. L., C. H. Lear, and J. W. B. Rae (2012), The evolution of pCO2, ice volume and climate during the middle Miocene, *Earth and Planetary Science Letters*, *341-344*, 243–254, doi:10.1016/j.epsl.2012.06.007.

Foster, G.L., Hönisch, B., Paris, G., Dwyer, G.S., Rae, J.W.B., Elliott, T., Gaillardet, J., Hemming, N.G., Louvat, P., Vengosh, A. (2013), Interlaboratory comparison of boron isotope analyses of boric acid, seawater and marine CaCO3 by MC-ICPMS and NTIMS. Chemical Geology 358, 1–14. doi:10.1016/j.chemgeo.2013.08.027.

Friedrich, O., Schiebel, R., Wilson, P.A., Weldeab, S., Beer, C.J., Cooper, M.J., Fiebig, J. (2012), Influence of test size, water depth, and ecology on Mg/Ca, Sr/Ca, δ18O and δ13C in nine modern species of planktic foraminifers. Earth and Planetary Science Letters 319-320, 133–145. doi:10.1016/j.epsl.2011.12.002.

Froelich, P.N. (1980), Analysis of organic carbon in marine sediments. Limnol. Oceanogr. 25: 564-575.

Gaillardet, J., Lemarchand, D., Göpel, C., Manhès, G. (2001), Evaporation and sublimation of boric acid: application for boron purification from organic rich solutions. Geostandards Newsletter 25, 67–75.

Gibbs, S. J., H. M. Stoll, P. R. Bown, and T. J. Bralower (2010), Ocean acidification and surface water carbonate production across the Paleocene–Eocene thermal maximum, *Earth and Planetary Science Letters*, *295*(3-4), 583–592, doi:10.1016/j.epsl.2010.04.044.

Goñi, M. A., H. L. Aceves, R. C. Thunell, E. Tappa, D. Black, Y. Astor, R. Varela, and F. Muller-Karger (2003), Biogenic fluxes in the Cariaco Basin: a combined study of sinking particulates and underlying sediments, *Deep Sea Research Part I: Oceanographic Research Papers*, *50*(6), 781–807, doi:10.1016/S0967-0637(03)00060-8.

Goni, M., Woodworth, M., Aceves, H., Thunell, R., Tappa, E., Black, D., MullerKarger, F. and Varela, R. (2004), Generation, Transport and preservation of the alkenone based UK37 sea surface temperature index in the water column and sediments of the Cariaco Basin, Venezuela. Global Biogeochemical Cycles 18, GB2001, doi:10.1029/2003GB002132.

Gonzalez-Mora, B., F. J. Sierro, and J. A. Flores (2008), Controls of shell calcification in planktonic foraminifers, *Quaternary Science Reviews*, *27*(9-10), 956–961, doi:10.1016/j.quascirev.2008.01.008.

Goodman, P. J., Hazeleger, W., De Vries, P. & Cane, M. (2005), Pathways into the Pacific equatorial undercurrent: a trajectory analysis. *J. Phys. Oceanogr.* **35**, 2134–2151.

Hamilton, C.P., Spero, H.J., Bijma, J., Lea, D.W. (2008), Geochemical investigation of gametogenic calcite addition in the planktonic foraminifera< i> Orbulina universa</i>. Marine Micropaleontology 68, 256–267.

Healy-William, N, Ehrlich, R., and Williams, D. F. (1985), Morphometric and stable isotopic evidence for subpopulations of Globorotalia truncatulinoides: Journal of Foraminiferal Research, v. 15, p. 242-243.

Hecht, A. D., and S. M. Savin (1972), Phenotypic variation and oxygen isotope ratios in Recent planktonic foraminifera, *The Journal of Foraminiferal Research*, *2*(2), 55–67, doi:10.2113/gsjfr.2.2.55.

Hecht, A. D. (1976), An ecologic model for test size variation in Recent planktonic foraminifera; applications to the fossil record, *The Journal of Foraminiferal Research*, *6*(4), 295–311, doi:10.2113/gsjfr.6.4.295.

Hemleben, C., M. Spindler and O. R. Anderson (1989). Modern Planktonic Foraminifera, pp. 363, Springer-Verlag, New York, doi: 10.1007/978-1-4612-3544-6.

Hemleben, C., Bijma, J. (1994), Foraminiferal population dynamics and stable carbon isotopes. In: Zahn, R. (Ed.), Carbon Cycling in the Glacial Ocean: Constraints on the Ocean's Role in Global Change. NATO ASI Series. Springer-Verlag, Berlin, pp. 145–166.

Hemming, N.G., Hanson, G.N. (1992), Boron isotopic composition and concentration in modern marine carbonates. Geochim. Cosmochim. Acta 56, 537–543.

Hemming, N.G., Hönisch, B. (2007), Chapter Seventeen Boron Isotopes in Marine Carbonate Sediments and the pH of the Ocean, in: Developments in Marine Geology. Elsevier, pp. 717–734.

Henehan, M. J. et al. (2013), Calibration of the boron isotope proxy in the planktonic foraminifera Globigerinoides ruber for use in palaeo-CO2 reconstruction, *Earth and Planetary Science Letters*, *364*, 111–122, doi:10.1016/j.epsl.2012.12.029.

Hoegh-Guldberg, O. et al. (2007), Coral Reefs Under Rapid Climate Change and Ocean Acidification, *Science*, *318*(5857), 1737–1742, doi:10.1126/science.1152509.

Honisch, B. et al. (2012), The Geological Record of Ocean Acidification, *Science*, *335*(6072), 1058–1063, doi:10.1126/science.1208277.

Huber, B.T., Bijma, J., Darling, K.F. (1997), Cryptic speciation in the living planktonic foraminifer Globigerinella siphonifera (d'Orbigny). Paleobiology 23, 33–62.

Iglesias-Rodriguez, M. D. et al. (2008), Phytoplankton Calcification in a High-CO2 World, *Science*, *320*(5874), 336–340, doi:10.1126/science.1154122.

Ishikawa, T., Nagaishi, K. (2011), High-precision isotopic analysis of boron by positive thermal ionization mass spectrometry with sample preheating. Journal of Analytical Atomic Spectrometry 26, 359. doi:10.1039/c0ja00060d.

Jorgensen, B. B., J. Erez, N. P. Revsbech, and Y. Cohen (1985), Symbiotic photosynthesis in a planktonic foraminiferan, Globigerinoides sacculifer (Brady), studied with microelectrodes1, *Limnol. Oceanogr*, *30*(6), 1253–1267.

Kennett, J. P. (1976), Phenotypic variation in some Recent and late Cenozoic planktonic foraminifera, in Hedley, R. H., and Adams, C. D. (eds.), Foraminifera, v. 2: Academic Press, London, p.111-169.

Kessler, W.S. (2006), The circulation of the eastern tropical Pacific: a review. Progress in Oceanography 69 (2–4), 181–217.

Kienast, M., S. S. Kienast, S. E. Calvert, T. I. Eglinton, G. Mollenhauer, R. François, and A. C. Mix (2006), Eastern Pacific cooling and Atlantic overturning circulation during the last deglaciation, Nature, 443, 846–849, doi:10.1038/nature05222.

King, A., and W. Howard (2005), delta O-18 seasonality of planktonic foraminifera from Southern Ocean sediment traps: Latitudinal gradients and implications for paleoclimate reconstructions, *Marine Micropaleontology*, *56*(1-2), 1–24, doi:10.1016/j.marmicro.2005.02.008.

Klaas, C., and D. E. Archer (2002), Association of sinking organic matter with various types of mineral ballast in the deep sea: Implications for the rain ratio, *Global Biogeochemical Cycles*, *16*(4), 63–1–63–14, doi:10.1029/2001GB001765.

Klochko, K., Kaufman, A.J., Yao, W., Byrne, R.H., Tossell, J.A. (2006), Experimental measurement of boron isotope fractionation in seawater. Earth and Planetary Science Letters 248, 276–285. doi:10.1016/j.epsl.2006.05.034.

Knowlton, N. (1993), Sibling species in the sea. A. Rev. Ecol. Syst. 24, 189–216.

Kucera, M., Darling, K.F. (2002), Cryptic species of planktonic foraminifera: their effect on palaeoceanographic reconstructions. Philosophical Transactions of the Royal Society A: Mathematical, Physical and Engineering Sciences 360, 695–718. doi:10.1098/rsta.2001.0962.

Kuroyanagi, A., M. Tsuchiya, H. Kawahata, and H. Kitazato (2008), The occurrence of two genotypes of the planktonic foraminifer Globigerinoides ruber (white) and paleo-environmental implications, *Marine Micropaleontology*, *68*(3-4), 236–243, doi:10.1016/j.marmicro.2008.04.004.

Lea, D.W., Martin, P.A., Chan, D.A., Spero, H.J. (1995), Calcum uptake and calcification rate in the planktonic foraminifer Orbulina universa. J. Foram. Res. 25 (1), 14–23.

Lea, D. W., T. A. Mashiotta, and Spero, H. J. (1999), Controls on magnesium and strontium uptake in planktonic foraminifera determined by live culturing, *Geochimica et Cosmochimica Acta*, *63*(16), 2369–2379.

Lea, D. W., Pak D. K., and Spero, H. J. (2000), Climate impact of late Quaternary equatorial Pacific sea surface temperature variations, Science, 289, 1719–1724.

Liu, Y.-W., Aciego, S.M., Wanamaker, A.D., Sell, B.K. (2013), A high-throughput system for boron microsublimation and isotope analysis by total evaporation thermal ionization mass spectrometry: New boron microsublimation technique and isotope analysis by TE-TIMS. Rapid Communications in Mass Spectrometry 27, 1705–1714. doi:10.1002/rcm.6619.

Lombard, F., L. Labeyrie, E. Michel, H. J. Spero, and D. W. Lea (2009), Modelling the temperature dependent growth rates of planktic foraminifera, *Marine Micropaleontology*, *70*(1-2), 1–7, doi:10.1016/j.marmicro.2008.09.004.

Lombard, F., R. E. da Rocha, J. Bijma, and J. P. Gattuso (2010), Effect of carbonate ion concentration and irradiance on calcification in planktonic foraminifera, *Biogeosciences*, *7*(1), 247–255, doi:10.5194/bg-7-247-2010.

Loubere, P., M. Richaud, and S. Mireles (2007), Variability in tropical thermocline nutrient chemistry on the glacial/interglacial timescale, *Deep Sea Research Part II: Topical Studies in Oceanography*, *54*(5-7), 747–761, doi:10.1016/j.dsr2.2007.01.005.

Lorenzoni, L., C. Hu, R. Varela, G. Arias, L. Guzman and F. Muller-Karger (2011), Bio-optical characteristics of Cariaco Basin (Caribbean Sea) waters. Continental Shelf Research, 31: 582–593.

Lueker, T. J., A. G. Dickson, and C. D. Keeling (2000), Ocean pCO2 calculated from dissolved inorganic carbon, alkalinity, and equations for K1 and K2: validation based on laboratory measurements of CO2 in gas and seawater at equilibrium, *Marine Chemistry*, *70*(1–3), 105 – 119, doi:10.1016/S0304-4203(00)00022-0.

Lüthi, D. et al. (2008), High-resolution carbon dioxide concentration record 650,000–800,000 years before present, *Nature*, *453*(7193), 379–382, doi:10.1038/nature06949.

Manno, C., N. Morata, and R. Bellerby (2012), Effect of ocean acidification and temperature increase on the planktonic foraminifer Neogloboquadrina pachyderma (sinistral), *Polar Biology*, *35*(9), 1311–1319, doi:10.1007/s00300-012-1174-7.

Marchitto, T. M., S. J. Lehman, J. D. Ortiz, J. Fluckiger, and A. van Geen (2007), Marine Radiocarbon Evidence for the Mechanism of Deglacial Atmospheric CO2 Rise, *Science*, *316*(5830), 1456–1459, doi:10.1126/science.1138679.

Marcott, S. A. et al. (2014), Centennial-scale changes in the global carbon cycle during the last deglaciation, *Nature*, *514*(7524), 616–619.

Marshall, B.J., Thunell, R.C., Henehan, M.J., Astor, Y., Wejnert, K.E. (2013), Planktonic foraminiferal area density as a proxy for carbonate ion concentration: A calibration study using the Cariaco Basin ocean time series: foraminiferal area density [CO32-] proxy. Paleoceanography 28, 363–376. doi:10.1002/palo.20034.

Martinez-Boti, M. A., Marino, G., Foster, G. L., Ziveri, P., Henehan, M. J., Rae, J. W. B., Mortyn, P. G., et al. (2015). Boron isotope evidence for oceanic carbon dioxide leakage during the last deglaciation. *Nature*, *518*(7538), 219-222. Nature Publishing Group, a division of Macmillan Publishers Limited. All Rights Reserved. Retrieved from http://dx.doi.org/10.1038/nature14155.

Mekik, F., and L. Raterink (2008), Effects of surface ocean conditions on deep-sea calcite dissolution proxies in the tropical Pacific, *Paleoceanography*, *23*(1), doi:10.1029/2007PA001433.

McConnell, M. C., R. C. Thunell, L. Lorenzoni, Y. Astor, J. D. Wright, and R. Fairbanks (2009), Seasonal variability in the salinity and oxygen isotopic composition of seawater from the Cariaco Basin, Venezuela: Implications for paleosalinity reconstructions, *Geochemistry Geophysics Geosystems*, *10*(6), doi:10.1029/2008GC002035.

Miles, J., and M. Shevlin (2001). Applying Regression and Correlation: a Guide for Student Researchers, Sage Publication, London.

Millero, F. J., W. Yao, K. Lee, J.-Z. Zhang, and D. M. Campbell (1998), Carbonate system in the waters near the Galapagos Islands, Deep Sea Res., Part II, 45, 1115–1134.

Misra, S., Owen, R., Kerr, J., Greaves, M., and Elderfield, H. (2014), Determination of δ11B by HR-10 ICP-MS from mass limited samples: application to natural carbonates and water samples,Geochim. Cosmochim. Ac., 140, 531–552, 2014.

Morard, R., Quillévéré, F., Escarguel, G., de Garidel-Thoron, T., de Vargas, C., Kucera, M. (2013), Ecological modeling of the temperature dependence of cryptic species of planktonic Foraminifera in the Southern Hemisphere. Palaeogeography, Palaeoclimatology, Palaeoecology 391, 13–33. doi:10.1016/j.palaeo.2013.05.011

Morard, R., Quillévéré, F., Escarguel, G., Ujiie, Y., de Garidel-Thoron, T., Norris, R.D., de Vargas, C. (2009), Morphological recognition of cryptic species in the planktonic foraminifer Orbulina universa. Marine Micropaleontology 71, 148–165. doi:10.1016/j.marmicro.2009.03.001.

Moy, A. D., W. R. Howard, S. G. Bray, and T. W. Trull (2009), Reduced calcification in modern Southern Ocean planktonic foraminifera, *Nature Geoscience*, *2*(4), 276–280, doi:10.1038/ngeo460.

Mulitza, S., T. Wolff, J. Pätzold, W. Hale, and G. Wefer (1998), Temperature sensitivity of planktic foraminifera and its influence on the oxygen isotope record, *Marine Micropaleontology*, *33*(3–4), 223 – 240, doi:10.1016/S0377-8398(97)00040-6.

Mulitza, S., D. Boltovskoy, B. Donner, H. Meggers, A. Paul, and G. Wefer, 2003, Temperature:$\delta^{18}O$ relationships of planktonic foraminifera collected from surface waters.: Palaeogeography, Palaeoclimatology, Palaeoecology, v. 202, p. 143-152, DOI:10.1016/S0031-0182(03)00633-3.

Muller-Karger, F. et al. (2000), Sediment record linked to surface processes in the Cariaco Basin, *Eos, Transactions American Geophysical Union*, *81*(45), 529–535, doi:10.1029/EO081i045p00529-01.

Muller-Karger, F. et al. (2001), Annual cycle of primary production in the Cariaco Basin: Response to upwelling and implications for vertical export, *Journal of Geophysical Research-Oceans*, *106*(C3), 4527–4542, doi:10.1029/1999JC000291.

Naik, S. S., and P. D. Naidu (2007), Calcite dissolution along a transect in the western tropical Indian Ocean: A multiproxy approach, *Geochemistry, Geophysics, Geosystems*, *8*(8), n/a–n/a, doi:10.1029/2007GC001615.

Naik, S. S., P. D. Naidu, P. Govil, and S. Godad (2010), Relationship between weights of planktonic foraminifer shell and surface water CO3= concentration during the Holocene and Last Glacial Period, *Marine Geology*, *275*(1-4), 278–282, doi:10.1016/j.margeo.2010.05.004.

Numberger, L., C. Hemleben, R. Hoffmann, A. Mackensen, H. Schulz, J.-M. Wunderlich, and M. Kucera (2009), Habitats, abundance patterns and isotopic signals of morphotypes of the planktonic foraminifer Globigerinoides ruber (d'Orbigny) in the eastern Mediterranean Sea since the Marine Isotopic Stage 12, *Marine Micropaleontology*, *73*(1-2), 90–104, doi:10.1016/j.marmicro.2009.07.004.

Okai, T. et al. (2002), Preparation of a New Geological Survey of Japan Geochemical Reference Material: Coral JCp-1. Geostandards Newsletter, 26(1), pp.95–99.

Ortiz, J.D., Mix, A.C., Wheeler, P.A. and Key, R.M. (2000), Anthropogenic CO2 invasion into the northeast Pacific based on concurrent d13C_DIC and nutrient profiles from the California Current, Global Biogeochemical Cycles, Vol. 14 , No. 3 , p. 917.

Orr, J. C. et al. (2005), Anthropogenic ocean acidification over the twenty-first century and its impact on calcifying organisms, *Nature*, *437*(7059), 681–686, doi:10.1038/nature04095.

Palmer, M.R. (2003), A 23,000-Year Record of Surface Water pH and PCO2 in the Western Equatorial Pacific Ocean. Science 300, 480–482. doi:10.1126/science.1080796

Pearson, P.N., Palmer, M.R. (2000), Atmospheric carbon dioxide concentrations over the past 60 million years. Nature 406, 695–699.

Pedersen, T. F., B. Nielsen, and M. Pickering (1991), Timing of late Quaternary productivity pulses in the Panama Basin and implications for atmospheric CO2, Paleoceanography, 6(6),657– 678,

Pelletier, G., E. Lewis, D. Wallace (2007) CO2sys_ver16.xls: A Calculator for the CO_2 System in Seawater for Microsoft Excel/VBA. Washington State Department of Ecology/Brookhaven National Laboratory, Olympia, WA/Upton, NY, USA.

Pennington, J. T., K. L. Mahoney, V. S. Kuwahara, D. D. Kolber, R. Calienes, and F. P. Chavez (2006), Primary production in the eastern tropical Pacific: A review, *Progress in Oceanography*, *69*(2-4), 285–317, doi:10.1016/j.pocean.2006.03.012.

Petit, R.J., Hu, F.S., Dick, C.W. (2008), Forests of the Past: A Window to Future Changes. Science 320, 1450–1452. doi:10.1126/science.1155457.

Rae, J.W.B., Foster, G.L., Schmidt, D.N., Elliott, T. (2011), Boron isotopes and B/Ca in benthic foraminifera: Proxies for the deep ocean carbonate system. Earth and Planetary Science Letters 302, 403–413. doi:10.1016/j.epsl.2010.12.034.

Rae, J.W.B., Sarnthein, M., Foster, G.L., Ridgwell, A., Grootes, P.M., Elliott, T. (2014), Deep water formation in the North Pacific and deglacial CO_2 rise: N Pacific deep water and deglacial CO2. Paleoceanography 29, 645–667. doi:10.1002/2013PA002570.

Ren, H., Sigman, D.M., Thunell, R.C., Prokopenko, M.G. (2012) Nitrogen isotopic composition of planktonic foraminifera from the modern ocean and recent sediments. Limnology and Oceanography 57, 1011–1024. doi:10.4319/lo.2012.57.4.1011.

Revelle, R. and Suess, H. E. (1957), Carbon Dioxide Exchange Between Atmosphere and Ocean and the Question of an Increase of Atmospheric CO_2 during the Past Decades. Tellus, 9: 18–27. doi: 10.1111/j.2153-3490.1957.tb01849.

Richey, J. N., R. Z. Poore, B. P. Flower, and D. J. Hollander (2012), Ecological controls on the shell geochemistry of pink and white Globigerinoides ruber in the northern Gulf of Mexico: Implications for paleoceanographic reconstruction, *Marine Micropaleontology*, *82-83*, 28–37, doi:10.1016/j.marmicro.2011.10.002.

Ridgwell, A., and R. Zeebe (2005), The role of the global carbonate cycle in the regulation and evolution of the Earth system, *Earth and Planetary Science Letters*, *234*(3-4), 299–315, doi:10.1016/j.epsl.2005.03.006.

Riebesell, U., I. Zondervan, B. Rost, P. Tortell, R. Zeebe, and F. Morel (2000), Reduced calcification of marine plankton in response to increased atmospheric CO2, *Nature*, *407*(6802), 364–367, doi:10.1038/35030078.

Ries, J. B., A. L. Cohen, and D. C. McCorkle (2009), Marine calcifiers exhibit mixed responses to CO2-induced ocean acidification, *Geology*, *37*(12), 1131–1134, doi:10.1130/G30210A.1.

Rink, S., M. Kühl, J. Bijma, and H. J. Spero (1998), Microsensor studies of photosynthesis and respiration in the symbiotic foraminifer Orbulina universa, *Marine Biology*, *131*(4), 583–595.

Russell, A. D., B. Hönisch, H. J. Spero, and D. W. Lea (2004), Effects of seawater carbonate ion concentration and temperature on shell U, Mg, and Sr in cultured planktonic foraminifera, *Geochimica et Cosmochimica Acta*, *68*(21), 4347–4361, doi:10.1016/j.gca.2004.03.013.

Sabine, C. L. et al. (2004), The Oceanic Sink for Anthropogenic CO2, *Science*, *305*(5682), 367–371, doi:10.1126/science.1097403.

Saito, T., Thompson, P. R., and Breger, D. (1981), Systematic Index of Recent and Pleistocene Planktonic Foraminifera: University of Tokyo Press, 190 p.

Sanyal A., Hemming N. G., Broecker W. S., Lea D. W., Spero H. J., and Hanson G. N. (1996), Oceanic pH control on the boron isotopic composition of foraminifera: Evidence from culture experiments. *Paleoceanography*, *11*(5), 513–517, doi: 10.1029/96PA01858.

Sanyal, A., N. G. Hemming, W. S. Broecker, and G. N. Hanson (1997), Changes in pH in the eastern equatorial Pacific across stage 5–6 boundary based on boron isotopes in foraminifera, Global Biogeochem. Cycles, 11(1), 125–133, doi:10.1029/97GB00223.

Sanyal, A., and J. Bijma (1999), A comparative study of the northwest Africa and eastern equatorial Pacific upwelling zones as sources of CO2 during glacial periods based on boron isotope paleo-pH estimation, Paleoceanography, 14(6), 753–759, doi:10.1029/1999PA900036.

Saikku, R., L. Stott, and R. Thunell (2009), A bi-polar signal recorded in the western tropical Pacific: Northern and Southern Hemisphere climate records from the Pacific warm pool during the last Ice Age, *Quaternary Science Reviews*, *28*(23-24), 2374–2385, doi:10.1016/j.quascirev.2009.05.007.

Sarmiento, J.L., Gruber, N., Brzezinski, M.A., Dunne, J.P., 2004. High-latitude controls of thermocline nutrients and low latitude biological productivity. Nature 427, 56e60.

Sautter, L.R., Thunell, R.C., 1991. Seasonal Variability in the δ18O and δ13C of Planktonic Foraminifera from an Upwelling Environment: Sediment Trap Results from the San Pedro Basin, Southern California Bight. Paleoceanography 6, 307–334. doi:10.1029/91PA00385.

Sautter, L. R., and R. C. Thunell (1991a), Seasonal Variability in the δ18O and δ13C of Planktonic Foraminifera from an Upwelling Environment: Sediment Trap Results

from the San Pedro Basin, Southern California Bight, *Paleoceanography*, *6*(3), 307–334, doi:10.1029/91PA00385.

Schiebel, R. (2002), Planktic foraminiferal sedimentation and the marine calcite budget, *Global Biogeochemical Cycles*, *16*(4), doi:10.1029/2001GB001459.

Schmidt, D. N., S. Renaud, J. Bollmann, R. Schiebel, and H. R. Thierstein (2004), Size distribution of Holocene planktic foraminifer assemblages: biogeography, ecology and adaptation, *Marine Micropaleontology*, *50*(3-4), 319–338, doi:10.1016/S0377-8398(03)00098-7.

Schmitt, J. (2012), Rise from Ice Cores 2 Carbon Isotope Constraints on the Deglacial CO, *Science*, *1217161*(711), 336.

Schmittner A, Galbraith ED (2008) Glacial greenhouse-gas fluctuations controlled by ocean circulation changes. Nature 456(7220):373–376.

Sigman, D. M., and E. A. Boyle (2000), Glacial/interglacial variations in atmospheric carbon dioxide, Nature, 407, 859–869.

Skinner, L. C., A. E. Scrivner, D. Vance, S. Barker, S. Fallon, and C. Waelbroeck (2013), North Atlantic versus Southern Ocean contributions to a deglacial surge in deep ocean ventilation, *Geology*, *41*(6), 667–670, doi:10.1130/G34133.1.

Skinner, L. C., C. Waelbroeck, A. E. Scrivner, and S. J. Fallon (2014), Radiocarbon evidence for alternating northern and southern sources of ventilation of the deep Atlantic carbon pool during the last deglaciation, *Proceedings of the National Academy of Sciences*, *111*(15), 5480–5484, doi:10.1073/pnas.1400668111.

Spero, H. J. (1987), Symbiosis in the planktonic foraminifer, Orbulina universa, and the isolation of its symbiotic dinoflagellate, Gymnodinium bdii sp. nov. J. Phycol. 23:307-317.

Spero, H. J. and De Niro, M.J. (1987), The influence of symbiont photosynthesis on the δO-18 and δC-13 values of planktonic foraminiferal calcite. Symbiosis, v. 4, p/ 213-228.

Spero, H. J. (1988), Ultrastructural examination of chamber morphogenesis and biomineralization in the planktonic foraminifer Orbulina universa: Marine Biology, v. 99, p. 9-20.

Spero, H. J. & Williams, D. F. (1988), Extracting environmental information from planktonic foraminiferal d13C data. Nature, 335, 717–719.

Spero, H. J., and Williams, D. F. (1989), Opening the carbon isotope "vital effect" black box. 1. Seasonal temperatures in the euphotic zone, Paleoceanography4,(6), 593-601.

Spero, H. J., Lerche, I. & Williams, D. F. (1991), Opening the carbon isotope "vital effect" black box, 2,quantitative model for interpreting foraminiferal carbon isotope data. Paleoceanography, 6, 639–655.

Spero, H. J. (1992), Do planktic foraminifera accurately record shifts in the carbon isotopic composition of seawater ΣCO2?, *Marine Micropaleontology*, *19*(4), 275–285, doi:10.1016/0377-8398(92)90033-G.

Spero, H. J., J. Bijma, D. W. Lea, and B. E. Bemis (1997), Effect of seawater carbonate concentration on foraminiferal carbon and oxygen isotopes, *Nature*, *390*, 497–500, doi:10.1038/37333.

Spero, H. J. (2002), The Cause of Carbon Isotope Minimum Events on Glacial Terminations, *Science*, *296*(5567), 522–525, doi:10.1126/science.1069401.

Spero, H. J., K. M. Mielke, E. M. Kalve, D. W. Lea, and D. K. Pak (2003), Multispecies approach to reconstructing eastern equatorial Pacific thermocline hydrography during the past 360 kyr, Paleoceanography, 18(1), 1022, doi:10.1029/2002PA000814.

Spero, H. J., S. M. Eggins, A. D. Russell, L. Vetter, M. R. Kilburn, and B. Hönisch (2015), Timing and mechanism for intratest Mg/Ca variability in a living planktic foraminifer, *Earth and Planetary Science Letters*, *409*, 32–42, doi:10.1016/j.epsl.2014.10.030.

Spivack, A.J., Edmond, J.M. (1987), Boron isotope exchange between seawater and the oceanic-crust. Geochimica et Cosmochimica Acta 51 (5), 1033–1043.

Spivack, A.J., You, C.-F., Smith, H.J. (1993), Foraminiferal boron isotope ratios as a proxy for surface ocean pH over the past 21 Myr. Nature 363, 149–151.

Steinke, S., Chiu, H. Y., Yu, P.S., Shen, C. C., Löwemark, L., Mii, H. S. and Chen, M. T. (2005), Mg/Ca ratios of two *Globigerinoides ruber* (white) morphotypes: Implications for reconstructing past tropical/subtropical surface water conditions: *G. RUBER* (WHITE) MG/CA RATIOS, *Geochemistry, Geophysics, Geosystems*, *6*(11), n/a–n/a, doi:10.1029/2005GC000926.

Stewart, I.A., Darling, K.F., Kroon, D., Wade, C.M., Troelstra, S.R., 2001. Genotypic variability on subarctic Atlantic planktic foraminifera. Mar. Micropaleontol. 43, 143–153.

Stuiver, M., Reimer, P. J., and Reimer, R. W. 2005. CALIB 5.0. [WWW program and documentation].

Takashi, O. et al. (2004), Collaborative analysis of GSJ/AIST geochemical reference materials JCp-1 (Coral) and JCt-1 (Giant Clam). Chikyu Kagaku, 38(4), pp.281–286.

Takahashi, K., and A. W. H. Be (1984), Planktonic-foraminifera - factors controlling sinking speeds, *Deep Sea Research Part A: Oceanographic Research Papers*, *31*(12), 1477–1500, doi:10.1016/0198-0149(84)90083-9.

Takahashi, T. et al. (2009), Climatological mean and decadal change in surface ocean pCO_2, and net sea-air CO_2 flux over the global oceans. *Deep-Sea Res. I* **56**, 2075–2076.

Tedesco, K., R. Thunell, Y. Astor, and F. Muller-Karger (2007), The oxygen isotope composition of planktonic foraminifera from the Cariaco Basin, Venezuela: Seasonal and interannual variations, *Marine Micropaleontology*, *62*(3), 180–193, doi:10.1016/j.marmicro.2006.08.002.

Tendal, 0. (1990), Why are Foraminiferida foraminifers? In C. Hemleben, M. A. Kaminski, W. Kuhnt, and D. B. Scott, eds. Paleocology, biostratigraphy, paleoceanography and taxonomy of agglutinated foraminifera. NATO ASI Series C 327:13- 18. Kluwer, Boston.

Toggweiler, J.R., Dixon, K., Broecker, W.S., 1991. The Peru upwelling and the ventilation of the South Pacific thermocline. Journal of Geophysical Research 96, 20467–20497.

Tolderlund, S., and BE, A. W. H. (1971), Seasonal distribution of planktonic foraminifera in the western North Atlantic: Micropaleontology, v. 17, p. 297-329.

Thunell, R. C., R. Varela, M. Llano, J. Collister, F. Muller-Karger, and R. Bohrer (2000), Organic carbon fluxes, degradation, and accumulation in an anoxic basin: Sediment trap results from the Cariaco Basin, *Limnology and Oceanography*, 300–308.

Turich, C., Schouten, H., Thunell, R., Varela, R., Astor, Y. and Wakeham, S. (2013), Comparison of TEX86 and temperature proxies in sinking particles in the Cariaco Basin, Deep-Sea Research 78, 115-133.

Van Hoecke, K., Devulder, V., Claeys, P., Degryse, P., Vanhaecke, F. (2014), Comparison of microsublimation and ion exchange chromatography for boron isolation preceding its isotopic analysis via multi-collector ICP-MS. J. Anal. At. Spectrom. 29, 1819–1826. doi:10.1039/C4JA00111G.

Vengosh, A., Starinsky, A., Kolodny, Y., Chivas, A.R. (1991), Boron-isotope geochemistry as a tracer for the evolution of brines and associated hot springs from the Dead Sea, Israel. Geochimica Cosmochimica Acta 55, 1689–1695.

Wang, L. (2000), Isotopic signals in two morphotypes of *Globigerinoides ruber* (white) from the South China Sea: implications for monsoon climate change during the last glacial cycle, *Palaeogeography, Palaeoclimatology, Palaeoecology*, *161*(3), 381–394.

Wang, B.S., You, C.F., Huang, K.F., Wu, S.F., Aggarwal, S.K., Chung, C.H., Lin, P.Y. (2010), Direct separation of boron from Na- and Ca-rich matrices by sublimation for stable isotope measurement by MC-ICP-MS. Talanta 82, 1378–1384. doi:10.1016/j.talanta.2010.07.010.

Wejnert, K. E. (2011), Seasonal and annual variability in elemental and isotopic proxies of past ocean conditions: Results from the Guaymas and Cariaco Basins, PhD dissertation, Marine Science Program, University of South Carolina (United States), 236 pp.

Wolf-Gladrow, D. A., J. Bijma, and R. E. Zeebe (1999), Model simulation of the carbonate chemistry in the microenvironment of symbiont bearing foraminifera, *Marine Chemistry*, *64*(3), 181–198, doi: 10.1016/S0304-4203(98)00074-7.

Wolff, E. W., J. Chappellaz, T. Blunier, S. O. Rasmussen, and A. Svensson (2010), Millennial-scale variability during the last glacial: The ice core record, *Quaternary Science Reviews*, *29*(21-22), 2828–2838, doi:10.1016/j.quascirev.2009.10.013.

Zeebe, R. E. (1999), An explanation of the effect of seawater carbonate concentration on foraminiferal oxygen isotopes, Geochim. Cosmochim. Acta, 63, 2001–2007.

Zeebe, R. E. and D. A. Wolf-Gladrow (2001), CO2 in Seawater: Equilibrium, Kinetics, Isotopes. Elsevier Oceanography Series, 65, pp. 346, Amsterdam.

Zeebe, R. E., J. C. Zachos, K. Caldeira, and T. Tyrrell (2008), Carbon Emissions and Acidification, *Science*, *321*(5885), 51–52, doi:10.1126/science.1159124.

Zeebe, R. E. (2012), History of Seawater Carbonate Chemistry, Atmospheric CO2, and Ocean Acidification, *Annual Review of Earth and Planetary Sciences*, *40*(1), 141–165, doi:10.1146/annurev-earth-042711-105521.

APPENDIX A – CHAPTER 1 COPYRIGHT PERMISSIONS

JOHN WILEY AND SONS LICENSE TERMS AND CONDITIONS

Mar 03, 2015

This Agreement between Brittney J Marshall ("You") and John Wiley and Sons ("John Wiley and Sons") consists of your license details and the terms and conditions provided by John Wiley and Sons and Copyright Clearance Center.

License Number	3581540190248
License date	Mar 03, 2015
Licensed Content Publisher	John Wiley and Sons
Licensed Content Publication	Paleoceanography
Licensed Content Title	Planktonic foraminiferal area density as a proxy for carbonate ion concentration: A calibration study using the Cariaco Basin ocean time series
Licensed Content Author	Brittney J. Marshall,Robert C. Thunell,Michael J. Henehan,Yrene Astor,Katherine E. Wejnert
Licensed Content Date	Jun 30, 2013
Pages	14
Type of use	Dissertation/Thesis
Requestor type	Author of this Wiley article
Format	Print and electronic
Portion	Full article
Will you be translating?	No
Title of your thesis / dissertation	PROXY DEVELOPMENT AND APPLICATION FOR THE SURFACE OCEAN CARBONATE SYSTEM
Expected completion date	Mar 2015
Expected size (number of pages)	200